University of Southampton

Diamond Light Source

ISIS Neutron and Muon Source

Faculty of Engineering and Physical Sciences

School of Chemistry

Electrodeposition of 3D Nanostructured Materials Using a Lyotropic Liquid Crystal Template

Joshua White

Thesis for the degree of Doctor of Philosophy

Supervisors:

Dr. Iris Nandhakumar, Dr. Nick Terrill, Dr. Diego Alba Venero

Dr. Chris Nicklin, Dr. Neil White

Abstract

This thesis explores the technique of electrodeposition of materials through liquid crystal templates. Electrodeposition through liquid crystal templates offers a promising technique which enables us to fabricate intricate and ordered nanomaterials which have enhanced catalytic performance and properties. The liquid crystal phase of interest is the double diamond phase formed by the non-ionic surfactant phytantriol and its derivates with the addition of Brij-56. The main objective of this work is to deposit cadmium telluride (CdTe), platinum (Pt) and palladium (Pd) through this soft-template, and the characterisation of the resulting nanostructured materials using a wide array of techniques such as scanning electron microscopy (SEM), transmission electron microscopy (TEM), X-ray diffraction (XRD), energy dispersive X-ray spectroscopy (EDX), electrochemistry and small-angle X-ray scattering (SAXS). Another goal for this work is to design and develop a 3D printable electrochemical cell which enables in-situ small angle scattering experiments that is capable of monitoring the templated electrodeposition process.

Utilising the phytantriol/Brij-56 as a scaffold, electrodeposition was employed to successfully fabricate stoichiometric mesoporous CdTe as revealed by EDX. TEM revealed that the resulting CdTe had a 3D mesoporous morphology with an average nanowire diameter of 5.3 ± 0.8 nm and an average pore width of 7.0 ± 1.2 nm. Reflectivity measurements were used to determine the band gap of the nanostructured CdTe, which was calculated to be 1.65 ± 0.06 eV, which is an increase from 1.45 eV for bulk CdTe showing how the resulting morphology of the material influences its properties.

By varying the amount of Brij-56 in the phytantriol we could electrodeposit Pd with a single diamond phase with control over the lattice size. By increasing the Brij-56 content in the template we saw an increase in lattice parameter and nanowire diameter of resulting Pd. By adding 20 weight percent (wt%) Brij-56 to the phytantriol we increased the lattice parameter and nanowire diameter of the Pd from 143.7 ± 1.6 Å and 2.9 ± 0.1 nm to 217.3 ± 6.9 Å and 5.9 ± 0.3 nm. The lattice parameter in this work refers to the distance between repeating unit cells in the nanostructure or liquid crystal. It was found that the electrocatalytic performance of the single diamond Pd was size dependent for the electrooxidation of formic acid. There was an increase in peak current density of 177 A g^{-1} for the Pd with larger lattice parameter

produced from phytantriol with 20 wt% Brij-56. This work highlighted that by tuning the size of the resulting nanostructure we can alter the catalytic performance of the material.

For the first time the single diamond phase of Pt produced by electrodeposition through phytantriol was tested for its performance for the oxygen reduction reaction in alkaline conditions. The resulting Pt showed comparable performance to commercial Pt/C with a positive shift in half-wave potential of 30 mV. The single diamond phase Pt showed enhanced durability compared to Pt/C with a lower relative loss in electroactive surface area after potential cycling.

Custom-made electrochemical cells were successfully designed, and 3D printed which provided bespoke sample environments for in-situ small angle scattering experiments. These cells were used in collaborative experiments with the University of Bath and the University of Glasgow, enabling a wide range of experiments to be performed on the DL-SAXS and I22 beamline at the Diamond Light Source, LoQ and ZOOM at ISIS Neutron and Muon Source. The experiments performed in these cells ranged from monitoring the electrodeposition of metals and semiconductors through liquid crystal templates to monitoring the growth of electropolymerised gels.

Contents

List of figures

Research Thesis: Declaration of Authorship

Print name: Joshua White

Title of thesis: Soft-templated 3D nanostructured materials via electrodeposition

I declare that this thesis and the work presented in it are my own and has been generated by me as the result of my own original research.

I confirm that:

1. This work was done wholly or mainly while in candidature for a research degree at this University;

2. Where any part of this thesis has previously been submitted for a degree or any other qualification at this University or any other institution, this has been clearly stated;

3. Where I have consulted the published work of others, this is always clearly attributed;

4. Where I have quoted from the work of others, the source is always given. With the exception of such quotations, this thesis is entirely my own work;

5. I have acknowledged all main sources of help;

6. Where the thesis is based on work done by myself jointly with others, I have made clear exactly what was done by others and what I have contributed myself;

7. None of this work has been published before submission

Signature: Date: 31/08/2024

Acknowledgements

I would like to express my deepest gratitude to my supervisors, Dr. Iris Nandhakumar, Dr. Nick Terrill and Dr. Diego Alba Venero for their guidance, invaluable insights, and encouragement throughout this journey. Your expertise and support have been instrumental in shaping this thesis and in my growth as a researcher.

I am profoundly grateful to my colleagues, particularly Dr. Samuel Perry at The University of Southampton whose stimulating discussions, and collaborative spirit have enriched my academic experience. Their diverse perspectives and knowledge have been a source of inspiration and have significantly contributed to the development of this work. A massive thanks is also in order for Wanli Liu, Stephen Williams, Jack Macklin and Dr. Adam Squires who joined me for long shifts during beamtime experiments.

Special thanks are due to my girlfriend, Lia Bennett, whose patience, love, and belief in me have been my pillar of strength during the highs and lows of this academic pursuit. Your understanding, encouragement, and support have been the cornerstone of my perseverance.

List of abbreviations

AFC - Alkaline fuel cells

BSE - Backscattered electrons

CV – Cyclic voltammetry

D-phytantriol – Deuterated phytantriol

EDX - Energy dispersive X-ray

EDTA - Ethylenediaminetetraacetic acid

ECSA - electroactive surface area

FAO - Formic acid oxidation

FC-12 - Dodecyl (ferrocenylmethyl) dimethylammonium bromide

FTO - Fluorine doped tin oxide

HCPA - hexachloroplatinic acid

ITO - Indium tin oxide

LSV – Linear sweep voltammetry

MO - Monoolein

ORR - Oxygen reduction reaction

RDE - Rotating disc electrode

SAS - Small angle scattering

SAXS - Small angle X-ray scattering

SANS - Small angle neutron scattering

SCE - Saturated calomel electrode

SEM - Scanning electron microscopy

SE - Secondary electrons

SD-Pt - Single diamond Pt

TEM - Transmission electron microscopy

Wt% - Weight percent

XRD - X-ray diffraction

HIM – Helium ion microscopy

DVD – Digital versatile disc

1. Introduction

1.1. Liquid crystal templating

Liquid crystals are a type of material that combine properties of both liquids (flow) and solid crystals (anisotropic physical parameters). There are two main groups of liquid crystals, thermotropic and lyotropic, for this project lyotropic liquid crystals will be used. Lyotropic liquid crystals are those formed from the dissolution of amphiphilic molecules in a polar solvent. Amphiphilic molecules possess both hydrophobic (non-polar) and hydrophilic (polar) regions, typically in the form of a polar head group and a non-polar hydrocarbon tail. These amphiphilic lipids can form different lyotropic liquid crystal phases such as micellar, lamellar, hexagonal, and cubic. The parameters that determine what phases are formed are the concentrations of the material in the solvent, the type of solvent, the material, and the temperature. Common lyotropic liquid crystal phases that can be formed from amphiphilic molecules are illustrated in Figure 1 below. These molecules self-organise into liquid crystals to maximise favourable interactions with the solution.

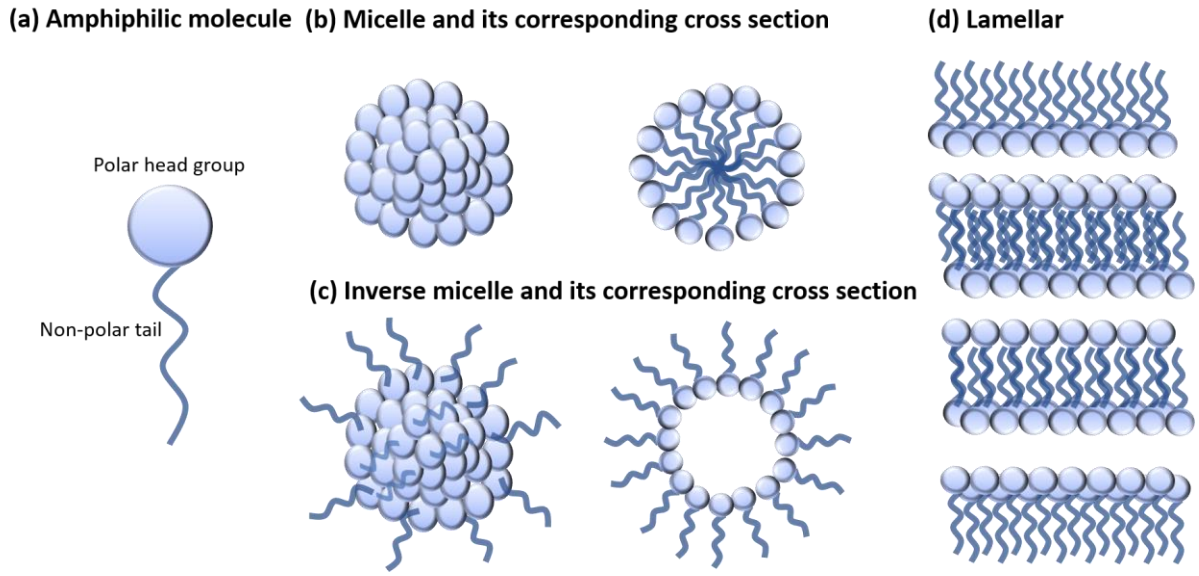

Figure 1 A figure depicting an amphiphilic molecule with a polar head group and a non-polar tail (a). Some of the common lyotropic liquid crystal phases such as micelle and its cross section (b), an inverse micelle and its cross section (c) and lamellar (c).

It has been seen in the literature that lyotropic liquid crystals have been successfully utilised as templates for nanostructuring various materials such as metals and semiconductors.[1–6] The process of liquid crystal templating involves using the ordered structures of liquids crystals as a scaffold to direct the growth of a material during the electrodeposition process. The deposited materials inherit structural features of the liquid crystal template, which can lead to complex architectures being formed. After deposition the template is removed by washing away the liquid crystal in a solvent, leaving behind the deposited material. A simple diagram of the liquid crystal templating process is shown in Figure 2, which shows a material being electrodeposited on a working electrode through a liquid crystal, followed by the removal of the template leaving behind the deposited material.

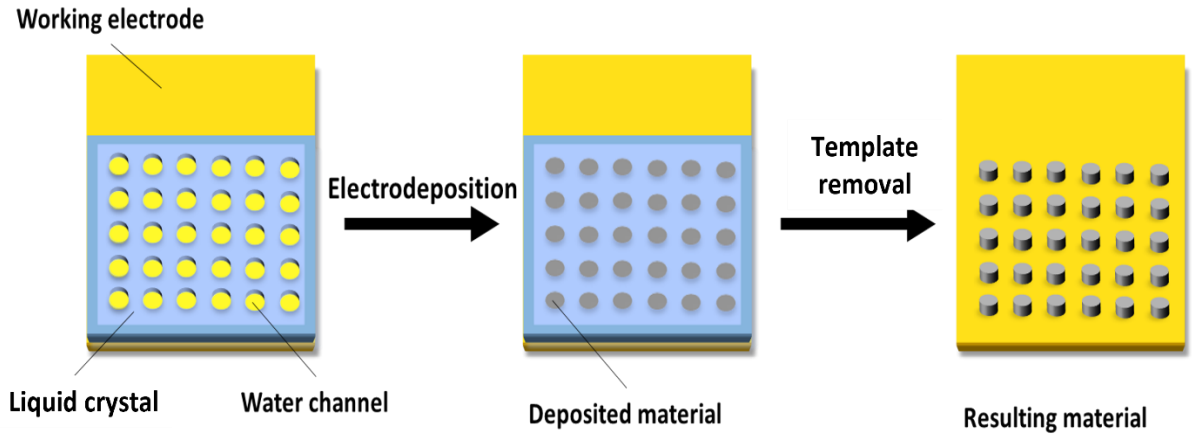

Figure 2 A simple diagram of the liquid crystal templating process, followed by template removal.

Attard *et al*.[7] at the University of Southampton were the first to create mesoporous Pt thin films by employing the electrodeposition of Pt through the hexagonal phase of the liquid crystal formed by $C_{16}EO_8$. The resulting Pt had a highly porous structure consisting of cylindrical holes of 25 ± 2 Å in diameter arranged on a hexagonal lattice revealed by TEM. Using cyclic voltammetry, the specific surface area of the fabricated Pt was determined to be 22 ± 2 $m^2 g^{-1}$ which was around 5 times higher than Pt grown in the absence of the template (4.5 ± 0.5 $m^2 g^{-1}$).

Gabriel *et al.*[6] successfully fabricated nanostructured tellurium dioxide films via electrodeposition using the hexagonal lyotropic liquid crystal phase of the non-ionic surfactant octaethyleneglycol monohexadecyl ether ($C_{16}EO_8$) as a template. This was achieved

by stepping the potential from 0.5 to -0.7 V vs SMSE (saturated mercurous sulphate electrode). After template removal by soaking in water, transmission electron microscopy (TEM) and small angle X-ray scattering (SAXS) revealed the resulting structure had hexagonal close-packed cylindrical pores with a pore diameter of 30 Å and a wall thickness of 28 Å.

For this project the molecule of interest is phytantriol, which is a non-ionic lipid surfactant, and its chemical structure is shown in Figure 3.

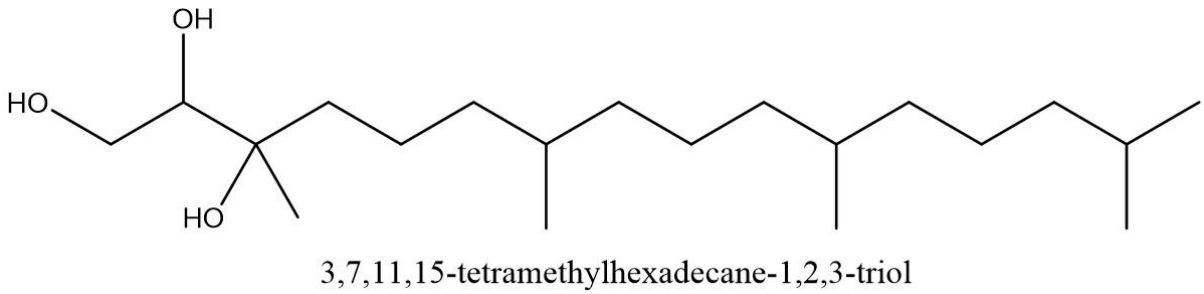

3,7,11,15-tetramethylhexadecane-1,2,3-triol

Figure 3. The chemical structure of phytantriol (3,7,11,15-tetramethylhexadecane-1,2,3-triol) created in ChemDraw 18.1

Phytantriol is of interest as a soft template due to the fact it forms an inverse bicontinuous cubic phase (Q_{224}), also called the double diamond phase, in excess water. Phytantriol is composed of a polar head group with three hydroxyl groups, and a long non-polar hydrocarbon tail. The combination of these regions results in two opposing forces when the molecule is exposed to water, the polar head group has an affinity for water whereas the non-polar hydrocarbon tail has repulsive interactions with water. The combination of these forces leads the molecule to form different liquid crystal phases, depending on the conditions, in order to satisfy these two forces. The phytantriol/water system was studied by Barauskas *et al.*[8] with the resulting phase diagram shown in Figure 4. From the phase diagram it can be seen that the double diamond (Q_{224}) phase is stable at room temperature in excess water. This makes phytantriol an ideal candidate as a soft template as it allows for aqueous electrolytes at ambient conditions to be used, which are attractive for electrodeposition.

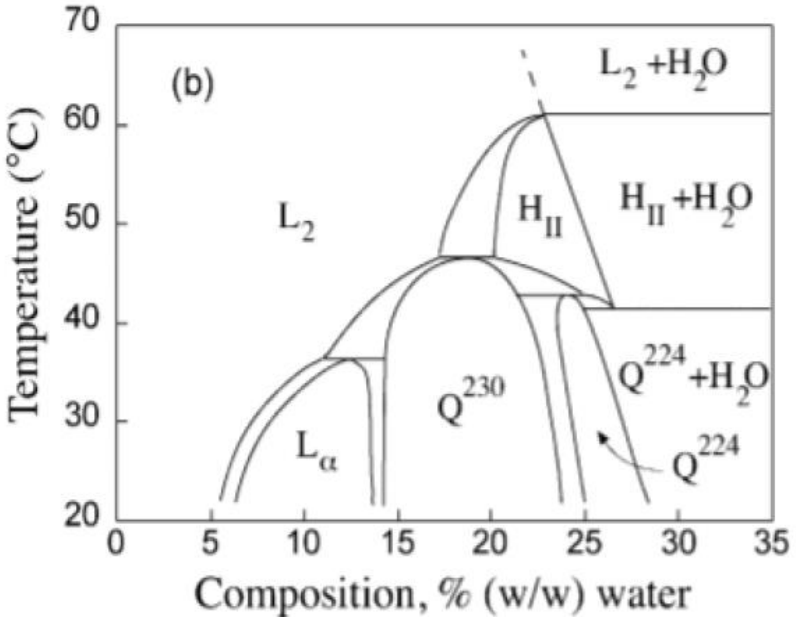

Figure 4 Phase diagram of the phytantriol-water system as a function of temperature.[8]

The double diamond phase (Q_{224}) of phytantriol, depicted in Figure 5 (a), has two independent water channels that run through the structure highlighted in red and blue. These water channels have a diameter of around 2 to 3 nm. It has been reported that when metals and semiconductors are electrodeposited through these water channels the deposition occurs asymmetrically through one of the channels.[9,10] This leads to the resulting deposited material having single diamond (Q_{227}) morphology (Figure 5 b). [4,9,11–13]

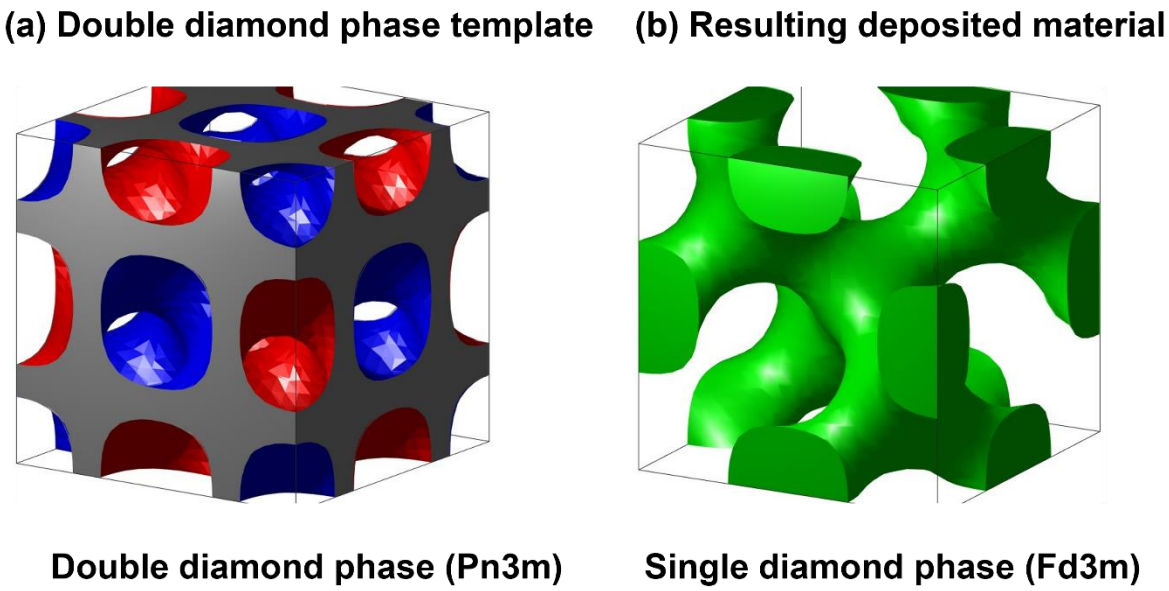

Figure 5. The structure of the double diamond phase formed by the lipid bilayer with the two individual water channel networks flowing through the structure highlighted in red and blue (a). The structure of the single diamond phase, which is formed by the deposited material (b).

The current understanding of why the deposition occurs asymmetrically in only one of the water channels is due to one of the channels being capped by the surfactant, with no access to the electrode surface or the external electrolyte.[9] It is suggested that one of the water channels being closed to the external solution occurs to preserve the lipid bilayer topology.[14] There is no direct proof of this phenomenon[10] but evidence that support this theory lies in atomic force microscopy images of the liquid crystal/water interface showing features of spacing consistent with a single network.[15]

Burton *et al.*[3] fabricated a 3D interconnected nanowire network films of bismuth sulphide with single diamond (Q_{227}) topology via electrodeposition using phytantriol as a soft template. The bismuth sulphide films were made via potentiostatic electrodeposition at a potential of -0.4 V vs SCE (saturated calomel electrode) from an aqueous solution containing 100 mM $Bi(NO_3)_3$, 100 mM $Na_2S_2O_3$ and 200 mM EDTA (ethylenediaminetetraacetic acid) on a gold electrode through phytantriol. TEM (transmission electron microscopy) and SAXS (small angle X-ray scattering) measurements revealed the deposited bismuth sulphide to have single diamond topology with a lattice parameter of 140 ± 3 Å. This is approximately double that of phytantriol (69 ± 1 Å) and shows that the deposition occurs in only one of the two water channels as there is a reduction in symmetry.

The same group[16] also used phytantriol as a template to electrodeposit novel Bi_2Te_3 nanostructures. This was achieved by potentiostatic electrodeposition through phytantriol modified gold electrodes. EDX (energy dispersive X-ray) measurements revealed that stoichiometric Bi_2Te_3 films could be produced over a deposition range of 0.375 to -0.05 V vs SCE. SAXS and HIM (helium ion microscopy) measurements of the nanotemplated material revealed that the material had a disordered structure with the average diameter ranging from 60 to 150 ± 10 Å. This was unexpected as the phytantriol water channels in the template has diameters of 20 to 30 Å, so the deposited material was much larger than expected and did not exhibit the single diamond phase. Thermoelectric measurements conducted on the nanostructured Bi_2Te_3 films yielded a Seebeck coefficient of -88 μV K^{-1} which is 46 % higher when compared to other electrodeposited Bi_2Te_3 films with a thickness of several hundreds

of micrometres (~-60 μV K^{-1}). This work demonstrates that the resulting material deposited through phytantriol can still exhibit enhanced properties even if the resulting material does not form the intended single diamond phase.

Another material fabricated by the same group[12] using phytantriol as a template for electrodeposition was Pd. The surface area of the Pd deposited through the template had a specific surface area of 28.3 $m^2 g^{-1}$ which showed a 42 % increase compared to palladium black (20 m^2 g^{-1}) and a much larger area than non-templated Pd at 2.11 m^2 g^{-1}. Due to the outstanding properties of Pd for catalysis the material was then tested for its application in alkaline fuel cells with a series of electrochemical experiments of methanol, ethanol, and glycerol oxidation. In each instance, there was a peak current seen for the oxidation, which was larger for the single diamond Pd when compared to Pd black and non-templated Pd due to the increase in surface area. The recorded peak current of 1100 A g^{-1} for methanol oxidation claimed to be the largest seen in the literature for Pd and Pt. It was also claimed that the peak current for the glycerol oxidation was also the largest compared to literature values for palladium.

The study on the electrodeposition of mesoporous nanostructured Pt through phytantriol has also been reported in the literature.[9,17–19] Akbar *et al.* explored the optimum conditions for the electrodeposition of platinum through phytantriol by varying the deposition potential and type of substrate. Electrodeposition was achieved by stepping the potential from 0.6 V to a potential between -0.1 to -0.35 V vs Ag/AgCl in 8 wt% hexachloroplatinic acid solution (HCPA). After the deposition, the phytantriol template was removed by soaking in ethanol and the structural properties of the resulting films were analysed by SAXS. The SAXS measurements, (Figure 6) show that mesoporous Pt deposited at -0.2 V vs Ag/AgCl (b) exhibits prominent Bragg peaks with relative positions of 1/d in the ratio $\sqrt{3}$ / $\sqrt{8}$ which corresponds to the (111) and (220) plane of single diamond morphology. It can also be seen that Pt deposited at potentials more negative than -0.2 V show a gradual loss of structure. Akbar *et al.* also demonstrated that platinum can be deposited through phytantriol on a variety of electrodes such as Pt, Au and FTO (fluorine doped tin oxide) with SAXS data revealing well defined patterns, confirming the Pt had single diamond morphology.[17]

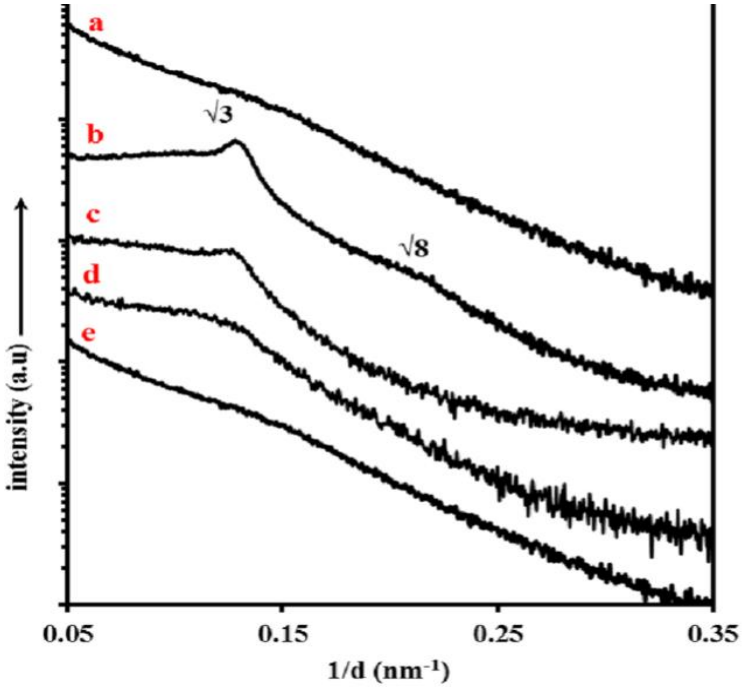

Figure 6 SAXS patterns recorded for platinum deposits through phytantriol at different potentials of (a) -0.15 V, (b) -0.2 V, (c) -0.25 V, (d) -0.3 V and (e) -0.35 V vs Ag/AgCl at room temperature on gold electrodes. Taken from[17]

They also used cyclic voltammetry (CV) in order to measure the electrochemical active surface area (ECSA) of the mesoporous nanostructured platinum framework deposited through phytantriol. The Pt nanostructure was found to have a specific electrochemical surface area of 40 $m^2 g^{-1}$ which is high for unsupported Pt. [9]

A system that is of extreme interest to this work is the phytantriol/Brij-56 system. Brij-56 is a non-ionic surfactant with the chemical formula $C_{36}H_{74}O_{11}$ $(C_{16}EO)_{n\sim10}$. Akbar *et al.* reported that introducing Brij-56 as a co-surfactant to phytantriol acts to swell the double diamond structure via a mechanism called lipid modular curvation which is shown in **Error! Reference source not found.**.[20] Brij-56 has a larger hydrophilic head group compared to phytantriol and a smaller hydrophobic tail, therefore its introduction into the lipid bilayer disrupts the regular packing of phytantriol molecules, leading to a swelling of the double diamond phase due to a relaxation of the curvature. As the swelling arises from a reduction in the curvature, the increase in lattice parameter with increasing Brij-56 content is due to an increase in the diameter of the water channels not a thickening of the lipid bilayer, leading to thicker nanowires when a material is deposited through the swollen templates.

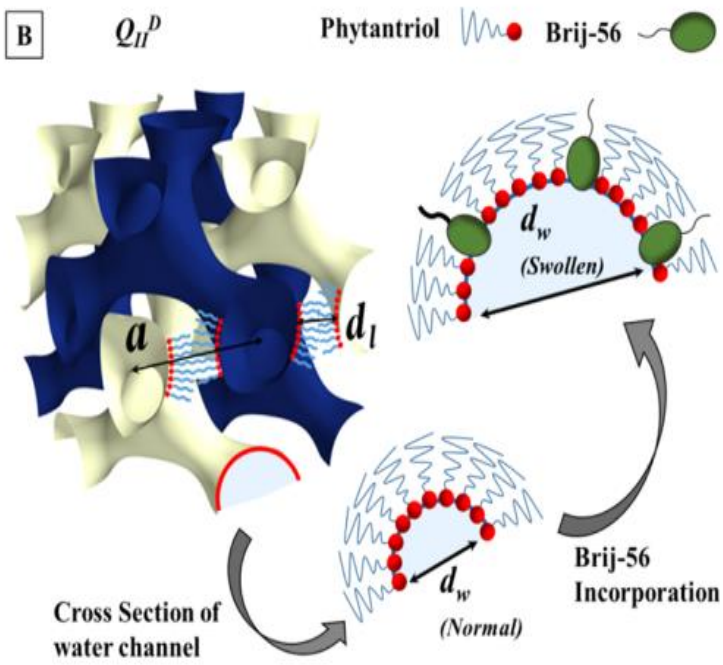

Figure 7 Schematic expressing the two independent water channels of the double diamond phase separated by a lipid bilayer, where a represents the lattice parameter and d_l represents the lipid bilayer thickness. The cross section of a water channel with a regular diameter (d_w) of pure phytantriol and the swollen water channel after the addition of Brij-56 molecules. Taken from.[20]

The lattice parameter of the double diamond phase formed by phytantriol increased from 70.0 ± 0.2 Å to 128.0 ± 0.2 Å with the addition of Brij-56 by 20 wt%. The differing sizes of the template was then used to fabricate Pt by galvanostatic displacement and electrodeposition, with control of the materials pore and wire dimensions.[20] This demonstrated a method in which single diamond material can be fabricated with control over the materials size. In this work we explore the addition of Brij-56 to the phytantriol template in order to fine-tune the properties of single diamond phase Pd for the formic acid oxidation reaction.

It is clear from the literature that electrodeposition through the inverse cubic phase of phytantriol provides a promising synthetic route for the fabrication of 3D nanostructures of semiconductor and metal materials that have an application in thermoelectrics, photovoltaics, electronics, and catalysis. In this work we will explore the use of phytantriol and phytantriol/Brij-56 as a soft template to electrodeposit nanostructured CdTe, Pd and Pt and how the resulting nanostructure affects the materials properties.

The next chapter of this thesis will detail the experimental techniques and methodologies extensively employed throughout the research. Subsequent chapters will introduce each project along with their respective results and conclusions.

The sequence of the results chapters begins with the electrodeposition of mesoporous CdTe using the double diamond phase of phytantriol/Brij-56. The second results chapter investigates the use of the Brij-56 additive in the double diamond phase of phytantriol to control the size of electrodeposited single diamond Pd and examines how this size variation influences its properties in the formic acid oxidation reaction.

The third results chapter focuses on the application of single diamond Pt for the oxygen production reaction, comparing its performance and durability with commercial catalysts. The following chapter describes the use of pulse electrodeposition of Pt through the phytantriol/Brij-56 template to create a more ordered and homogeneous nanostructure.

The final results chapter presents the design and fabrication of a novel 3D printed electrochemical cell used for in-situ small-angle scattering experiments.

2. Experimental Techniques

This section of the thesis delves into the experimental techniques and methodologies extensively utilised in this research to fabricate intricate nanomaterials via electrodeposition. The electrodeposition process is thoroughly described, along with material characterization techniques including X-ray diffraction, small-angle X-ray scattering, and scanning electron microscopy.

2.1. Cyclic voltammetry

Cyclic voltammetry (CV) is a powerful electrochemical technique which can be used a tool to analyse electroactive species, study kinetics, reaction mechanisms and much more. The technique involves applying a triangular potential waveform to an electrochemical cell while measuring the current response. Typically, a three-electrode setup is used which consists of a working electrode, a counter electrode, and a reference electrode (Figure 8).

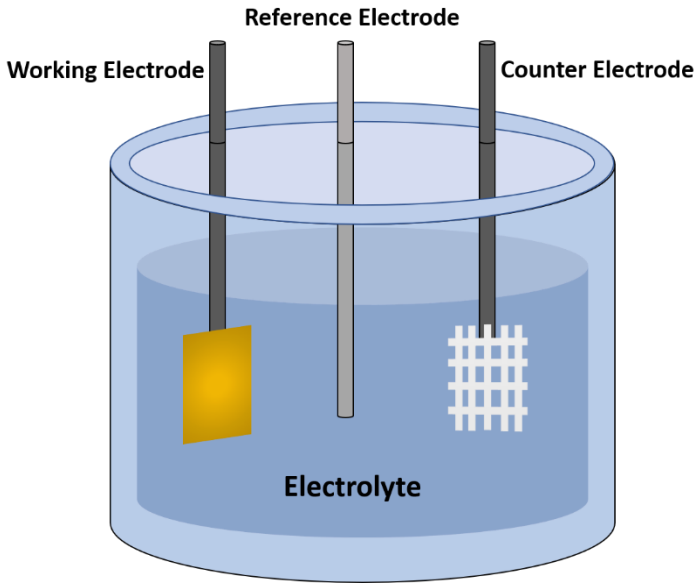

Figure 8 A basic diagram of a three-electrode setup consisting of a working, reference and counter electrode immersed in an electrolyte.

The potential of the working electrode is controlled versus the reference electrode. The cycling potential between these two electrodes is in the form of a forward and reverse linear sweep between two potentials. A typical potential waveform for CV is illustrated in Figure 9. The potential in this waveform is swept from E_1 to E_2 until it is swept back to E_1 again,

completing one cycle. This process is then repeated to give a second cycle and can be repeated for multiple cycles.

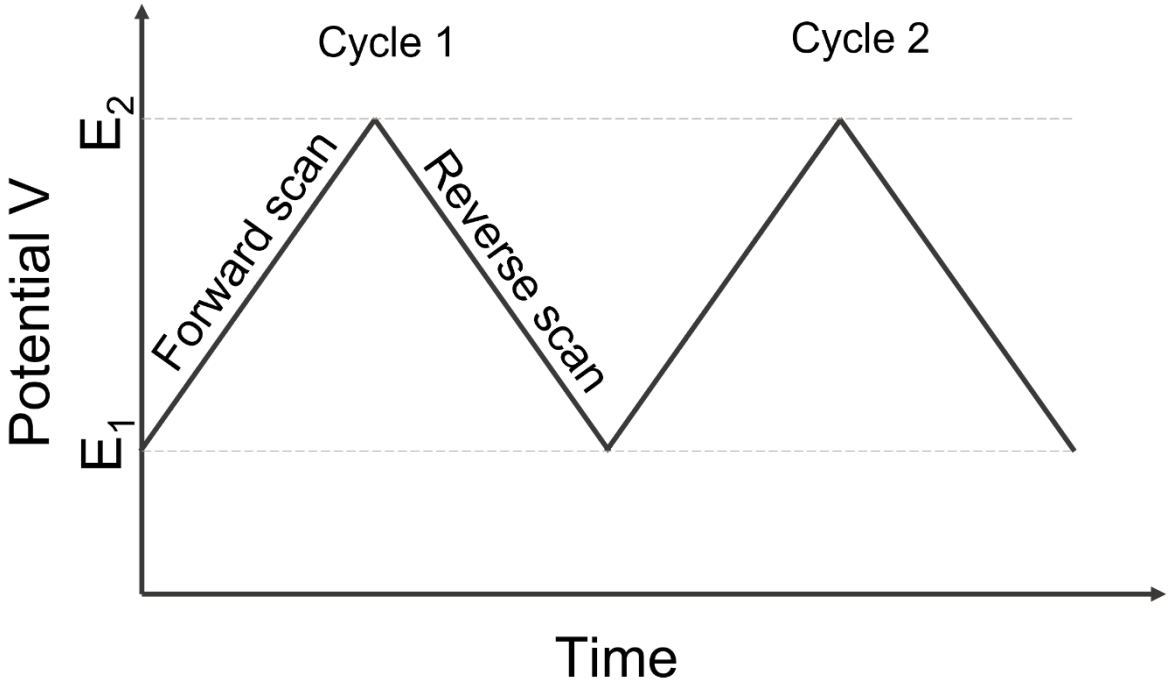

Figure 9. A typical perturbation waveform for cyclic voltammetry experiments, showing how the applied potential changes over time.

As the potential is cycled the current at the working electrode is measured and plotted against the potential producing a CV. Figure 10 portrays a basic CV for a reversible one electron redox reaction.

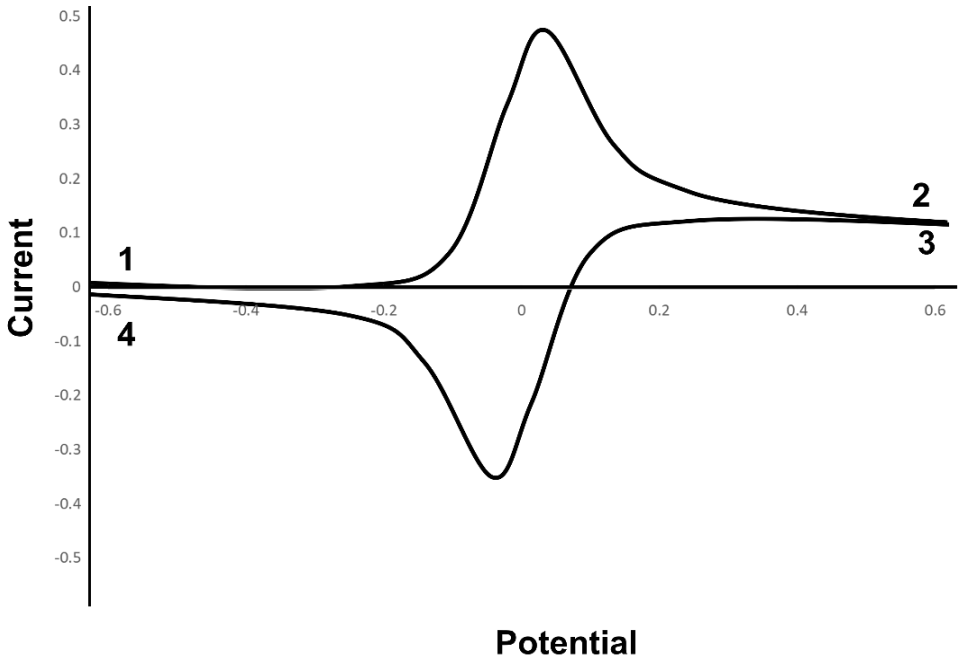

Figure 10 A cyclic voltammogram of a reversable 1 electron transfer process of a redox couple. The potential is swept from the starting position labelled 1 until it reaches position 2, at this point the potential is then swept back to the starting potential from positions 3 to 4.

The peak in the positive scan from position 1 to 2 (as shown in Figure 10) is a result of the oxidation process which is driven by the potential, causing a loss of an electron and the peak in the negative scan from position 3 to 4 is a result of reduction, in which the species is gaining an electron. This process is given by Equation 1. where O is the oxidised species, R is the reduced species and n is the number of electrons (e^-) involved in the electron transfer.

Equation 1

$$O_{(aq)} + ne^- \leftrightarrow R_{(aq)}$$

The characteristic shape of the CV is a result of diffusion of the species in solution to the electrode surface. Figure 11 portrays the process of a simple electrochemical reaction at an electrode surface.

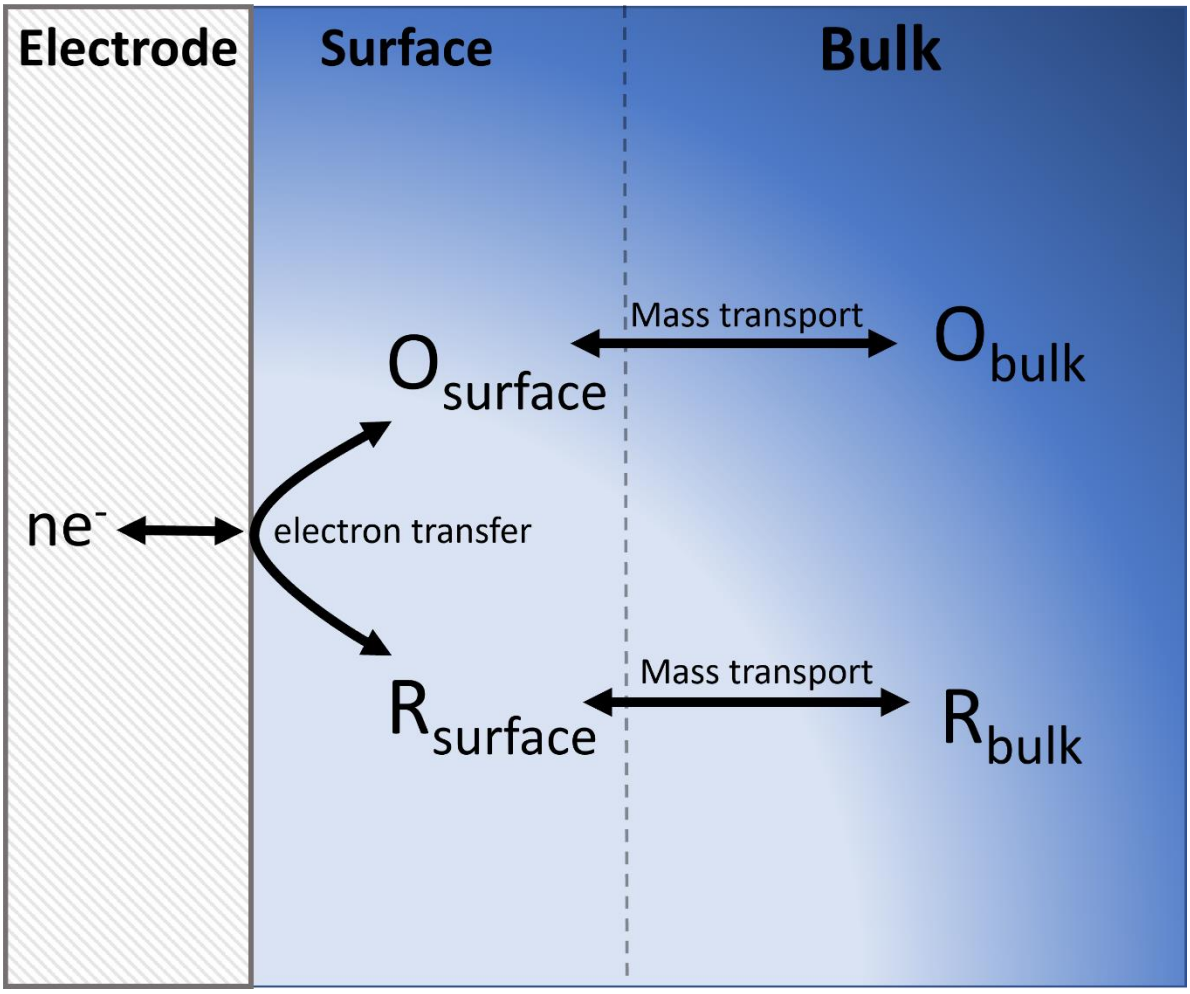

Figure 11. A diagram of the steps involved in a simple electrochemical reaction (oxidation & reduction) at an electrode surface. This involves the species diffusing from the bulk solution to the electrode surface. An electron transfer then occurs followed by the species diffusing back into the bulk.

For the reduction reaction of species $O_{(aq)}$ the first step is mass transport where O_{bulk} diffuses to the electrode surface becoming $O_{surface}$. The species then undergoes an electron transfer process, being reduced to $R_{surface}$ by gaining an electron from the electrode surface. The $R_{surface}$ species then diffuses back into the bulk. These processes lead to the oxidation and reduction peaks in Figure 10. Beyond the peak potential the electrode reaction is still occurring, however the electroactive species close to the surface is depleted causing the current to decrease over time. This means that the current produced is governed by the rate of diffusion of the species to the electrode surface from the bulk solution as shown in Figure 11 above. The magnitude of the peak current (i_p) is given by the Randles-Sevcik equation (Equation 2), where i_p is the peak current, n is the number of electrons involved in the transfer, F is the

Faraday constant, *R* is the gas constant, *T* is temperature, *A* is the area of the electrode, *C* is the concentration of the species, *D* is the diffusion coefficient and *v* is the scan rate.

Equation 2

$$i_p = 0.45\, nFAC \left(\frac{nFvD}{RT}\right)^{1/2}$$

An important relationship is that i_p is proportional to $v^{1/2}$ so increasing the scan rate 4-fold acts to double the peak current in a CV. Cyclic voltammetry provides a method of quickly analysing reduction and oxidation processes, such as electrodeposition and stripping of semiconductors and metals on a conductive substrate. It can be used as a starting guide to determine the deposition potential of the materials of interest. Figure 12 shows a typical CV and the perturbation waveform that is expected for the deposition of as solid phase onto a substrate followed by its stripping.

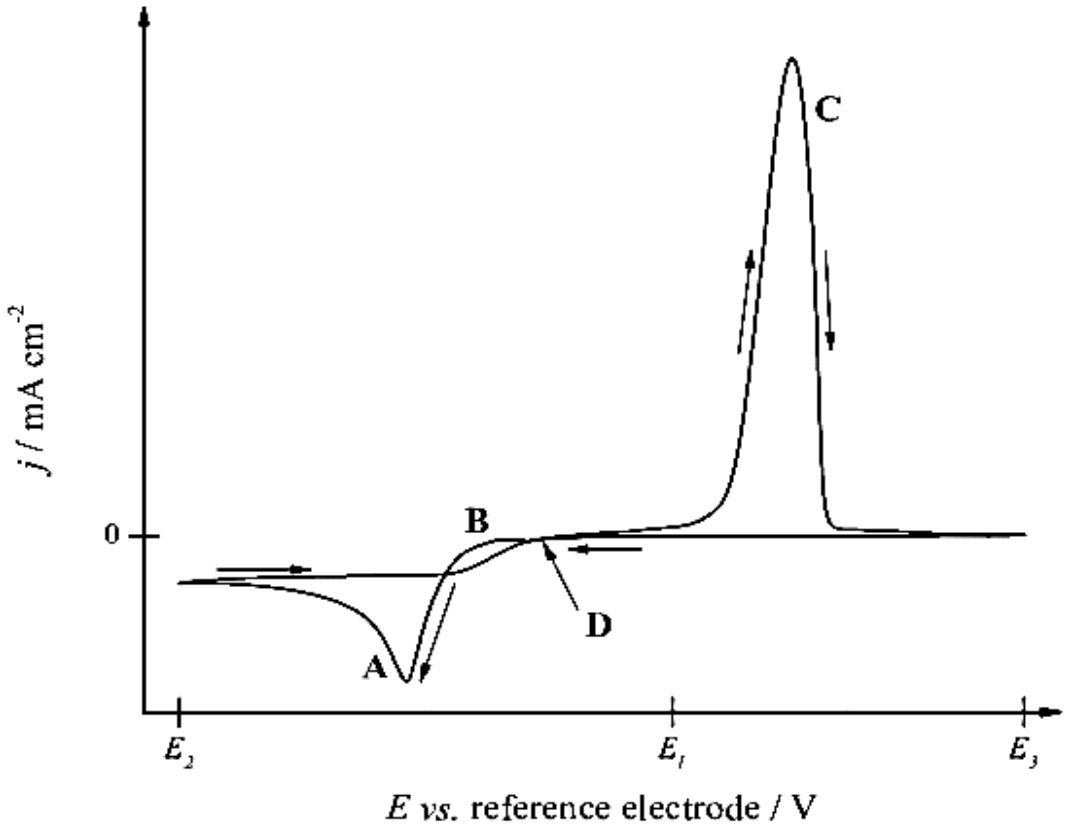

Figure 12. A typical cyclic voltammogram for the formation of a solid film on the surface of an electrode from an aqueous electrolyte and its subsequent stripping. Taken from.[43]

The cathodic peak labelled A on the forward scan is a result of the reduction process and the formation of a solid phase from the electrolyte solution on the electrode surface. The steep rise in current towards the peak is due to kinetically faster deposition at larger potentials until

the deposition becomes mass transport limited at more cathodic potentials. In the reverse scan, the point labelled B is the nucleation loop where the reverse scan crosses over the forward scan. This is due to the overpotential that is required to nucleate a new phase on a foreign substrate during the initial phase formation. The anodic peak, labelled C, is a result of the stripping (oxidation) of the solid phase on the electrode and its dissolution back into the solution. The current of this peak is large as the species is surface bound so there are no mass transport limitations. The point labelled D is the potential at which there is no current being passed, this is a good estimation of the equilibrium potential for the species.[43]

2.2. Chronoamperometry

Chronoamperometry is an electrochemical technique in which current is recorded as a function of time as the working electrode potential is stepped from a value at which no current flows to one where a reaction occurs on the surface producing a current. The results obtained allow for both qualitative and quantitative analysis of the system. A typical waveform of the potential of a chronoamperometry experiment is shown in Figure 13.

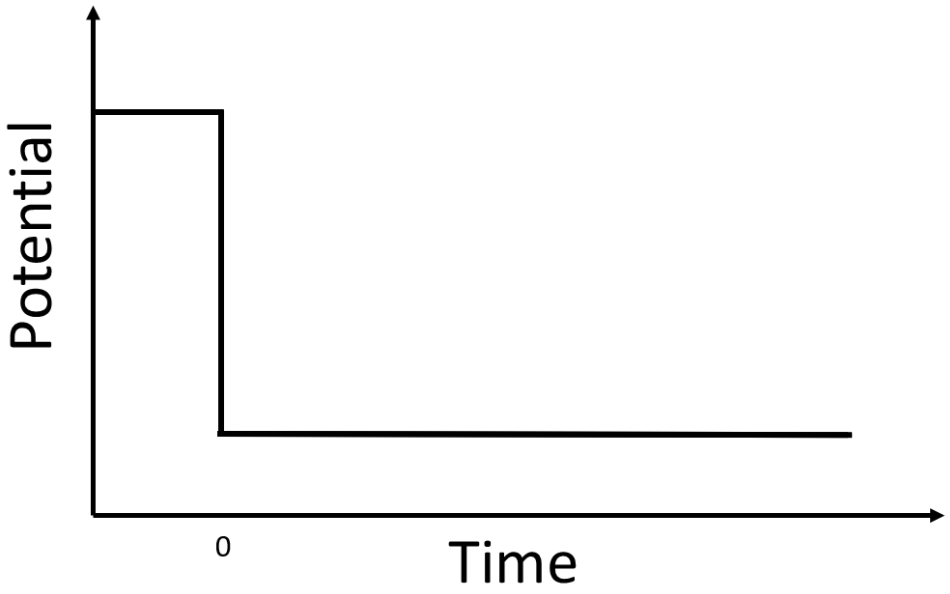

Figure 13 A typical waveform of chronoamperometry showing the potential against time.

In a solution containing a redox couple, the current response that is measured originates from the redox reaction occurring on the surface of the working electrode (i.e a deposition on the surface). Chronoamperometry can therefore be used as a means to record the current passed over time during an electrodeposition process.

2.3. Electrodeposition

A thin film can be grown on an electrode from an electrolyte by applying a potential for a fixed period of time. This procedure is known as potentiostatic electrodeposition. The equilibrium potential, E_e, is given by the Nernst equation which describes the potential of an electrode in a standard electrochemical system (Equation 3), where E_e is the equilibrium potential, $E^{\emptyset}$ is the standard electrode potential, R is the gas constant, T is the temperature and O and R are the concentration of the species at the electrode surface. The overpotential (η) shown in Equation 4, is the difference between the applied potential (E) and the equilibrium potential (E_e). The chosen deposition potential has a very significant impact on the electrochemistry that occurs on the surface affecting properties such as the kinetics, the morphology, crystal structure and electronic properties of the deposited films.

Equation 3

$$E_e = E^{\emptyset} + RTln\frac{[O]}{[R]}$$

Equation 4

$$\eta = E - E_e$$

When the applied potential is equal to the equilibrium potential, the overpotential is zero and the current/current density will be zero as no net chemical reaction/change is occurring. When the applied potential is very close to the equilibrium potential, the overpotential will be low and the rate of electron transfer is very slow and is the rate determining step for the deposition. When the overpotential is moderately larger, the rate of electron transfer and mass transport are similar, so the system is in a state of mixed control. When the overpotential is much greater, the rate of electron transfer at the surface is extremely fast and therefore mass transport becomes the rate determining step. At this stage the current density becomes independent of the potential as it is in a mass transport-controlled regime.

Figure 14 is a simple graph showing the typical current vs time recorded during a potentiostatic electrodeposition experiment in which the nucleation and growth of a solid phase on the working electrode occurs, along with the associated potential waveform.

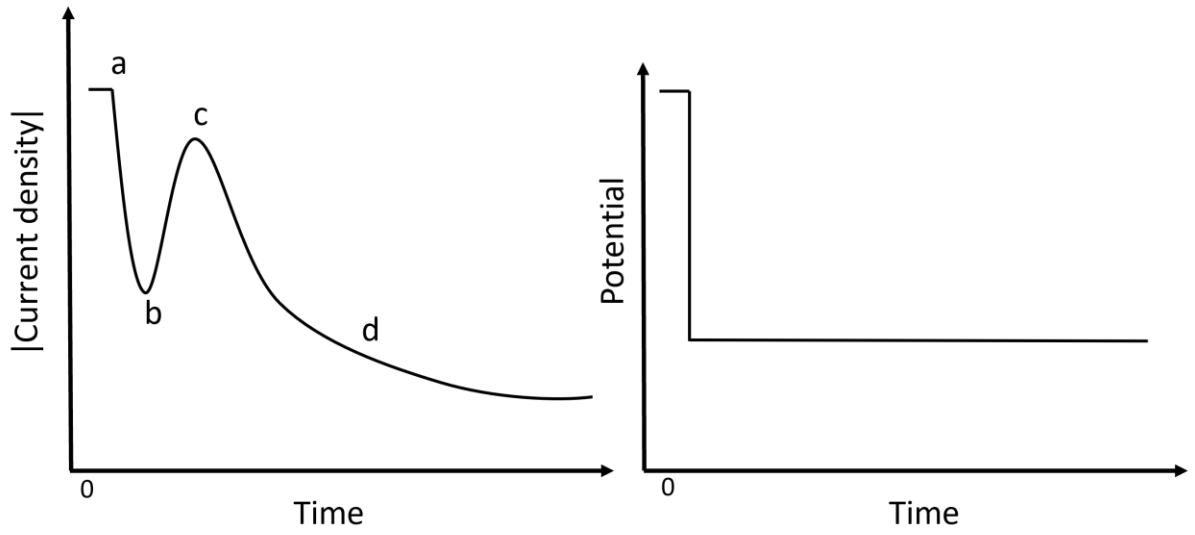

Figure 14 A simple graph showing the general current against time graph obtained during nucleation and growth of a solid phase on an electrodes surface during a potentiostatic electrodeposition experiment.

The initial drop in current from (a) to (b) in Figure 14 is a result of charging of the double layer during the electrodeposition process. The change in current from (b) to (c) is from the formation and growth of the nuclei being deposited on the surface of the electrode. From (c) to (d) and beyond the current decreases over time for the continuous deposition, the process is diffusion controlled and relies on the active species diffusing to the electrode.[43]

The current against time transients collected during electrodeposition can be used to calculate the amount of material deposited, the film thickness and the specific surface area. This is due to Faraday's law, which states that the amount of substance consumed or formed in an electron transfer is proportional to the charge (Q) passed, denoted by Equation 5 where m is the number of moles of substance formed, n is the number of electrons involved in the transfer and F is Faraday's constant (96485 C mol^{-1}).

Equation 5

$$Q = mnF$$

The charge passed is calculated from integrating the area under the curve for the current - time transient during the deposition.

An important value which will be used in order to compare the difference in surface area between films deposited with and without the liquid crystal templates, is the specific surface area (S_p) given by Equation 6, where ECSA is the electroactive surface area of deposited

material and *W* is the mass calculated using Equation 7 and *M* is the molar mass of the material.

Equation 6

$$S_p = \left(\frac{ECSA}{W}\right)$$

Equation 7

$$W = \frac{QM}{nF}$$

The film thickness of a material on the electrode surface can be determined from Equation 8 where M is the molecular weight, ρ is the density and A_{geo} is the area of the electrode.

Equation 8

$$film\ thickness = \frac{QM}{4F\rho A_{geo}}$$

2.4. Pulse Electrodeposition

In this work we will also utilise pulse electrodeposition to deposit material through the liquid crystal templates. Pulse electrodeposition is an electrochemical technique which involves depositing a material by applying periodic potential pulses, as opposed to a continuous potential as described before for regular electrodeposition. Pulse electrodeposition gives us control over more parameters than typical electrodeposition. We can control the pulse durations, the amplitude of the pulses, the number of pulses and the frequency. A typical pulse electrodeposition waveform is shown in Figure 15 (a). The applied potential is switched between two values of E_1 and E_2 and we have control over the times these potentials are applied for. Here E_1 represents a potential in which no electrochemistry occurs and E_2 is a potential in which electrodeposition occurs (denoted t_{off} and t_{on} respectively). A typical current response for pulse electrodeposition is shown in Figure 15 (b) which shows that when the 'off' potential is applied the current tends to zero, whereas when the 'on' potential is applied the current becomes cathodic and tends to a value which is related to the rate of electrodeposition.

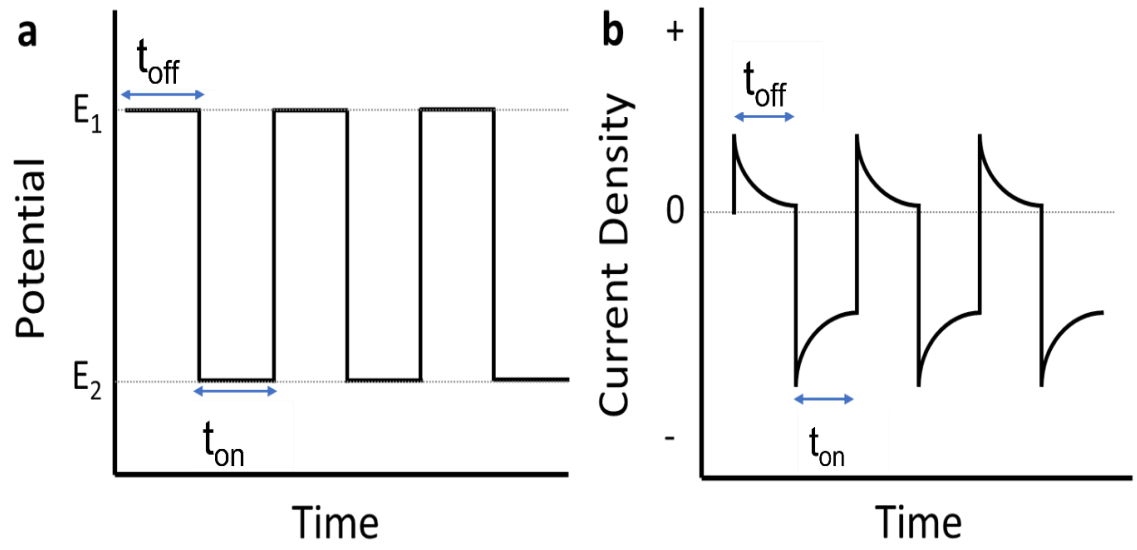

Figure 15 (a) a typical pulse electrodeposition waveform and (b) the current response for a typical pulse electrodeposition.

2.5. Surface area determination

Cyclic voltammetry can be used to measure the electroactive surface area (ECSA) of materials. The ECSA of a material is the actual area of the catalyst surface on which the electrochemical reaction of interest occurs.[21] This is determined by assessing the amount of charge passed during specific electrochemical reactions. If we assume that the reaction involves the formation or removal of a monolayer on the electrode surface, we can calculate the ECSA using Equation 9 where ECSA is the surface area, n_a is the number of moles of species on the surface, N_a is Avogadro's constant and d_m is the surface atom density.

Equation 9

$$ECSA = \frac{n_a N_a}{d_m}$$

This technique will be used in this project to determine the ECSA of Pt and Pd films. This is achieved through cyclic voltammetry in H_2SO_4. A typical CV of a platinum electrode in H_2SO_4 is shown in Figure 16.

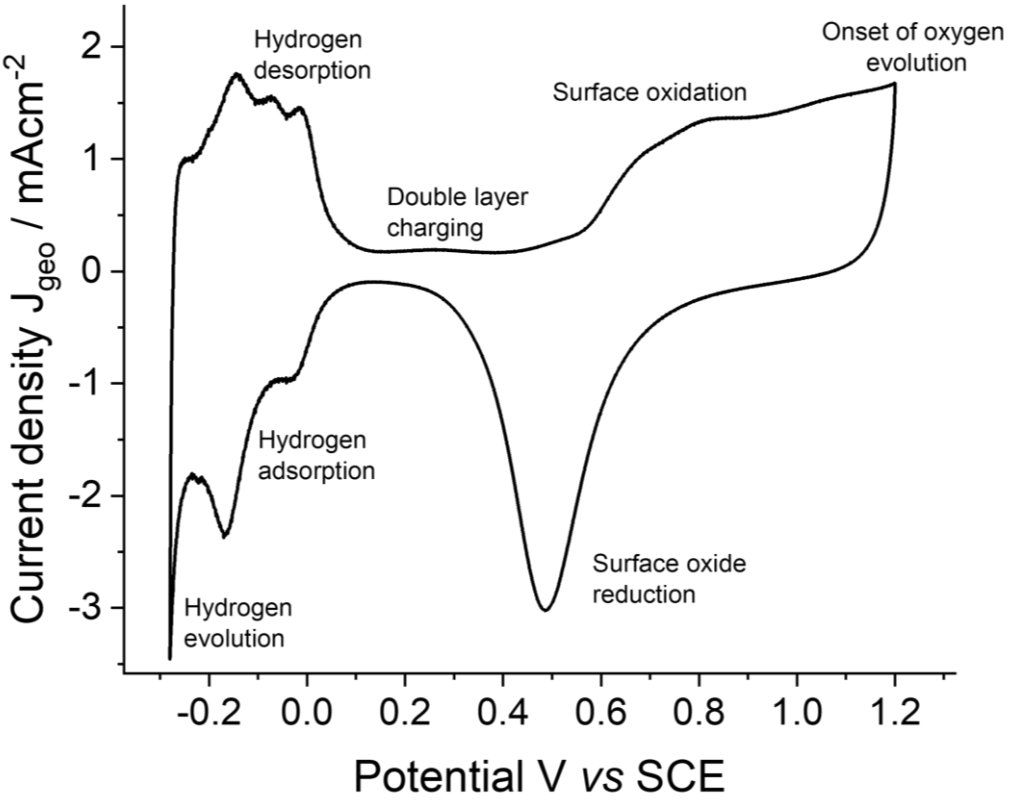

Figure 16 Cyclic voltammogram for a Pt electrode in 0.5 M sulphuric acid solution at a scan rate of 20 mV s^{-1} at room temperature which has been degassed with N_2 to remove O_2.

The area of interest to determine the surface area of Pt is the hydrogen absorption region highlighted in Figure 16 which occurs via Equation 10.

Equation 10

$$H^+_{(aq)} + e^- + M_{(site)} \rightarrow H_{(ads)}$$

As the adsorption of a hydrogen atom on a platinum site is a one electron charge transfer process the number of moles of hydrogen atoms adsorbed can be calculated by Equation 11 where Q_m is the charge passed when a monolayer of hydrogen atoms is formed on the electrode surface and *F* is Faraday's constant.

Equation 11

$$n_a = \frac{Q_m}{F}$$

Using Equation 11, and inputting values of d_m and *e*, Equation 9 can be rewritten as Equation 12, where *e* is the electron charge $(1.602 \times 10^{-19} C)$.

Equation 12

$$ECSA = \frac{Q_m N_a}{F d_m} = \frac{Q_m}{e d_m}$$

The charge is then determined mathematically by integrating the hydrogen adsorption region, however, there is still a charge contribution from the double layer charge region, so this needs to be subtracted from Q to give Q_m, giving the final equation:

Equation 13

$$Q_m = \frac{1}{\nu}\int_{V_0}^{V} I\, dV - Q_{dl}$$

In order to determine the surface area of Pd the same process is employed using the surface oxide reduction peak.

The roughness factor (*RF*) of the electrodeposited materials through the templates can also be determined. The roughness factor is the ratio between the electroactive surface area of an electrode and its geometric surface area. This value allows us to compare the change in surface area between templated and non-templated materials. The roughness factor is calculated by Equation 14.

Equation 14

$$RF = \frac{ECSA}{geometrical\ surface\ area}$$

2.6. Transmission Electron Microscopy (TEM)

TEM is a powerful tool for the study of nanomaterials. It utilises electrons as an imaging source, that strongly interacts with matter,[22] making it suitable to probe materials in the nanometre region. A transmission electron microscope has a complex setup, however for simplicity it can be split into its main components; the illumination system composed of a filament in which electrons are produced, the condenser lens which acts to deflect and focus the electron beam and the objective lens (and lenses below this) which acts to produce the final image of the sample by projecting an image on the detector (phosphorescent screen or detector). The general set up discussed here can be seen in Figure 17**.** The high energy electron beam that passes through the ultra-thin sample carries information about the sample and is focused and magnified by electromagnetic lenses to form the image.

Transmission electron microscopes can produce images of a much better resolution compared to optical light microscopes as the optimal resolution relies on the wavelength of the illumination source. The resolution of a microscope is given by Equation 15, where *d* is

the minimum resolvable distance between two points, λ is the wavelength of the illumination source, n is the index of refraction and α is the half angle.

Equation 15

$$d = \frac{\lambda}{2nsin\alpha}$$

The much higher resolutions that are possible using electrons as opposed to light is due to the de Broglie wavelength of an electron being much smaller compared to the wavelength of light, so higher resolution can be obtained. The wavelength of an electron is given in Equation 16, where $\lambda_e$is the de Broglie wavelength of the electron, h is Planck's constant, $m_0$is the resting mass of an electron, E is the energy of the electron and c is the speed of light.

Equation 16

$$\lambda_e = \frac{h}{\sqrt{2m_0E(1+\frac{E}{2m_0c^2})}}$$

TEMs have spatial resolutions of around 0.2 nm,[23] making them an extremely common technique used among many fields including materials science, nanotechnology, medical, biological and life sciences for imaging materials.

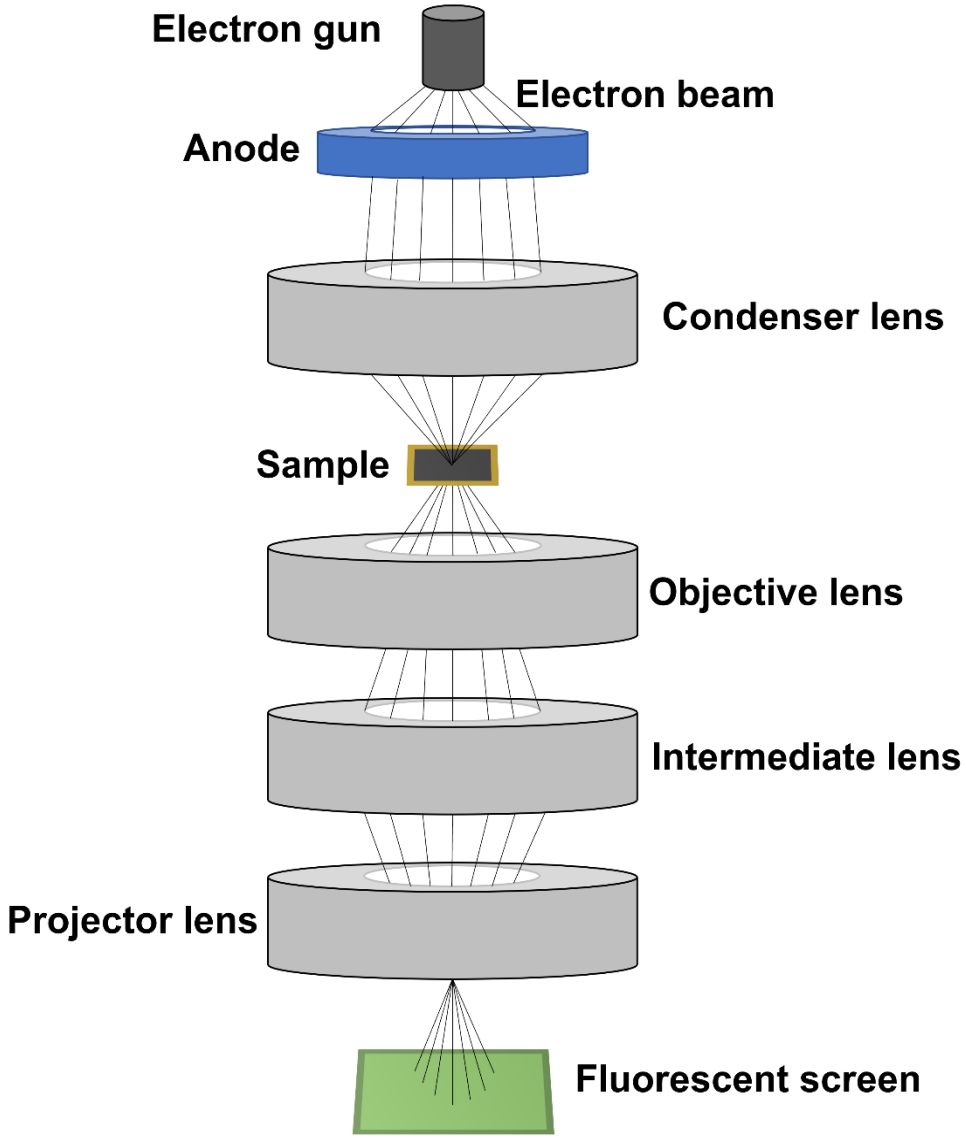

Figure 17 A basic diagram of a transmission electron microscope portraying the main components of the electron gun, anode, lenses, sample stage and detector.

2.7. Scanning Electron Microscope (SEM)

SEM is a powerful tool in the characterisation and imaging of thin films and nanostructured materials by taking advantage of the properties of electrons to produce images at great resolutions. Typical SEMs have resolution of a few nm, with ultrahigh-resolution SEMs having resolutions of 0.4 nm.[24] An SEM consists of a column in which an electron beam (produced by an electron gun) is accelerated to desired voltages, typically between 5-40 kV, and is focused by lenses to a desired spot and then deflected by pairs of scanning coils rastering the beam in the x and y plane. A typical SEM instrument is shown below in Figure 18.

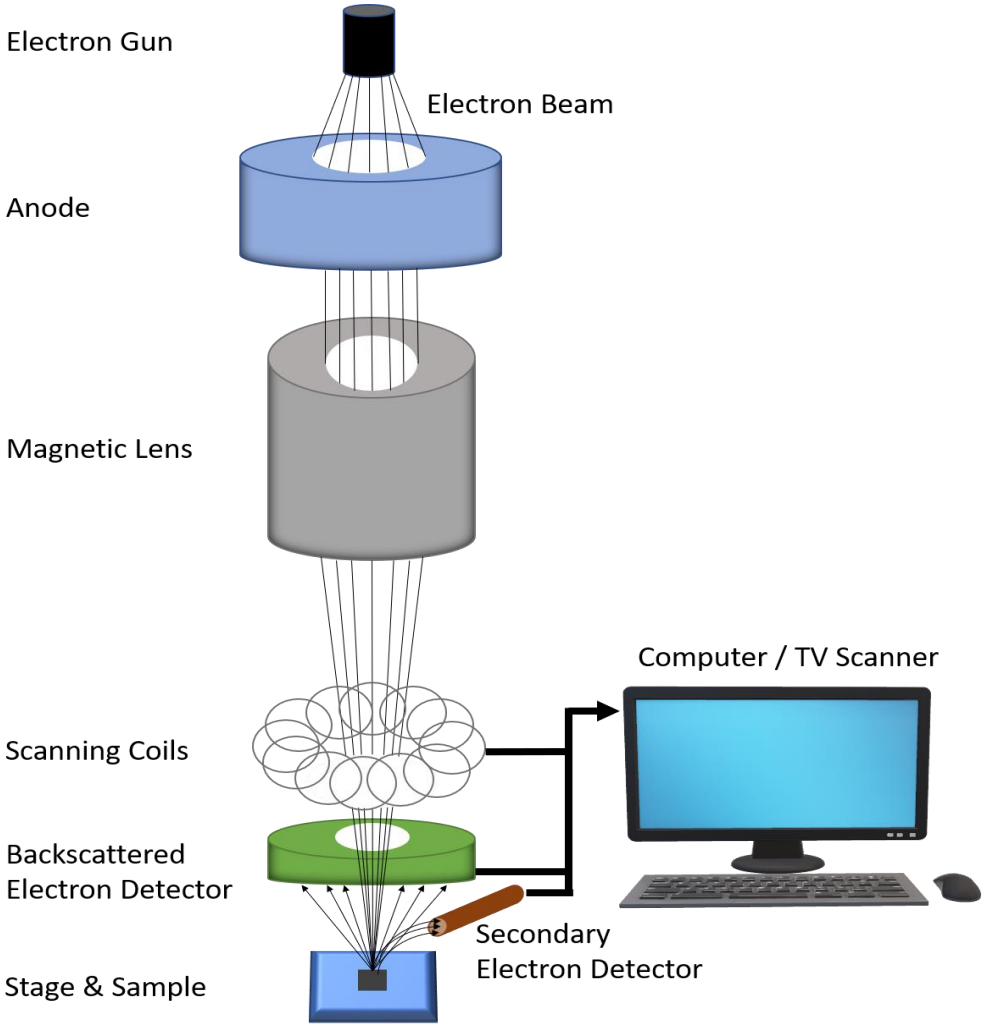

Figure 18 A basic diagram of a scanning electron microscope portraying the main components of the electron gun, anode, magnetic lens, electron beam, scanning coils, backscattered electron detector, secondary electron detector, sample stage and computer.

SEM images are created as incoming electrons interact with the samples surface and secondary electrons (SE) and backscattered electrons (BSE) are then emitted from the surface carrying information about the surface morphology. This effect is illustrated in Figure 19 portraying how SE And BSE are produced by surface interactions. Secondary electrons are a result of the primary electron beam transferring ample energy to an electron in the sample overcoming its work function and emitting it as a SE with energy typically less than 50 eV. SEs are only emitted from the surface of the sample and the interaction is an inelastic collision. Elastic scattering occurs when an electron from the primary beam is scattered by atomic nuclei from the surface resulting in backscattered electrons with comparable energies to the primary electron energy usually much higher than 50 eV.

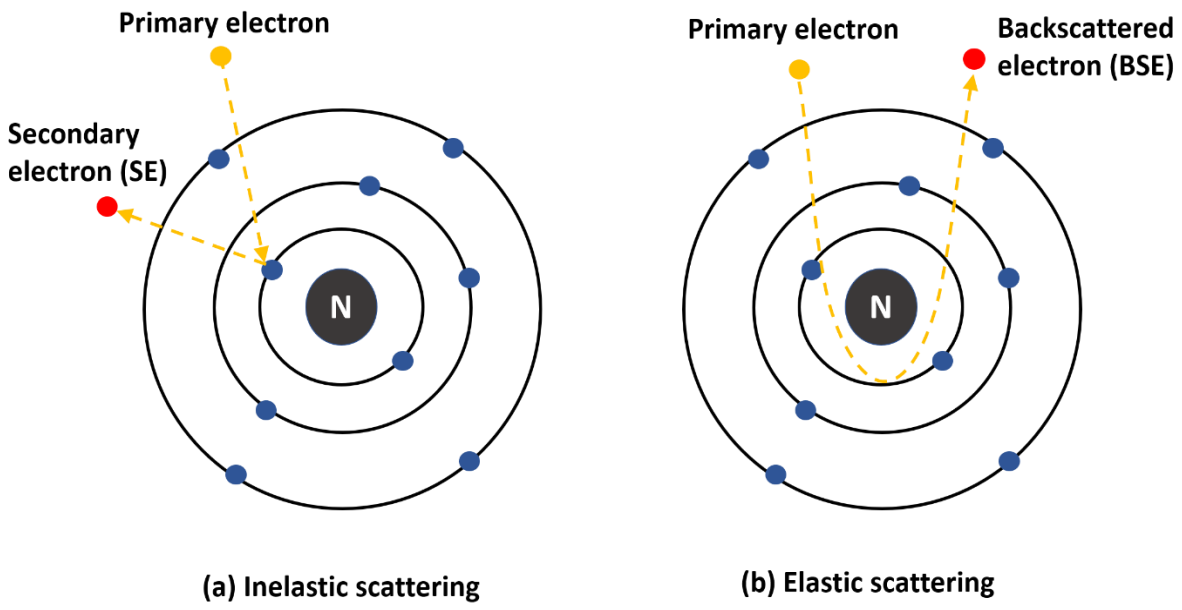

Figure 19. A figure showing how inelastic scattering from a primary electron produces a secondary electron (a), and how elastic scattering from a primary electron produces backscattered electrons (b).

The image is formed as secondary electrons are detected by a scintillator-photomultiplier system, amplified, and then converted to produce a two-dimensional image of the sample in which the brightness of the signal depends on the intensity of secondary electrons reaching the detector. The BSE detector above the sample collects the backscattered electrons which are scattered by nuclei. Heavier nuclei backscatter electrons more strongly than light atomic nuclei so they appear much brighter in the image and allow contrast to be seen between different elements.

This technique will play a vital role throughout this project in order to image the surface of the deposited thin films looking at their morphologies. It will also be coupled with energy dispersive X-ray spectroscopy (EDX) in order to determine the composition of the films.

2.8. Energy dispersive X-ray spectroscopy

Energy dispersive X-ray spectroscopy is a surface analytical technique in which elemental information is gained which can be used to identify elements that make up a sample and their quantities. An electron beam (typically from an SEM) hits a sample exciting an electron in the atoms inner shell causing its ejection from the atom leaving an electron hole. The void is then filled by an electron residing in a higher energy shell expelling its energy in the form of X-rays which has energy equal to the difference in energy levels of the shells. These X-rays which

energies are characteristic of elements then hit the detector and are recorded. EDX will be used to measure the stoichiometry electrodeposited CdTe thin films.

2.9. X-ray Diffraction (XRD)

X-ray diffraction is a technique that makes it possible to investigate the crystallography of materials. Diffraction occurs due to distances between atoms being similar to the wavelength of the incident X-rays, which is typically in the order of angstroms. The X-rays interact with the electrons in the atoms leading to either constructive or deconstructive interference of the X-rays. Constructive interference is achieved when the Bragg condition (Equation 17) is fulfilled where *d* is the spacing between diffracting planes, ϑ is the incident angle in degrees and *n* is any integer representing the order of reflection and λ is the photons wavelength. This effect is shown in Figure 20.

Equation 17

$$n\lambda = 2d_{hkl}sin(\theta)$$

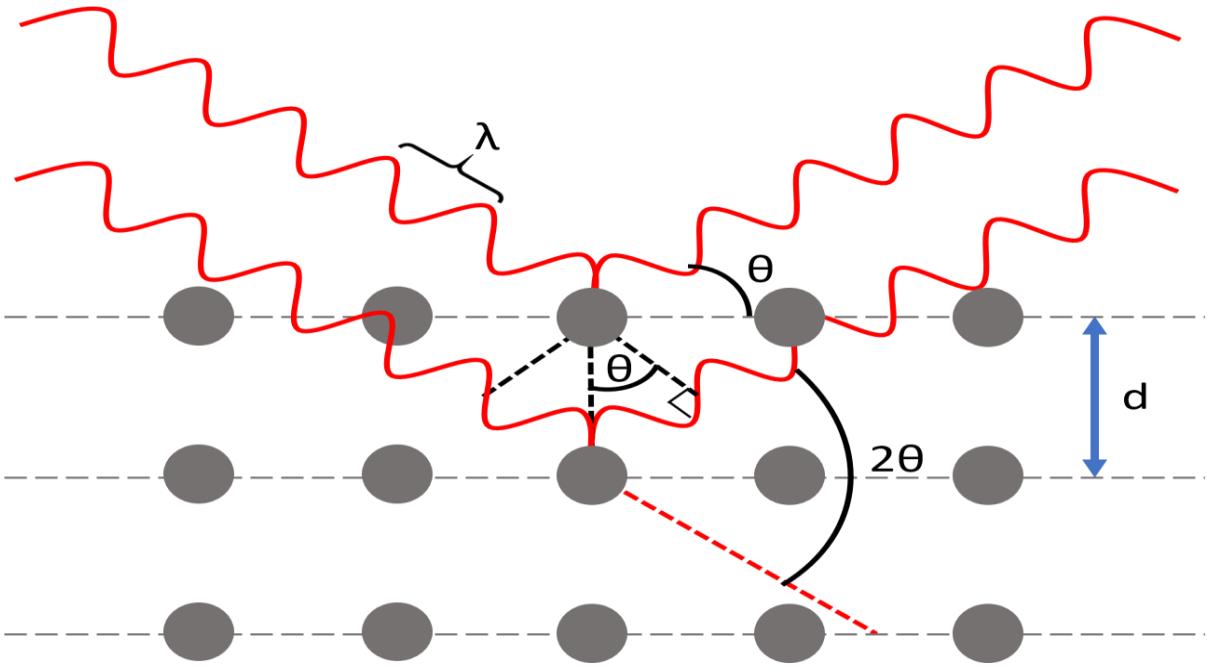

Figure 20. A geometrical representation of the Bragg equation (Equation 17) in which incoming X-ray photons undergo constructive interference after interacting with matter.

XRD will be used in this project to analyse electrodeposited materials and the XRD patterns obtained can be compared to a database by the International Centre for diffraction data (ICDD) of previously studied materials. It can be used to identify phases of materials. XRD

patterns can also be used to estimate the crystallite size from the extent of the peak broadening using the Scherrer equation (Equation 18).

Equation 18

$$D_{hkl} = \frac{K\lambda}{\beta cos\,(\theta)}$$

Where D_{xyz} is the crystallite size, K is the shape factor constant, λ is the X-ray wavelength, β is the full width half maximum intensity of the peak and θ is the diffraction angle.

2.10. Small angle X-ray scattering (SAXS)

Small angle X-ray scattering is a technique in which a focused beam of X-rays is used to obtain the shape and structural information of materials. SAXS can be performed on both solids and materials in solution and is often used to probe flexible materials such as proteins and other soft matter materials. SAXS is a contrast method in which the scattering signal is derived from the difference in electron density from the sample compared to a background (solution, air, substrate or a combination of them). In SAXS diffuse scattering and diffraction can occur which each provide information about the structure of materials. Diffuse scattering arises from the irregular non-periodic arrangement of structures which appears as a continuous background in the pattern. Diffraction occurs from the result of periodic and ordered structures as X-rays interact with repeating units within the sample. In SAXS the term q is the scattering vector. The scattering vector represents the change in momentum transfer of the X-rays from the interaction with the sample. q is defined by Equation 19 where θ is the scattering angle and λ is the wavelength of the incident X-rays. The scattering vector q is inversely proportional to the distance between scatterers in the sample which is shown in the second part of Equation 19. A graphical representation of q is highlighted in Figure 21.

Equation 19

$$q = \frac{(4\pi sin\theta)}{\lambda} \qquad q = \frac{2\pi}{d}$$

As the material of interest in this project will have cubic symmetry, unless stated otherwise, the lattice parameter (a_0) can be determined from the (d_{hkl}) diffraction peaks using Equation 20.

Equation 20

$$a_0 = d_{hkl} \times \sqrt{h^2 + k^2 + l^2}$$

SAXS will be used in order to determine the morphology of lipid templates and deposited materials as they possess dimensions within the range suitable for SAXS analysis. Space groups are used to describe the unit cells of structures in three dimensions, and the symmetry groups portray the regular repeating structure in electron density so the Bragg peaks can be predicted from a scattering experiment. Table 1 summarises expected scattering patterns from different liquid crystal phases.

Table 1 A list of the space groups and characteristic Bragg peaks and miller indices for the structured discussed in this thesis.

Structure	Space group	Peak ratios	Miller indices
Double diamond	Pn3m	√2, √3, √4, √6, √8, √9	(110), (111), (200), (211), (220), (221)
Single Diamond	Fd3m	√3, √8, √11, √12	(111), (220), (311), (222)
Lamellar		1, 2, 3 ,4	(100), (110), (111), (200)
Primitive	Lm3m	√2, √4, √6, √8	(110), (200), (211), (220)
Gyroid	La3d	√6, √8, √14, √16	(211), (220), (321), (400)

We can use SAXS to calculate the liquid crystal's water channel widths and the electrodeposited materials nanowire diameter and pore widths by using the Bragg peaks and a geometric model of the single and double diamond phase. To determine the liquid crystal's water channel diameter and the deposited materials nanowire diameter from SAXS we use Equation 21 and Equation 22 respectively. [25] Equation 22 makes the assumption that the nanowire diameter is equal to the water channel diameter of the template.

Equation 21
$$d_w = 2(0.391a(Q_{II}^{D}) - l)$$

Equation 22
$$d_n = 2(0.391\frac{a(M)}{2} - l)$$

Where d_w is the water channel diameter, d_n is the nanowire diameter, $a\left(\mathrm{Q}_{\mathrm{II}}^{\mathrm{D}}\right)$ is the template lattice parameter, $a(\mathrm{M})$ is the deposited material lattice parameter and l is the lipid monolayer thickness, which is 1.36 nm calculated by Meikle *et al*.[26] The lipid monolayer thickness is assumed to remained unchanged for the phytantriol templates with Brij-56 additives. In order to estimate the pore width of the single diameter material we use Equation 23.

Equation 23

$$Pore\ width = \frac{a(M)}{\sqrt{2}} - d_n$$

The majority of SAXS results shown in this work will be collected in transmission mode unless otherwise stated. The typical set-up for transmission SAXS experiments is shown in Figure 21. Here we can see the X-ray beam passing through a sample of interest, to the detector in which a scattering pattern is collected.

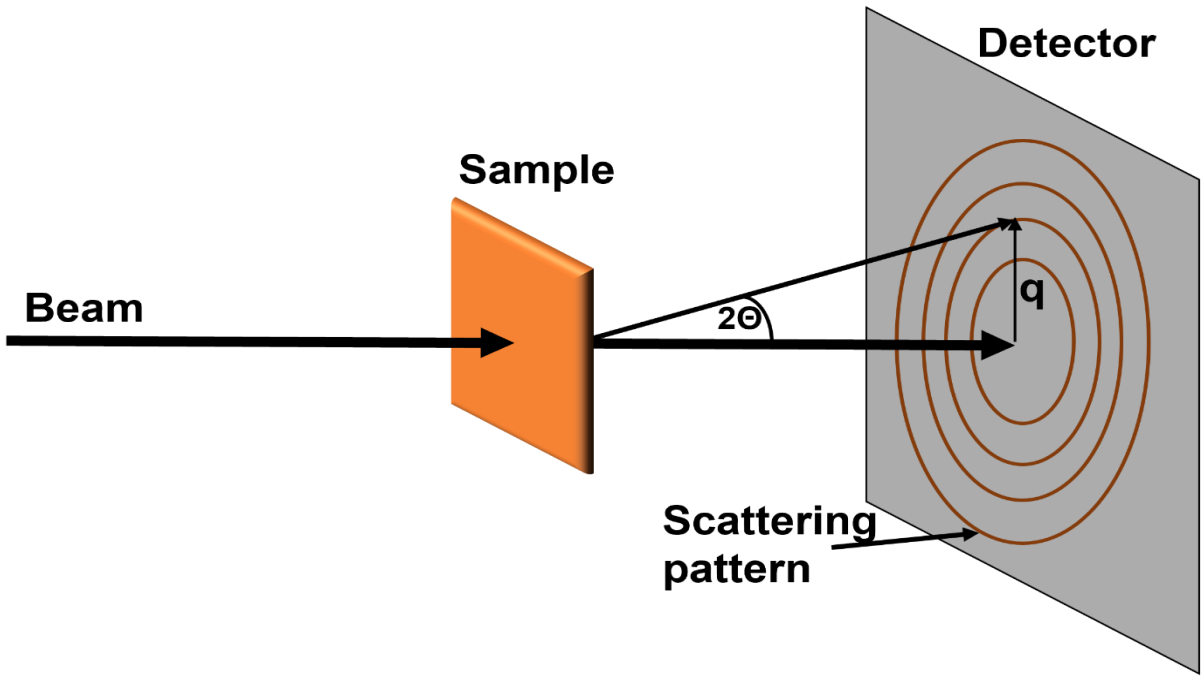

Figure 21 A simple schematic of how small angle scattering (SAXS) is collected in transmission mode with the beam going perpendicular through the sample to the detector.

SAXS not only gives us information on the morphology of samples, it can also provide information about the relative orientation of unit cells within a structure. Polydomain samples result in scattering patterns of even intensity around the beam centre that are known as Debye Scherrer rings which are shown in Figure 22. Debye Scherrer rings are formed by X-

rays that are diffracted by a crystal lattice causing constructive interference of the X-rays at specific angles, governed by Bragg's law. As polydomain materials are randomly orientated this occurs at all angles leading to a diffraction ring with even intensity. Samples that are orientated produce a specific pattern of dots relative to the orientation of the sample to the beam shown in Figure 22. This occurs as orientated single crystal-like materials will only diffract at certain angles, dictated by Bragg's law.

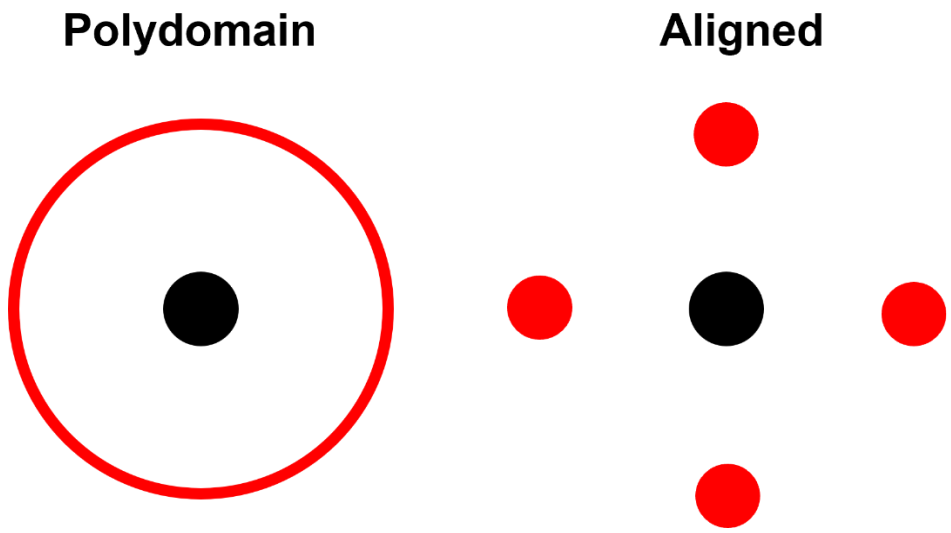

Figure 22 X-ray scattering patterns resulting from polydomain and single-crystalline materials.

2.11. Small angle neutron scattering (SANS)

Small angle neutron scattering is similar to SAXS but uses neutrons as the probe. For neutrons the interaction with matter is with the nuclei (neutrons and protons) of atoms whereas X-rays interact with the electron shells of atoms. Due to the interaction with nuclei as opposed to the electron shell there is a much different contrast environment across the periodic table when compared to X-rays. The scattering length density of neutrons does not increase with increasing atomic number, in fact it varies quite randomly and is also isotope sensitive. Figure 23 shows how the scattering length densities of neutrons varies with increasing atomic number. This is an important property of neutrons as it allows contrast between light elements.[27]

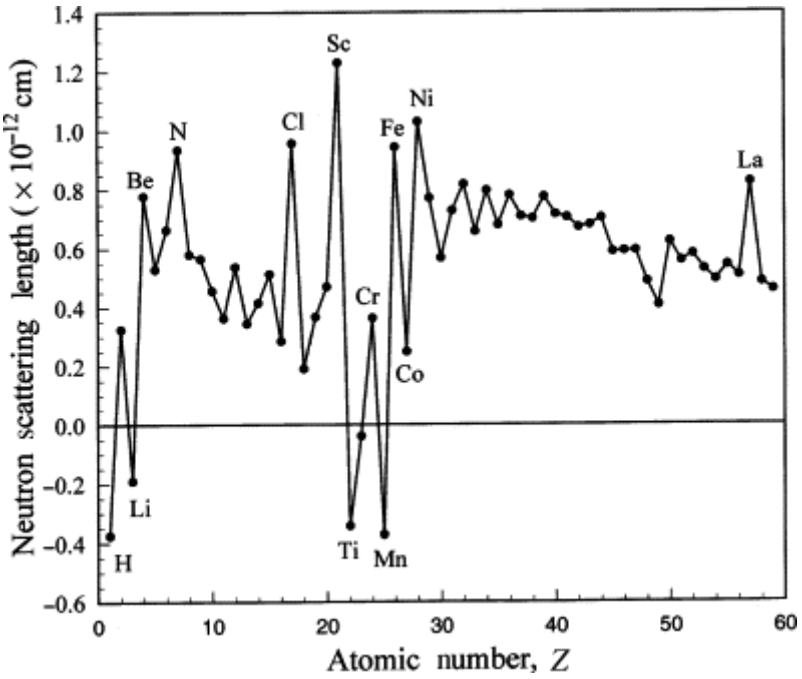

Figure 23 Neutron scattering length as a function of atomic number.[27]

One commonly utilised property of SANS is the fact there is a large contrast between the bound coherent scattering length between hydrogen atoms (H) and deuterium atoms (D) of -3.74 and 6.67 fm respectively. The scattering length density (SLD) of a system is from the sum of the coherent scattering length of each atom per unit volume given by Equation 24, where b_c is the bound coherent scattering length of i^{th} of n atoms in a molecule with molecular volume given by v_m.[28]

Equation 24

$$SLD = \frac{\sum_{i=1}^{n} b_c}{v_m}$$

The scattering length densities of species used in this work are highlighted in Table 2.

Table 2 The neutron scattering length densities (SLD) of species used in this work.

Species	SLD (Å^{-2})
H_2O	-5.6×10^{-7}
D_2O	6.5×10^{-6}
Phytantriol	-1.1×10^{-7}
D-phytantriol	6.8×10^{-6}
Pt	6.4×10^{-6}

This allows for precise contrast tuning and matching by varying the concentrations of H_2O or D_2O in the solution containing the sample of interest or by deuterating samples that contain hydrogen by replacing the hydrogen with deuterium. As the overall scattering is a result of scattering from all the components in a system the ratio of H_2O to D_2O changes the overall scattering.

This effect is highlighted in Figure 24, which shows how the scattering length density of water, lipids, proteins and DNA changes with increasing D_2O content.[29] In this project one of the aims is to perform in-situ SANS during electrodeposition where deuterated phytantriol is used as the template along with D_2O being mixed in with the electrolyte in order to contrast match parts of the system, to selectively monitor different parts of the system during the deposition process.

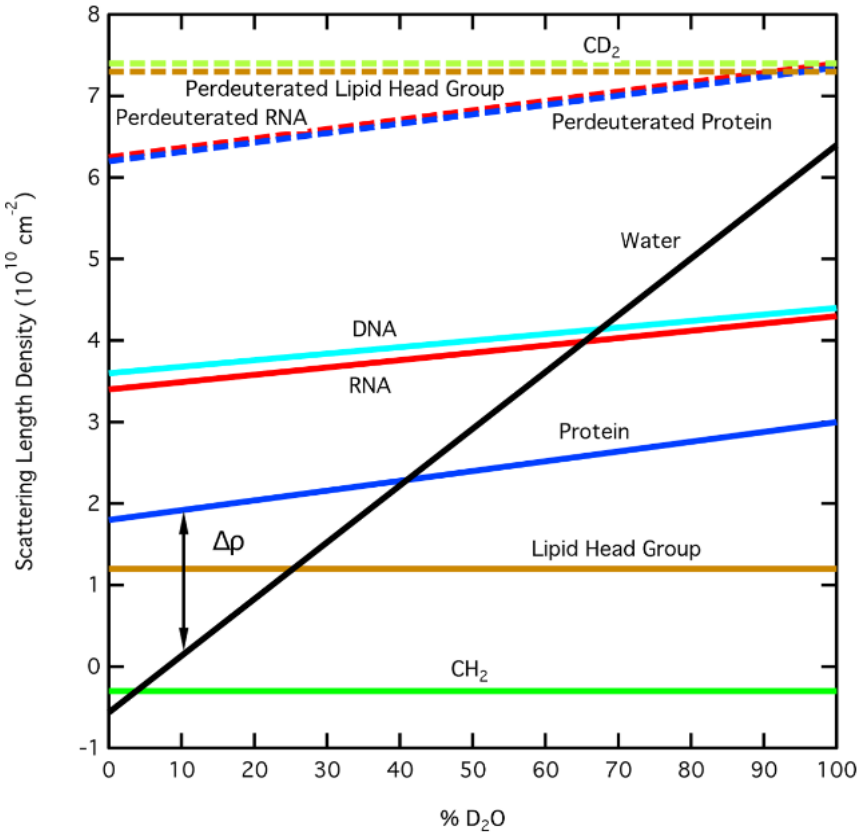

Figure 24 The neutron scattering length densities as a function of D_2O content in water, lipid, protein, and DNA. Taken from[29]

2.12. Reflectivity

Reflectivity is a technique that is used in material science to investigate the optical properties of materials such as semiconductors and thin films. The technique involves measuring the intensity of reflected light as a function of the wavelength of the incident light. This is a non-destructive technique which offers valuable information of a material's electronic structure and optical properties. By analysing the reflectivity spectra, it is possible to determine the band gap of a material. In this work reflectivity will be used to determine the bandgap of CdTe thin films.

In the next chapter, the electrodeposition of CdTe through the double diamond phase of phytantriol/Brij-56 will be thoroughly examined. The discussion will focus on how the deposition potential influences the stoichiometry of the resulting thin film. The material will be characterized using a range of techniques, including Small Angle X-ray Scattering (SAXS), Transmission Electron Microscopy (TEM), Scanning Electron Microscopy (SEM), Energy Dispersive X-ray Spectroscopy (EDX), and X-ray Diffraction (XRD).

3. Electrodeposition of CdTe

3.1. Introduction

In this project the aim is to electrodeposit the semiconductor CdTe through the liquid crystal template to create a novel 3D nanostructured material to improve the materials properties for photovoltaic applications. In order to achieve this goal, it is important to understand the basics of what semiconductors are and why their properties make them a good material for photovoltaics. Semiconductors are a class of materials which have an electrical conductivity between that of a metal and an insulator. This behaviour originates from the difference in the material's band gap, which represents the minimum amount of energy needed to excite an electron from the valence band to the conduction band, simplified and represented by Figure 25.

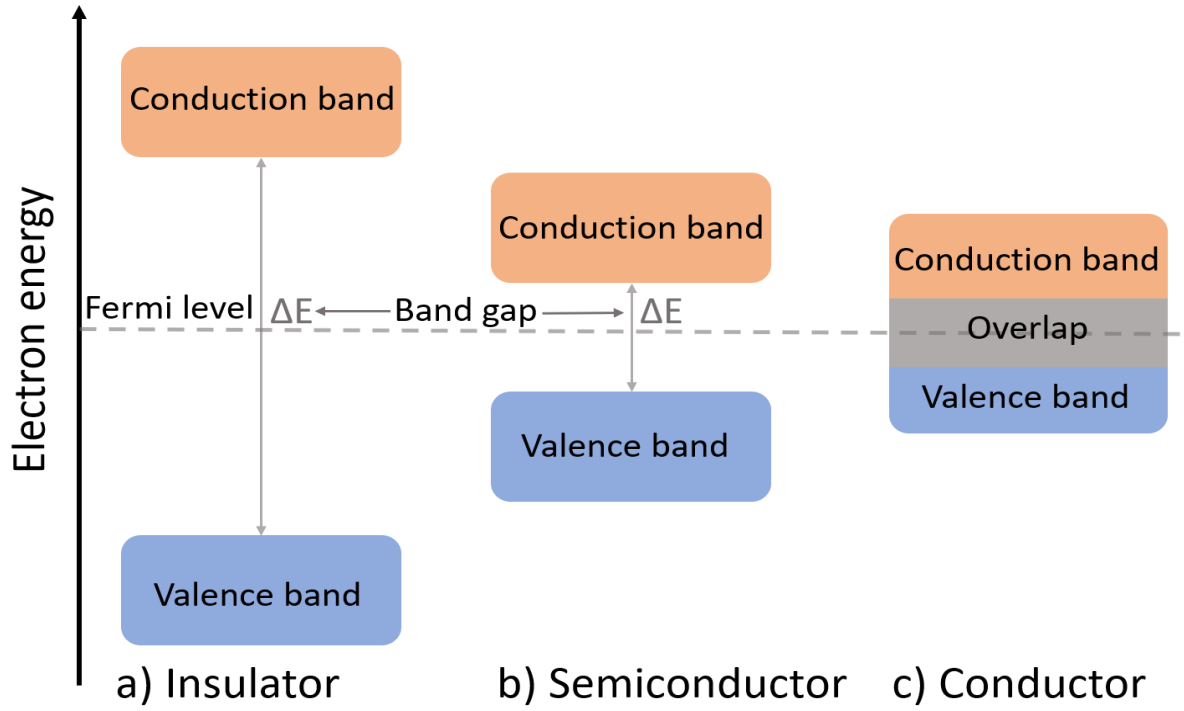

Figure 25. A simple energy diagram expressing the valence band (blue) and conduction band (orange) of insulators, semiconductors, and conductors. The Fermi level is the energy level at which the probability of finding an electron is 50 % at absolute zero. It is the reference point for the distribution of electrons within the energy bands of a material.

In conductors (metals) the valence band overlaps with the conduction band making valance electrons free to move into the conduction band to participate in conduction. Insulators have a very poor electrical conductivity due to the filled valence band and large energy difference

between the valence and conduction band so electrons cannot flow. The Fermi level is the energy level at which the probability of finding an electron is 50 % at absolute zero. It is the reference point for the distribution of electrons within the energy bands of a material.

The same is true for semiconductors however the band gap is small enough that when the electrons are excited (typically from heat or photons) a finite number of them can overcome the band gap conducting small amounts of electricity. This process means the semiconductor can now take part in conduction as a result of an electron hole being left in the valence band.

Besides basic intrinsic semiconductors such as silicon, two other types of semiconductor materials exist which are n-type and p-type semiconductors, these materials are typically made by introducing impurities or doping other elements into intrinsic semiconductors. A simple energy diagram depicting the valence and conductions bands of n and p-type semiconductors is shown in Figure 26. n-type semiconductors major charge carriers are electrons, and the minority charge carriers are holes, the Fermi level for n-types lies closer to the conduction band than the valence band. Silicon can be made into an n-type by doping with arsenic and phosphorous as this makes the silicon become slightly electron rich. P-type semiconductors have positive holes as the majority charge carrier and electrons as the minority carrier, and the Fermi level lies closer to the valence band than the conduction band as shown in Figure 26. Silicon can be made into a p-type semiconductor by doping with gallium or boron as these elements are electron deficient compared to silicon, so the semiconductor then has a higher concentration of holes than electrons.

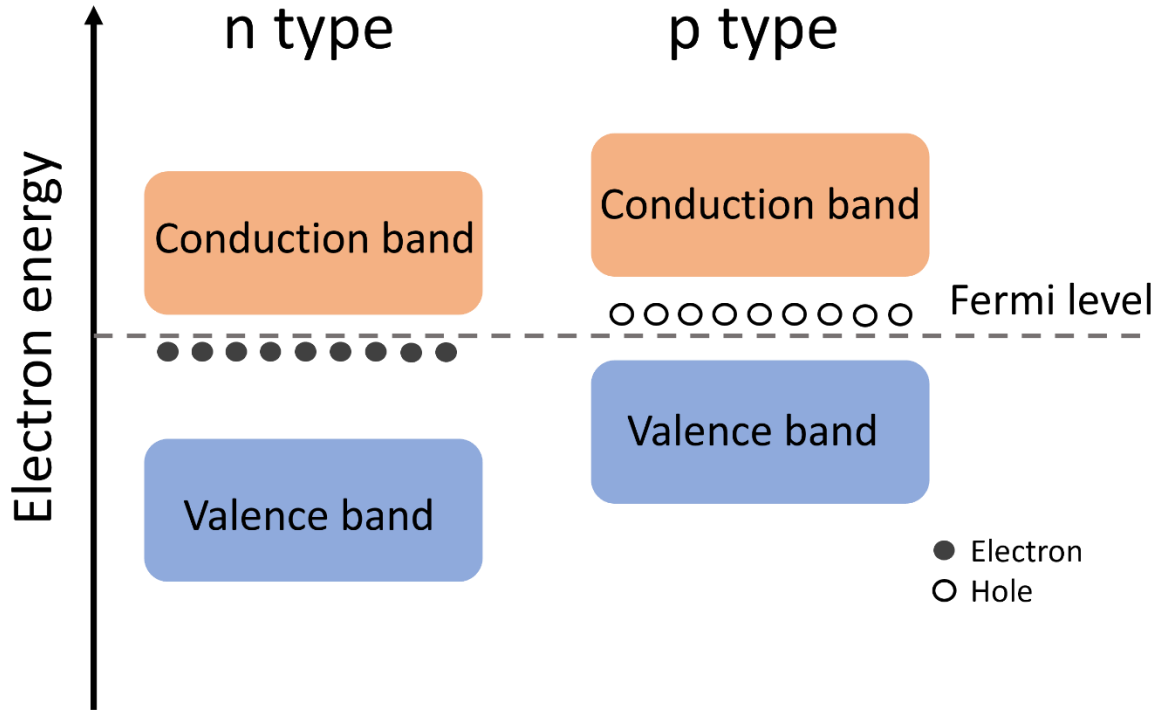

Figure 26 A simple energy diagram expressing the valence band (blue) and conduction band (orange) of n and p-type semiconductors. The black circles represent electrons and the white circles represent holes.

A P-N junction is created by combining n and p-type semiconductors which is very important as it forms the basics of how photovoltaic materials work. A junction is then created as there is an electrical density gradient between the n and p-type materials. Electrons from the n-type region diffuse across the junction into the p-type region and holes from the p-type region diffuse across to the n-type region combining with each other. This diffusion process occurs until an equilibrium is reached and there is a formation of a depletion region in which there are no mobile charge carriers. As electrons diffuse away from the n-type region they leave behind a positive region and as holes leave the p-type region they leave behind a negative region. This creates an electric field that opposes any further diffusion of charge carriers across the junction. A diagram of a P-N junction is shown in Figure 27.

P-N junctions are important in the fabrication of semiconductor devices for wide applications in electronic devices, diodes, transistors, LED and solar cells. The interest of this work is the photovoltaic properties of the semiconductor CdTe.

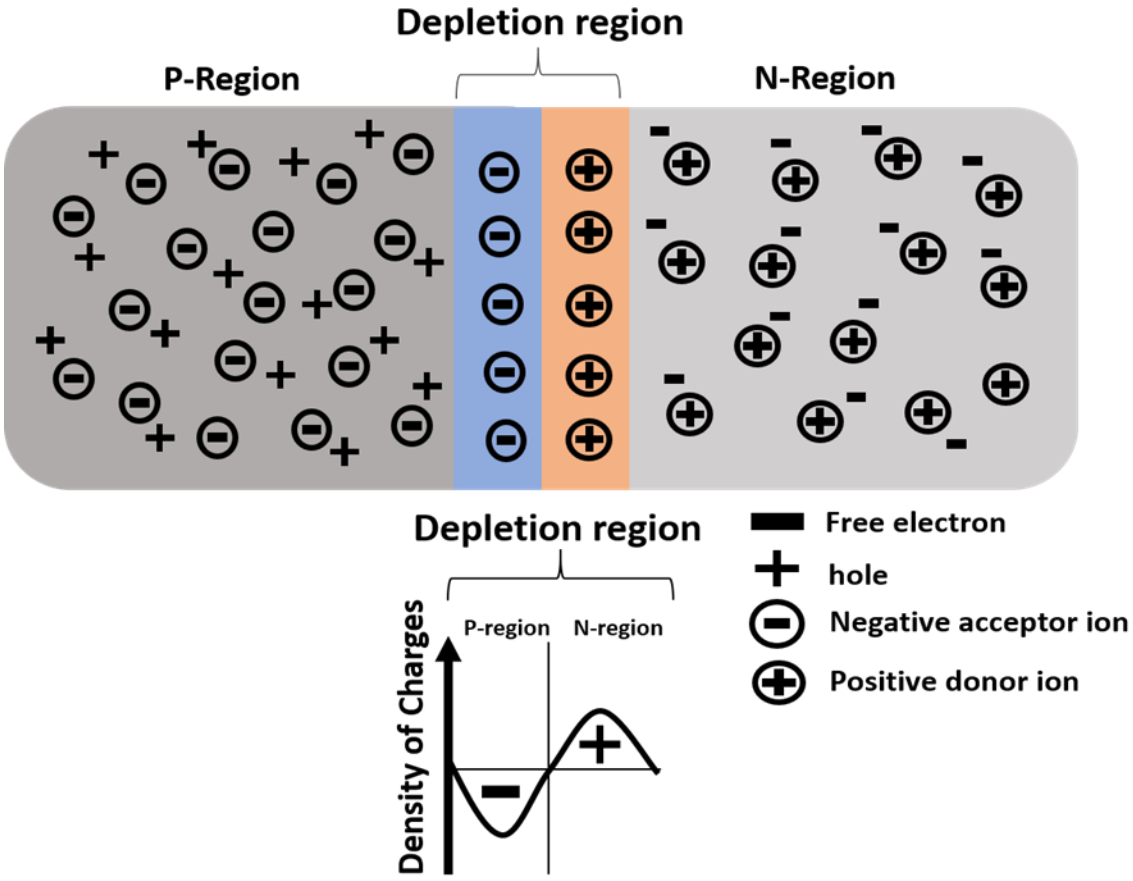

Figure 27. A diagram depicting a P-N junction formed between an n and p-type semiconductor highlighting the depletion zone formed along with the relative density of charge carriers across the P-N junction.

Solar cells are able to convert solar energy and convert it into useful electrical energy. The sun contains a large natural amount of sustainable energy which can be used as a greener energy source than fossil fuels. Solar cells are devices which take advantage of the photovoltaic effect. This effect converts photons of light into a useable electric energy and are made from semiconductor devices. A simple solar cell consisting of a P-N junction is shown in Figure 28, which highlights how the incident photons excite electrons, which creates an exciton pair (electron and a hole). These excitons due to their charges and the electric field, (junction potential), which exists in the P-N junction causes them to move in a single direction. The electron is attracted towards the n-type material and the hole is attracted towards the p-type material.

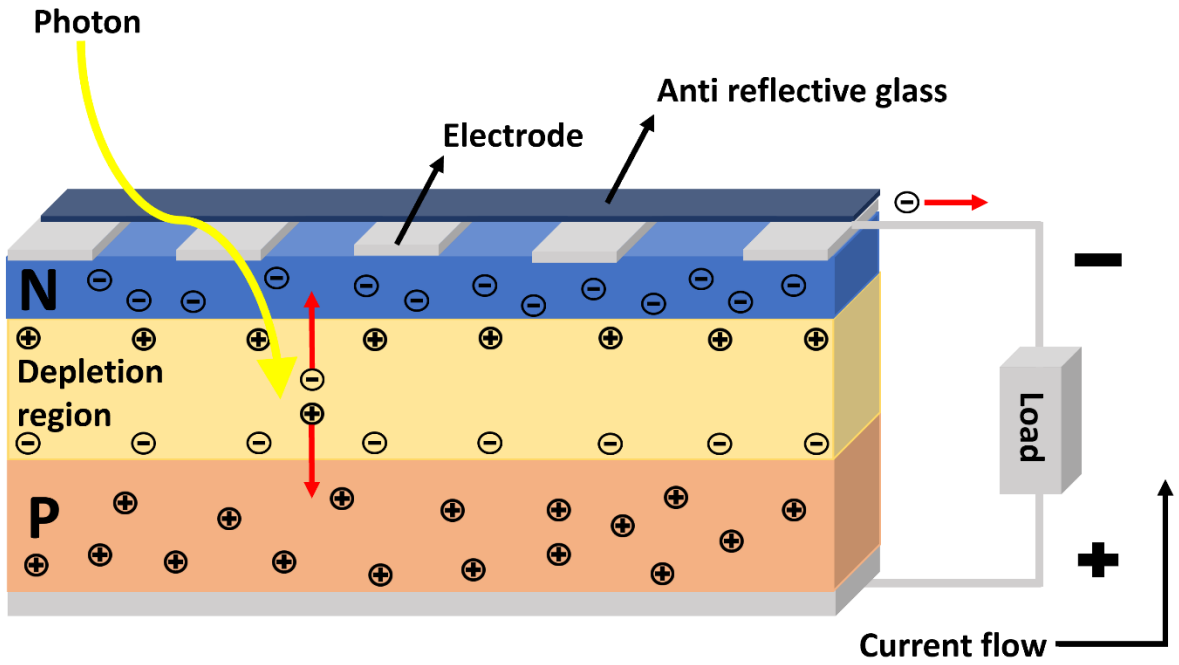

Figure 28 A diagram illustrating a basic solar cell consisting of N and P-type semiconductor materials forming a P-N junction connected to an external load. There is anti-reflective glass which acts to allow photons of light enter the material to excite an electron.

The excitons then become a majority carrier and migrate through the external load producing a current flow. The electric field produced in the depletion region is important in solar cells as the lifetime of excitons is very small and if they recombine in the depletion region, they cannot migrate through the material to produce a current. The electric field acts to lengthen the lifetime of these excitons making the solar cell possible.

For solar cells an ideal band gap is required in order for the material to absorb as much of the incoming sunlight as possible. The majority of the solar energy that reaches Earth is in the visible light region of the electromagnetic spectrum. Light with energy lower than the materials band gap will not be absorbed. Theoretical studies calculate that a semiconductor's ideal bandgap for maximum sunlight absorption and efficiency is 1.39 eV.[30] The maximum efficiency of single junction solar cells is known as the Shockley-Queisser limit. This uses the black body radiation model. Black body radiation is the light emitted from an object that absorbs all of the light shone on it. A black body model of 5800 K is well matched to our sun's spectral emission so this can be used to calculate the theoretical maximum energy that can be gained from a single junction solar cell. This model makes the assumption that each photon

greater than the bandgap creates an exciton pair and that all energy absorbed is converted into electrical energy. By comparing this to the total power incident on the solar cell a best-case scenario can be determined. Using this model and comparing the solar cell efficiency to the bandgap, Figure 29 , it can be seen that the maximum efficiency is around 32-33 % and occurs when the band gap lies between 1.1 and 1.4 eV.[31] The material of interest in this work is CdTe which is a semiconductor with a band gap of around 1.45 eV making it a near ideal material for solar cell applications.

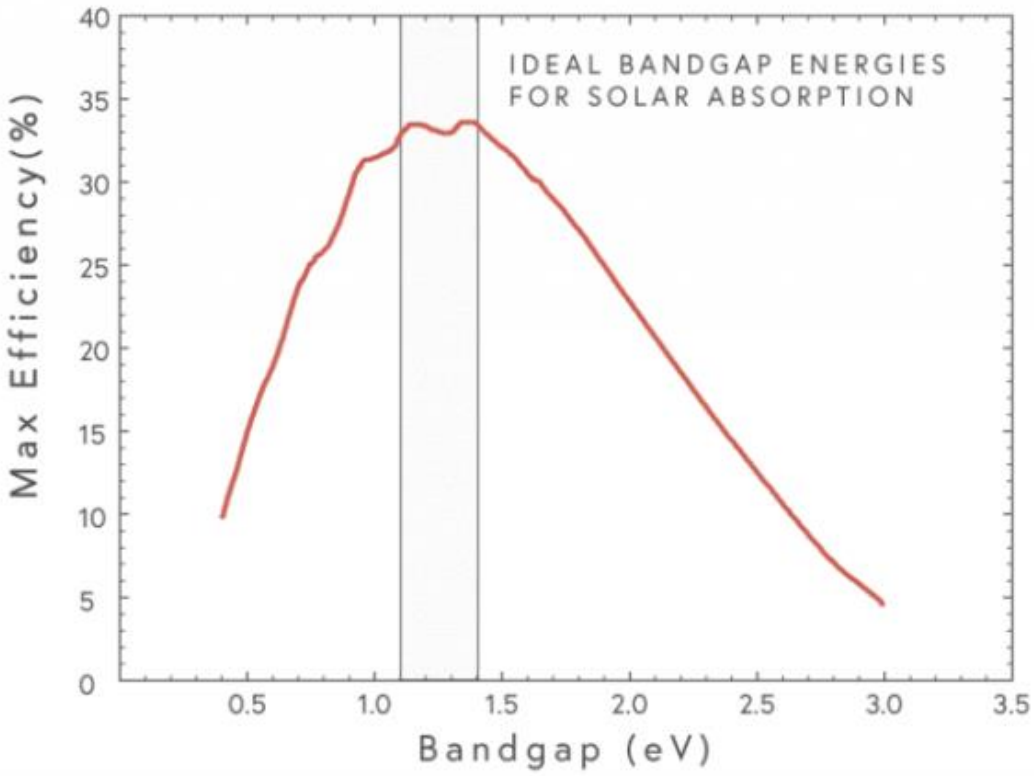

Figure 29 A graph depicting the maximum solar efficiency for different band gap energies.[31]

Nanostructured materials such as thin films, nanorods, nanowires and quantum dot structures are being studied for application in solar cells as they enable the fabrication of low-cost, high efficiency devices. Solar cells can be improved by increasing the efficiency of the device by creating absorber materials of a higher quality or by reducing the cost of device fabrication while maintaining a high efficiency. Both methods act to reduce the cost per kilowatt-hour of electrical energy that is produced, which is an important factor in determining if a solar cell is fit for purpose in real world applications. Nanostructured semiconductor materials can improve the efficiency of solar cells as some of the properties are influenced by the nanostructure such as carrier and exciton separation, charge extraction

and exciton recombination.[32]The large surface areas and different topologies that nanostructures can have compared to bulk materials can also improve the amount of light absorbed (light trapping), reducing the amount of light reflected from the surface, improving the cells efficiency.

A common way in which nanostructures are used to increase solar cell efficiency is by light trapping.[33–35] Light trapping occurs when the optical path length of the incident light is several times larger than the actual devices thickness. The optical path length of a device is equal to the distance an unabsorbed photon may travel within a device before it escapes. Light trapping improves the absorption by increasing the optical path length, which increases the likelihood of the photon being absorbed. This can be achieved by nanostructuring which can lead to textured surfaces which act to increase the optical path length of photons as depicted in Figure 30.

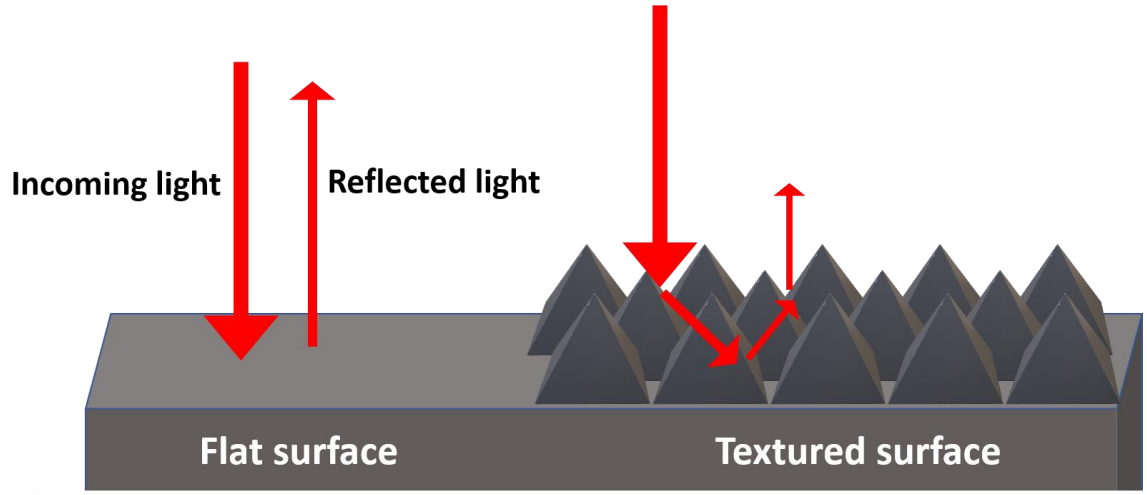

Figure 30 A simple diagram describing how surface texturing can increase the optical path length of incident light by angles reflection.

An increase in the absorption allows for a lower absorber layer thickness, so significantly less material is needed, reducing the production cost of the solar cell. Light trapping can also increase the solar cell efficiency as thinner devices can improve the photogenerated charge carrier collection with less constraints on the diffusion lengths.[34]

Garnett and Yang[33] used this method of creating nanostructured material in order to use light trapping to increase the light absorption of a silicon based solar cell. A silicon nanowire array was fabricated by a method consisting of four steps being silica bead synthesis, a dip-coating

process to form a self-assembled silica bead monolayer on a silicon surface, deep reactive ion etching to form a nanowire array and diffusion to form the P-N junction. The resulting 5 µm long silicon nanowires produced a solar cell device which gave a solar cell efficiency of 5.3 % which was a significant increase from their previous work on a similar device which was 0.5 %.[36] Optical measurements determined the increase in efficiency was from the light trapping effect as there was a maximum light trapping path length enhancement factor of 1.7 to 73 depending on the nanowire geometry.

It has also been well established that when semiconductors have dimensions between 1 to 100 nm the optical and electronic properties become size dependent, particularly the band gap energy.[37] The size dependent properties of nanostructured semiconductors can arise from the quantum confinement effect. The quantum confinement effect is a phenomenon in which the motion of charge carries like electrons and holes are restricted spatially in one, two or three dimensions. This confinement leads to quantified energy levels and results in unique electronic and optical properties.

In this project mesoporous CdTe films were fabricated via electrodeposition through a lyotropic liquid crystal template, and the resulting material will be characterised using a wide array of techniques.

Cadmium telluride (CdTe) is a semiconductor material which has extremely suitable properties for solar cell applications. CdTe adopts a Zinc blend (cubic) structure[38] shown in Figure 31 and has a bandgap of 1.45 eV which is a near ideal bandgap for the theoretical maximum photovoltaic conversion efficiency of 31%.[39] CdTe also has a short adsorption length which reduces recombination of excitons at grain boundaries so a large fraction of the photogenerated carriers are generated in the depletion region, allowing a more efficient collection.[40]

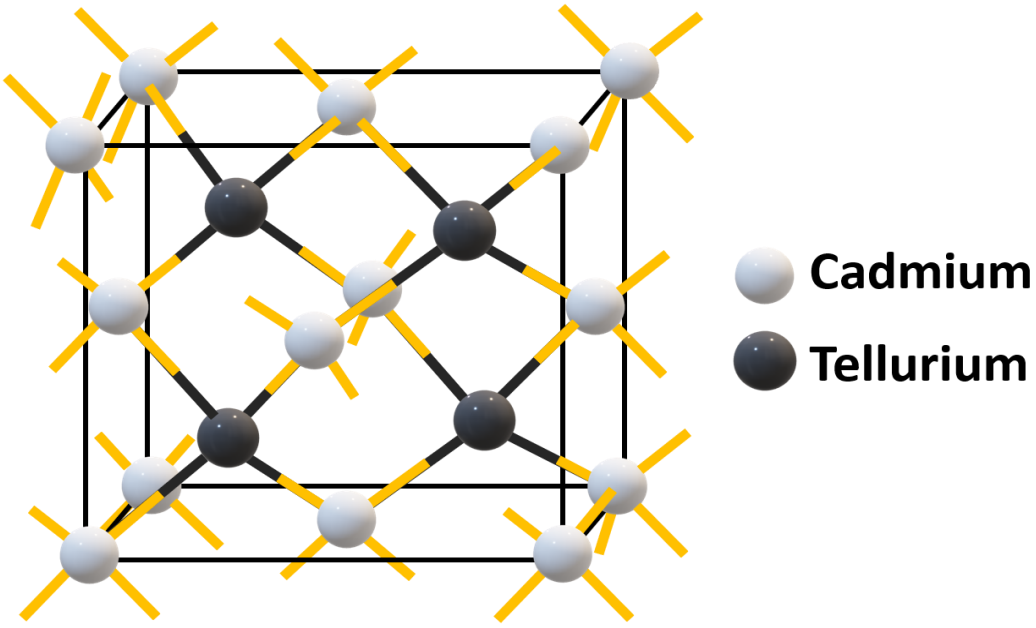

Figure 31 The zinc blende structure adopted by cadmium telluride (CdTe), with cadmium and tellurium expressed by white and black spheres respectively.

The acceleration of research into CdTe based solar cells started in the 1970s and within a single decade, devices were produced with efficiencies over 10%. In 1993 Britt *et al.* used chemical bath deposition to create CdS films followed by close-space sublimation of p-type CdTe films to fabricate CdS/CdTe solar cells with an area greater than 1 cm^2 with a reported efficiency of 15.8%.[40] The improvement of CdTe based solar cells then became stagnant for almost another decade with not much progress being made until 2001 when Wu *et al.* fabricated a modified CTO/ZTO/CdS/CdTe solar cell which had a reported efficiency of 16.5 %[41] which is only 0.6% higher than the previous work done by Britt *et al* (15.8 %). However, First Solar Company made quick progress in the development in CdTe based solar cells producing lab-scale efficiencies of 22 % in 2017 and currently produce solar panels with an efficiency of 18 % and are the largest thin film solar panel manufacturer for CdTe based solar cells.[42–44]

For this project electrodeposition was the chosen technique to produce thin films and 3D nanostructured networks of CdTe through phytantriol/Brij-56. The electrodeposition of CdTe is widely reported in literature.[45–51] CdTe can be intrinsically doped during its growth process to be either an n or p-type semiconductor material by altering its stoichiometry. If the material is cadmium rich, it tends to exhibit n-type conductivity, whereas if it is tellurium rich,

it tends to exhibit p-type conductivity. When fabricating CdTe via electrodeposition, the stoichiometry of the material can be influenced by the deposition potential.

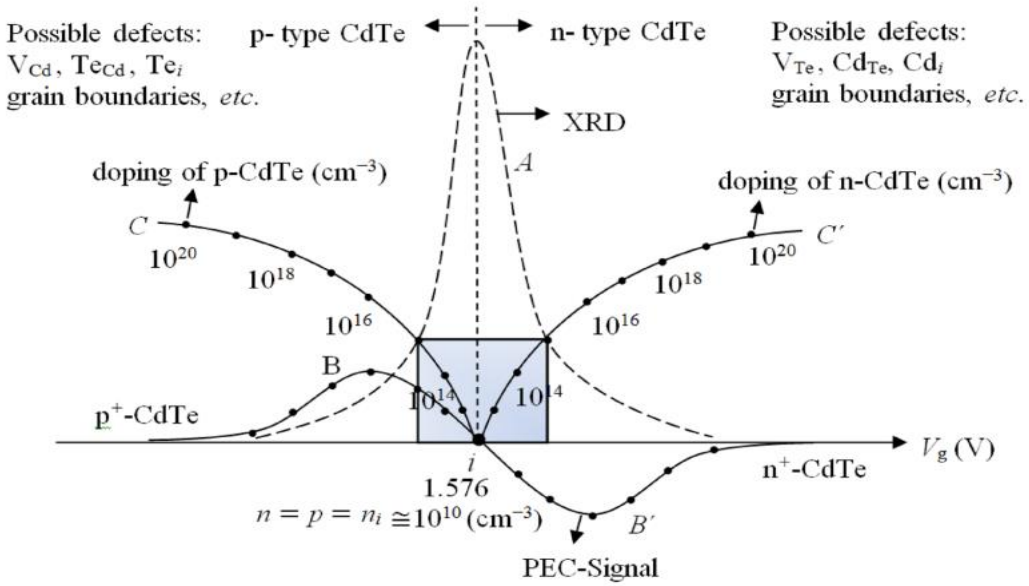

Figure 32 The graphical representation of summarised results from literature of electrodeposited CdTe layers taken from Dharmadasa et al.[49] *V_g represents a deposition potential in which stoichiometric and highly crystalline (as shown by XRD) CdTe is produced. The line B shows the variation in electrical conduction type and C shows the doping concentrations across the deposition potential range.*

Figure 32 expresses how the properties of electrodeposited CdTe vary with the deposition potential.[49] V_g represents the deposition potential in which stoichiometric CdTe is grown. By altering the deposition potential, it is possible to intrinsically dope the material with excess Cd or Te making the material either n or p-type. By selecting a potential that preferentially drives the deposition of Cd or Te, it is possible to control the composition of the resulting CdTe.

Oluyamo *et al.* recently reported how electrodeposition and post-treatment of CdTe films by annealing can be used to fine tune the properties of CdTe. CdTe films were produced by cathodic deposition on FTO (fluorine doped tin oxide) electrodes from an aqueous electrolyte solution of cadmium sulphate, tellurium oxide and an ammonium complexing agent. The optical energy band gap was found to decrease from 1.98 to 1.43 eV with increasing deposition time for the as deposited films and decreased from 1.90 to 1.38 eV for the films annealed at 350 ^oC for 20 minutes. The variation of band gap with deposition time has been described to be from a reduction in surface density leading to large surface to area ratio in

the thin films and from quantum confinement effects in which optical properties become size dependent. It was also revealed that the as deposited CdTe thin films were n-type due to them being cadmium rich but after being annealed the CdTe became a p-type semiconductor.[50] It is clear that electrodeposition is a very powerful technique in CdTe fabrication.

In order to enhance the properties of CdTe further efforts have been made to electrodeposit CdTe through templates in order to create nanostructured CdTe.[46,48,52–56] Sima *et al.* created nanorod and tube arrays of CdTe using electrodeposition in polycarbonate ion track membranes, using both acidic and basic conditions. The ion track membranes were prepared by irradiating polycarbonate foils with heavy ions producing cylindrical damage zones which are chemically more active than the surrounding material. The polycarbonate was then etched in an aqueous alkaline solution of 5 M NaOH with 10 % methanol at 50 ^{o}C which produced cylindrical pores with diameters ranging from 100 to 2000 nm depending on etching times. Post deposition the polymer membrane was removed by dissolving it in CH_2Cl_2. The CdTe nanorods produced from the acidic electrolyte solution were around 1000 nm in diameter and EDX measurements revealed an atomic ratio of Cd/Te of 9/1 which is far from the desired ratio of 1/1. When Sima *et al.* did the deposition in basic media nanowires were produced with an atomic ratio of Cd/Te of 1/1.4 for the larger wires and 1/1.4 for the smaller wires which was an improvement. The nanowires produced from this method ranged from 100 to 2000 nm but it was reported the smaller wires would break when the template was removed.[51]

The issue with electrodeposition through hard templates is that it requires harsh chemicals, high amounts of energy and multiple steps in order to prepare and remove the templates. However, electrodeposition through soft templates (liquid crystal templating) provides a one-pot method with easy removal of the template using safer solvents such as ethanol. Previously Nandhakumar *et al.*[48] reported the electrodeposition of high quality, nanostructured mesoporous CdTe films through the non-ionic surfactant octaethyleneglycol monohexadecyl ether ($C_{16}EO_8$). The aqueous electrolyte solution used comprised of 0.15 M $CdSO_4$ and 0.005 M TeO_2 in 2M H_2SO_4 mixed in a 1:1 ratio with 50 wt% of $C_{16}EO_8$ in de-ionised water. The $CdSO_4$ and TeO_2 dissolved in the aqueous domain of the hexagonal lyotropic liquid crystalline phase

of $C_{16}EO_8$. Cathodic electrodeposition was then performed on gold on glass working electrodes by stepping the potential from 0 V to a potential in the range of -0.54 to -0.65 V *vs* SCE for times of 5 to 16 hours. The post-treatment of the CdTe films involved removing the $C_{16}E0_8$ template by soaking the films in de-ionised water for 24 hours replacing the water every 2 hours until all the surfactant was removed. Low-angle XRD revealed a diffraction peak at 1.52^o which was assigned to diffraction from a hexagonal lattice with lattice parameter of 69 Å. Direct evidence of the nanostructured CdTe films was revealed by TEM images, Figure 33, which shows a hexagonal array of cylindrical pores with an average pore-to-pore distance of 70 Å. EDX results also confirmed that the deposition potential influenced the stoichiometry of the CdTe films.

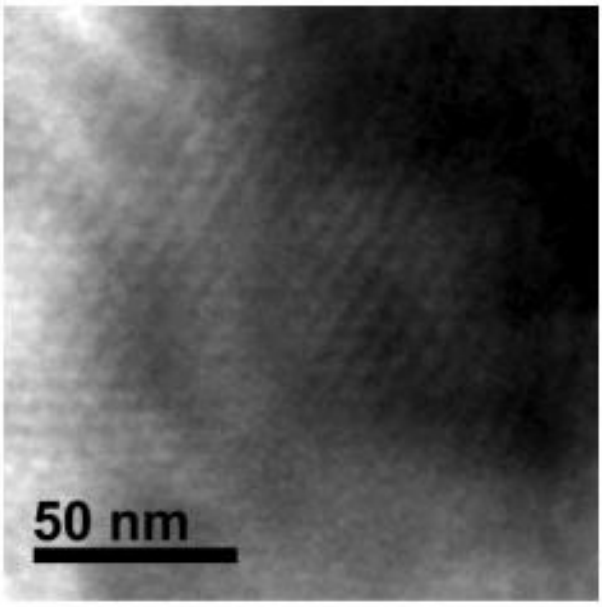

Figure 33 TEM image of CdTe electrodeposited from the hexagonal liquid crystalline phase of $C_{16}EO_8$. Taken from.[48]

Li *et al*.[47] successfully electrodeposited mesoporous CdTe films from lyotropic liquid crystalline phases of octaethyleneglycol monohexadecyl ether ($C_{16}EO_8$). The CdTe films were electrodeposited on a CdS working electrode from a 50 wt% $C_{16}EO_8$ and 50 wt% aqueous solution containing 0.15 M $CdSO_4$ and 0.005 M TeO_2 in 0.5 M citric acid at pH 1.75 and 50 ^{o}C at potentials between -0.58 V t0 -0.65 V vs SCE. Figure 34 shows the schematic of the templating process of mesoporous CdTe through $C_{16}EO_8$ onto a CdS substrate.

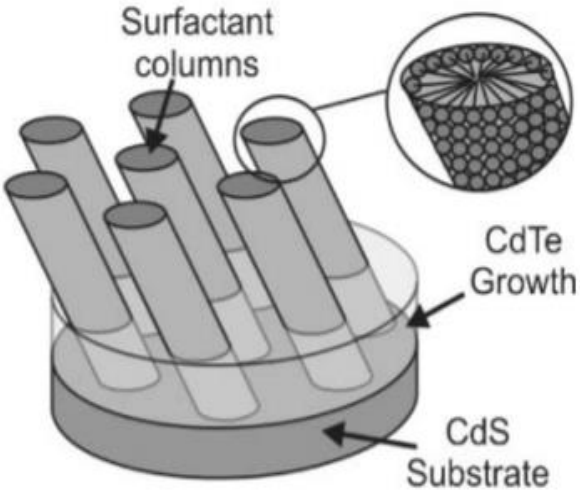

Figure 34 A schematic of the templating process used for the electrodeposition of mesoporous CdTe on CdS substrates from the hexagonal phase formed by the surfactant $C_{16}EO_8$. Taken from.[47]

EDX measurements revealed that the stoichiometric CdTe films were deposited over the potential range -0.58 to 0.65 V vs SCE and SEM imaging revealed that the structures produced had a smoother surface of closely packed fine crystallites (with a diameter less than 50 nm) compared to CdTe films deposited without the $C_{16}EO_8$ template, which exhibited larger aggregates. TEM and low-angle XRD revealed the CdTe to have a hexagonal structure with a d spacing of 57 Å (pore-to-pore distance of 66 Å) and the (100) diffraction peak from the XRD proves the ordered mesophase structure in the template is preserved in the deposited CdTe. Photocurrent measurements were performed on both the bulk and mesoporous CdTe films recording bandgap values of 1.50 ± 0.05 eV and 1.50 ± 0.15 eV which is in agreement with the expected bandgap value for CdTe at room temperature.

From the literature, it is clear that the electrodeposition of CdTe via lyotropic liquid crystalline phases of surfactants is possible and produces high quality films with tuneable properties, making this an attractive synthetic route for producing CdTe films for photovoltaic application. The mesoporous structure should produce a film with higher absorption compared to a non-templated thin film due to light trapping increasing the optical path length due to the nanostructure.

The aim for this project is to produce novel mesoporous single diamond phase CdTe films via electrodeposition through the bicontinuous inverse cubic phase of the non-ionic surfactant

phytantriol. The resulting nanostructure will be characterised by a series of techniques such as SEM, EDX, and SAXS.

3.2. Experimental

3.2.1. Solution recipes

An aqueous solution of 0.15 M $CdSO_4$, 0.005 M TeO_2 in 2 M H_2SO_4 was used as the electrolyte solution for the electrodeposition of both templated and non-templated CdTe films.

3.2.2. Electrode preparation

The working electrode used was a Si wafer with a 20 nm sputtered Ti adhesion layer followed by a 200 nm evaporated Au layer. Before cyclic voltammetry and electrodeposition experiments, the electrodes were thoroughly cleaned by 10 minutes of sonication in isopropyl alcohol (IPA) and deionised water subsequently. Nail polish was used to create a 1 cm by 1cm working electrode area. For SAXS experiments Au-DVD electrodes from Delkin Devices were used for SAXS experiments by cutting them to size and removing the insulation layer by cleaving the DVD revealing the gold surface. A 1 cm by 1 cm working electrode area was created using nail polish as a mask.

To prepare the electrodes with the liquid crystal templates, the electrodes were dip coated in a phytantriol/Brij-56: ethanol solution in a ratio of 1:2 by weight and allowed to dry for at least an hour so that ethanol evaporated, leaving behind a thin film on the electrode. The lipid covered electrodes were immersed in the electrolyte solution for at least 30 mins before cyclic voltammetry or electrodeposition experiments to allow the lipid to hydrate forming the desired double desired phase.

3.2.3. Electrodeposition and template removal

Electrodeposition experiments were performed using a three-electrode setup with a working electrode, a Pt-gauze counter electrode and SCE reference electrode. Electrodeposition was performed by stepping the potential from 0 V *vs SCE* to a potential in which CdTe deposited for a set period of time using an Ivium VERTEX potentiostat controlled using IviumSoft.

To remove the lipid template after deposition, the working electrode was soaked in ethanol for a minimum of 30 minutes then left to dry in air.

3.2.4. Small angle X-ray scattering

For SAXS experiments performed on I22 at the Diamond Light Source,[57] the working electrodes used were Au/DVDs. A camera length of 4.5 m was used with a beam energy of 12.4 keV. For the in-situ experiments conducted on the offline SAXS instrument, Xeuss, at the Diamond Light Source, a camera length of 1.5 meters was used. The experiments utilised a beam energy of 9.2 keV, generated by a Ga MetalJet source.

3.2.5. TEM

In order to prep TEM samples, a drop of ethanol was placed on the CdTe thin films after template removal and the sample was scratched using a blade creating a suspension of CdTe in the ethanol. A small amount of this suspension was then dropped onto a TEM grid and left to dry overnight to create the TEM sample. TEM images were taken on a JEOL JSM-2100PLUS.

3.3. Cyclic voltammetry

In order to analyse the electrochemistry of the system CVs were first taken of the individual solutions, followed by the mixed precursor solution used to make the thin films. The proposed mechanism for CdTe electrodeposition in acidic media was described by Engelken *et al*. [58] which is as follows:

Equation 25 $$Cd^{2+}_{(aq)} + 2e^- \rightarrow Cd_{(s)}$$

Equation 26 $$HTeO_2{}^+_{(aq)} + 3H^+ + 4e^- \rightarrow Te_{(s)} + 2H_2O$$

Equation 27 $$Te_{(s)} + Cd^{2+}_{(aq)}\ 2e^- \rightarrow CdTe_{(s)}$$

The cathodic peak at -0.72 V *vs* SCE in Figure 35 (a) is a result from the cadmium reduction as described in Equation 25. The anodic peak at -0.65 V *vs* SCE is from stripping of the cadmium from the electrode surface. The cathodic peak at -0.38 V *vs* SCE in Figure 35 (b) is a result from the tellurium reduction/deposition which can be explained by Equation 26 and the anodic peak at 0.6 V *vs* SCE is from the tellurium stripping. Figure 35 (c) reveals that for the mixed electrolyte solution the deposition of tellurium starts at -0.3 V and bulk cadmium deposition begins at -0.73 V *vs* SCE. Therefore, somewhere in the region between these potentials stoichiometric CdTe films can be deposited.

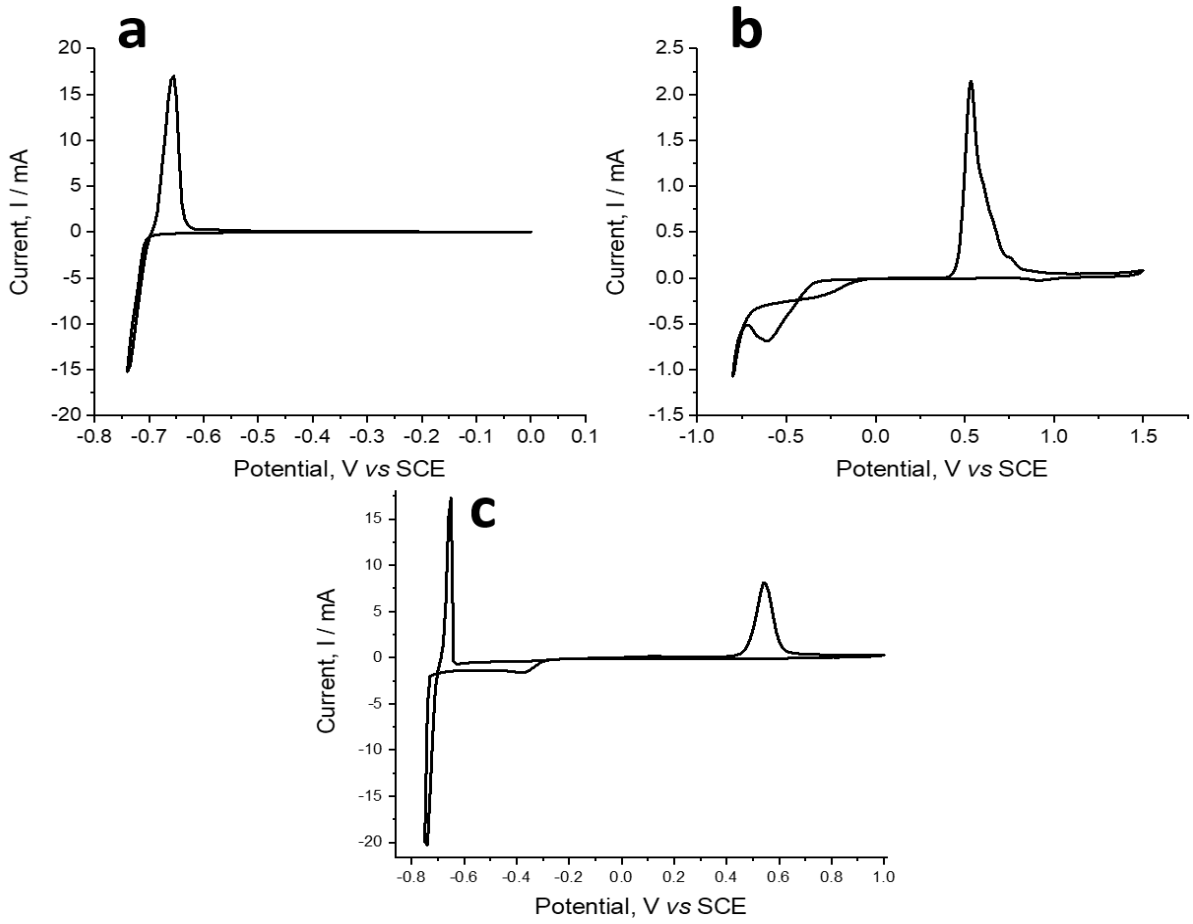

Figure 35 Cyclic voltammograms taken at 50 mV s^{-1} on a 1 cm^2 Au/Si electrode at room temperature of (a). 0.15 M $CdSO_4$ in 2 M H_2SO_4, (b) 0.005 M TeO_2 in 2 M H_2SO_4 and (c) 0.15 M $CdSO_4$, 0.005 M TeO_2 in 2 M H_2SO_4.

3.4. Thin film electrodeposition

In order to produce stoichiometric CdTe thin films the potential was stepped from 0 V to between -0.5 to -0.72 V *vs* SCE for 1 hour. The current vs time transients for this series of thin film electrodepositions are shown in Figure 36. The transients in (a) have an average current response below 1 mA which corresponds to a slow rate of deposition compared to (b) which shows that when the deposition potential was -0.72 V *vs* SCE the rate of deposition was much higher and increased over time as shown by a much larger current. This larger current response and more rapid deposition was a result of excess cadmium being deposited which was revealed by EDX.

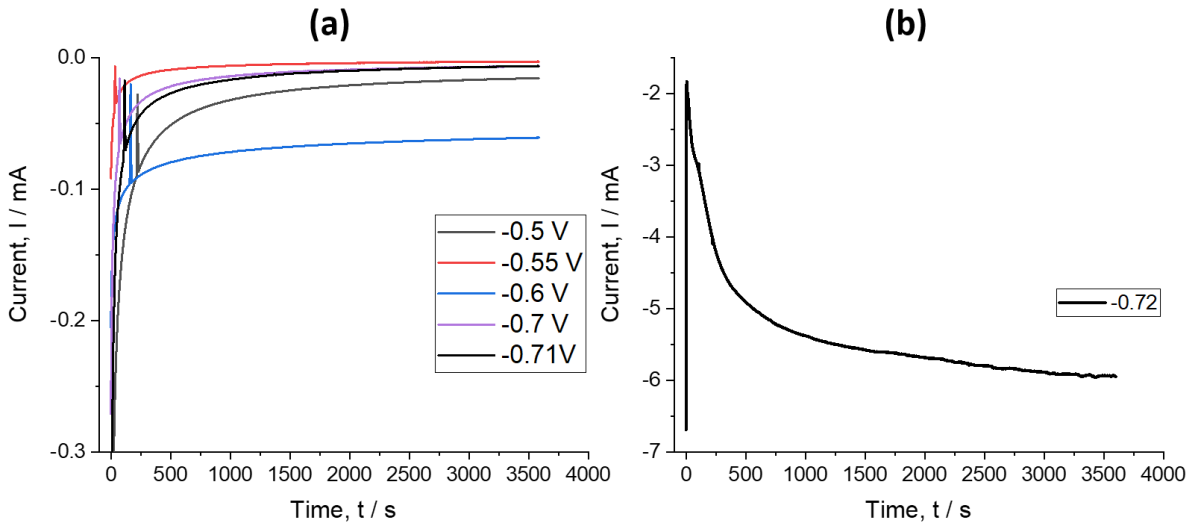

Figure 36 Time vs current transients for the electrodeposition of CdTe on Au/Si electrodes for 1 hour at potentials of (a) -0.50, -0.55, -0.60, -0.70, -0.71 V vs SCE and (b) -0.72 V vs SCE.

EDX was used in order to measure the stoichiometry of the CdTe films. The stoichiometry of the deposited films as measured by EDX are shown in Table 3.

Table 3 The atomic percentage of cadmium and tellurium in CdTe thin films grown for 1 hour at deposition potential of -0.50, -0.55, -0.60, -0.65, -0.70 and -0.72 V vs SCE as measured by EDX.

Deposition potential, V *vs* SCE	**Cd, atomic %**	**Te, atomic %**
-0.50	36 ± 3	64 ± 4
-0.55	35 ± 4	65 ± 6
-0.60	39± 1	61 ± 2
-0.65	34 ± 1	66 ± 2
-0.70	36 ± 1	64 ± 2
-0.72	62 ± 1	39 ± 1

EDX revealed that films grown between -0.50 and -0.70 V *vs* SCE were tellurium rich and the film grown at -0.72 V was cadmium rich. Therefore, it was theorised that there is a potential window between -0.70 and -0.72 V *vs* SCE in which stoichiometric CdTe can be deposited.

CdTe thin films were then grown at potentials of -0.705, -0.71 and -0.715 V *vs* SCE with the atomic percentages of Cd and Te measured by EDX shown in Table 4.

Table 4 The atomic percentage of cadmium and tellurium in CdTe thin films grown for 1 hour at deposition potential of -0.705 -0.71 and -0.715 V vs SCE as measured by EDX.

Deposition potential, V *vs* SCE	**Cd, atomic %**	**Te, atomic %**
-0.705	49 ± 1	51 ± 1
-0.71	45 ± 1	55 ± 1
-0.715	66 ± 1	34 ± 1

The thin film grown at -0.705 V *vs* SCE gave a stoichiometric film with a ratio of 1:1 for Cd:Te within error. The EDX pattern for this film is shown in Figure 37. The slightly tellurium rich film would make the material p-type which is a desired property for application in the CdTe/CdS single junction solar cell.

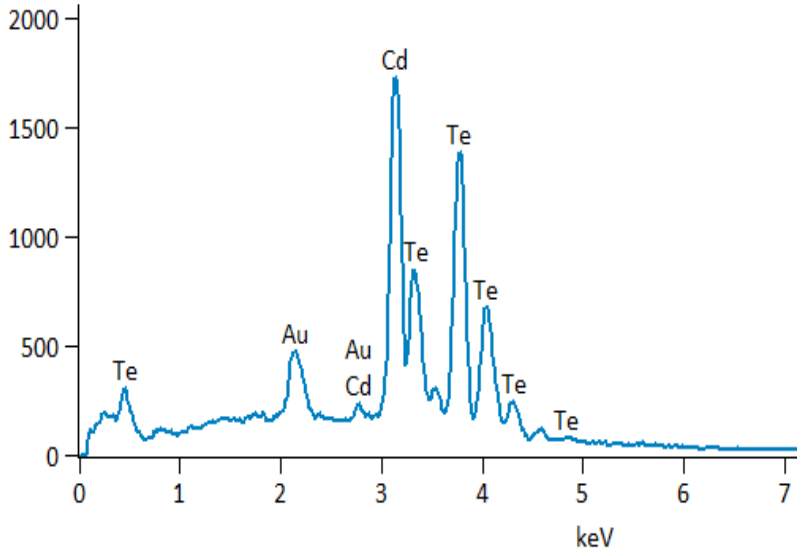

Figure 37 EDX spectrogram of as deposited CdTe electrodeposited on Au/Si at a potential of -0.705 vs SCE for 1 hour after template removal with a beam energy of 15 kV.

3.5. SEM

SEM images of the as deposited CdTe grown at -0.705 V *vs* SCE are shown in Figure 38. From the low magnification image, we can see that the film is very uniform and upon zooming in we can see that the CdTe forms a 'popcorn' like structure.

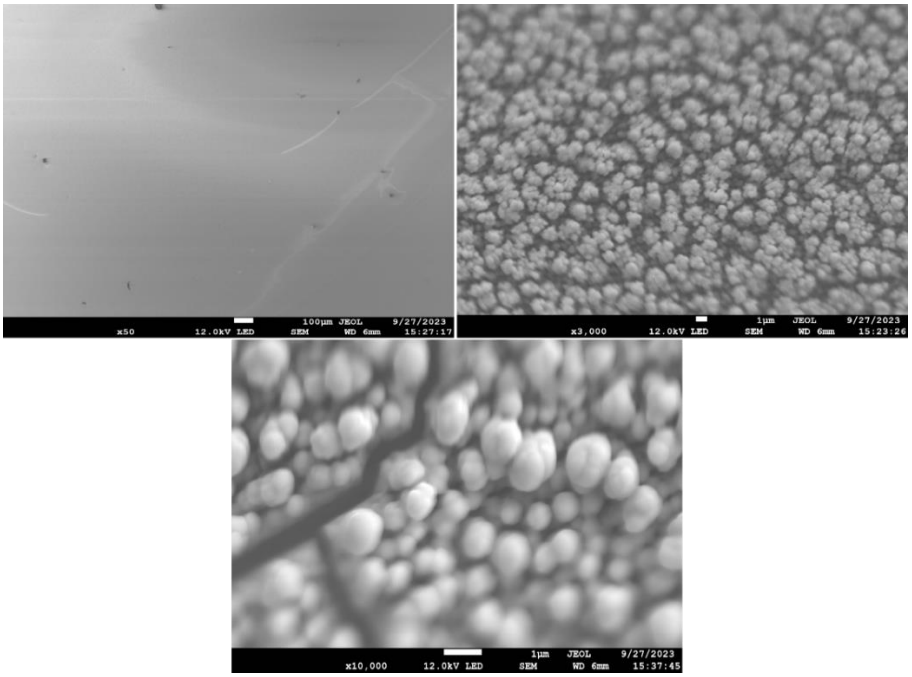

Figure 38 SEM images at different magnifications of CdTe electrodeposited on Au/Si at a potential of -0.705 vs SCE.

3.6. XRD

X-ray diffraction was performed on the CdTe thin films grown at -0.705 V *vs* SCE and the results are shown in Figure 39. The XRD pattern matches the reference XRD pattern for CdTe from the ICDD database (file No: 00-015-0770), confirming that CdTe had been electrodeposited. The shoulder peak at a 2θ value of 37.9° was due to the (111) Au peak from the substrate.

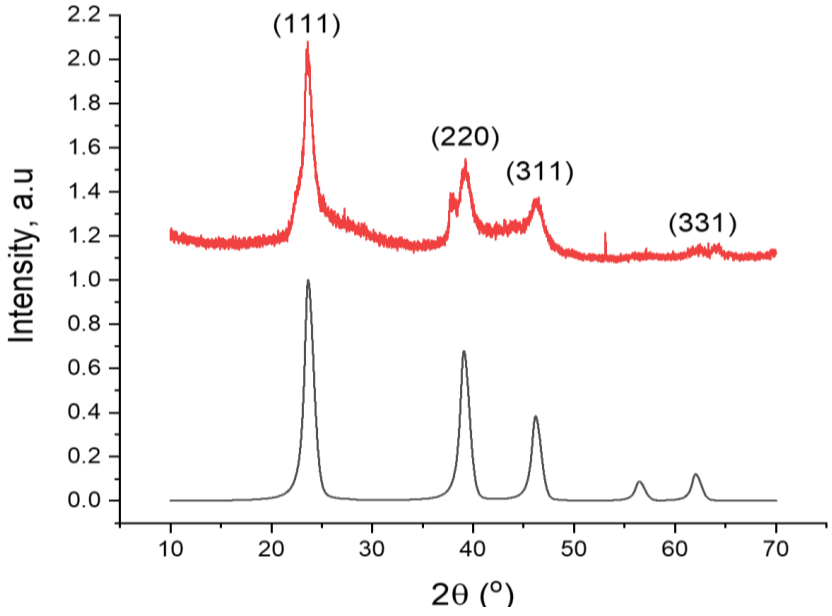

Figure 39 XRD pattern of an as deposited CdTe thin film grown at -0.705 V vs SCE for 1 hour on a Au/Si electrode (red). An insert of the CdTe XRD pattern from the ICDD database 'file No: 00-015-0770'(black).

3.7. SAXS study on phytantriol

In order to measure the resulting structure of phytantriol in the CdTe electrolyte solution samples were sent to the I22 beamline at the Diamond Light Source for SAXS measurements. A series of 2 mm capillaries were filled with a 2:1 by weight solution of ethanol to phytantriol. The capillaries where then left to dry overnight in order to let the ethanol evaporate leaving the inside walls of the capillaries lined with a thin film layer of phytantriol. The phytantriol lined capillaries were then filled with the CdTe electrolyte solution, sealed with fast setting epoxy and shipped to Diamond Light Source. The 1D integrated SAXS pattern, shown in Figure 40, exhibits a typical pattern for phytantriol in the double diamond phase, confirming that the phytantriol is stable in the electrolyte. The lattice parameter of phytantriol was determined to be 68.4 ± 0.2 Å and an average water channel diameter of 2.1 ± 0.1 nm was calculated, which is consistent with literature values.[11]

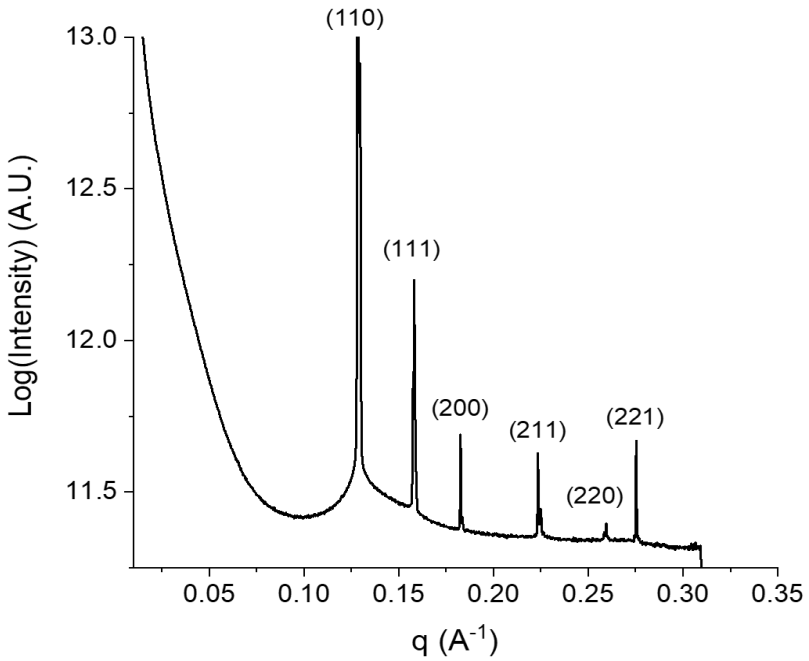

Figure 40 1D integrated SAXS pattern of a phytantriol lined capillary filled with aqueous 0.15 M $CdSO_4$, 0.005 M TeO_2 in 2 M H_2SO_4.

3.8. Cyclic voltammetry

Cyclic voltammetry was used again in order to assess how the phytantriol template affects the electrochemistry of the system. The CV in Figure 41, has the tellurium reduction peak

starting at -0.3 V *vs* SCE and the bulk cadmium reduction peak at -0.76 V *vs* SCE. Unlike the CV in Figure 35 (c), there is a significant reduction of the max current for the cadmium stripping peak which suggests that the presence of the phytantriol thin film template inhibits cadmium stripping during potential sweep experiments. From the CV the stoichiometric CdTe deposition potential would lie between the values of -0.5 and -0.75 V *vs* SCE.

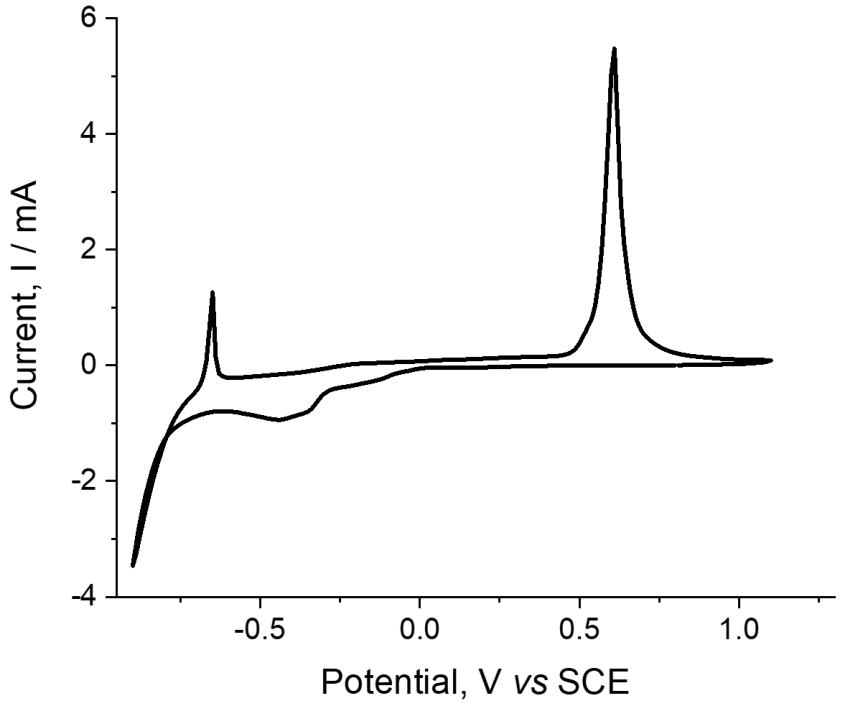

Figure 41 Cyclic voltammograms taken at 50 m Vs^{-1} at room temperature of 0.15 M $CdSO_4$, 0.005 M TeO_2 in 2 M H_2SO_4 on a phytantriol covered Au/Si electrode, area 1 cm^2.

3.9. Electrodeposition through the template

In order to produce stoichiometric CdTe thin films through the template the potential was stepped from 0 V to between -0.70 and -0.72 V. The stoichiometry of these films were analysed by EDX and summarised in Table 5.

Table 5 The atomic percentage of cadmium and tellurium in CdTe thin films grown at different potentials through phytantriol.

Deposition potential, V *vs* SCE	**Cd, atomic %**	**Te, atomic %**

-0.7	39 ± 2	61 ± 1
-0.705	47 ± 2	53 ± 1
-0.71	50 ± 1	50 ± 1
-0.72	55 ± 1	45 ± 1

EDX of the film grown at -0.71 V *vs* SCE for 1 hour through phytantriol shows that the film is stoichiometric within error. However, SEM images of the film are given in Figure 42, which shows a uniform underlayer film with random larger growths present. EDX revealed that the larger growths have a much higher cadmium content than the underlayer having up to 71 % Cd. EDX also revealed that the underlayer was slightly tellurium rich compared to the stoichiometric ratio. As with the untemplated CdTe, stoichiometric CdTe within error was achieved using a deposition potential of -0.705 V *vs* SCE. The resulting film, Figure 42 (c), shows a uniform film that has a popcorn like structure. This popcorn like structure was also seen for CdTe grown in the same conditions in the absence of the phytantriol template. This could be an indication that the templated electrodeposition was not successful however at these magnifications we would not be able to resolve the single diamond structure if it was present.

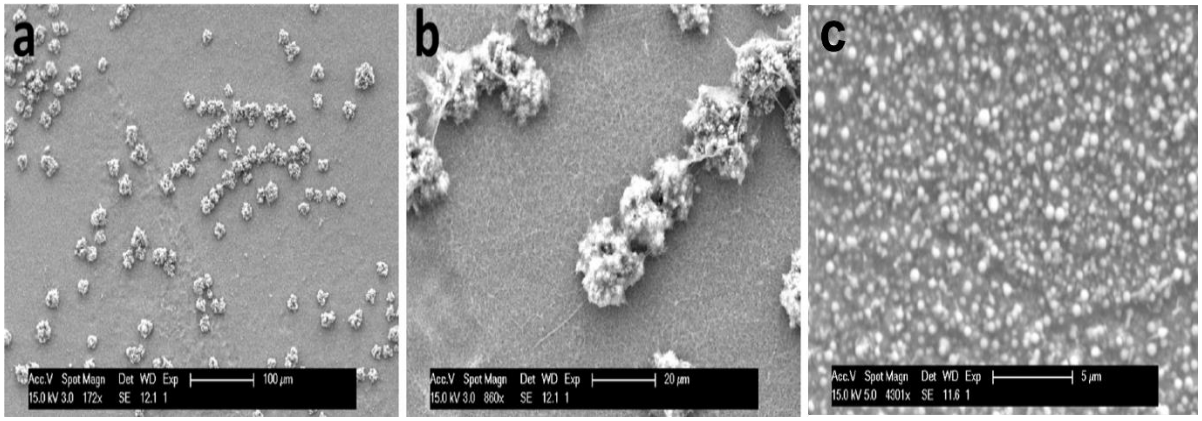

Figure 42 SEM images of CdTe electrodeposited on Au/Si electrode through phytantriol at a potential of -0.72 V (a & b) and -0.705 V (c) vs SCE.

3.10. SAXS of CdTe

To measure the structure of CdTe electrodeposited through phytantriol. SAXS was performed on the CdTe after template removal. If the CdTe did indeed have a single diamond phase, then Bragg peaks would be expected to appear at around 0.08 and 0.13 $Å^{-1}$. Figure 43 shows no features at 0.08 $Å^{-1}$ indicating that the templated deposition was not successful in producing a single diamond phase CdTe.

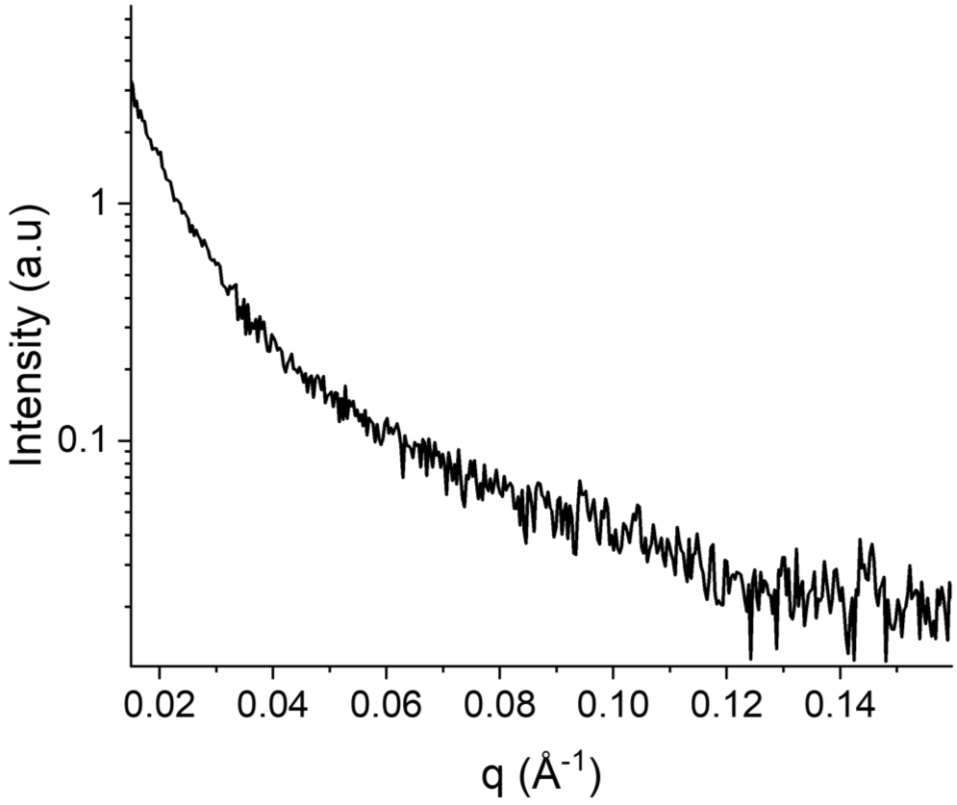

Figure 43 1D integrated SAXS pattern of CdTe thin film electrodeposited at a potential of -0.705 V vs SCE through phytantriol.

In order to try and successfully deposit CdTe with single diamond morphology, an altered version of the phytantriol template was employed. We theorised that the narrow water channels may have been a problem in the successful deposition of CdTe due to constraints within the channels. Phytantriol mixed with Brij-56 at 20 wt% was then explored as an alternative template, as this system also forms the double diamond phase but has larger water channels of around 6.3 nm compared to 2.1 nm for pure phytantriol. With larger water channels for the CdTe to deposit through, we theorised there would be less constraints and a successful deposition would occur.

To verify the structure of phytantriol/Brij-56(20 wt%) in the CdTe electrolyte, SAXS was performed on a phytantriol/Brij-56(20 wt%) lined 2 mm capillary filled with electrolyte solution. The Bragg peaks in Figure 44 show that the new template still formed a stable double diamond phase in the CdTe electrolyte. From the peak positions the template had a lattice parameter of 115.7 ± 0.2 Å and a water channel diameter of 6.3 ± 0.1 nm. These values were consistent with literature values of phytantriol/Brij-56(20 wt%) previously reported.[20]

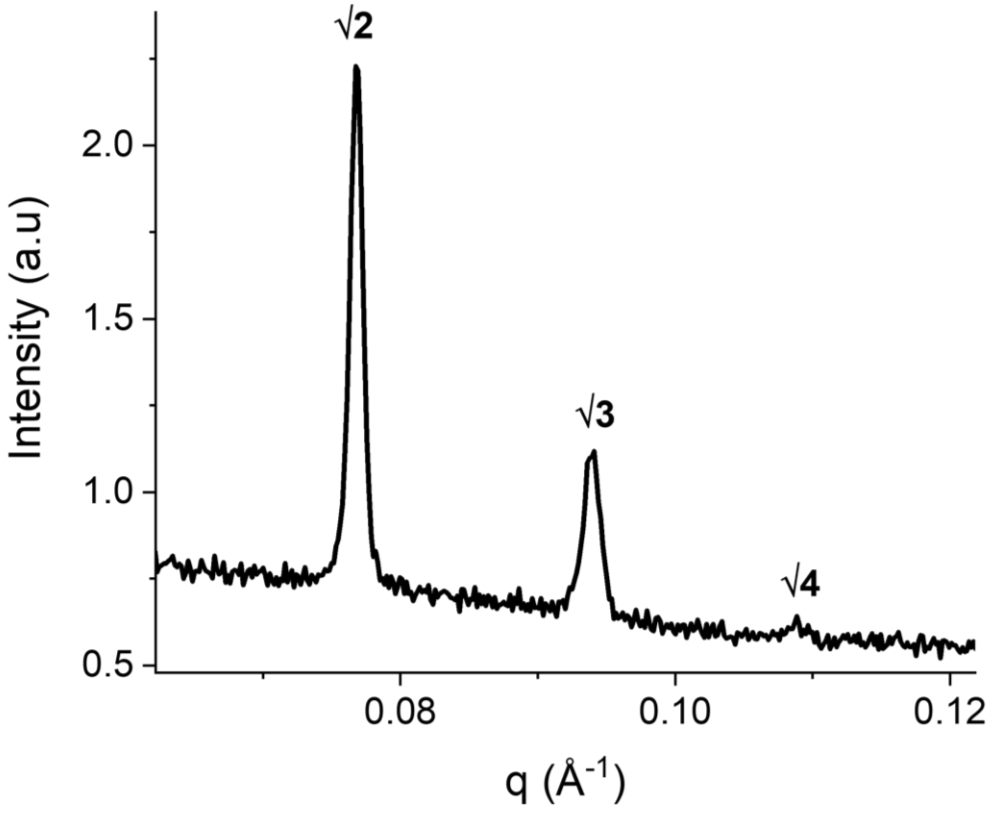

Figure 44 1D integrated SAXS pattern of a phytantriol/Brij-56 (20 wt%) lined capillary filled with aqueous 0.15 M $CdSO_4$, 0.005 M TeO_2 in 2 M H_2SO_4.

3.11. SEM and EDX

CdTe was then electrodeposited through the phytantriol/Brij-56(20 wt%) template by stepping the potential from 0 to -0.705 V *vs* SCE for 3 and a half hours. The resulting film was analysed by SEM and EDX after template removal. Figure 45 shows that the resulting film appears uniform when viewed from a low magnification and EDX revealed that the film was stoichiometric within error.

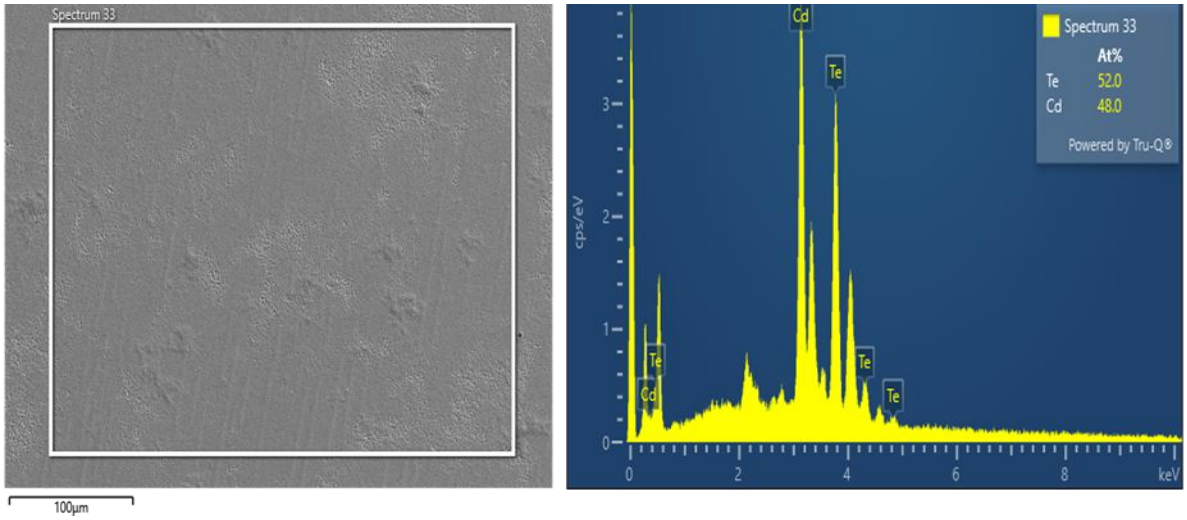

Figure 45 SEM image of CdTe electrodeposited through phytantriol/Brij-56 (20 wt%) at a potential of -0.705 V from a solution containing aqueous 0.15 M $CdSO_4$, 0.005 M TeO_2 in 2 M H_2SO_4 and the associated EDX spectra.

3.12. XRD

XRD was performed on the CdTe thin film grown at -0.705 V *vs* SCE through phytantriol/Brij-56 (20 wt%) and the results are shown in. The XRD pattern matches the "file No: 00-015-0770" for CdTe on the ICDD database confirming that CdTe had been electrodeposited. Due to the film being very thin the peaks from the substrate are very strong for this XRD pattern.

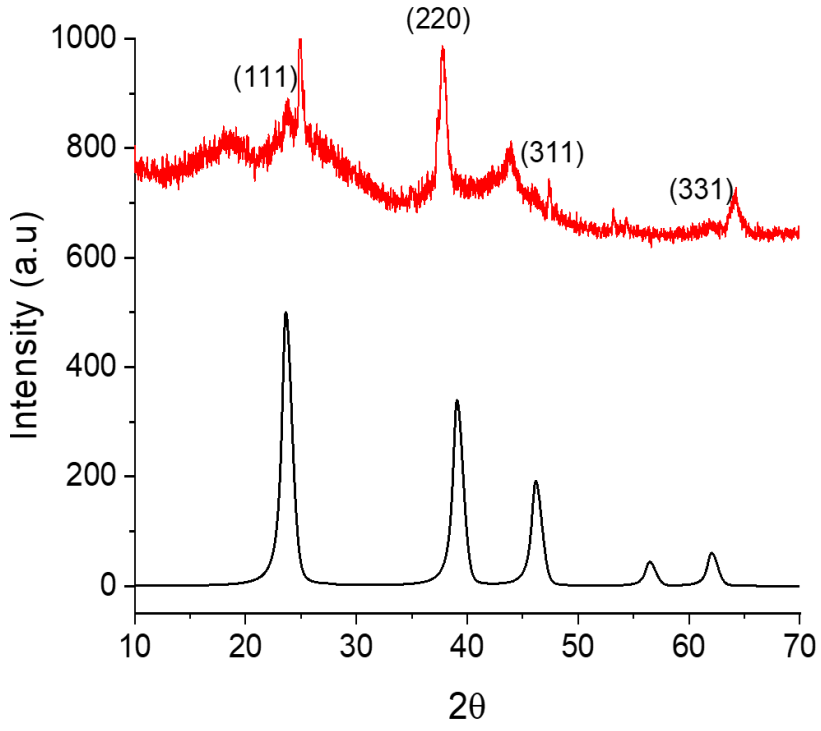

Figure 46 X-ray diffraction data of CdTe thin film grown at -0.705 V vs SCE through phytantriol/Brij-56 (20 wt%) on a Au-DVD electrode (red). Insert of CdTe XRD pattern from the ICDD database file No: 00-015-0770 (black).

3.13. SAXS of nanostructured CdTe

To confirm that using the new template gave us a successful deposition of CdTe in the single diamond phase, SAXS was again employed. The 1D integrated SAXS pattern of the as deposited CdTe after template removal, Figure 47, revealed one broad peak at a position of 0.05 $Å^{-1}$. Having a broad peak at the expected *q* position suggests that the CdTe has some degree of nanostructuring which is an improvement over using the pure phytantriol template. The fact this peak is extremely broad is a result of the structure being very disordered, and as only one peak is present, we cannot use the SAXS data in order to confirm that the material has a single diamond phase. However, the peak position does match the expected value from literature of Pt grown through phytantriol/Brij-56 (20 wt%), which means we could still have a somewhat successful electrodeposition through the template. When compared to the SAXS pattern in Figure 43, there is a considerable improvement as we have gone from having no peaks to having a broad peak at the expected *q* position. Assuming that the peak observed at $q = 0.05\ Å^{-1}$ corresponds to the (111) reflection of the single diamond phase, using Equation 20, Equation 21 and Equation 22 we can extract structural information about the CdTe which is summarised in Table 6.

Table 6 A summary of the structural information extracted from the SAXS data on CdTe electrodeposited through phytantriol/Brij-56 (20 wt%)

Lattice parameter / Å	Nanowire diameter / nm	Pore width / nm
218.0 ± 1.0	5.8 ± 0.8	9.6 ± 0.8

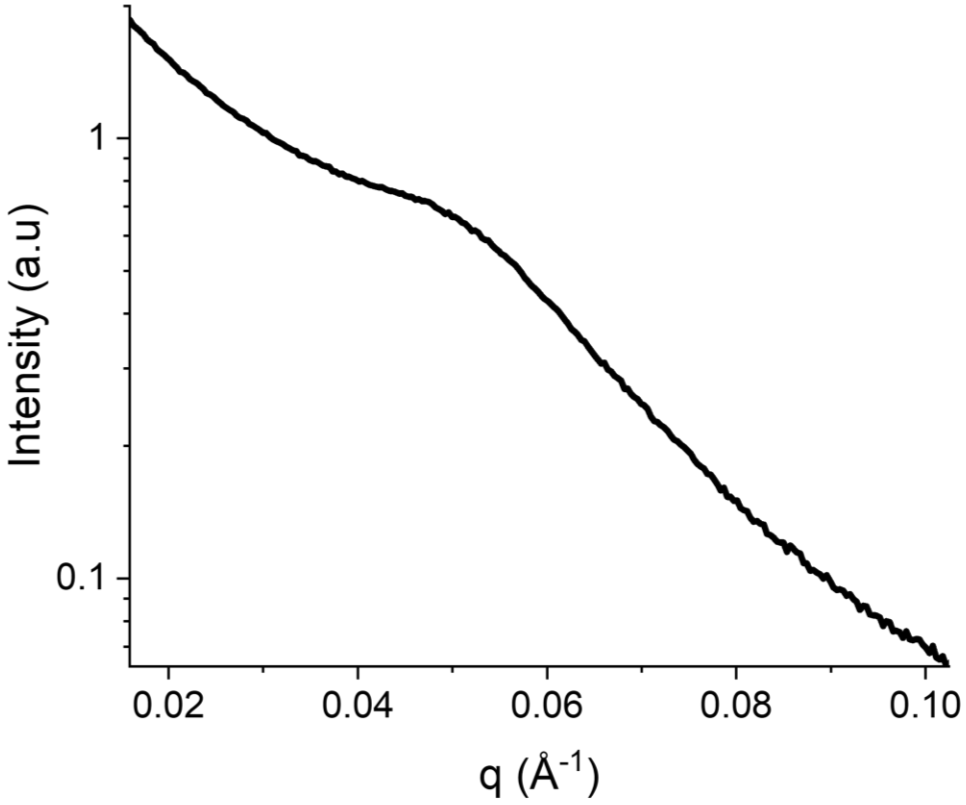

Figure 47 1D integrated SAXS pattern of CdTe thin film electrodeposited at a potential of -0.705 V vs SCE through phytantriol/Brij-56 (20 wt%).

This data suggests that we have produced CdTe in the single diamond phase with an average nanowire thickness of 5.8 nm however we cannot conclusively describe this material as single diamond phase without further evidence.

3.14. SEM and TEM of nanostructured CdTe

To provide further evidence that the CdTe successfully formed the single diamond phase, SEM was used to image the structure. SEM of the as deposited CdTe, Figure 48, gave no indication that the structure adopted a single diamond architecture. It was not possible to distinguish an ordered porous nanowire network as we expected. However, SEM did reveal that the structure was porous and to some degree interconnected. A highly porous stoichiometric CdTe thin film grown by soft-templated electrodeposition could still have great properties in the application of a photovoltaic material due to the nature of the fabrication being a green, one-pot synthesis at room temperature, which yields a thin film directly. Although the CdTe may not adopt a single diamond phase as we had expected the material may still exhibit excellent photovoltaic properties.

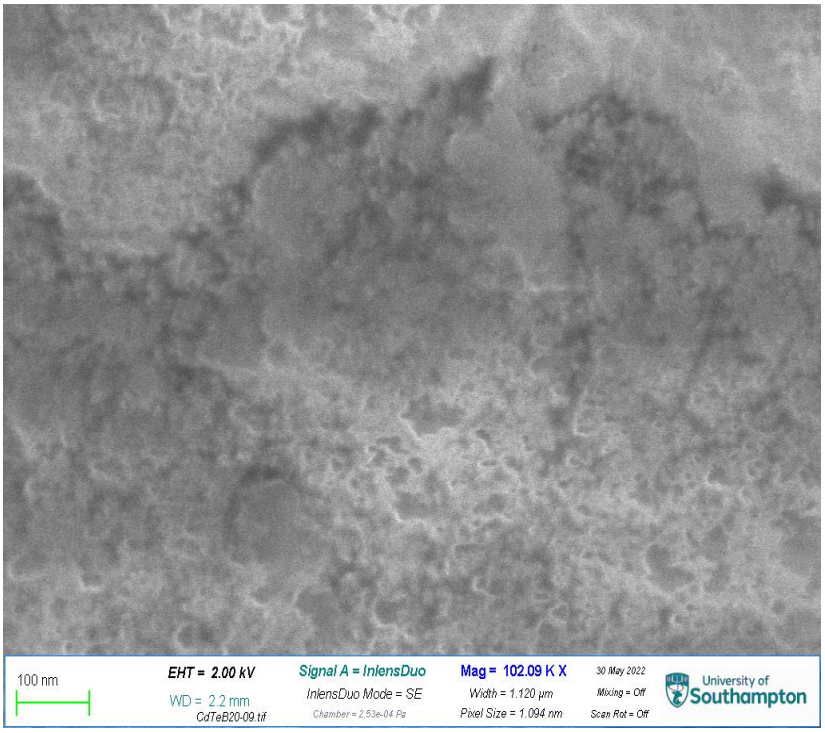

Figure 48 SEM image of CdTe electrodeposited through phytantriol/Brij-56 (20 wt%) at a deposition potential of -0.705 V vs *SCE on Au/DVD electrode).*

To gather more detailed structural information about the CdTe, TEM was also performed to gather higher quality images of the material. The TEM images are shown below in Figure 49 and provide more detail on the structure of CdTe. It is apparent that the material is indeed highly mesoporous and contains regions that do resemble the single diamond phase which may give rise to the reason why we see a very weak broad peak in the SAXS. Using the TEM images multiple wire thicknesses and pore widths were measured however due to the quality of the images it was difficult to get an accurate measure of these values. The measured size distributions are shown in Figure 50 with the results summarised in Table 7, values calculated using SAXS are also shown for comparison.

Table 7 A summary of the structural information extracted from TEM images of CdTe electrodeposited through phytantriol/Brij-56 (20 wt%). Also includes data repeated from Table 6 for comparison of results.

Nanowire diameter (SAXS) / nm	Nanowire diameter (TEM) / nm	Pore width (SAXS) / nm	Pore width (TEM) / nm
5.8 ± 0.8	5.3 ± 0.8	9.6 ± 0.8	7.0 ± 1.2

.

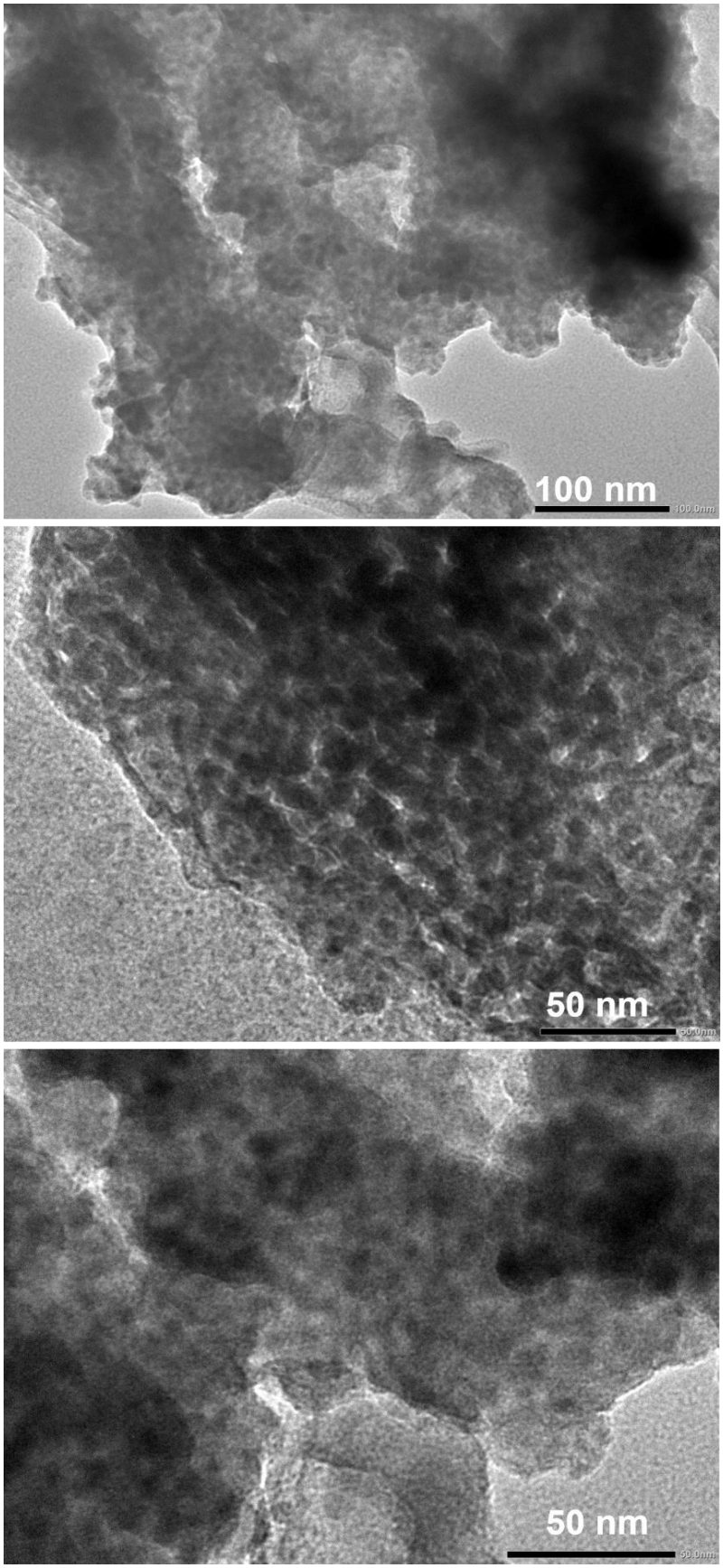

Figure 49 TEM images of CdTe electrodeposited through phytantriol/Brij-56 (20 wt%) at a deposition of -0.705 V vs SCE.

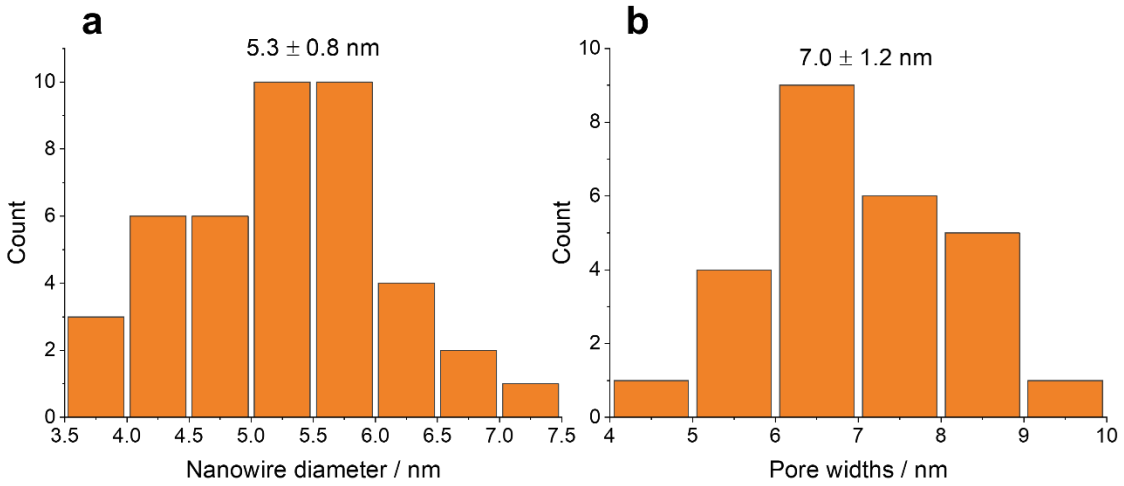

Figure 50 Size distribution graphs of the nanowire diameter (a) and pore widths (b) extracted from TEM images of CdTe electrodeposited through phytantriol/Brij-56 (20 wt%).

The nanowire diameters measured from TEM and SAXS are in reasonable agreement with each other however the measured pore widths are much smaller than that calculated from SAXS. Due to the small volume of sample probed by TEM there is a large associated error with these values. Overall imaging the structure has allowed us to confirm that the produced CdTe is mesoporous and has regions that are similar to the single diamond phase. It appears that the electrodeposition within the template is not perfect at producing single diamond phase CdTe, however there was an improvement when switching from pure phytantriol to the phytantriol/Brij-56(20 wt%) template.

3.15. *In-situ* SAXS of nanostructured CdTe

To get a better understanding on why the templated deposition was not working as well as that reported for Pt using the same system, an in-situ SAXS experiment was conducted using a custom-made 3D printed electrochemical cell to monitor both the template and the growth of CdTe simultaneously during electrodeposition. It is possible to monitor both the material and template simultaneously as the deposited material grows with a single diamond (Fd3m) morphology and the template has a double diamond (Pn3m) cubic phase. They therefore produce different scattering signals appearing as peaks in different positions in SAXS.

A novel 3D printed electrochemical cell was used which enabled us to perform in-situ SAXS experiments to monitor the templated electrodeposition of CdTe. The Cell design is discussed in further detail in a chapter 7. The cell allows us to collect time-resolved data on both the liquid crystal template and CdTe during the deposition process giving us more information about the system. The experiment was performed on the Xeuss offline SAXS instrument at The Diamond Light Source. The experiment was performed in transmission mode perpendicular to the working electrode. The results from the in-situ experiment are shown in Figure 51, which show 1D integrated SAXS patterns taken at different times throughout the electrodeposition of CdTe through phytantriol/Brij-56(20 wt%). Initially the $\sqrt{2}$ peak of the lipid template can be seen with a peak position of, 0.082 Å $^{-1}$. This gives the template a lattice parameter of 108 Å. It can be seen that over the course of the electrodeposition the broad 'bump/peak', which we assign to the $\sqrt{3}$ peak for the growth of single diamond phase CdTe, develops overtime. This feature increasing in intensity over time is a result of CdTe being deposited within the template.

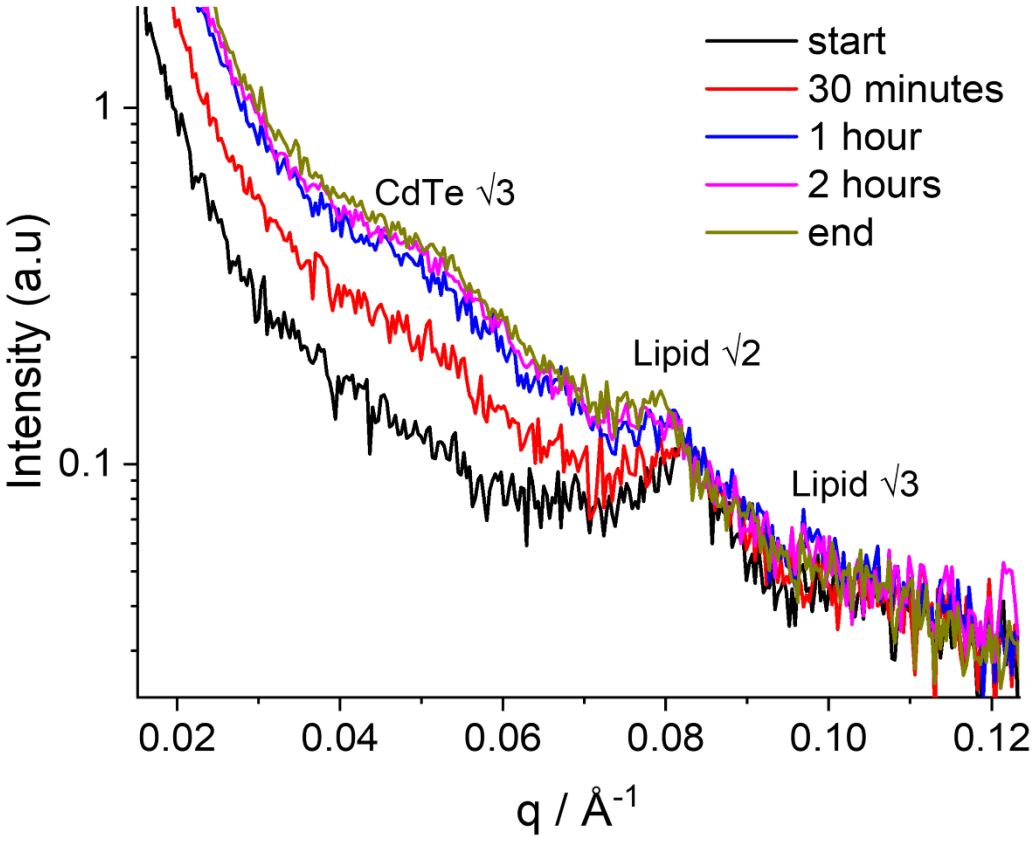

Figure 51 1D integrated SAXS pattern of CdTe thin film electrodeposited at a potential of -0.705 V vs SCE through phytantriol/Brij-56 (20 wt%) at time interval's during deposition.

Performing this experiment in-situ and monitoring the growth has provided us with valuable information about the electrodeposition process and information can be extracted from it. As the CdTe feature grows as a broad bump/peak we can conclude that CdTe directly grows poorly within the template. The broad feature we see in the 1D integrated SAXS after template removal is not a result from the single diamond phase CdTe being unstable after deposition and degrading over time. This data also provides evidence that the template removal procedure of washing the film in ethanol for 30 minutes is not the reason the material does not exhibit a single diamond phase morphology, as the lack of a sharp Bragg peak is seen during the materials growth. This in-situ experiment also gives us some insight into why the deposition does not occur smoothly as expected. It can be seen that the lipid peak changes *q* position and becomes broader throughout the deposition of CdTe. This shift to lower *q* is a result from the double diamond phase of phytantriol/Brij-56(20 wt%) swelling so the water channels are becoming larger. The broadening of the peak is a result of a loss of order of the lattice parameter or a degradation of the template. As there is instability in the template during the electrodeposition this could be a reason why we have poor filling of the template by CdTe. This data demonstrates that performing in-situ experiments using SAXS is a powerful tool in gaining a better understanding of a system of interest.

3.16. Reflectivity and band gap

Reflectivity data on the CdTe thin film deposited through phytantriol/Brij-56(20 wt%) were collected and shown in Figure 52 along with the associated Tauc plot.

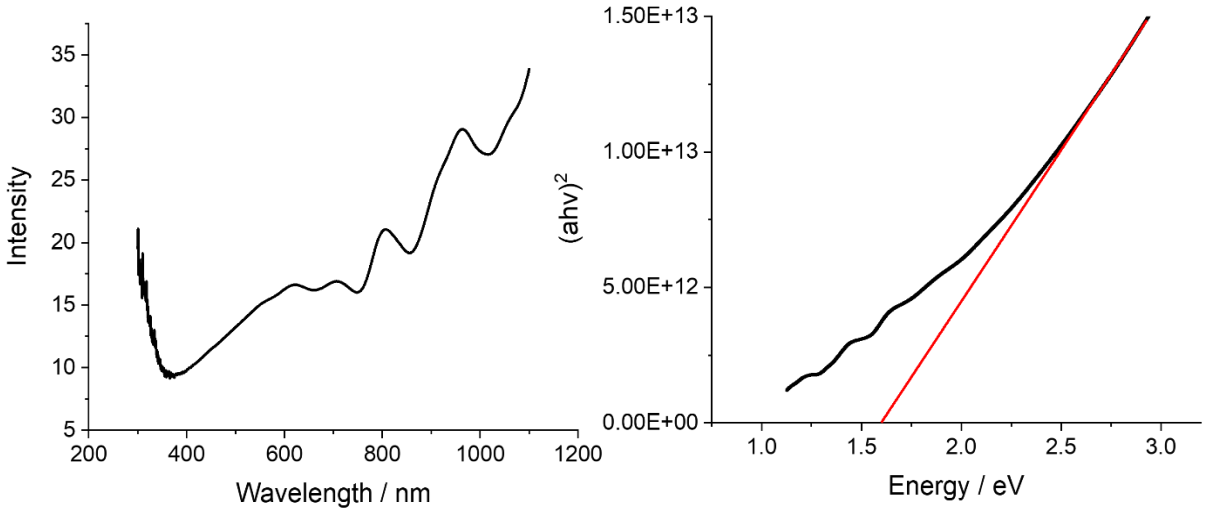

Figure 52 Reflectivity data of CdTe thin film electrodeposited through phytantriol/Brij-56 (20 wt%) and the associated Tauc plot.

The reflectivity data is converted to absorption according to the Kubelka-Munk (K-M) theory,[59] which is described by Equation 28.

Equation 28

$$F(R^{\infty}) = \frac{(1-R^{\infty})^2}{2R^{\infty}}$$

Where $F(R^{\infty})$ is the Kubelka-Munk function and R^{∞} is the reflectance. $F(R^{\infty})$ is then used to replace α in the Equation 29, where α is the absorption coefficient, hv is the incident light frequency, A is the proportionality constant, n is the electronic transition (in this case ½ for direct transition) and E_g is the band gap.

Equation 29

$$(\alpha hv)^{1/n} = A(hv - E_g)$$

A Tauc plot of $(\alpha hv)^{1/n}$ is then plotted versus hv in which a linear extrapolation of $(\alpha hv)^{1/n}$ to zero gives the band gap energy. The band gap for the CdTe deposited through phytantriol/Brij-56(20 wt%) was calculated to be 1.65 ± 0.06 eV. This value is higher than the band gap reported for bulk CdTe (1.45 – 1.5 eV). A shift in the band gap to slightly higher values could be due to the nanostructuring of the material. As mentioned in the introduction, at the nanoscale the band gap of a material is dependent on size and typically increases with decreasing size. This change in band gap in CdTe at the nanoscale has been reported in the literature.[60–63] Singh *et al.* formulated a theoretical model based on the cohesive energy of nanocrystals compared to bulk crystals which related size and shape dependencies of semiconductor band gaps. They reported a change in band gap from 1.50 to 1.85 eV for CdTe nanospheres of sizes 20 to 2 nm respectively and a change from 1.50 to 1.71 of CdTe nanowires of diameter 10 nm to 2 nm.[62] Using this model and a value of 5.5 nm for our nanowire diameter (averaged from SAXS and TEM) the nanosphere model predicts a band gap of 1.61 eV and the nanowire model predicts a band gap of 1.56 eV which is consistent with our measured band gap of 1.65 ± 0.06 eV. Mastai *et al.* also utilised electrodeposition to fabricate CdTe nanocrystalline films that were slightly tellurium rich (5-10 % Te excess). They reported that CdTe with a crystal size of 6.5 and 5.0 nm had band gaps of 1.6 and 1.9 eV respectively.[63] These results are also in agreement with our recorded band gap. Donega *et al.* explored the size dependency of the band gap of CdTe quantum dots and found that the size dependency was dominated by quantum confinement effects.[60] It is therefore likely that the blue shift of around 0.15 eV from bulk CdTe recorded for our film is mainly due to quantum

confinement with the architecture creating a network of wires. It is clear that having control over the size and architecture of CdTe at the nanoscale is extremely important in fine-tuning the desired properties. 1.65 eV is close to the bang gap window in which photovoltaic material have the most efficient absorption of solar radiation. It is therefore likely that CdTe produced via this method could have good application for solar photovoltaics.

3.17. Conclusions

Here we demonstrate that using a previously established method of templating a material by using the double diamond phase of phytantriol to produce single diamond phase CdTe was not possible under the same conditions that could successfully produce templated Pt films. By utilising the versatility and tunability of this templating method we showed that by introducing a co-surfactant (Brij-56) we managed to improve the deposition process and yielded a stoichiometric mesoporous thin film of CdTe. The material did not exhibit a single diamond phase, however it did still exhibit a 3D mesoporous structure, as measured by TEM. The resulting film was still highly porous and formed an interconnected nanowire network. The band gap of the templated CdTe was calculated to be 1.65 ± 0.06 eV which is consistent with literature reports and lies close to the optimum region for efficient solar radiation absorption.

We utilised a custom made in-situ cell in order to gain more information about why the templating method was not working as well as we hoped. It was determined that template degradation during the deposition process was likely the leading cause for this. Ageing of the sample or the template removal process was not preventing the CdTe from exhibiting a perfect single diamond phase. The application of this in-situ experiments provided a powerful tool into gathering new insights into the electrodeposition process.

We have demonstrated that soft-templated electrodeposition, utilising the double diamond phase of phytantriol/Brij-56 (20 wt%) can be used to fabricate stoichiometric mesoporous CdTe thin film. This method provides a one-pot synthesis method which can directly produce thin films of CdTe, which could be utilised for solar photovoltaic application. Due to the highly porous nature of this film and its band gap we theorise that the material might exhibit great solar photovoltaic properties.

3.18. Future Work

There are multiple directions in which this work should be continued, and I will outline a few that I believe would be of most importance.

The obvious next step for this project would be to determine the photovoltaic properties of the templated CdTe. A solar simulator can be used to characterise the material under standardised conditions and I-V curves can be used to provide information on the material's electrical properties such as open circuit voltage, short-circuit current and maximum power. If the CdTe shows promising properties and high efficiencies, the next step that follows would be to electrodeposit templated CdTe directly onto FTO or ITO electrodes with the aim of creating CdS/CdTe single junction solar cell devices at the lab scale and measuring the devices properties and efficiency.

This project could also go in a different direction, and one could utilise other liquid crystal templates to produce novel architectures of CdTe from electrodeposition. There are many liquid crystal phases that be explored for their use as a soft template.

The electrodeposition of other semiconductor materials through the phytantriol could also be explored. Semiconductors such as ZnO, SnSe and Sb_2S_3 could be explored which could yield materials with interesting properties.

The next chapter explores the electrodeposition of single diamond phase Pd through the phytantriol/Brij-56 template, emphasising the control over the nanostructure size. The effect of the size of the resulting material will be tested for the formic acid oxidation reaction.

4. Pd nanostructuring with size control

4.1. Introduction

As previously mentioned, single diamond Pd has exhibited excellent catalytic activity towards the methanol, ethanol, and glycerol electrooxidation reaction.[13] Having control over the nanowire thickness and pore sizes of the single diamond Pd could allow us to tailor the properties of the material, potentially enhancing its catalytic performance. In this chapter we aim to produce single diamond Pd with varying size by utilising swelling of the phytantriol template by the addition of differing amounts of co-surfactant Brij-56. We will then assess how the size of the single diamond Pd affects the materials properties and its performance for the formic acid electrooxidation. Previously, Ding *et al.* reported that single diamond phase Pd had excellent catalytic performance for the formic acid oxidation, so this reaction was chosen to assess how altering the lattice parameter of the material affected its performance.[64]

Formic acid fuel cells are a sub-category of proton exchange membrane fuels cells in which the fuel formic acid is oxidised and converted into CO_2. Formic acid fuel cells have special features when compared to hydrogen fuel cells due to its high energy conversion rate, fast response rate and formic acid can be easily transported and stored.[65–67] Formic acid fuel cells offer a technology that can aid our aim of developing renewable energy sources moving away from fossil fuels. The use of formic acid as a fuel is renewable as formic acid can be produced from biomass, or other renewable sources such as carbon capture from industrial processes. The CO_2 can be a part of a closed carbon cycle as to not contribute to greenhouse gas emmisions.[68–72]

Formic acid can also be used for hydrogen storage and transportation as formic acid can be produced by the hydrogenation of CO_2 and then hydrogen can be released from formic acid through its catalytic decomposition, which aids in overcoming the challenges associated with storage and transportation of hydrogen gas.[68,73,74]

A typical diagram showing a formic acid fuel cell is shown in Figure 53. The diagram shows that formic acid (HCOOH) is oxidised at the anode being converted into CO_2, and protons. The

protons then cross the membrane, and electrons pass through an external circuit to the cathode in which oxygen is reduced producing H_2O.

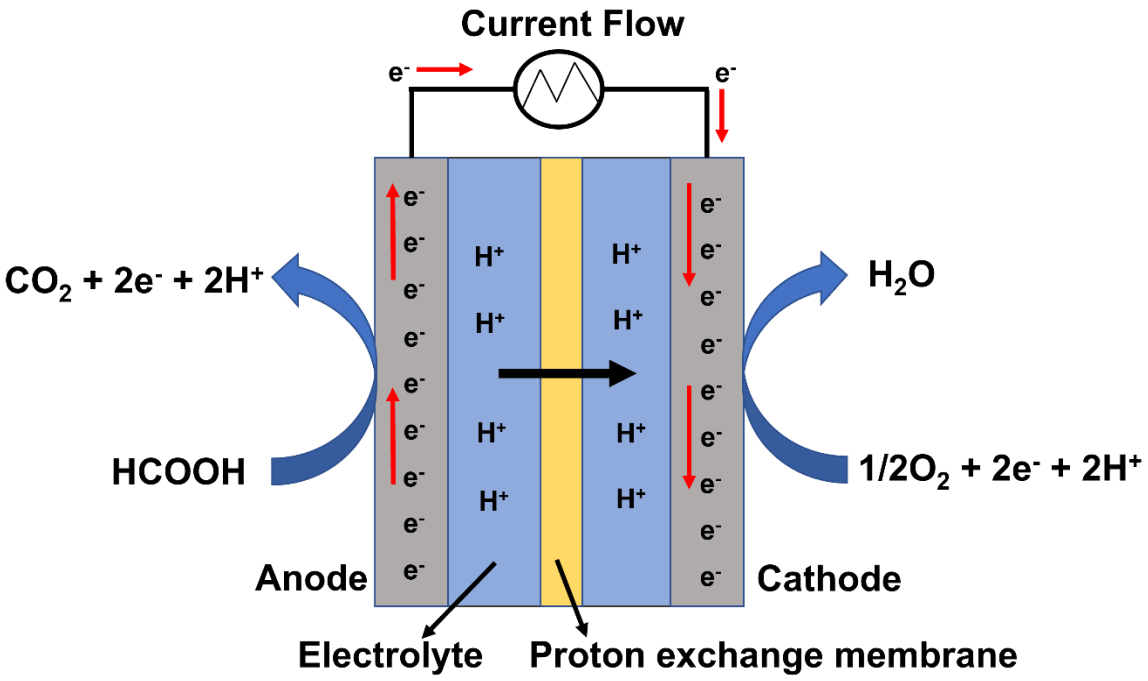

Figure 53 A diagram of a basic formic acid fuel cell showing the oxidation of formic acid into CO_2 at the anode with the transfer of protons through the proton exchange membrane to the cathode.

The formic acid oxidation is a very complex reaction with many different pathways and different intermediate species being formed.[65,67,75,76] The basic understanding is that there are two main pathways for the oxidation to occur: the direct pathway given by Equation 30 and an indirect pathway which proceeds via a strongly adsorbing CO intermediate (Equation 31 & Equation 32).

Equation 30

$$HCOOH \rightarrow reactive\ intermediates$$

$$\rightarrow CO_2 + 2H^+ + 2e^-$$

Equation 31

$$HCOOH \rightarrow CO_{ads} + H_2O$$

Equation 32

$$CO_{ads} + H_2O \rightarrow CO_2 + 2H^+ + 2e^-$$

It is well known that Pt and Pd are the best-known catalysts for the electrooxidation of formic acid. Pt tends to exhibit higher catalytic activity whereas Pd tends to be more tolerant to CO poisoning. [77–79] It is accepted that formic acid oxidation mainly occurs via the direct

dehydrogenation pathway (Equation 30) on Pd,[80–82] whereas for Pt it occurs via the indirect pathway.[83–85] Researchers have therefore opted to use Pd as the primary catalyst material and there are several approaches to improve the performance of Pd catalysts such as alloying with other metals,[86–88] creating Pd on high surface area supports[89–91] and manipulating the shape and architecture of Pd by creating core-shell structures,[92,93] Pd nano-chains,[94] three dimensional nanostructures[64,95] and nanorods.[96] Suo and Hsing synthesised Pd nanoparticles on a high surface area carbon support with control over the Pd size by using a reduction technique with ethylene glycol. The supported Pd nanoparticles had different sizes of 3.9, 5.2, 6.1 and 7.5 nm and exhibited size-dependent electrochemical properties for the formic acid electrooxidation. It was found that the Pd nanoparticles with an average particle size of 6.1 nm had the highest formic acid oxidation activity.[97] Lu *et al.* also investigated the size-dependent performance of Pd nanoparticles for the formic acid oxidation. They electrodeposited Pd nanoparticles onto a highly orientated pyrolytic graphene substrate by using a potentiostatic double pulse technique and controlled the size of the Pd by adjusting the during of the growth pulse. The height of the Pd nanowires deposited ranged from 3 to 50 nm. They reported that Pd nanoparticles smaller than 15 nm without strict shape control are not well suited for the formic acid oxidation due to a high edge-to-terrace ratio that can become quickly poisoned by CO produced at edge and corner sites at low potential.[98] Zhou *et al.* investigated how size affects the catalytic and electronic properties of unsupported Pd nanoparticles for the electrooxidation of formic acid. They tested nanoparticles in the size range of 9 to 40 nm and reported that the highest catalytic activity was seen for the smaller nanoparticles of 9 and 11 nm. They reported that the smaller particles displayed the highest valence band centre downshift with respect to the Fermi level which is consistent with an enhancement of the d-band hybridisation. They stated that the lower d-band centre results in a decrease in the adsorption energy of the formate intermediate which enhances the rate of formic acid decomposition via the direct path.[99] It is clear that the size and shape of nanostructured Pd can influence its properties and its performance for the formic acid oxidation.

In this chapter we aim to prepare Pd with a single diamond phase with control over the lattice parameter of the material by using the curvature lipid modulation technique used by Akbar *et al*.[20] We will characterise the material using a wide array of techniques such as cyclic

voltammetry, SAXS, TEM and XRD and test how controlling the size of the Pd influences its performance for the formic acid oxidation.

4.2. Experimental

4.2.1. Solution recipe

The electrolyte used for this work was the same as that used previously by Burton *et al.* [12] consisting of 50 mM $(NH_4)_2PdCl_4$ and 1 M NH_4Cl in 1 M HCl. For surface area studies 0.5 M H_2SO_4 was bubbled with N_2 for 20 minutes to removed dissolved oxygen from the electrolyte. For the formic acid oxidation 0.5 M N_2 saturated HCOOH in 0.5 M H_2SO_4 was used.

4.2.2. Electrode preparation

For SAXS experiments Pd was electrodeposited onto gold archival DVD's from Delkin Devices cut to shape and masked using nail polish to create a ≈ 1 x 1 cm working electrode. These electrodes were cleaned before use by soaking in acetone then deionised water for 10 minutes subsequently.

For electrochemical experiments either a 2 mm Au disc electrode or a 3 mm Au rotating disc electrode (RDE) was used. The electrodes were polished with 1.0 and 0.3 µm alumina polish before use.

For the template modified electrodes the electrodes were dipped in a solution containing phytantriol (with a desired amount of Brij-56 co-surfactant) in a 1 to 2 weight ratio in ethanol then left to dry in air for at least 1 hour, leaving behind a thin film template on the electrode surface. The modified electrodes were then immersed in the electrolyte and left to hydrate for a minimum of 30 minutes before electrodeposition to allow to template to hydrate, forming the desired double diamond phase.

4.2.3. Electrodeposition and template removal

Electrodeposition experiments were performed using a three-electrode setup with a working electrode, a Pt-gauze counter electrode and SCE reference electrode. Electrodeposition was performed by stepping the potential from 0.4 V *vs SCE* to a 0.1 V *vs* SCE for a set period of time using an Ivium VERTEX potentiostat controlled using IviumSoft.

To remove the lipid template after deposition, the working electrode was soaked in ethanol for a minimum of 30 minutes then left to dry in air.

4.2.4. TEM

In order to prepare TEM samples, a drop of ethanol was placed on the Pd thin films after template removal and the sample was scratched using a blade creating a suspension of Pd in the ethanol. A small amount of this suspension was then dropped onto a TEM grid and left to dry overnight to create the TEM sample.

4.2.5. SAXS

For SAXS experiments performed at I22 at the Diamond Light Source, the electrodes used were gold archival DVDs from Delkin Devices (Au/DVD). A camera length of 4.5 m was used with a beam energy of 12.4 keV for all experiments. For the in-situ experiments carried out on I22, a custom-made 3D printed cell (discussed in detail in later chapter) was used with the sample perpendicular to the beam. The cell hosted a three-electrode set-up controlled by an Ivium Vertex potentiostat which was remotely accessed from outside the experimental hutch.

4.3. SAXS of the phytantriol/Brij-56 system

SAXS was used to measure the structure of phytantriol and phytantriol/Brij-56 mixtures in the Pd electrolyte. Figure 54 shows 1D integrated SAXS patterns which confirm that all of the templates formed the desired double diamond phase and the expected trend of increasing lattice parameter with Brij-56 content was seen. The results from the SAXS patterns are given in Table 8 which show the lattice parameter and water channel diameter increases from 69.8 ± 0.1 Å and 2.8 ± 0.2 nm for pure phytantriol to 127.2 ± 0.2 Å and 7.2 ± 0.3 nm with 20% Brij-56 additive. These results are in agreement with that seen for this system in HCPA.[20] From these results it is likely that we will be able to deposit Pd through the different swollen templates to give single diamond Pd nanostructures with tuneable size control.

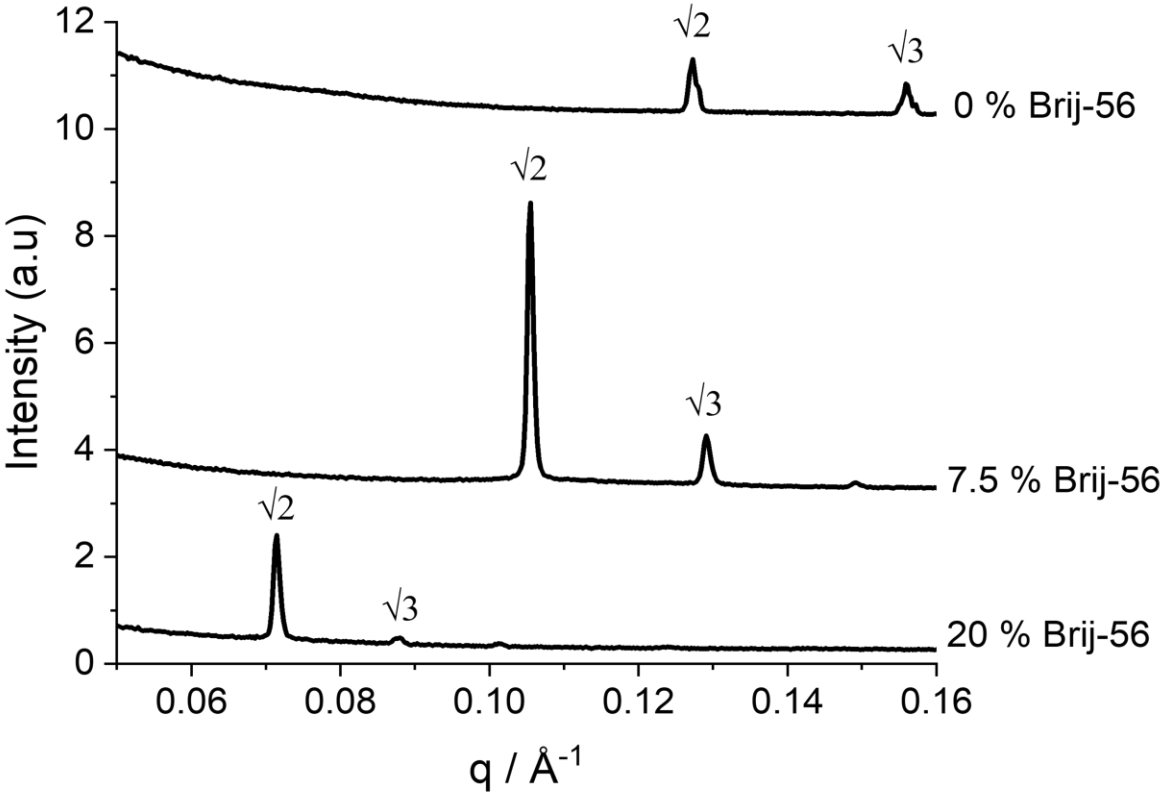

Figure 54 1D integrated SAXS patterns of phytantriol with differing amounts of Brij-56 additive in excess 50 mM $(NH_4)_2PdCl_4$ and 1 M NH_4Cl in 1 M HCl. Taken in transmission mode on the I22 beamline at the Diamond Light Source.

Table 8 A table reporting the structural information determined from SAXS of phytantriol/ Brij-56 mixtures in 50 mM $(NH_4)_2PdCl_4$ and 1 M NH_4Cl in 1 M HCl.

Template	phase	Lattice parameter (Å)	Water channel width (nm)
Phytantriol/0% Brij-56	Double diamond	69.8 ± 0.1	2.8 ± 0.2
Phytantriol/7.5% Brij-56	Double diamond	84.0 ± 0.1	3.9 ± 0.2
Phytantriol/20%Brij-56	Double diamond	127.2 ± 0.2	7.2 ± 0.3

4.4. Pd electrodeposition

Cyclic voltammetry was used to assess the reduction and oxidation potentials of Pd using a three-electrode setup with a 2 mm Au-disc electrode as the working electrode, SCE reference and Pt gauze counter electrode. Prior to sweeping the potential the 50 mM $(NH_4)_2PdCl_4$ and 1 M NH_4Cl in 1 M HCl solution was purged with nitrogen for 15 minutes to remove dissolved oxygen. The CV in Figure 55 shows a cathodic peak corresponding to the reduction (deposition) of Pd^{2+} at 0.04 V *vs* SCE (Equation 33). The anodic peak at 0.5 V *vs* SCE corresponds to the oxidation (stripping) of Pd (Equation 34). These reactions occur via Equation 33 and Equation 34 below. From this CV a deposition potential of 0.1 V *vs* SCE was chosen, the same deposition potential used previously by Burton *et al*.[12]

Equation 33 $$Pd^{2+} + 2e^- \rightarrow Pd_{(s)}$$

Equation 34 $$Pd_{(s)} \rightarrow Pd^{2+} + 2e^-$$

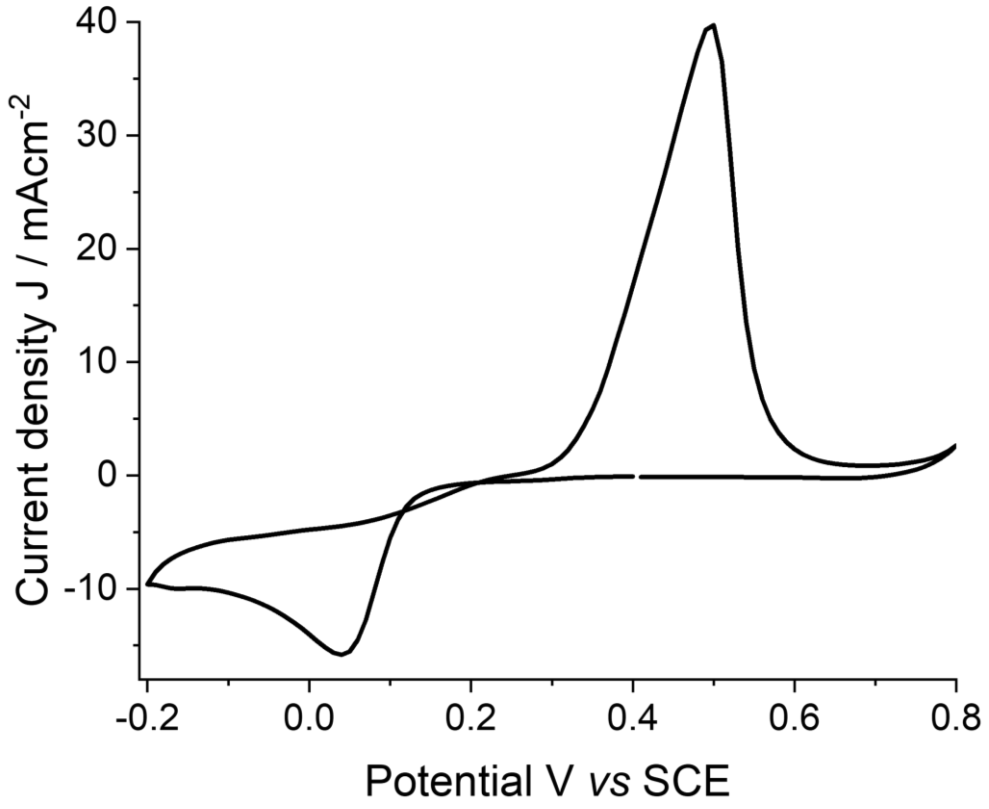

Figure 55 A CV with a sweep rate of 50 mV s^{-1} taken on a 2 mm Au-disc electrode in an electrolyte of 50 mM $(NH_4)_2PdCl_4$ and 1 M NH_4Cl in 1 M HCl.

Pd was then electrodeposited through the different templates by applying a potential of 0.1 V *vs* SCE until a set amount of charge had passed (22 mC). The current time transients are presented in Figure 56 and are typical for templated electrodeposition. As previously reported with Pt the current density also increases with the amount of Brij-56, this is due to larger water channels within the template allowing for more diffusion of Pd to the electrode surface, therefore less time is required to pass the same amount of charge.

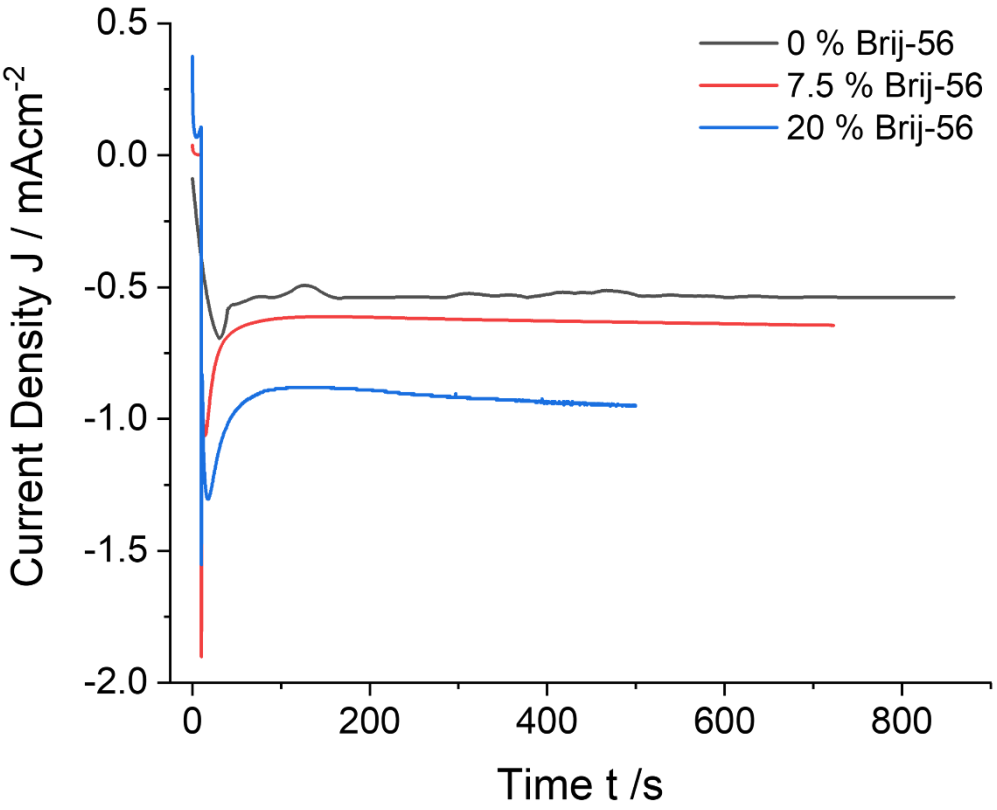

Figure 56 Current time transient of Pd electrodeposited on a 2 mm Au-disc electrode through phytantriol (black), phytantriol/Brij-56 (7.5%) (red) and phytantriol/Brij-56 (20%) (blue) from an electrolyte of 50 mM $(NH_4)_2PdCl_4$ and 1 M NH_4Cl in 1 M HCl. The applied potential was 0.1 V vs SCE, and the deposition charge was -14.3 mC.

4.5. Surface area determination

In order to determine the electrochemical active surface area (ECSA) of the as deposited Pd films, cyclic voltammetry was performed in N_2-saturated 0.5 M H_2SO_4. Initially for all films the potential was swept between -0.2 and 1.4 V *vs* SCE at 300 mV s^{-1} until the CV stabilised (this usually occurred after around 15 cycles). The potential was then cycled between these values at a scan rate of 20 mV s^{-1} leading to the CVs shown in Figure 57. For all Pd films hydrogen adsorption is seen on the cathodic scan from 0.05 to -0.1 V *vs* SCE and hydrogen desorption

can be seen on the anodic sweep from -0.1 to 0.05 V *vs* SCE. The cathodic peak at -0.15 V *vs* SCE is from hydrogen absorption and the anodic peak at -0.14 V *vs* SCE is from the hydrogen extraction from the Pd lattice. For the Pd films electrodeposited through the templates there are distinct hydrogen adsorption peaks which occur from different surface environments, this is typically seen with single diamond architecture[12] and these peaks are not seen for untemplated Pd. Distinctive hydrogen adsorption peaks have been previously seen for other reports of Pd nanostructures.[12,100,101] Anodic peaks are seen from the formation of surface oxides from 0.5 to 0.9 *vs* SCE and a cathodic peak from the surface oxide stripping is seen between 0.5 and 0.3 V *vs* SCE. From the CVs in Figure 57 the peak currents for Pd electrodeposited through the templates are much larger than the Pd grown in the absence of a template. This is an indication of a much higher electroactive surface area.

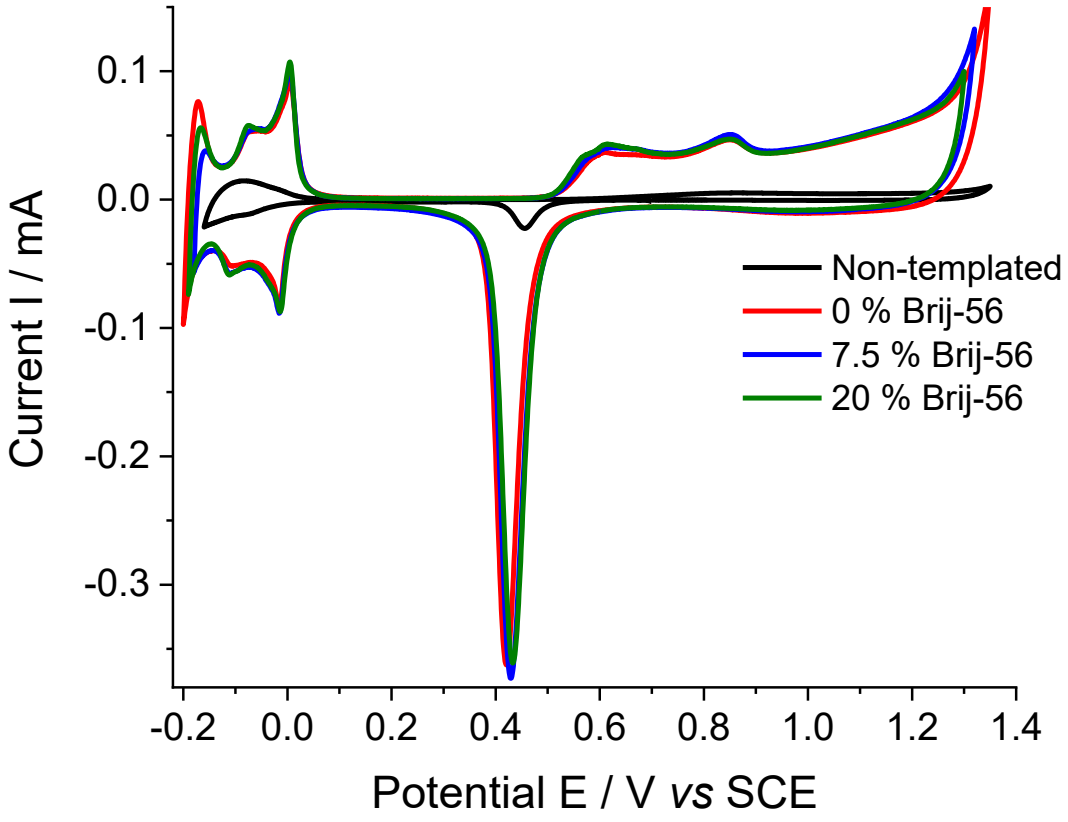

Figure 57 Cyclic voltammograms taken in 0.5 M H_2SO_4 recorded at 20 m $Vs^{-1}$with non-templated Pd, and templated Pd from phytantriol(red), phytantriol/Brij-56 (7.5%) (blue) and phytantriol/Brij-56 (20%) (green). For all CVs the second scan is shown so the full oxygen stripping can be observed.

To determine the electrochemical active surface area, the oxide stripping peaks were integrated between 0.6 and 0.3 V *vs* SCE and a conversion factor of 424 μCcm^{-2} was used as

given by Rands and Wood.[102] The reason the hydrogen absorption peaks are not used for this calculation is that Pd can have spillover of hydrogen atoms from the surface to subsurface sites whereas the oxide layer typically forms a well defined monolayer on the Pd surface.

The surface areas and roughness factor (RF) calculated for the Pd films are given in Table 9.

To calculate specific surface area of the palladium films the amount of Pd deposited was calculated by converting the charge passed during deposition into mass by using Faraday's law (Equation 5). The active surface area was then divided by the mass of Pd to give the specific surface areas given in Table 9. There is an increase in specific surface area of around 10-fold for the templated Pd film through phytantriol compared to the untemplated Pd. This is in line with previous work by Burton *et al.* in which a 13.5 times increase was seen using the phytantriol template.[12]

Table 9 A table listing the surface area, specific surface area and roughness factor of electrodeposited Pd calculated from cyclic voltammetry studies.

Template	**ECSA (cm^2)**	**RF**	**Specific surface area (m^2g^{-1})**
No template	0.4 ± 0.2	5.1 ± 2.5	3.0 ± 1.5
Phytantriol/0% Brij-56	3.8 ± 0.3	53.3 ± 4.0	30.3 ± 2.3
Phytantriol/7.5% Brij-56	4.1 ± 0.8	57.4 ± 10.6	33.5 ± 6.2
Phytantriol/20%Brij-56	3.5 ± 0.9	49.0 ± 12.7	33.0 ± 3.5

Interestingly, the specific surface area for the templated Pd with varying amounts of Brij-56 additive did not have any significant changes within error. As we introduce more Brij-56 into the template, we swell the template leading to single diamond Pd with larger nanowire diameters and a larger lattice parameter. We therefore expect to see a trend of decreasing surface area with increasing Brij-56 content as we would expect an inverse relationship between the specific surface area and the lattice parameter as the surface area to volume ratio decreases with increasing size. Akbar *et al.*[20] reported that for Pt grown with differing

lattice parameters using this technique the specific surface area decreased with increasing Brij-56 in the template. It was reported that the specific surface area did not follow an inverse relationship with lattice parameter and the loss in surface area was much greater due to Pt occupying increasingly larger proportion of the unit cell.

A reason why we do not see a reduction in surface area may be that for Pd larger pores in the single diamond structure may give us better access to the surface. The reported specific surface area for Pd grown through phytantriol in this work is 30 $m^2 g^{-1}$ whereas for Pt we have measured specific surface areas up to 42 $m^2 g^{-1}$ so the active surface area is lower for Pd.[9] Another potential reason why the expected surface area trend is not being followed is that the electrodeposition within the template may not be successful or we are not depositing Pd with increasing lattice parameter.

To gather information on whether Pd would deposit within the template uniformly at different thicknesses, Pd was deposited for several different charges between 14.3 and 28 mC. The roughness factor was then determined by cyclic voltammetry in 0.5 M H_2SO_4 as before for each templated Pd film and the roughness factor was plotted against charge passed (proportional to amount of Pd deposited). The results from this experiment are shown in Figure 58. The roughness factor and therefore surface area of the Pd nanostructures increases proportionally with increasing charge as a thicker Pd film is being deposited. The linear relationship demonstrates that we have uniformly accessible surface areas for our 3D nanostructures grown within the templates at different thicknesses. This therefore proves that we are uniformly depositing within the phytantriol/Brij-56 templates.

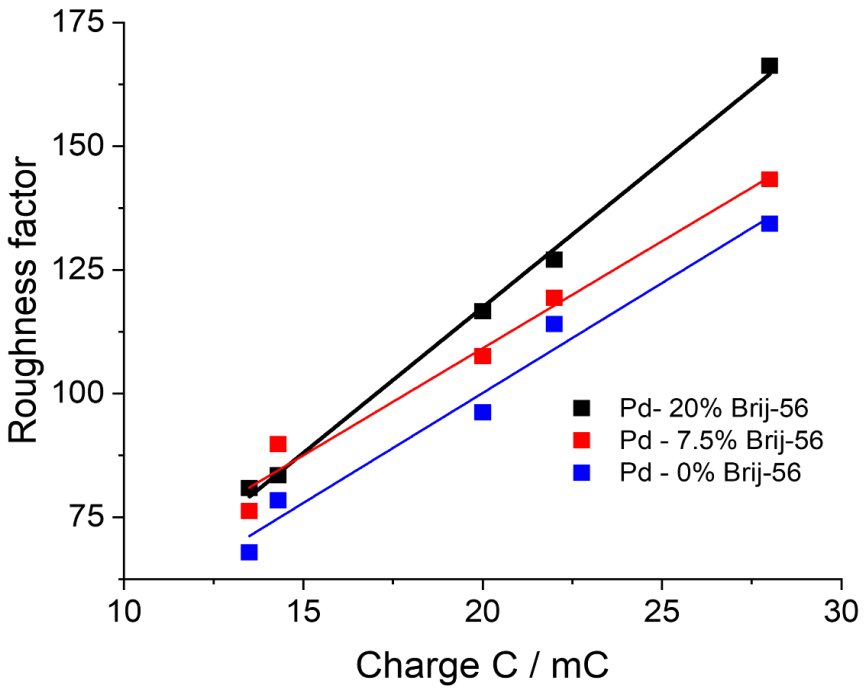

Figure 58 The roughness factor against the total charge passed during the electrodeposition of Pd at a potential of 0.1 V vs SCE through the phytantriol/Brij-56 templates.

4.6. SAXS of Pd

SAXS was used in order to analyse the structure of Pd electrodeposited through the phytantriol/Brij-56 templates after template removal in ethanol. 1D integrated SAXS patterns in Figure 59 show that for Pd produced from all templates a Bragg peak is seen which is in the expected position for a single diamond phase material. However, as only one Bragg peak is seen in each case it cannot be said definitively that the Pd has formed the single diamond phase. Since the peak is sharp and in the expected position and the measured specific surface areas are similar to that seen previously, it is likely that we have successfully formed single diamond phase Pd in all cases. The results extracted from these SAXS patterns are reported in Table 10 and reveal that the lattice parameter and nanowire diameter of the electrodeposited Pd increases from 143.7 ± 1.6 Å and 2.9 ± 0.1 nm to 217.3 ± 6.9 Å and 5.9 ± 0.3 nm when the amount of Brij-56 introduced to the templated changes from 0 % to 20 % respectively.

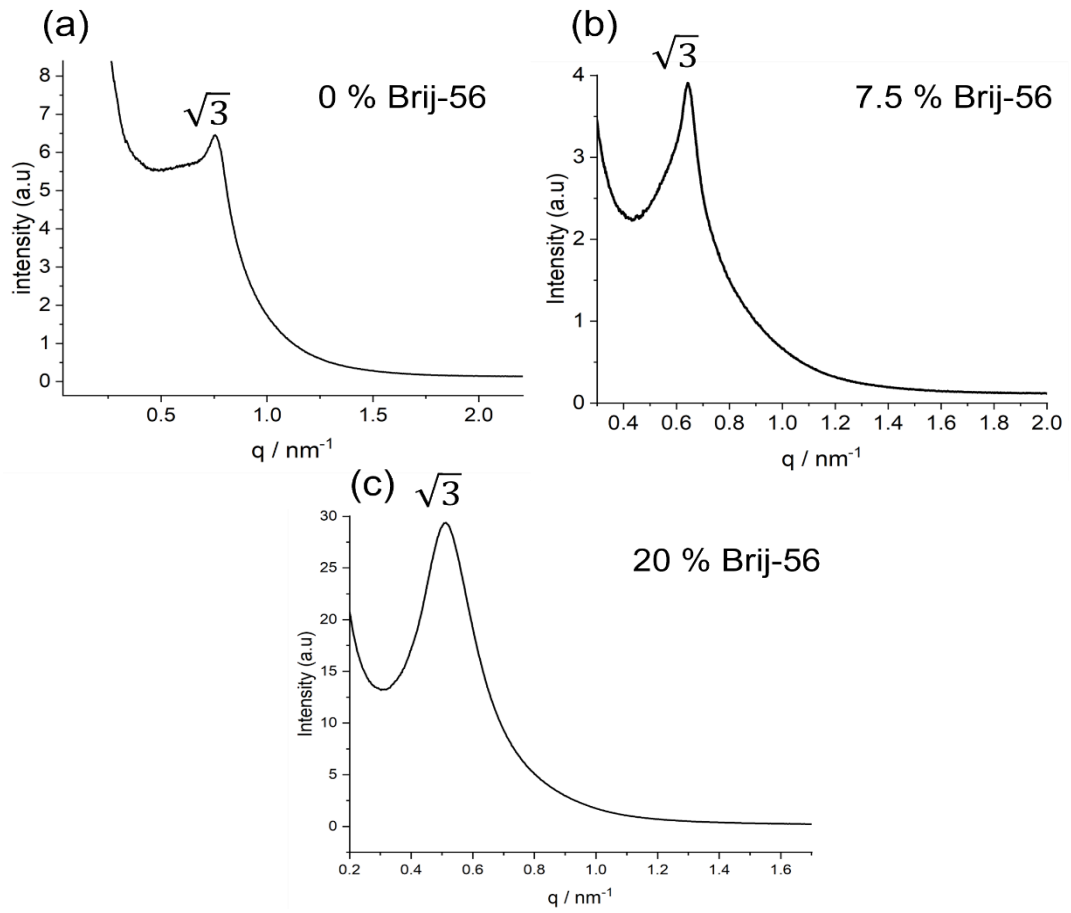

Figure 59 1D integrated SAXS patterns of Pd thin films electrodeposited on Au/DVD electrodes by applying a potential of 0.1 V vs SCE for 1800s through phytantriol (a) phytantriol/Brij-56 (7.5%) (b) and phytantriol/Brij-56 (20%) (c) after template removal by soaking in ethanol for 30 minutes.

Table 10 A table reporting the results extracted from SAXS of Pd thin films electrodeposited on phytantriol/Brij-56 modified Au-DVD electrodes by applying a potential of 0.1 V vs SCE for 1800 s after template removal in ethanol.

Template	Lattice parameter (template) / Å	Lattice parameter (Pd) / Å	Nanowire diameter / nm	Pore width / nm
Phytantriol/0% Brij-56	69.8 ± 0.1	143.7 ± 1.6	2.9 ± 0.1	7.3 ± 0.1
Phytantriol/7.5% Brij-56	84.0 ± 0.1	169.3 ± 2.8	3.9 ± 0.1	8.1 ± 0.2
Phytantriol/20%Brij-56	127.2 ± 0.2	217.3 ± 6.9	5.9 ± 0.3	9.6 ± 0.2

4.7. In-situ SAXS

In order to provide further evidence that the Pd being grown through phytantriol and phytantriol/Brij-56 were growing inside the template, in-situ SAXS during electrodeposition

was performed on I22 at the Diamond Light source using a custom-made 3D printed electrochemical cell. The in-situ measurements, shown in Figure 60, were performed in transmission mode with the X-ray beam going through the windows of the cell and the phytantriol/Brij-56 modified Au-DVD electrodes perpendicular to the incoming beam. 1D integrated SAXS patterns are taken at intervals during the electrodeposition of Pd at a potential of 0.1 V *vs* SCE through the phytantriol/Brij-56 templates. Bragg peaks from the lipid template can be seen clearly throughout the depositions and they remain stable showing that there is no template degradation or changes to its size or phase. For all cases, a single peak from the Pd is seen growing in intensity over time, with an expected *q* value for the $\sqrt{3}$ single diamond Bragg peak. Although a second peak is not seen, the peak growing over time at the expected *q* position for single diamond Pd is a good indication that we are successfully growing single diamond Pd.

The current time transients for the electrodeposition of Pd through the phytantriol/Brij-56 (7.5 wt%) template had a short circuit occur after around 500 seconds, which is shown by a large spike in current. As the cell was moving during the deposition, I believe there was a short circuit and current was being passed through something external, this can also explain why the Pd Bragg peak did not grow much in intensity pass the 10-minute mark. The insert shows that the initial current being passed was typical for that of Pd electrodeposition through the template. For the electrodeposition of Pd through phytantriol/Brij-56 (20 wt%) the deposition was halted after 15 minutes due to the SAXS detector being saturated, which led to it being shut down before the experiment finished. However, we can clearly see stable lipid peaks and a growing peak for the Pd in the expected *q* position along with a clean current response that is typical for templated electrodeposition.

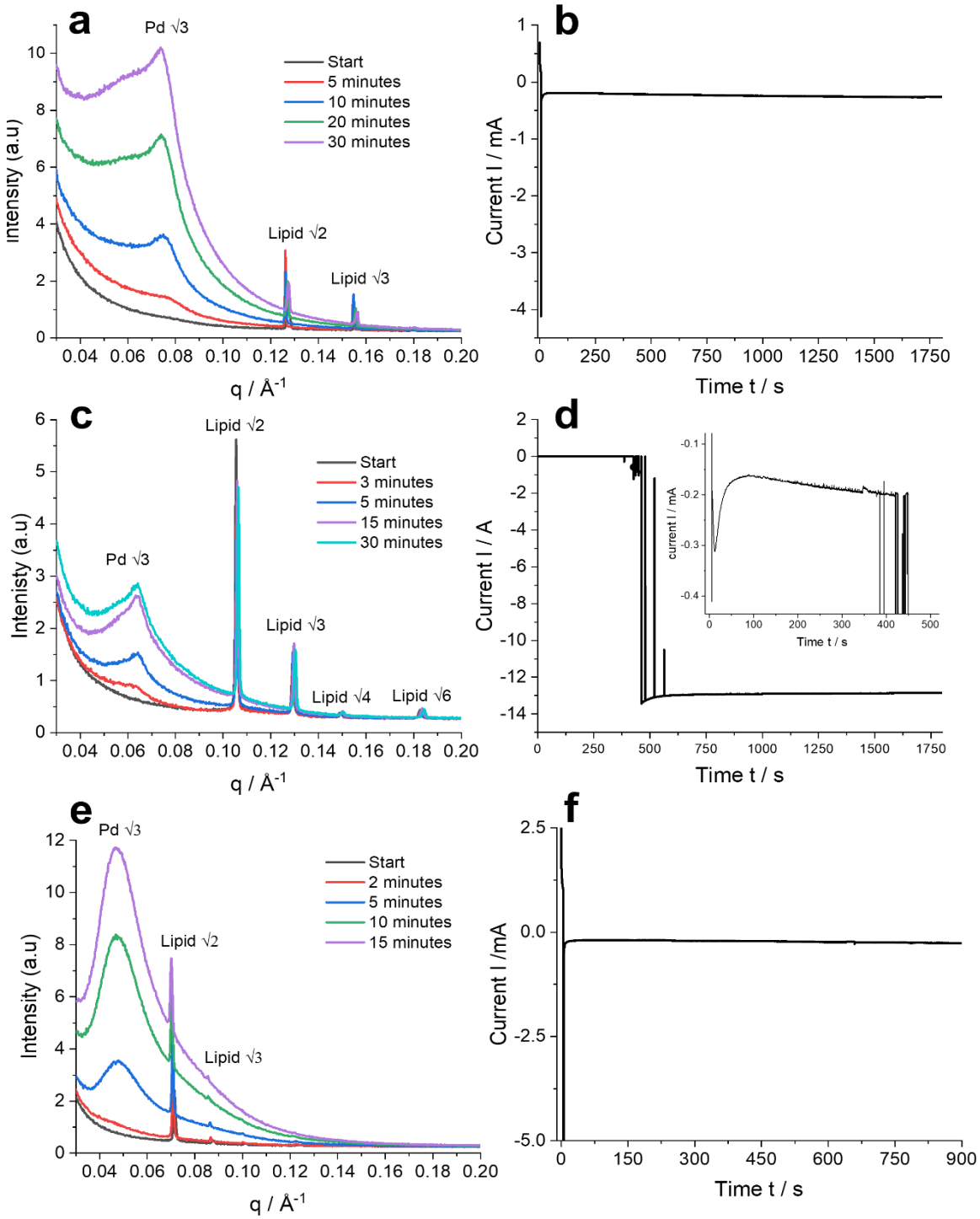

Figure 60 1D integrated SAXS patterns taken at different time intervals along with the associated current-time transient for Pd electrodeposited at a potential of 0.1 V vs SCE through phytantriol (a &b), phytantriol/Brij-56 (7.5 wt%) (c & d) along with an insert highlighting the short circuit and phytantriol/Brij-56 (20 wt%) (e & f).

4.8. TEM

To provide further evidence that we successfully electrodeposited single diamond phase Pd with control over size, we used TEM to obtain high quality images of the material. The images

were collected on a JEOL JSM-2100PLUS. Figure 61 shows TEM images of Pd electrodeposited through the pure phytantriol template. From these images we can see that the Pd has successfully formed the desired single diamond structure. We can see a 3D interconnected nanowire network that is highly porous. From these images we have measured the average nanowire diameter to be 2.4 ± 0.3 nm, this value is slightly lower than that measured by SAXS (2.9 ± 0.1 nm) but it is fairly consistent with expected values. Measuring the pore widths using TEM was difficult as the pores are not easily visible due to the orientation of the material, we therefore have poor statistics, and a distribution could not be fit. As measured by TEM we had pore widths varying from 5.5 to 8 nm in width.

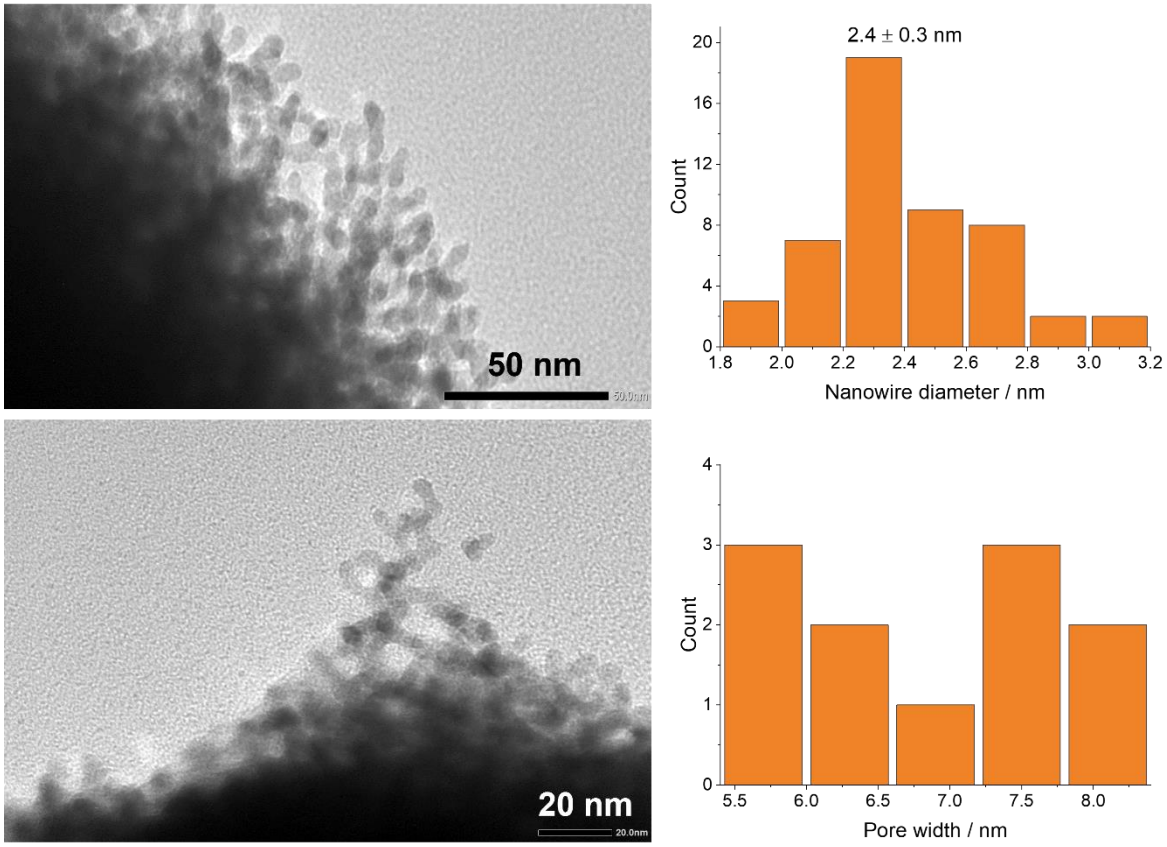

Figure 61 TEM images of Pd electrodeposited through phytantriol at a potential of 0.1 V *vs* SCE for 1800 s from a solution of 50 mM $(NH_4)_2PdCl_4$ and 1 M NH_4Cl in 1 M HCl at room temperature, along with the size distributions of the associated nanowire and pore dimensions.

TEM images for Pd grown through the phytantriol/Brij-56(7.5 wt%) template are shown in Figure 62. These images again prove that we have successfully electrodeposited single diamond phase Pd through the phytantriol/Brij-56(7.5 wt%) template. We can see the 3D interconnected nanowire network with individual nanowires being visible. Unfortunately, due

to the quality of the images and the orientation of the material we could not measure any values for the pore widths for this material. The average nanowire diameter for the material was measured to be 2.9 ± 0.4 nm which is lower than that calculated by SAXS (3.9 ± 0.1 nm). The nanowire diameter of Pd deposited through phytantriol/Brij-56(7.5 wt%) was 0.5 nm larger than that deposited through pure phytantriol (as measured by TEM). This data complements that from the SAXS data in which by adding Brij-56 we increase the lattice parameter and nanowire diameter of the deposited Pd.

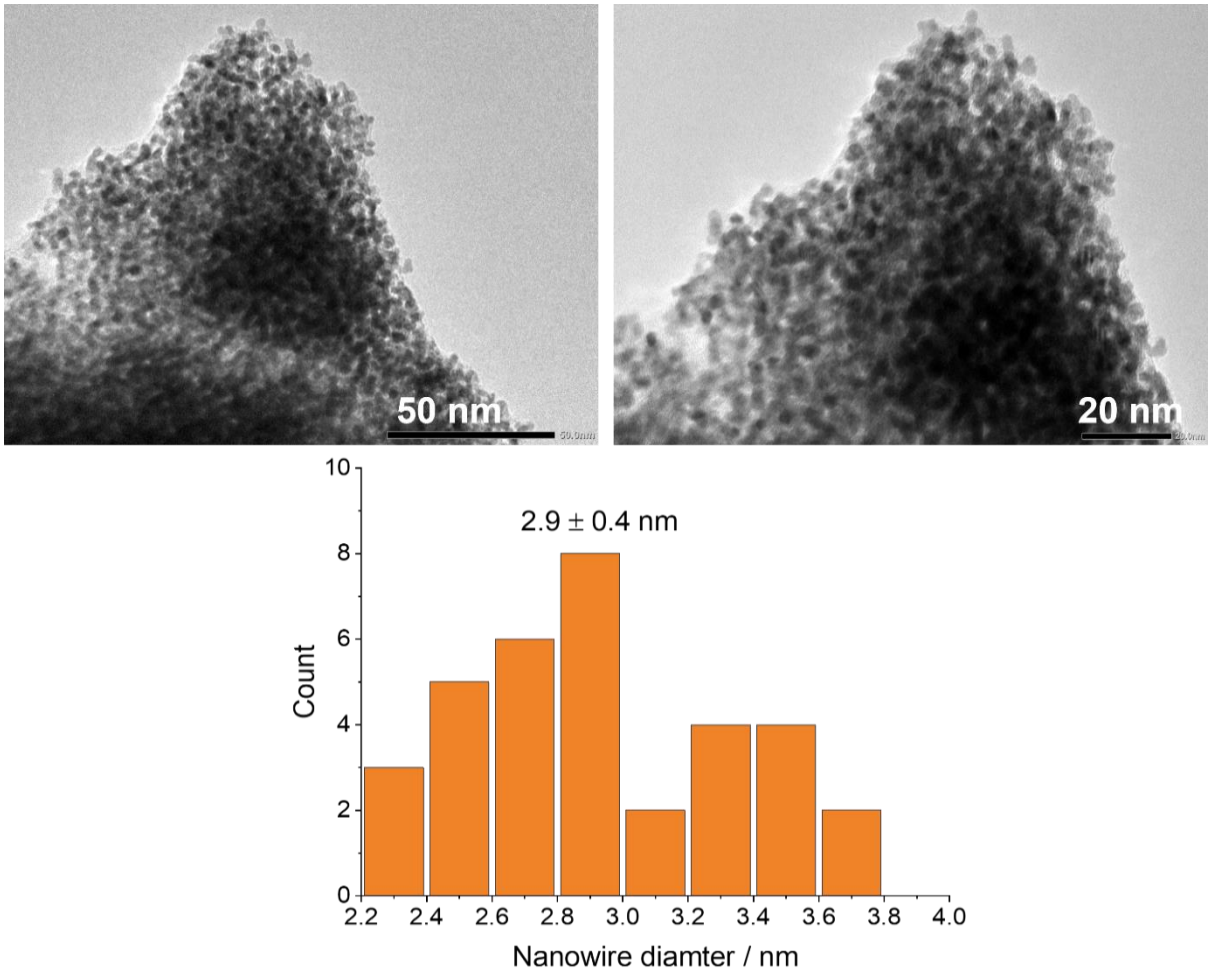

Figure 62 TEM images of Pd electrodeposited through phytantriol/Brij-56 (7.5 wt%) at a potential of 0.1 V *vs* SCE for 1800 s from a solution of 50 mM $(NH_4)_2PdCl_4$ and 1 M NH_4Cl in 1 M HCl at room temperature, along with the associated nanowire diameter distribution.

TEM images for Pd grown through the phytantriol/Brij-56 (20 wt%) template are shown in Figure 63. These images show we have successfully electrodeposited single diamond phase Pd through the phytantriol/Brij-56 (20 wt%) template. We can see individual nanowires in the single diamond phase however we cannot see any clear pores in these images. It is very

apparent in these images that the nanowire diameters are much larger than those from Pd deposited through pure phytantriol and phytantriol/Brij-56 (7.5 wt%). The average nanowire diameter for the material was measured to be 5.5 ± 0.8 nm which is within error of that calculated by SAXS (5.9 ± 0.3 nm).

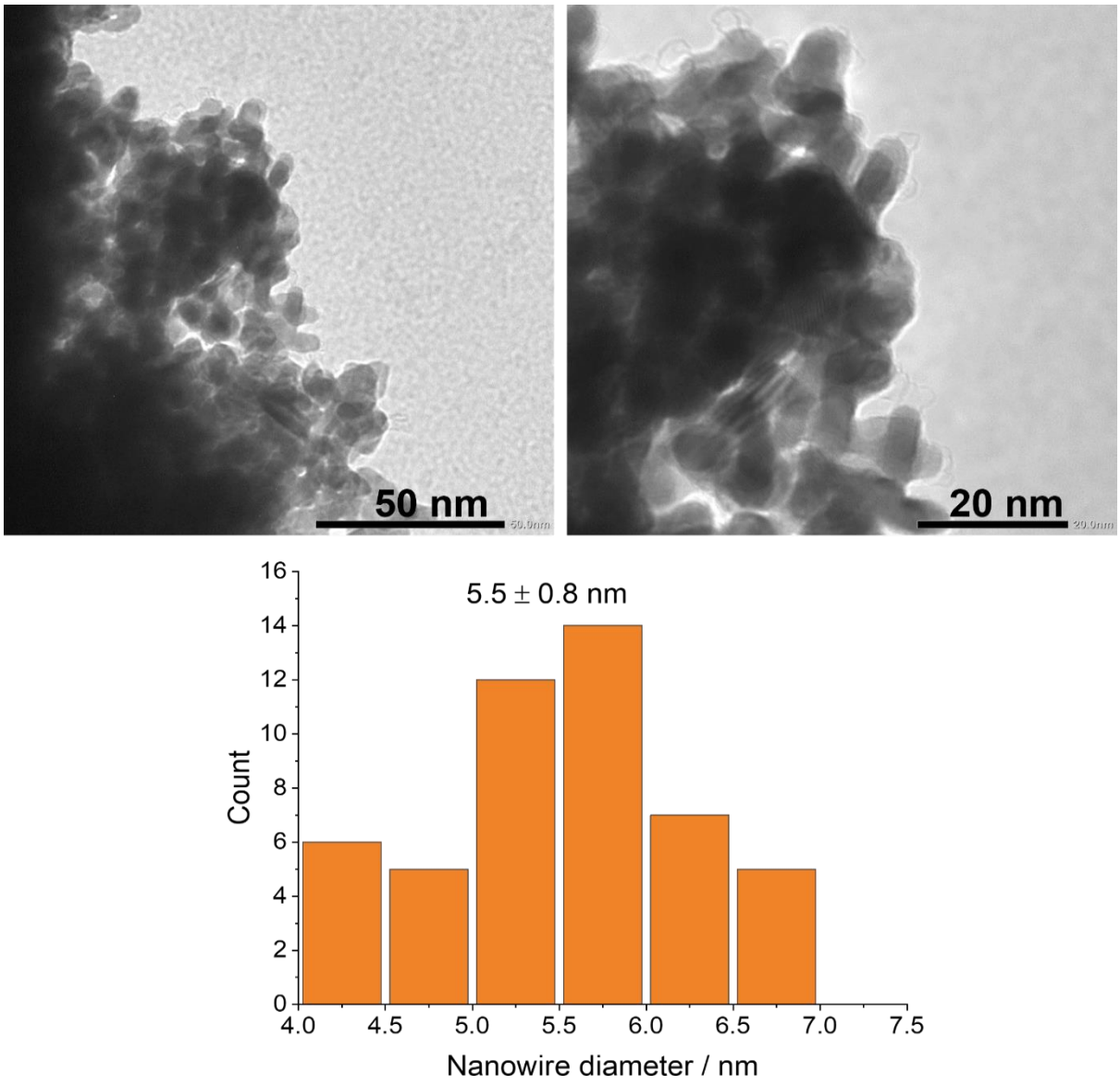

Figure 63 TEM images of Pd electrodeposited through phytantriol/Brij-56 (20 wt%) at a potential of 0.1 V vs SCE for 1800 s from a solution of 50 mM $(NH_4)_2PdCl_4$ and 1 M NH_4Cl in 1 M HCl at room temperature, along with the associated nanowire diameter distribution.

The measured values for the nanowire sizes for each Pd material is summarised in Table 11, which clearly shows the expected trend of increasing nanowire diameter with Brij-56 content. We see an increase from 2.4 to 5.5 nm when adding 20 wt% Brij-56 to the phytantriol template. These values and trend are consistent with the previous report with Pt.[19]

Table 11 A table summarising the phase seen and nanowire diameters measured from TEM images of Pd electrodeposited through various phytantriol/Brij-56 templates.

Template	phase	Nanowire diameter (nm)
Phytantriol/0% Brij-56	Single diamond	2.4 ± 0.3
Phytantriol/7.5% Brij-56	Single diamond	2.9 ± 0.4
Phytantriol/20%Brij-56	Single diamond	5.5 ± 0.8

4.9. XRD

XRD was performed on all Pd samples electrodeposited through all 3 templates. The XRD patterns, shown in Figure 64, match the pattern from the Pd reference filename; No: 00-001-120 from the IDCC database. This provides evidence that it is Pd we have electrodeposited and nothing else. The Pd (111), (200) and (220) peaks are all clearly visible matching reference Pd along with other Pd nanomaterials reported in literature.[103,104] We can also see peaks that match the Au (111), (200) and (220) from the reference pattern filename: No: 00-001-1174. These gold peaks originate from the Au layer present on the Au-DVD substrates from Delkin Devices.

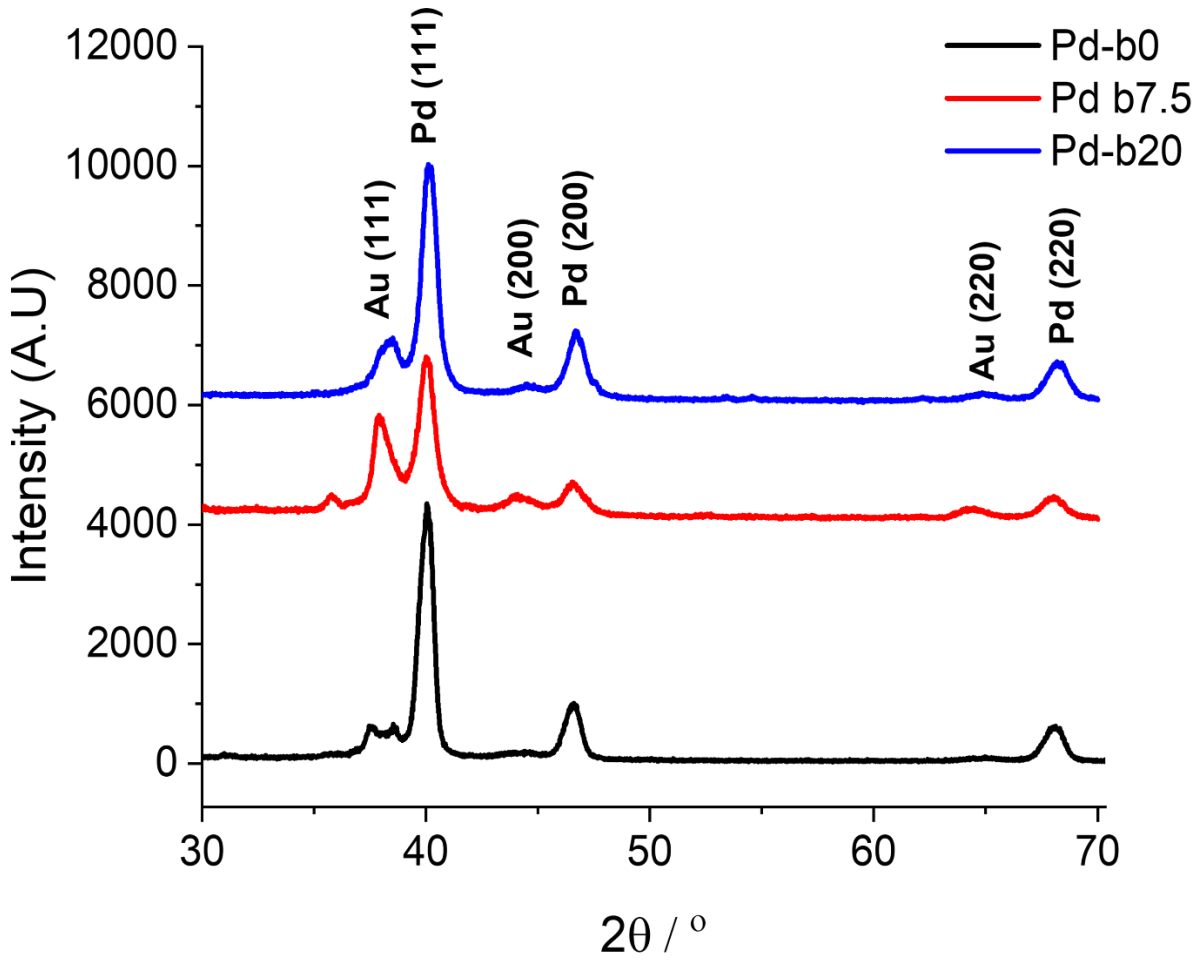

Figure 64 XRD patterns of thin films of Pd electrodeposited through various phytantriol/Brij-56 templates at a potential of 0.1 V vs SCE for 1800 s from a solution of 50 mM $(NH_4)_2PdCl_4$ and 1 M NH_4Cl in 1 M HCl at room temperature. The substrates were Au-DVD from Delkin devices. The peaks were matched to filename No: 1011110, CSD: data_1011110(COD) for Pd and No: 9013039, CSD: data_9013039(COD for Au.

4.10. Formic acid oxidation (FAO) against lattice parameter

Pd was electrodeposited on a 3 mm Au RDE until 22 mC of charge had passed, depositing 12.1 µg of Pd. To test the single diamond Pd's performance for the formic acid oxidation linear sweep voltammetry from -0.2 V to 0.8 V *vs* SCE at 50 mV s^{-1} at room temperature in 0.5 M H_2SO_4 and 0.5 M formic acid (N_2-saturated) was performed. Figure 65 revealed that templated Pd had a much higher performance compared to untemplated Pd, which was expected due to the large increase in surface area. The Pd electrodeposited through phytantriol and phytantriol/Brij-56(7.5 and 20 wt%) will be referred to as Pd-b0, Pd-b7.5 and Pd-b20 respectively going forward. Pd-b20 had the best performance for the FAO by expressing the largest peak current density when compared to Pd deposited through the other templates.

The performance for the formic acid oxidation when ranked on highest peak current density was Pd-b20 > Pd-b7.5 > Pd-b0 > untemplated Pd. This suggests that there is a trend of increasing performance with lattice parameter. It is also apparent that the peak potential is lower for Pd-b20 when compared to Pdb7.5, Pd-b0 and untemplated Pd. This lower peak potential means that the activation energy needed for the oxidation of formic acid is lowest for Pd-b20. This means that formic acid can be oxidised with less input energy, which makes for a more efficient catalyst. The typical peak potential for commercial Pd black (Johnson Matthey Corporation) catalyst is around 0.2 V *vs* SCE under the same conditions.[105] This result could be due to larger pores giving formic acid better access to the Pd surface area, and also larger pores may better facilitate the product (CO_2) leaving the surface and diffusing into the bulk solution.

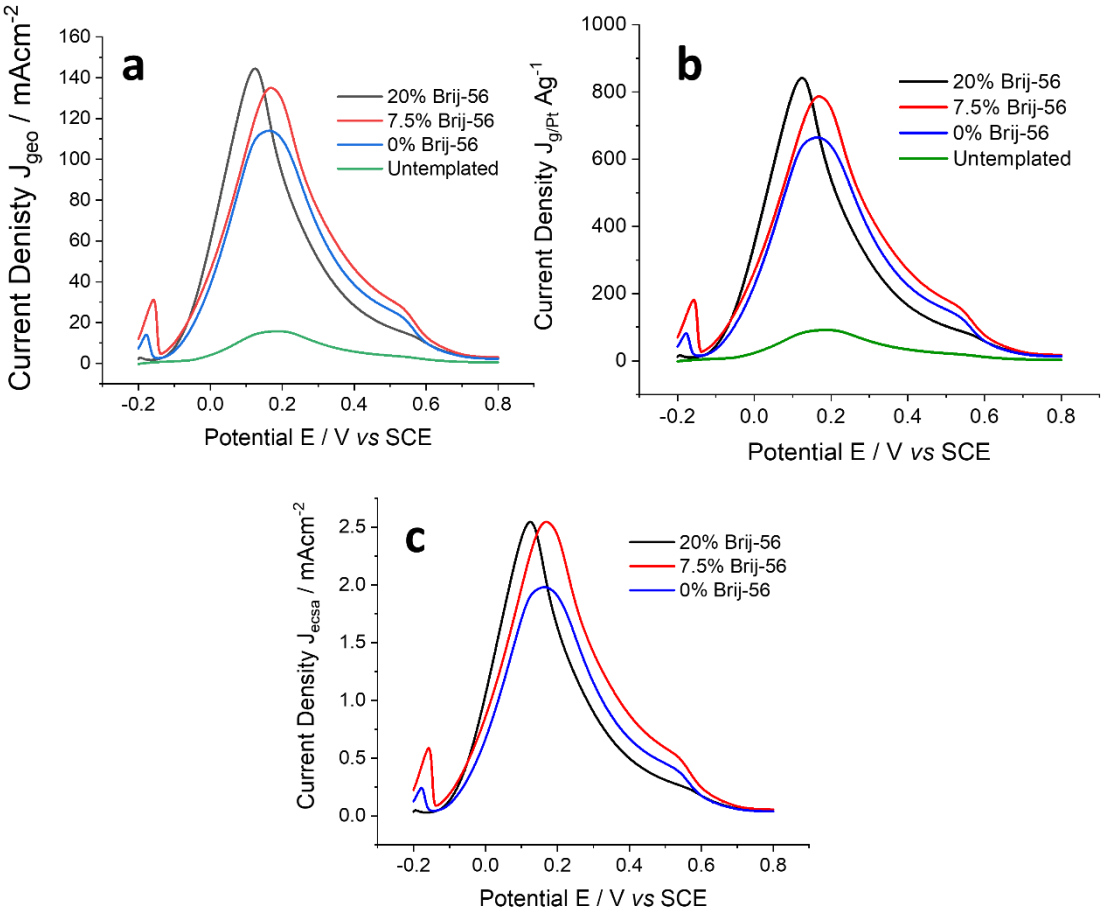

Figure 65 Cyclic voltammograms of formic acid electrooxidation on various Pd electrodes taken at a scan rate of 50 mV s^{-1} in a N_2-saturated solution containing 0.5 M formic acid in 0.5 M H_2SO_4. Normalised by geometric surface e area (a), mass of Pd (b) and electrochemical surface area (c).

The results from these experiments are summarised in Table 12. A common value reported in literature for the formic acid oxidation for the performance of a material is the peak current density normalised by mass of Pd. Figure 65 shows again the Pd produced by phytantriol/Brij-56 (20 wt%) which has the largest lattice parameter, nanowire diameter and pore size has the highest mass activity of 841 A g^{-1}. This value is 9 times larger than that recorded for untemplated Pd which shows a significant increase in activity. Maximising the mass activity for the formic acid oxidation is an important parameter in order to develop catalysts that are more affordable. The current densities reported here for single diamond Pd are comparable to literature values on recent Pd catalysts. The value from Pd-b20 of 841 mA mg^{-1} is larger than that reported for Pd black (98 mA mg^{-1}),[105] Pd-Sn-intermetallics (553 mA mg^{-1}),[105] Pd nanosheets (409 mA mg^{-1}),[106] Pd nanoparticles (660 mA mg^{-1}) and Cu_3Pd nanoparticles (302 mA mg^{-1}).[107] However there are still many reports of Pd catalysts with higher current density, mainly being alloy materials such as PdCu alloy nanosheets (4170 mA mg^{-1}),[108] $Pd_{87}Cu_{13}$tripods (1580 mA mg^{-1})[109] and Pd_1Bi_1/NG (2025 mAmg^{-1}).[110] Ding *et al.*[111] reported testing single diamond Pd (produced from pure phytantriol) for the formic acid oxidation. They studied how changing the deposition potential and temperature influences the single diamond Pd's performance. They reported that single diamond Pd produced through phytantriol had a peak current density of 3340 A g^{-1} which is 5 times larger than that recorded in this work under the same conditions for the same catalyst (Pd-b0 with 664.13 A g^{-1}).[111] Ding *et al.* also reported that their material had a specific surface area of 90.5 $m^2 g^{-1}$ which is much larger than that recorded for this work and previously by Burton *et al*.[12] Therefore, we will treat the results recorded form this work independent from that reported previously for this material and comparisons will be made internally between samples produced and tested in-house. Overall, the single diamond phase Pd shows great catalytic performance for the FAO and it can be produced easily from a green one-pot synthesis method which is very attractive.

Table 12 A table summarising the results from cyclic voltammetry of different Pd electrodes for the formic acid oxidation in 0.5 M formic acid in 0.5 M H_2SO_4 at 50 mV s^{-1} at room temperature.

Sample	Peak current (geo) / mA cm^{-2}	Peak current (mass Pd) / A g^{-1}	Peak current (ECSA) / mA cm^{-2}	Peak potential / V *vs* SCE
Pd-b0	114.0	664.1	2.0	0.16
Pd-b7.5	135.0	786.4	2.5	0.17
Pd-b20	144.5	841.4	2.5	0.13
Untemplated Pd	16.8	91.8	N/A	0.19

To assess how the different sizes of single diamond Pd affects the activity for FAO, the CVs were normalised by ECSA. The results from this are shown in Figure 65 (c) which shows that when normalised by ECSA Pd-b20 and Pd-b7.5 exhibit the same peak current density. This means the two materials have the same activity per Pd atom and the higher current density seen for Pb-b20 was due to it having a larger surface area. Both Pd-b20 and Pd-b7.5 have a higher activity per Pd atom when compared to Pd-b0. This demonstrates that having control over the size of the produced single diamond Pd is important as you can fine tune the material's properties in order to fabricate a higher performing catalyst.

In order to measure the kinetics of the formic acid oxidation on the different Pd samples, linear sweep voltammetry was performed at different scan rates in N_2 saturated 0.5 M HCOOH + 0.5 M H_2SO_4. After each potential sweep the electrode was rotated at 1600 rpm for 30 seconds followed by 5 minutes equilibration time in between scans. This was to remove any CO_2 bubbles that had been produced from the surface of the Pd. The peak potential shifts positively with the increase of scan rate, which indicates that the oxidation is an irreversible process. For an irreversible reaction, the peak current is expressed by a modified version of the Randles-Sevcik equation (Equation 35).[112]

Equation 35

$$J_p = 2.99 \times 10^5 n(\alpha n')^{1/2} C D^{1/2} v^{1/2}$$

Where J_p is the peak current density, n is the number of electrons involved in the transfer, n' is the electron number transferred in the rate determining step which in this case is 1, α is the charge transfer coefficient, C is the formic acid concentration, D is the diffusion coefficient and v is the sweep rate.

For an irreversible system, the peak potential is proportional to the log of the scan rate at 298 K given by Equation 36.[112]

Equation 36

$$\frac{dE_p}{dlogv} = \frac{29.6}{\alpha n'}$$

Figure 66 shows linear sweep voltammograms for the formic acid oxidation on untemplated Pd. Unfortunately, due to stability of the untemplated Pd only 3 different scan rates are present. After 3 scans we saw a deviation of the linear relation between peak current and the square root of the scan rate as the current density dropped considerably after multiple scans. This was most likely due to carbon monoxide poisoning of the Pd sites leading to a degradation of its performance. This was repeated many times for untemplated Pd but it was only possible to produce three consecutive voltammograms before sizeable degradation occurred. Therefore, these three values, following the Randles-Sevcik relationship was used to determine the kinetics. In order to determine the charge transfer coefficient, the peak potential at each scan rate was plotted against the log of the scan rate, which is shown in Figure 66 (b). The slope of this plot was used in Equation 36 to calculate a charge transfer coefficient value of 0.98 ± 0.03. A Randles-Sevcik plot was then made by plotting the peak current against the square root of the scan rate, Figure 66 (c). Using the slope from this plot and the previously determined α, the diffusion coefficient was determined to be $(2.2 \pm 0.6) \times 10^{-8}$ cm^2 s^{-1}.

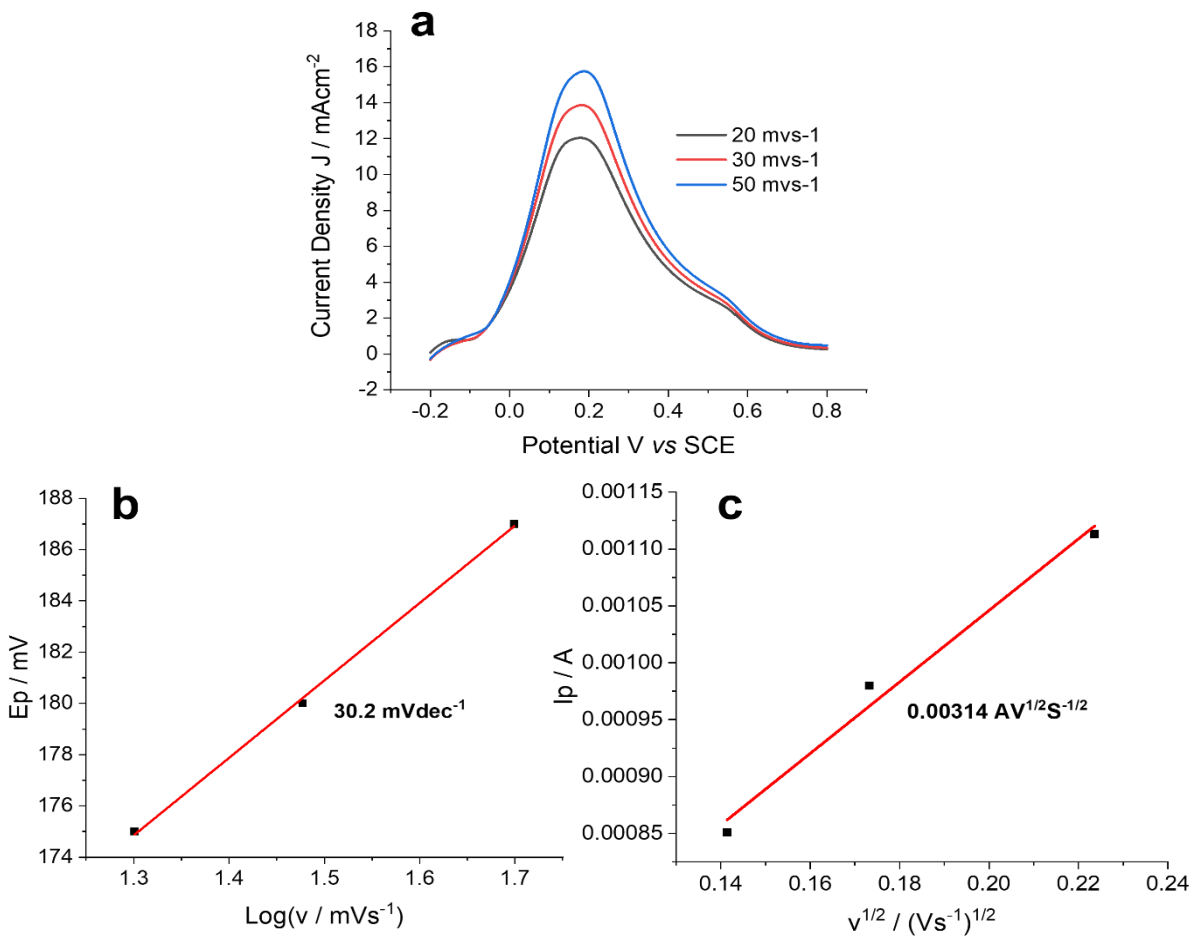

Figure 66 Linear sweep curves for the formic acid oxidation on untemplated Pd at different sweep rates in 0.5 M H_2SO_4 (a). A plot of the peak potential against log sweep rate (b) and a plot of the peak current against the square root of the sweep rate (c).

The same process was then applied to the Pd films produced via templating. The results for Pd-b0 are shown in Figure 67. The calculated value for the charge transfer coefficient and diffusion coefficient were determined to be 0.25 ± 0.01 and $(4.0 \pm 0.2) \times 10^{-6}$ cm^2 s^{-1}. The results for Pb-b7.5 and Pd-b20 are shown in Figure 68 and Figure 69 respectively. The charge transfer coefficient and diffusion coefficient calculated for Pd-b7.5 were 0.22 ± 0.01 and $(1.1 \pm 0.3) \times 10^{-5}$ cm^2 s^{-1}. The values calculated for Pd-b20 for the charge transfer and diffusion coefficients were 0.3 ± 0.01 and $(3.5 \pm 0.5) \times 10^{-6}$ cm^2 s^{-1}. These values for the charge transfer and diffusion coefficient are consistent with literature reports.[112,113]

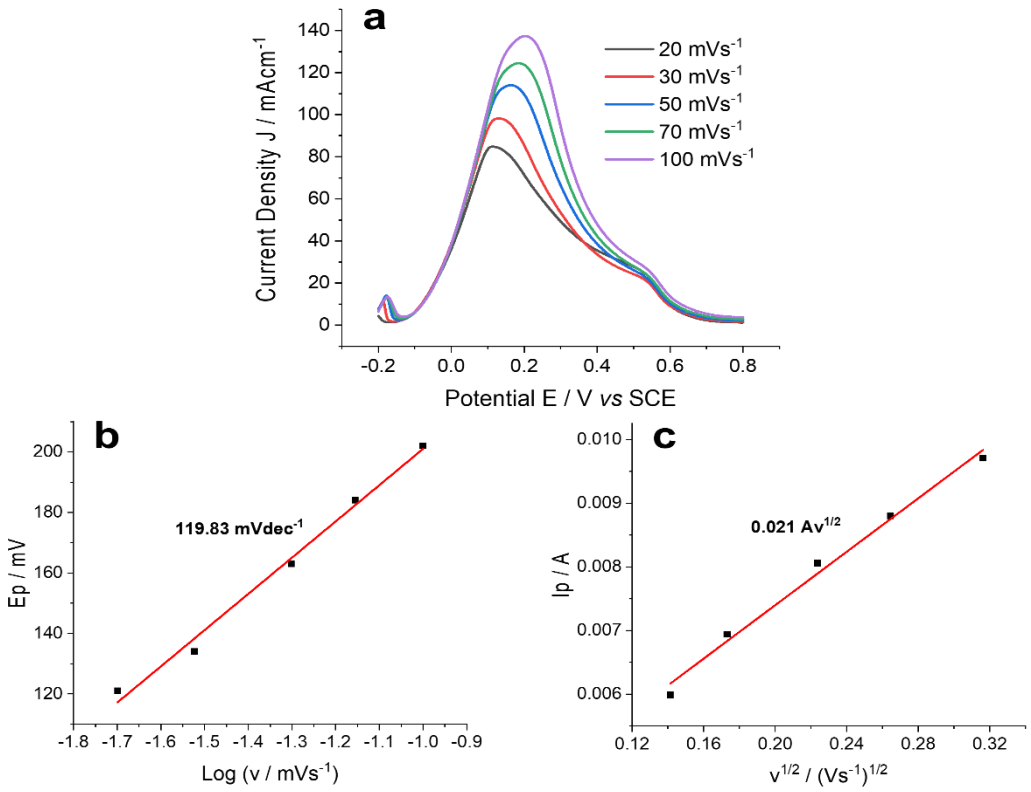

Figure 67 Linear sweep curves for the formic acid oxidation on Pb-b0 at different sweep rates in 0.5 M H_2SO_4 (a). A plot of the peak potential against log sweep rate (b) and a plot of the peak current against the square root of the sweep rate (c).

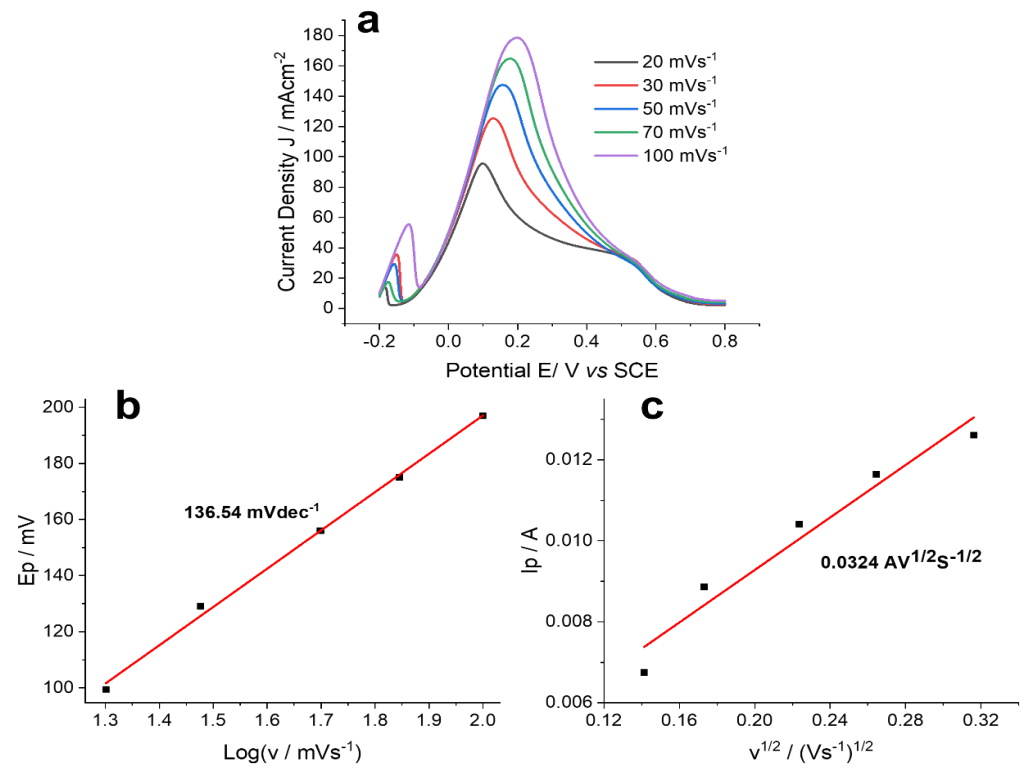

Figure 68 Linear sweep curves for the formic acid oxidation on Pb-b7.5 at different sweep rates in 0.5 M H_2SO_4 (a). A plot of the peak potential against log sweep rate (b) and a plot of the peak current against the square root of the sweep rate (c).

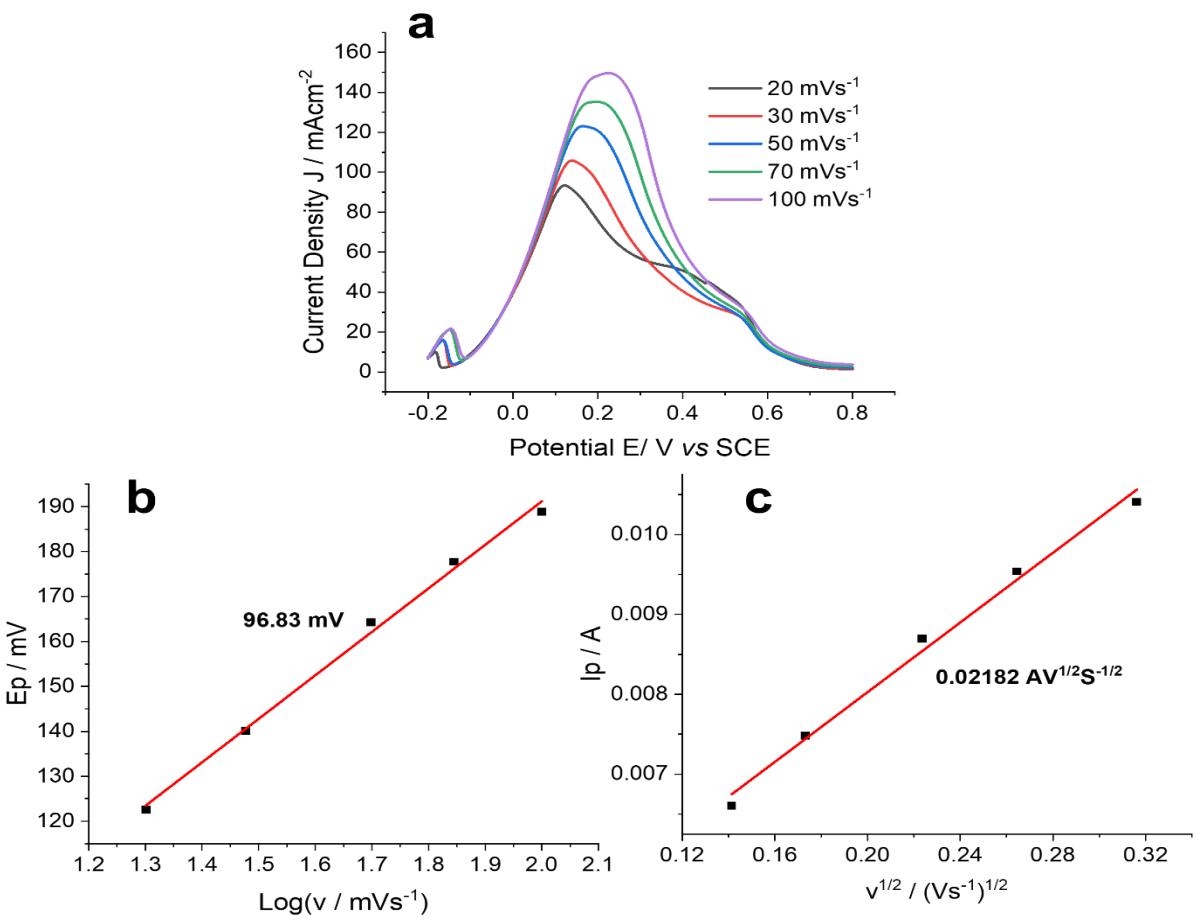

Figure 69 Linear sweep curves for the formic acid oxidation on Pb-b20 at different sweep rates in 0.5 M H_2SO_4 (a). A plot of the peak potential against log sweep rate (b) and a plot of the peak current against the square root of the sweep rate (c).

To compare the values between the untemplated Pd and single diamond Pd with differing size the results from the linear sweep voltammograms are summarised in Table 13.

Table 13 A summary of the charge transfer and diffusion coefficients determined by linear sweep voltammetry for the formic acid oxidation in 0.5 M HCOOH + 0.5 M H_2SO_4 for Pd.

Sample	Charge transfer coefficient (α)	Diffusion coefficient (D) / $cm^2\ s^{-1}$
Pd-b0	0.25 ± 0.01	$(4.0 \pm 0.2) \times 10^{-6}$
Pd-b7.5	0.22 ± 0.01	$(1.1 \pm 0.3) \times 10^{-5}$
Pd-b20	0.30 ± 0.01	$(3.5 \pm 0.5) \times 10^{-6}$
Untemplated Pd	0.98 ± 0.03	$(2.2 \pm 0.6) \times 10^{-8}$

To further assess the kinetics of the FAO on single diamond Pd of varying size Tafel analysis was used. A Tafel slope is used in electrochemistry to describe the relationship between current density and electrode potential and is given by Equation 37;

Equation 37

$$J = J_0 exp\left(\frac{\alpha nF(E-E_0)}{RT}\right)$$

Where J is current density, J_0 is the exchange current density, α is the charge transfer coefficient, n is the number of electrons transferred, F is Faraday's constant, R is the molar gas constant, T is the temperature and E is the electrode potential, E_0 is the equilibrium potential. A plot is then made of the potential against the logarithmic of current density, with the gradient being the Tafel slope (b) which is given by Equation 38.

Equation 38

$$b = \frac{\alpha nF}{RT}$$

A smaller Tafel slope is generally considered to be better than a higher one as this means there is a larger increase in current density with a given increase in overpotential. The potential of the linear sweep voltammograms at a scan rate of 20 mV s^{-1} was plotted against the log of the current, Figure 70. The slope of the linear regions was then determined by using a linear fit. The untemplated Pd exhibited the highest Tafel slope (158.3 mV dec^{-1}) whereas the single diamond Pd had a trend of smaller Tafel slope with increasing lattice parameter/size. As Pd-b20 exhibited the shallowest Tafel slope (70.5 mV dec^{-1}) it means that a smaller overpotential would be required to provide the same current density when compared to the other materials. This is important for performance as it means less of a driving force is needed for the reaction to occur.

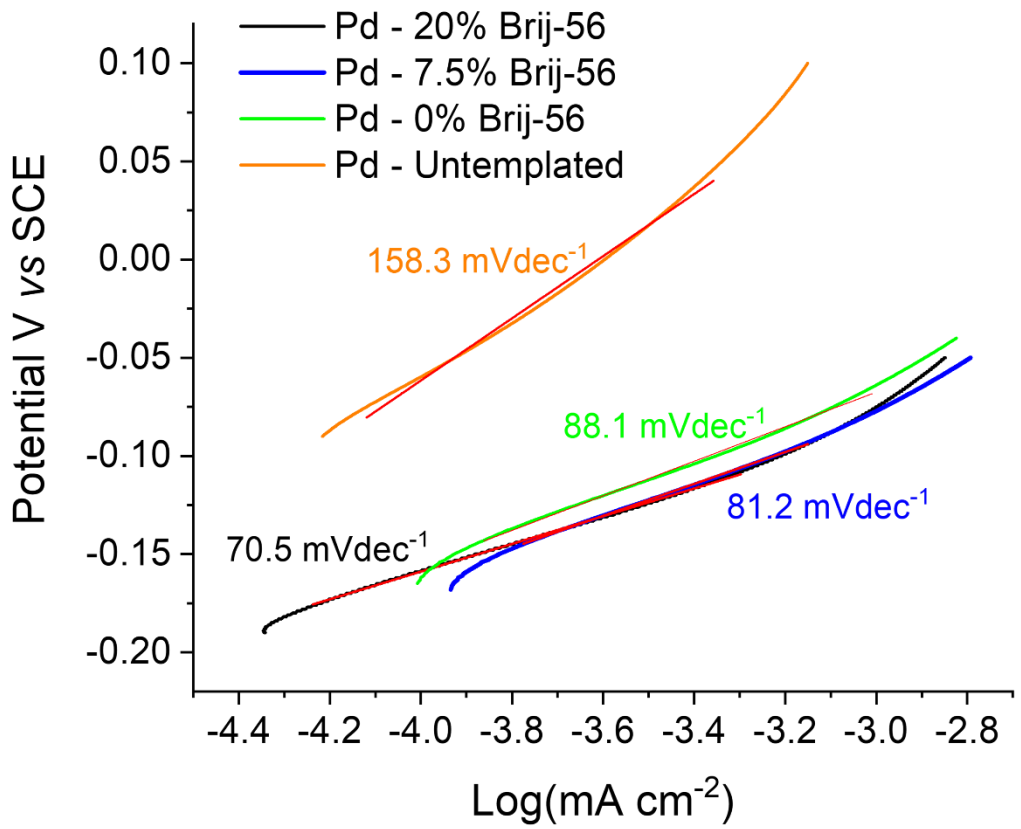

Figure 70 Tafel plot of log I against potential for the oxidation of 0.5 M HCOOH in 0.5 M H_2SO_4 solution on Pd electrodes at a scan rate of 20 mV s^{-1}. Linear fits for the data are shown in red.

Chronoamperometry was used in order to measure the single diamond Pd's performance under operating conditions by applying 0.2 V *vs* SCE for 10 minutes in N_2-saturated 0.5 M HCOOH in 0.5 M H_2SO_4. The results from these experiments are shown in Figure 71. From the current-time transients we can see that for all samples the initial current density straight after the potential step is extremely high in the ranges of 1250 to 1700 A g^{-1}. For all samples the current density dropped quite rapidly across 10 minutes and Figure 71 (b) shows an insert of the final 100 seconds of the chronoamperometry tests. This data reveals that after operating the catalysts for 10 minutes Pd-b0 has the highest current density with the lowest drop in current followed by Pd-b7.5 then Pd-b20. This is the opposite trend that was expected for performance, based of cyclic voltammetry experiments, Pd-b20 should have exhibited the highest current density. These results indicate that at 0.2 V *vs* SCE Pd produced via pure phytantriol has the best performance. The peak potential for Pd-b20 as revealed by cyclic voltammetry was much lower (1.25 *vs* SCE) compared to Pd-b0 (1.63 V *vs* SCE) so it may be

the case that we would see higher current density at lower operating potentials for Pd-b20 but when operating at larger potentials (0.2 V *vs* SCE) the activity of Pd-b20 may decrease. This could potentially come from mass transport limitations or increased energy losses leading to lower current density. The values of current density obtained after 10 minutes of operating at 0.2 V *vs* SCE for the single diamond Pd films are 143.7 A g^{-1}, 51.4 A g^{-1} and 33.2 A $g^{-1}$for Pd-b0, Pd-b7.5 and Pd-b20 respectively. These values are larger than those reported for recent catalysts in literature of Pt and PtPd on graphene oxide support and Pt on polydopamine graphene oxide[114] as well as commercial Pd/C.[115]

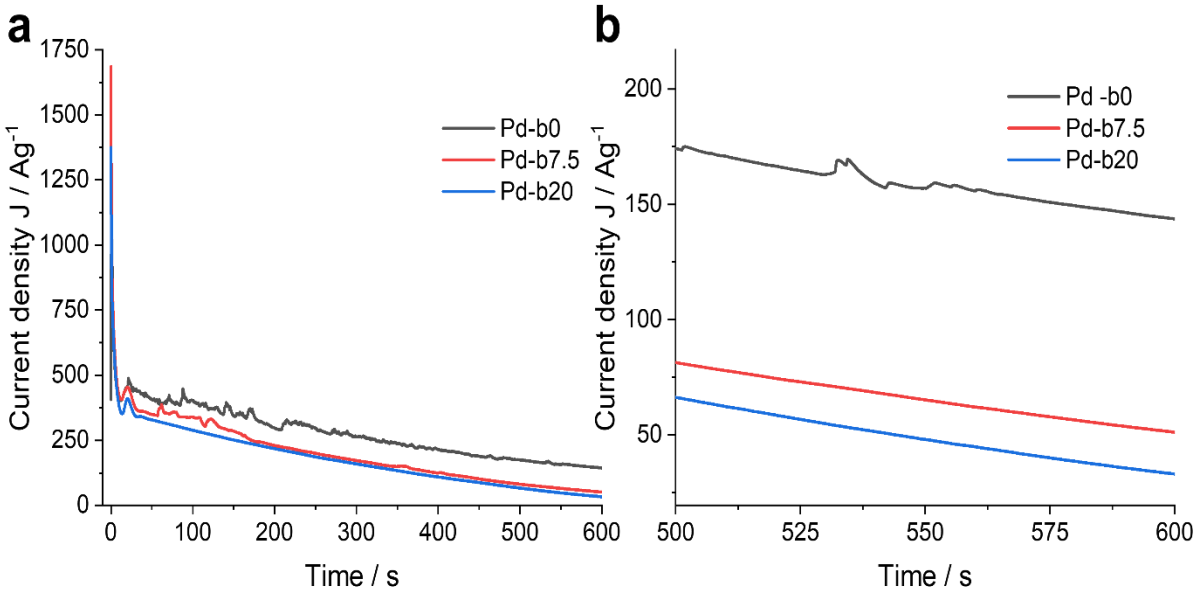

Figure 71 Current-time transients of the formic acid oxidation on Pd deposited through different phytantriol/Brij-56 templates at a potential of 0.2 V vs SCE for 10 minutes from a N_2-saturated solution of 0.5 M HCOOH in 0.5 M H_2SO_4.

4.11. Conclusions

We have successfully demonstrated that single diamond Pd can be electrodeposited through phytantriol/Brij-56 with control over the lattice parameter, nanowire diameter and pore width by controlling the amount of Brij-56 in the liquid crystal template. The material had its single diamond architecture confirmed by SAXS and TEM. The deposited Pd had a lattice parameter of 143.7 ± 1.6 Å and a nanowire diameter of 2.9 ± 0.1 nm when using phytantriol as a template which increased to 217.3 ± 6.9 Å and 5.9 ± 0.3 nm with the addition of 20 wt% Brij-56. It was found that Pd, produced via all three liquid crystal templates, had high electroactive surface areas of around 30 $m^2 g^{-1}$.

We used the formic acid oxidation in order to assess how altering the size of single diamond Pd affects its catalytic performance. Using cyclic voltammetry, we discovered that there was a trend in increasing peak current density with lattice parameter, so the larger single diamond Pd showed an increase in performance. This was further reflected with a trend in shallower Tafel slope with increasing lattice parameter, from 88.1 mV dec^{-1} to 70.5 mV dec^{-1}. However, we did find that upon testing the material using chronoamperometry at 0.2 V *vs* SCE the opposite trend was seen, and the current density after 10 minutes increased with smaller lattice parameter.

Overall, we have demonstrated that the size of single diamond Pd can be manipulated by using curvature modulation by the addition of a co-surfactant into the liquid crystal template. This provides us with a method of producing mesoporous Pd with tuneable properties using a one-pot synthesis method.

4.12. Future work

The next step for this project would be to further characterise the materials performance for the FAO. Stability of the material can be tested by performing chronoamperometry over long time scales or cyclic voltammetry could be used to test the material in an accelerated degradation regime. We can therefore measure if the size of the single diamond material affects its stability. The stability can be characterised by changes to the peak current densities or the electroactive surface area of the Pd.

Work should also be conducted in determining why an increase in lattice parameter of single diamond Pd leads to a better performance for the FAO. It is not yet clear if larger pores facilitate the diffusion of products and reactants, or if differing surface sites are the main contributor to differences in performance. This distinction merits further investigation.

Another direction this project could go in which I believe would be important work is the fabrication of single diamond phase Pd alloys such as PdCu, PdPt, PdW . These Pd alloys have been reported in literature to have enhanced catalytic performance for the formic acid oxidation reaction.[114,116,117] Pd alloys can benefit from higher stability and poisoning resistance so producing these alloys in the single diamond phase would be of great interest.

The next chapter focusses on the electrodeposition of single diamond phase Pt and its application for the oxygen reduction reaction in alkaline conditions. The research aim is to evaluate the electrochemical performance and durability of the single diamond Pt and compare it to a commercial Pt/C catalyst.

5. Single diamond Pt (SD-Pt) for the oxygen reduction reaction

5.1. Introduction

As the demand for energy continues to rise and concerns over greenhouse gas emissions and global warming intensify, there is an increasing urgency to transition towards cleaner and more efficient methods of energy production. One promising technology that can help to provide green energy is fuel cells. Fuel cells are electrochemical devices which are capable of converting chemical energy, typically in the form of hydrogen, into electrical energy through redox reactions. Unlike conventional combustion power sources, fuel cells can generate electrical energy with minimal to no emissions of CO_2 with the waste products primarily being heat and water, making them an important technology in the quest to reduce carbon emissions and prevent climate change.[118]

Fuel cells have attracted major attention as they are capable of providing high energy and power densities.[119–123] There are many different types of fuel cells from proton exchange membrane fuel cells (PEMFCs),[124–126] alkaline fuel cells (AFCs),[127–129] solid oxide fuel cells (SOFCs),[130–132] direct alcohol fuel cells (DAFCs)[133–135] and formic acid fuel cells (FAFCs).[136–138] All of these different types of fuel cells come with their unique advantages and disadvantages as well as different challenges. In this work we discuss alkaline fuel cells as we plan to use these conditions to test the single diamond phase of Pt as a cathode catalyst for the oxygen reduction reaction (ORR).

Alkaline fuel cells (AFCs) are a type of fuel cell that utilises an alkaline electrolyte (typically KOH) to electrochemically convert H_2 into electrical energy.[127,129] AFCs generate energy through redox reactions of a fuel and oxidant at the anode and cathode respectively. The reactions typically consist of the oxidation of hydrogen at the anode with the consumption of hydroxide ions given by the half equation (Equation 39) and reduction of oxygen with water to give hydroxide ions at the cathode given by the half equation (Equation 40).The overall reaction is given by Equation 41.

Equation 39 $$H_2 + 2OH^- \rightarrow 2H_2O + 2e^-$$

Equation 40 $$O_2 + 2H_2O + 4e^- \rightarrow 4OH^-$$

Equation 41 $$2H_2 + O_2 \rightarrow 2H_2O$$

A basic schematic for an AFC is shown in Figure 72, which shows an influx of oxygen to the cathode which is reduced into hydroxide ions, which then diffuse across to the anode, where they are consumed during the oxidation of hydrogen providing electrical energy producing water and heat as the by-products.

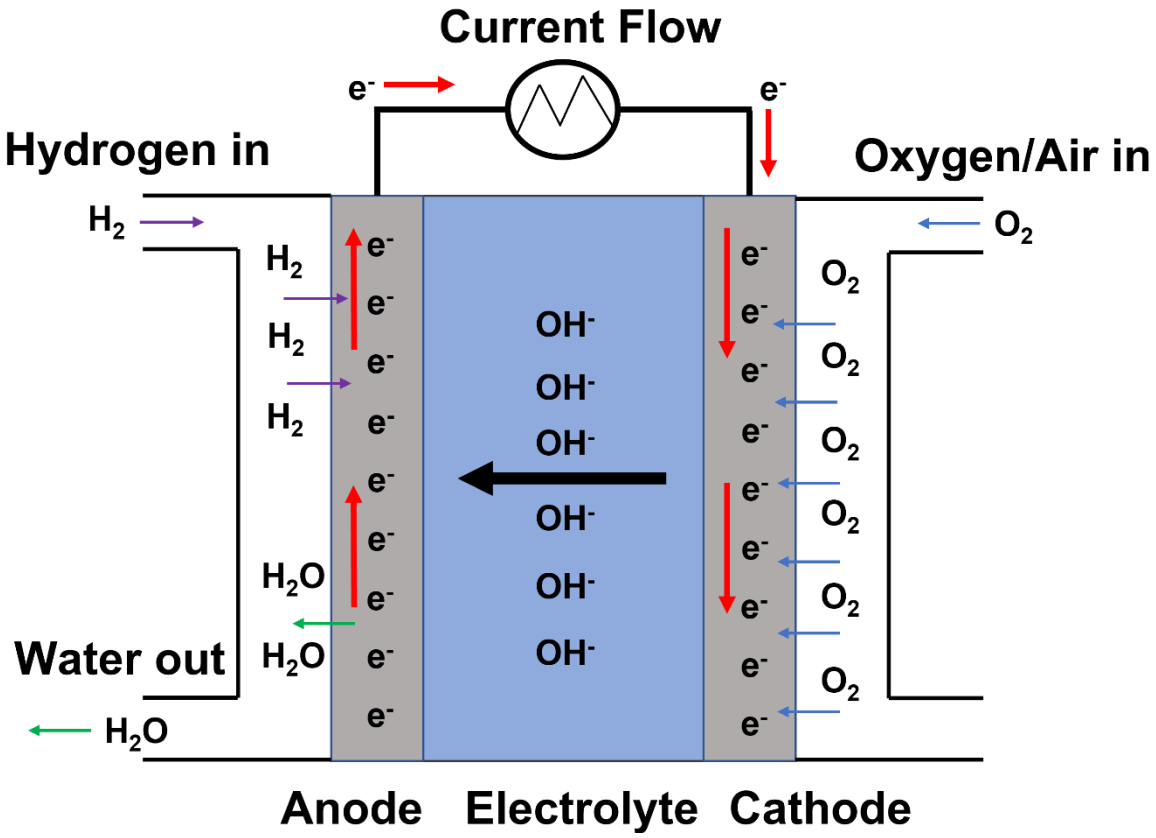

Figure 72 Basic diagram of an alkaline fuel cell (AFC), depicting the reduction of oxygen at the cathode, the migration of hydroxide ions to the anode where they participate in the oxidation of hydrogen into water.

As oxygen is used in fuel cells, a major challenge that we face is that they require efficient oxygen reduction reaction (ORR) catalysts, which are crucial to convert electrochemical energy.[139–141] This is a challenge due to the ORR being a limiting factor of the technology due to the high energy of the O=O bond (498 kJ mol^{-1}) and its sluggish kinetically slow activation.[142] It is reported that the ORR is much more efficient with better kinetics in high pH as opposed

to acidic conditions which is an advantage of alkaline fuel cells over acidic ones. In alkaline conditions, the ORR can take place through different pathways. The most desired pathway is the direct four-electron transfer which is given by Equation 42. The alternative indirect pathway occurs via Equation 43 and Equation 44 through the hydroperoxyl intermediate.

Equation 42 $$O_2 + 2H_2O + 4e^- \rightarrow 4OH^-$$

Equation 43 $$O_2 + H_2O + 2e^- \rightarrow HO_2^- + OH^-$$

Equation 44 $$HO_2^- + H_2O + 2e^- \rightarrow + 3OH^-$$

The indirect pathway is considered not to be ideal as the reaction is slower and less efficient. It is reported in the literature that the ORR occurs via the direct pathway on Pt-based catalysts.[143–145] Pt is considered to be the best catalyst for the ORR in alkaline media due to its very high catalytic activity and efficiency. However, this is a problem for alkaline fuel cells as Pt has a high cost and low earth abundancy.[146] Therefore, the current drive for research on cathode materials for AFCs involves exploring alternative non-precious metal catalysts, creating Pt-alloys or nanostructuring Pt in a bid to either lower the amount needed or by creating more efficient Pt materials. Common Pt-based catalysts reported in the literature that show good catalytic activity for the ORR are Pt nanoparticles supported on a high surface area carbon matrix.[128,147,148] Ruiz-Camacho *et al.*[128] synthesised Pt nanoparticles smaller than 10 nm supported on carbon nanotubes using a sonochemical method. The catalyst exhibited higher catalytic performance for the ORR in alkaline conditions when compared to a commercial Pt/C catalyst which was shown by a lower onset potential and higher half-wave potential. It also favoured the direct four-electron transfer pathway. Tachibana *et al.*[147] synthesised Pt nanoparticles on nitrogen doped porous carbon using a simple alcohol reduction method. The Pt nanoparticles had a size ranging from 1.9 to 3.0 nm and demonstrated high activity for the ORR in alkaline media. Miyatake and Shimizu prepared a Pt/Co alloy catalyst by a nano-capsule method. The alloy material showed good catalytic activity for the ORR in alkaline conditions however during durability tests the activity of the catalyst degraded due to particle agglomeration and dealloying.[148]

One of the major challenges of designing fuel cell materials is stability and durability. In order to create low cost and high performing catalysts the materials need to be stable under

operating conditions and have good durability in order to lengthen their lifetimes, so they can be used repeatedly. This is especially important when working with precious metals such as Pt due to the associated high cost of the material and its low abundance. It has been reported that the stability of commercial Pt/C catalysts suffers from a loss in electrochemical surface area during operation. [149] This loss in surface area is believed to be from a few different effects such as particle migration and agglomeration,[150] corrosion of the carbon support material leading to a loss of Pt nanoparticles,[151] and dissolution of Pt in the electrolyte.[152]

There is a drive to create Pt-based catalyst that have improved durability for the ORR. This is achieved in a few different ways by creating Pt-alloys which have poisoning resistance,[153,154] exploring different types of supports that offer better stability[155–158] or by creating support free catalysts.[159–161] Zhang *et al.*[155] explored the use of alternative support for Pt nanoparticles by fabricating a $Ti_3C_2T_x$ nanosheet support (called MXene) by using a modified LiF/HCl method. They then used an ultrasonication method to prepare a Pt/$Ti_3C_2T_x$ catalyst with a 20 % Pt mass fraction. The catalyst showed enhanced stability compared to Pt/C as it was reported that the catalyst structure was well maintained with a reduced degree of Pt particle agglomeration when tested for the ORR in alkaline conditions. Narayanamoorthy *et al.*[159] synthesised support free platinum nanowire networks using a one-step chemical reduction method. The Pt nanowire network had a high specific surface area of 120.5 $m^2 g^{-1}$, and after durability tests the supportless catalyst only had a drop in specific surface area of 22 % whereas the carbon support counterpart showed a decrease of 55 %, showing superior stability for the support free material for the ORR. Chen *et al.*[161] fabricated supportless Pt and PtPd nanotubes by employing a galvanostatic replacement technique. It was reported that during durability tests for the ORR in acidic media the supportless Pt nanotubes only had a loss in electroactive surface area of around 20 % after 1000 cycles whereas Pt/C and Pt black had a loss of 91 % and 50 % respectively.

In this chapter we study the performance and durability of the single diamond phase Pt (SD-Pt) nanomaterial for the oxygen reduction reaction in alkaline conditions. We will also test a commercial Pt/C catalyst in order to benchmark the SD-Pt's performance. There have been no previous reports in the literature of single diamond Pt being tested for the oxygen reduction. The unique architecture of the SD-Pt may lead to enhanced catalytic activity and

the self-supported nature of the material to increase the stability. SD-Pt could be a very promising cathode material for the ORR as we can fabricate the material using a one-pot synthesis method which can be done to completion within an hour. The process is also performed at room temperature in mild conditions making it an attractive synthesis method compared to the fabrication of Pt on carbon supports.[162,163] As the template is applied as a thin film on the electrode surface, this method in theory could be applied to any conductive substrate which means SD-Pt could potentially be deposited directly onto commonly used electrodes for fuel cells.

5.2. Experimental

5.2.1. Electrode preparation

All electrochemical experiments were performed on a 3 mm diameter Au RDE electrode which were polished with 1 and 0.3 µm grade alumina prior to use. All electrochemical studies were carried out using a typical three-electrode setup consisting of a 3 mm Au RDE working electrode, SCE reference and Pt gauze counter electrode.

For the SAXS and TEM experiments Pt was electrodeposited onto phytantriol modified Au/DVD electrodes from Delkin Devices.

In order to prepare the Pt/C catalyst a 20 wt% Pt on Vulcan carbon XC72R (purchased from Johnson Matthey) was measured out and mixed with 0.9 mL DI water, 0.5 ML IPA and 0.5 mL Nafion (used as purchased from Aldrich) to create an ink. 20 µL of the ink was then placed on the 3 mm Au RDE tip and allowed to dry to create the Pt/C catalyst.

5.2.2. Solution recipes

The electrolyte used for the electrodeposition of Pt was hexachloroplatinic acid (HCPA) solution (8 wt% in water) purchased from Aldrich. For the surface area experiments N_2-saturated 0.5 M H_2SO_4 was prepared by bubbling the solution with N_2 for at least 20 minutes to removed dissolved oxygen.

For the oxygen reduction reaction experiments O_2-saturatd 0.1 M KOH was prepared by bubbling the solution with O_2 for at least 20 minutes prior to use. All solutions were prepared in ultrapure Milli-Q water (18.2 MΩ).

5.2.3. Electrodeposition and template removal

Electrodeposition experiments were performed using a three-electrode setup with a working electrode, a Pt-gauze counter electrode and SCE reference electrode. Electrodeposition was performed by stepping the potential from 0.4 V *vs* SCE to -0.245 V vs SCE for a set period of time using an Ivium VERTEX potentiostat controlled using IviumSoft.

To remove the lipid template after deposition, the working electrode was soaked in ethanol for a minimum of 30 minutes then left to dry in air.

5.2.4. TEM

In order to prepare TEM samples, a drop of ethanol was placed on the Pt thin films after template removal and the sample was scratched using a blade creating a suspension of Pt in the ethanol. A small amount of this suspension was then dropped onto a TEM grid and left to dry overnight to create the TEM sample.

5.2.5. SAXS

For SAXS experiments performed at I22 at the Diamond Light Source, the electrodes used were gold archival DVDs from Delkin Devices (Au/DVD). A camera length of 4.5 m was used with a beam energy of 12.4 keV for all experiments. For the in-situ experiments carried out on I22, a custom-made 3D printed cell (discussed in detail in later chapter) was placed with the sample perpendicular to the beam. The cell hosted a three-electrode set-up controlled by an Ivium Vertex potentiostat which was remotely accessed from outside the experimental hutch.

5.3. Pt Electrodeposition

Before the deposition of Pt through the phytantriol template a CV was taken on a bare 3 mm Au RDE electrode in HCPA. The CV in Figure 73 shows the sequential reduction of $PtCl_6^{4-}$ to deposited Pt in the form of two cathodic peaks at -0.1 and -0.28 V vs SCE corresponding to Equation 45 and Equation 46 respectively. The oxidation peaks at 0.5 and 0.9 V *vs* SCE are from the oxidation of Pt.

Equation 45
$$PtCl_6{}^{4-}{}_{(aq)} + 2e^- \rightarrow PtCl_4{}^{2-}{}_{(aq)} + 2Cl^-$$

Equation 46
$$PtCl_4{}^{2-}{}_{(aq)} + 2e^- \rightarrow Pt + 4Cl^-$$

Using the previous literature report of the optimised deposition potential of Pt through phytantriol a deposition potential of -0.245 V vs SCE was chosen.[17] From the CV we can see that at this potential Pt electrodeposition will occur.

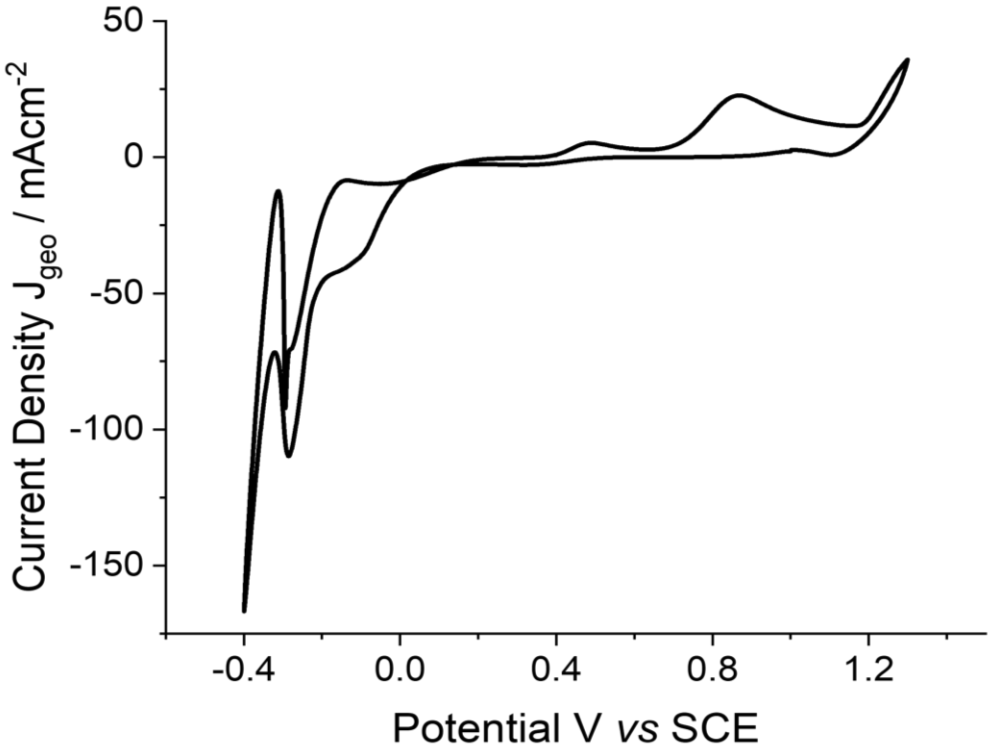

Figure 73 Cyclic voltammogram of in 8 wt% HCPA taken on a 3 mm Au electrode at a scan rate of 50 mV s^{-1} at room temperature.

Prior to deposition the working electrode was immersed in HCPA and left for at least 30 minutes in order to allow the template to hydrate forming the desired double diamond phase. Pt was then electrodeposited through the template by applying a potential of -0.245 V *vs* SCE and halted after 22 mC of charge had passed. This amount of charge, using Faraday's law (Equation 5) equates to 11.1 µg of Pt. The same procedure was then repeated in the absence of phytantriol to deposit untemplated Pt for comparison. The current time transients for the depositions are shown in Figure 74. The current response for the untemplated Pt electrodeposition is significantly higher than the templated Pt requiring much less time to pass 22 mC of charge. This is due to the template limiting the diffusion of Pt ions to the electrode surface as well as some of the electrode surface being blocked off. A lower steady current response is seen for the Pt deposited through phytantriol which is typical of a successful templated deposition.

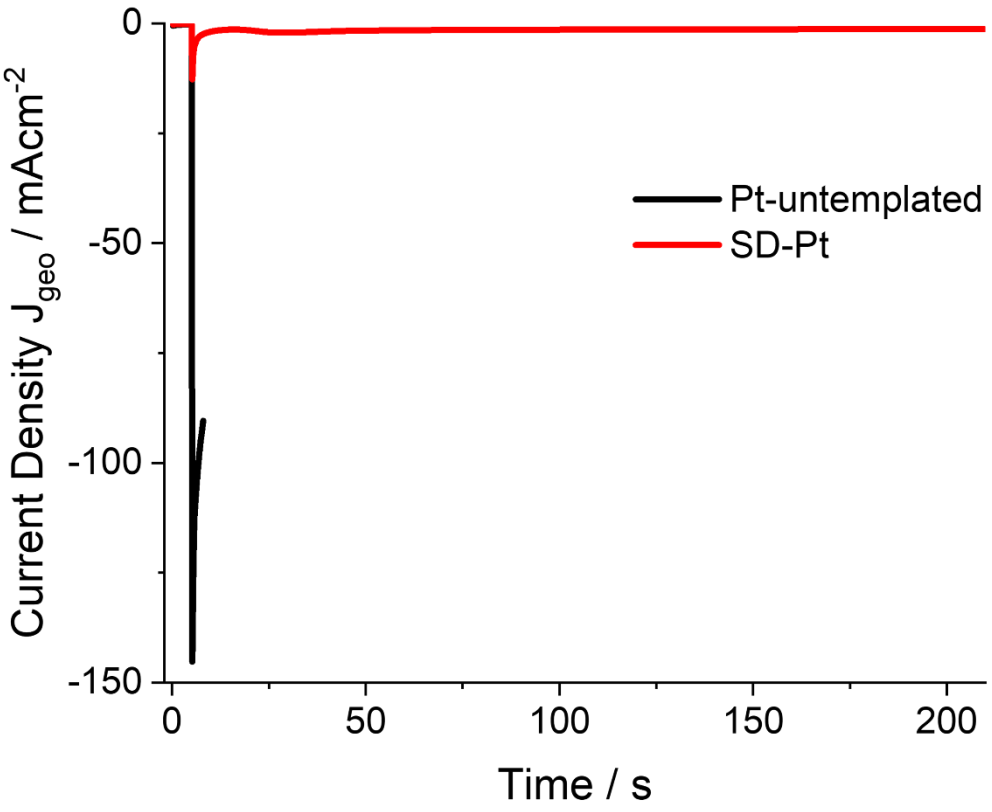

Figure 74 Current time transients for the electrodeposition of untemplated Pt and Pt deposited through phytantriol at a potential of -0.245 V vs SCE from a solution of 8 wt% hexachloroplatinic acid at room temperature. The electrodeposition was halted after 22 mC of charge had passed.

5.4. Surface area determination

Cyclic voltammetry in 0.5 M H_2SO_4 was used to determine the electrochemical active surface area (ECSA) of the Pt films. Prior to cyclic voltammetry the H_2SO_4 solution was purged with N_2 gas for at least 20 minutes to remove dissolved oxygen. Initially for all films the potential was swept between 0.1 and 1.3 V vs SCE at 300 mV s^{-1} until the CV stabilised (this usually occurred after around 20 cycles). The potential was then cycled between these values at a scan rate of 20 mV s^{-1} with the results shown in Figure 75. For all of the Pt films hydrogen adsorption is seen on the cathodic scan from 0.1 to -0.25 V vs SCE and hydrogen desorption can be seen on the anodic sweep from -0.25 to -0.85 V vs SCE. For the Pt films electrodeposited through the templates there are distinct hydrogen adsorption and desorption peaks which occur from different surface environments. These surface environments are from different facets of platinum 100 and 110 and are typically seen for nanostructured Pt.[164,165] On the anodic scan,

peaks are seen from the formation of surface oxides from 0.5 V *vs* SCE and on the cathodic scan a peak from the surface oxide stripping is seen between 0.9 and 0.15 V *vs* SCE.

The current densities for commercial Pt/C and SD-Pt are much larger than that of untemplated Pt which is typical for electrodes with a much larger surface area. To determine the surface area of the Pt films the reductive current for the hydrogen adsorption region was integrated and a widely accepted conversion factor of 210 µC cm^{-2} was used.[166,167] The specific surface area was then calculated by dividing the surface area by the mass of Pt. The results of these studies are shown in Table 14.

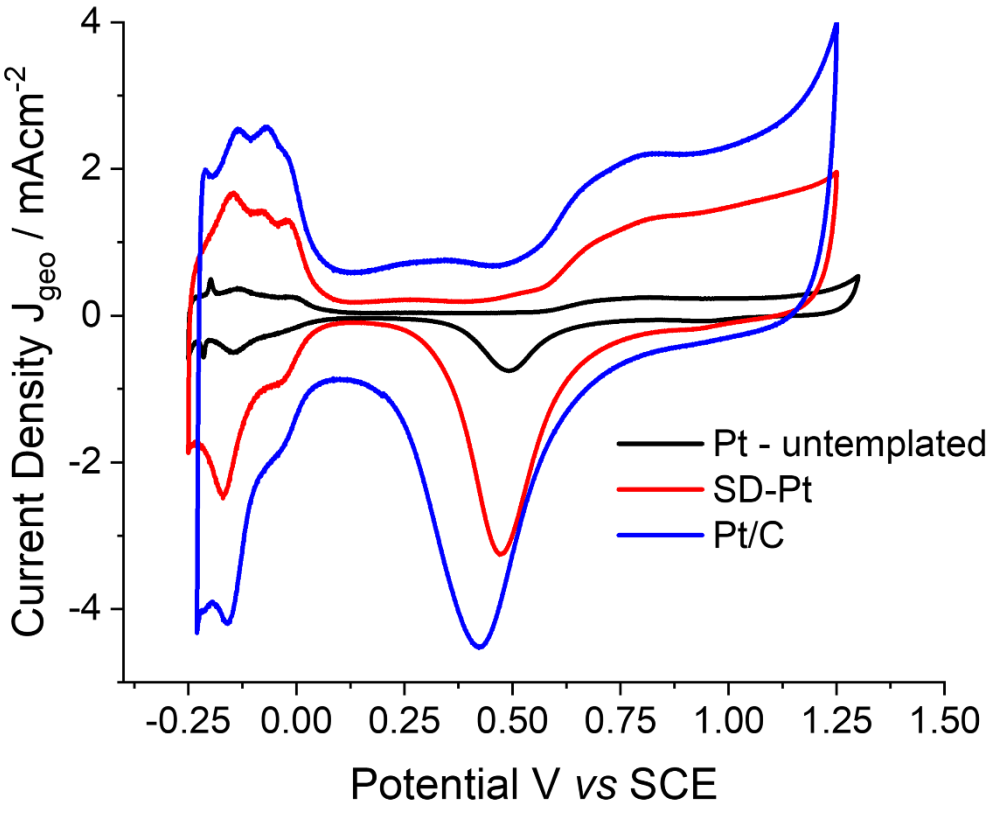

Figure 75 Cyclic voltammograms taken in 0.5 M H_2SO_4 recorded at 20 mV s^{-1} on untemplated Pt (black), single diamond Pt (red) and Pt/C commercial catalyst (blue). For all CVs the second scan is shown so the full oxygen stripping can be observed.

Table 14 A table summarises the surface area measurements of different Pt electrodes determined from cyclic voltammograms in 0.5 M H_2SO_4 at 20 mV s^{-1} at room temperature.

Sample	ECSA (cm^2)	RF	Specific surface area (m^2g^{-1})
Pt - untemplated	1.3 ± 0.6	18.88 ± 8.9	12.0 ± 5.6
SD-Pt	4.0 ± 0.5	55.9 ± 7.2	35.5 ± 4.6
Pt/C commercial	5.2 ± 0.5	73.4 ± 7.3	46.6 ± 4.7

There is an increase in specific surface area of around 3 times for the SD-Pt compared to the untemplated Pt. The specific surface area of 35.5 ± 4.6 $m^2\ g^{-1}$ for SD-Pt is consistent with literature reports for the material.[9,20] It was also determined that the commercial Pt/C catalyst had an even larger specific surface area of 46.6 ± 4.7 $m^2\ g^{-1}$, this is within the range of literature reports for Pt supported on carbon.[168–170]

5.5. SAXS

SAXS was performed on the Pt electrodeposited through phytantriol to obtain structural information on the material. SAXS was performed on I22 at the Diamond Light Source in transmission mode on Pt that was deposited onto a Au-DVD electrode through phytantriol at a potential of -0.245 V *vs* SCE for 5 minutes from an aqueous solution of HCPA. The resulting 1D integrated SAXS pattern is shown in Figure 76, in which Bragg peaks can be seen at *q* positions of 0.08 and 0.13 $Å^{-1}$, corresponding to the $\sqrt{3}$ and $\sqrt{8}$ peaks of the single diamond phase, confirming that the desired structure was achieved. The lattice parameter of the Pt was determined to be 136.0 ± 2.2 Å with the estimated nanowire and pore diameter to be 2.6 ± 0.2 nm and 6.4 ± 0.3 nm respectively. These values are consistent with previous literature reports of single diamond phase Pt produced via this method.[9,20]

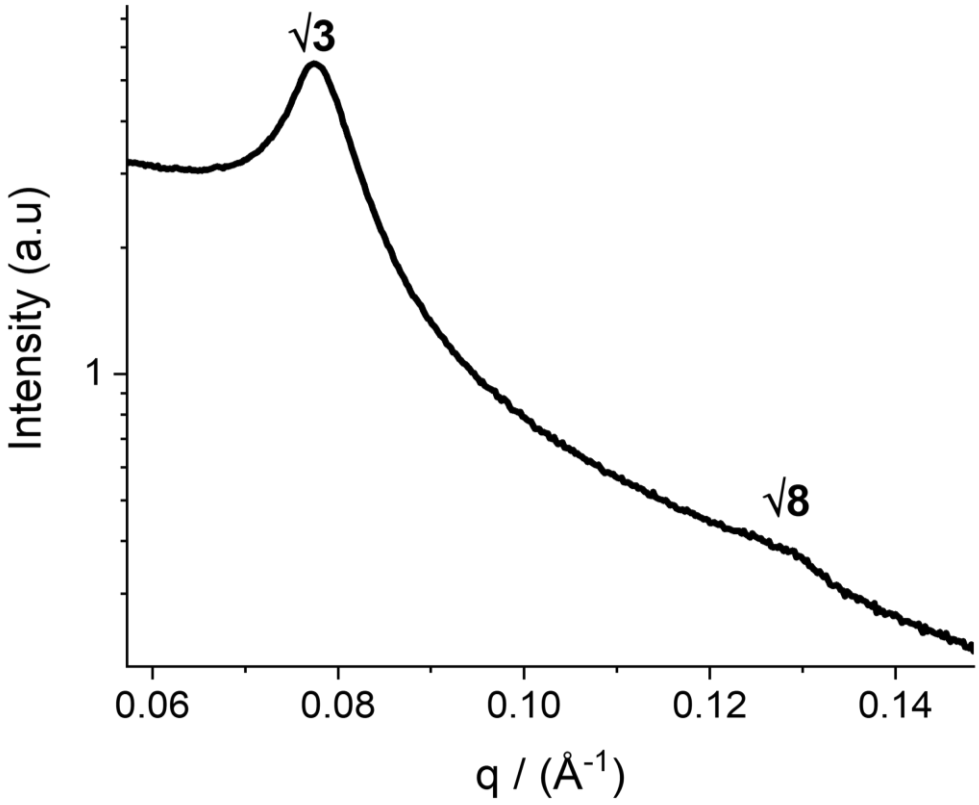

Figure 76 1D integrated SAXSS pattern of Pt electrodeposited through a phytantriol modified Au-DVD electrode at a potential of -0.245 V vs SCE for 5 minutes from a solution of aqueous 8 wt% hexachloroplatinic acid at room temperature.

5.6. TEM

To provide further evidence that the deposited Pt had the single diamond architecture TEM images were taken. The images shown at different magnifications in Figure 77 (a and b) reveal that the Pt did indeed exhibit a single diamond phase with the nanowire network being clearly visible in the images. The nanowire diameter was measured from these images and the average nanowire diameter was determined to be 2.5 ± 0.3 nm which matches the value determined by SAXS (2.6 ± 0.2 nm). The pore widths determined from the TEM images was 5.6 ± 0.8 nm which is also in line with that determined by SAXS (6.4 ± 0.3 nm) within error.

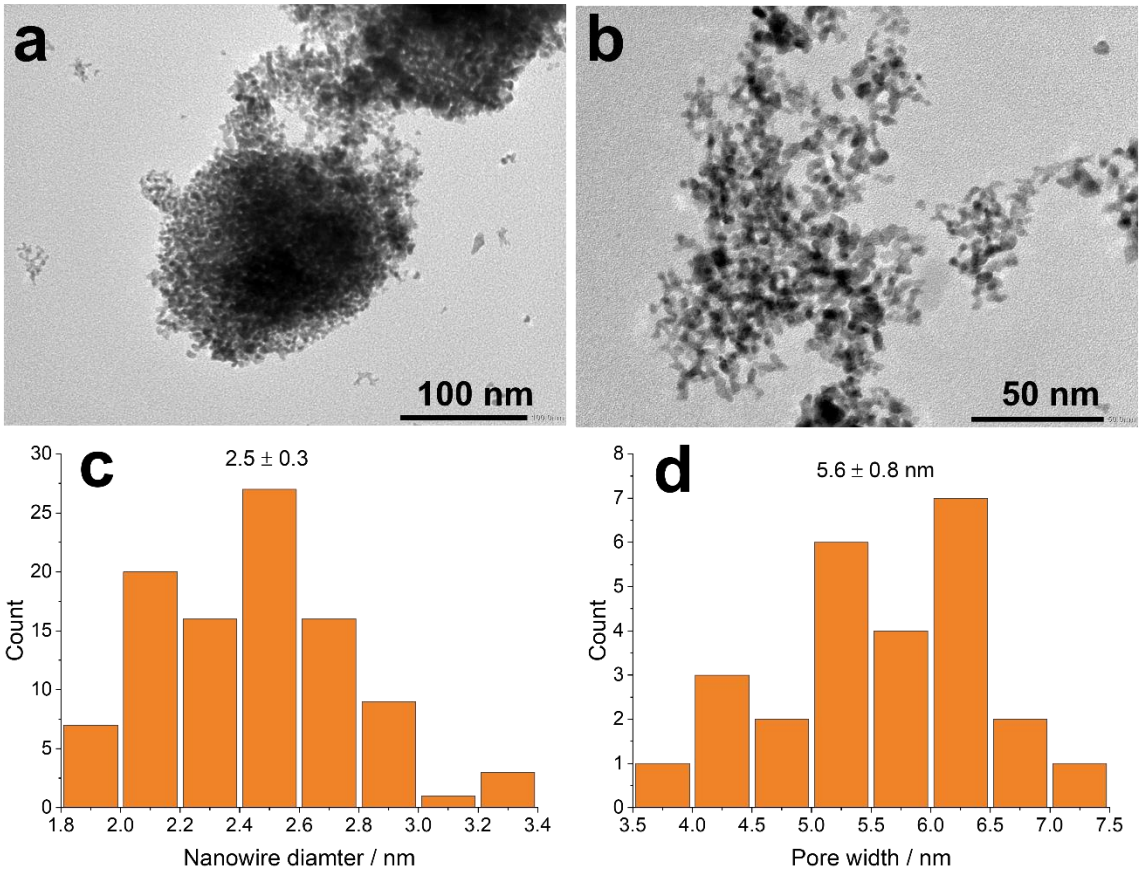

Figure 77 TEM images of Pt electrodeposited through phytantriol at -0.245 V vs SCE for 5 minutes from a solution of 8 wt% hexachloroplatinic acid at room temperature (a & b). The associated nanowire (c) and pore (d) diameter distributions.

5.7. Oxygen reduction reaction

To test the catalytic performance of the SD-Pt compared to commercial Pt/C for the oxygen reduction reaction, linear sweep voltammetry (LSV) was conducted for each material using an Autolab RDE 2. LSV was taken in O_2-saturated 0.1 M KOH at a scan rate of 10 mV s^{-1} with a rotation rate of 1600 rpm. The results from these experiments are shown in Figure 78 which reveal that SD-Pt and Pt/C have a significantly lower onset potential compared to untemplated Pt. This suggests that the activation energy for the ORR is much lower for the templated Pt. The onset potential for SD-Pt was 0.98 V *vs* RHE which is comparable to the onset of Pt/C (1.00 V *vs* RHE). There is also a positive shift in the half wave potential, $E_{1/2}$, of 20.7 mV for the SD-Pt compared to Pt/C when taken at a current density of 3.0 mA cm^{-2}. The half-wave potential represents the potential at which the current reaches half of the maximum value during oxygen reduction and it is a critical parameter used to assess the performance of electrocatalysts for the ORR. This signifies that SD-Pt has enhanced catalytic

activity compared to the commercial catalyst and a lower overpotential is needed in order to provide the same amount of current density. A positive shift in half-wave potential has also been reported in the literature for a similar material: Kibsgaard *et al.* reported a positive shift for double gyroid Pt compared to Pt/C. [171] One disadvantage of SD-Pt is that it exhibited a lower limiting current density when compared to Pt/C, however when we normalize the current by the electroactive surface area of the Pt electrodes, Figure 78 (b), the limiting current density for SD-Pt is higher. This indicates that the SD-Pt is more active compared to commercial Pt/C and the limiting current density was only higher in Figure 78 (a) due to Pt/C having a larger surface area. Kibsgaard *et al.* also reported superior activity for their double gyroid Pt structure, and it was determined that this increase in activity was due to the Pt having a smaller fraction of undercoordinated surface sites compared to Pt/C.[171] This may also be the case for single diamond Pt and could be the reason for the increased activity.

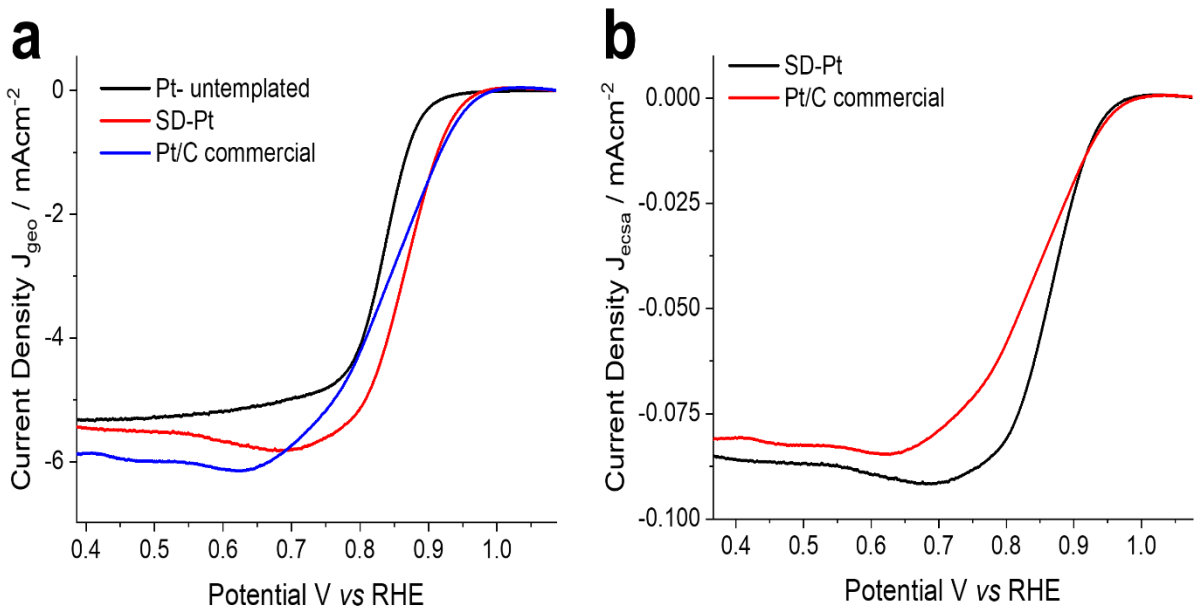

Figure 78 Linear sweep voltammograms of untemplated Pt, SD-Pt and Pt/C taken in 0.1 M KOH at room temperature at a scan rate of 10 mV s^{-1} and a rotation speed of 1600 rpm, normalized by geometric surface area (a) and electroactive surface area (b).

Table 15 compares the performance of SD-Pt against recent catalysts reported in the literature. It is apparent that SD-Pt has a similar performance with respect to the onset potential and half-wave potential when compared to other catalysts, however the advantage is that SD-Pt is prepared using a simple one-pot synthesis method at room temperature.

Table 15 A Table highlighting the performance of recent catalysts for the oxygen reduction reaction with values for the onset potential and half-wave potential.

Catalyst	Electrolyte	E_{onset} (V *vs* RHE)	$E_{1/2}$ (V *vs* RHE)	Reference
SD-Pt	0.1 M KOH	0.98	0.87	This work
Pt/C	0.1 M KOH	1.00	0.84	This work
Pt_2Pd_1	0.1 M KOH	0.97	0.89	[172]
Fe_3Ptt/N@C	0.1 M KOH	0.98	0.88	[173]
$Pt_{37}Cu_{56}Au_7$	0.1 M KOH	-	0.91	[174]
Pd_3Au/C	0.1 M KOH	0.99	0.87	[175]
SA-PtCoF	1 M KOH	0.95	0.88	[176]
IrMn/Fe3Mo3C	0.1 M KOH	1.03	0.89	[177]
CoSMe-0.5–800	0.1 M NaOH	0.95	0.85	[178]
CoS NWs@NSC-2	0.1 M KOH	0.93	0.84	[179]
ZrN	0.1 M KOH	0.93	0.80	[180]
NDC1000	0.1 M KOH	0.96	0.86	[181]
NC-Co SA	1 M KOH	1.00	0.87	[182]

To gain further insight into the performance of SD-Pt for the ORR in alkali conditions, Koutecky-Levich (K-L) analysis was performed on the Pt films to determine which pathway the ORR takes. Using a rotating disc electrode, linear sweep voltammetry was performed on each Pt film at rotation rates of 400 to 3600 rpm at a scan rate of 10 mV s^{-1}. The results from these experiments are shown in Figure 79. The relationship between current density and rotation rate is given by Equation 47 where J_{geo} is the measured current density with respect to the geometric area, J_k is the kinetic current density, ω is the rotation speed in rpm and B is the reciprocal of the slope.

Equation 47

$$\frac{1}{J_{geo}} = \frac{1}{J_k} + \frac{1}{B\omega^{1/2}}$$

B is given by Equation 48 where n is the number of electrons transferred, F is Faraday's constant (96485 C mol^{-1}), D_{O2} is the diffusion coefficient of O_2 in 0.1 M KOH (1.9×10^{-5} cm^2 s^{-1}), v is the kinetic viscosity (0.01 cm^2 s^{-1}), and C_{O_2} is the concentration of O_2 in 0.1 M KOH (1.2×10^{-3} mol L^{-1}). The constant of 0.2 is adopted when the rotating speed is in rpm.[183,184]

Equation 48

$$B = 0.2nFv^{-1/6}C_{O_2}D_{O_2}^{2/3}$$

The slope of the K-L plot is then used with Equation 48 to determine the number of electrons transferred and therefore determine the reaction pathway of the ORR. The calculated number of electrons transferred per oxygen molecule was 3.7 ± 0.1, 3.6 ± 0.1 and 4.2 ± 0.1 for

untemplated Pt, SD-Pt and Pt/C respectively. As the number of electrons transferred during the ORR was around 4 for all of the Pt samples, the reaction pathway occurs via the direct four-electron transfer pathway given in Equation 42. This is the desired pathway which has been showed to be more efficient and have better kinetics.

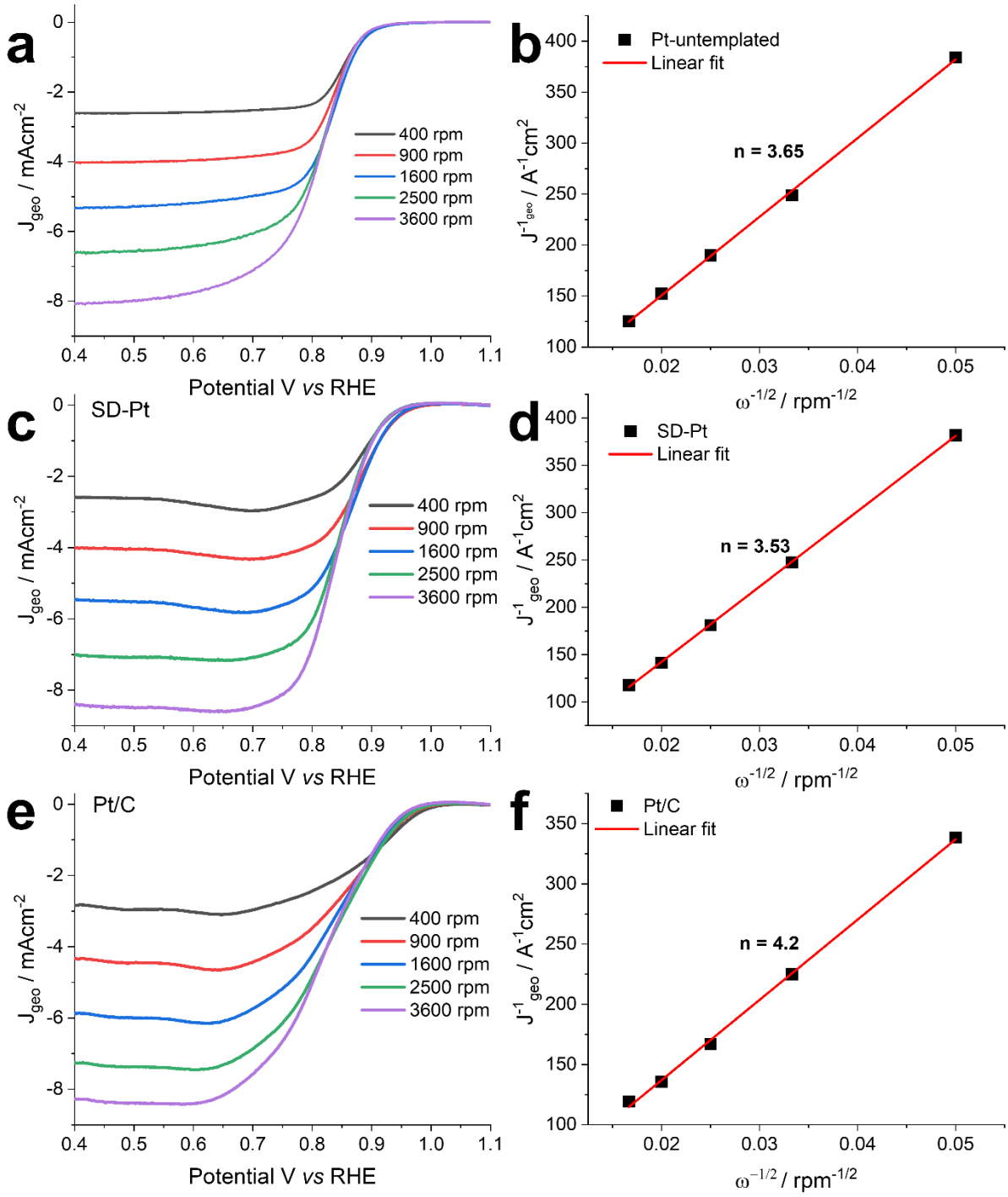

Figure 79 Linear sweep voltammograms taken at different rotation rates in O_2-saturated 0.1 M KOH at a scan rate of 10 mV s^{-1} along with the associated Koutecky-Levich plot of untemplated Pt (a & b), SD-Pt (c & d) and Pt/C (e & f).

5.8. Stability

The stability of the as prepared SD-Pt compared to the commercial Pt/C catalyst was tested via potential cycling. The potential was cycled from 0.1 to -0.5 V *vs* SCE at a scan rate of 2 V s^{-1} in O_2-saturated 0.1 M KOH for 10000 cycles. Linear sweep voltammetry was used after cycles 1000, 5000 and 10000 in fresh O_2-saturated 0.1 M KOH at a scan rate of 10 mV s^{-1} to assess how the cycling affected the performance of the catalysts. The results from the durability tests are shown in Figure 80, which reveal that after 10000 cycles SD-Pt only had a drop of 20.7 mV for the half-wave potential, whereas Pt/C, had a 41.6 mV drop. It was also noted that there was a significant drop in the limiting current density for Pt/C which dropped by 1.38 mA cm^{-2} measured at 0.5 V *vs* RHE whereas only a drop of 0.33 mA cm^{-2} was seen for SD-Pt. These results indicate that SD-Pt is significantly more stable than commercial Pt/C tested under the same conditions. A reason for the stability could be that the single diamond structure is a self-supporting 3D network on nanowires, so degradation of the support material is not present. Kibsgaard *et al.*[171] also reported that upon durability tests in the form of potential cycling, Pt/C had a much larger drop in the half-wave potential compared to double gyroid Pt.

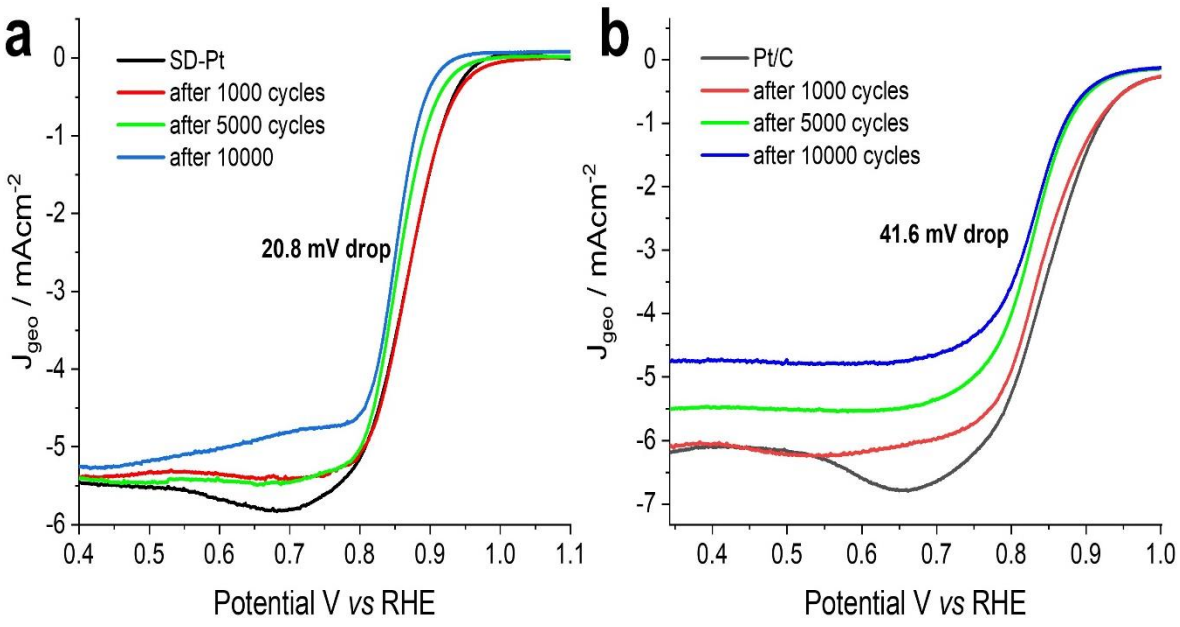

Figure 80 Linear sweep voltammograms of SD-Pt (a) and Pt/C (b) in O_2-saturated 0.1 M KOH at a scan rate of 10 mV $s^{-1}$and 1600 rpm before and after potential cycling for 1000, 5000 and 10000 cycles.

Surface area studies were also performed on the catalysts during the durability tests. In between cycles, cyclic voltammetry was performed in N_2-saturated 0.5 M H_2SO_4 at 20 mV s^{-1} in order to calculate the loss in surface area after potential cycling. The CVs are shown in Figure 81 (a and b) that were taken after cycles 1000, 5000 and 10000. We can see a clear loss in current density in the hydrogen adsorption region with increasing number of cycling, meaning we have a loss of surface area for both materials. Figure 81 (c) shows the relative loss in active surface area with number of cycles for SD-Pt and Pt/C. After 1000 cycles there is a significant drop in surface area for Pt/C of around 40 % whereas SD-Pt only had a loss 20 % showing better durability. However, after 5000 cycles both catalysts showed a similar decrease in surface area of around 55 %. After the full 10000 cycles SD-Pt had a 62 % loss of surface area whereas Pt/C had a loss of 65 %. Both catalysts showed a similar loss off surface area during the durability tests however SD-Pt showed higher catalytic activity at the end of the durability tests showing that is has superior performance.

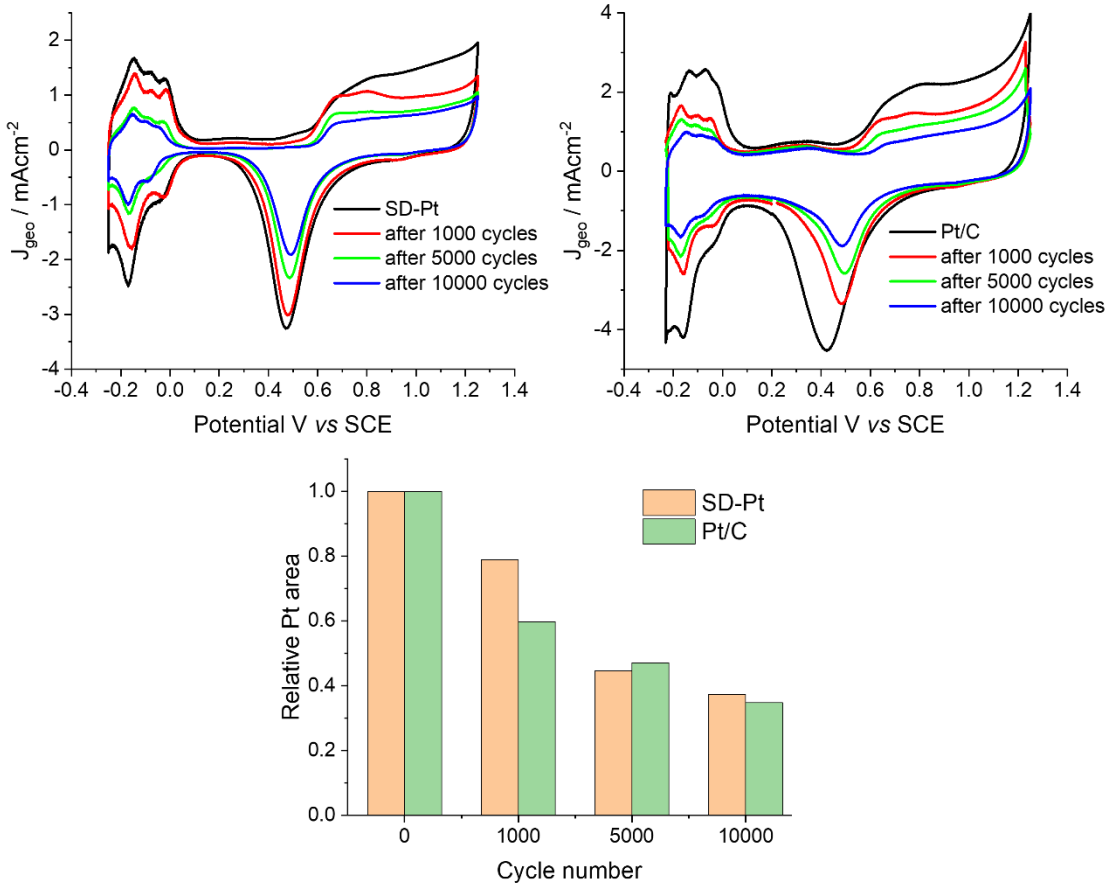

Figure 81 Comparison of the electroactive surface area degradation of SD-Pt (a) and Pt/C (b) with potential cycling taken by cyclic voltammetry in N_2-saturated 0.5 M H_2SO_4 at 20 mV s^{-1}. Relative loss in Pt surface area with number of cycles measured by hydrogen underpotential deposition (c).

5.9. Conclusions

Overall, we have demonstrated that SD-Pt is an attractive catalyst for the ORR reaction under alkali conditions. SD-Pt showed enhanced performance when compared to commercial Pt/C when tested using linear sweep voltammetry in 0.1 M KOH, by exhibiting a larger limiting current density when normalised by electroactive surface area and having a more positive half-wave potential. Using Koutecky-Levich analysis we determined that the prominent reaction pathway for the ORR was the desired four-electron direct pathway. Durability tests revealed that SD-Pt has better stability than Pt/C having a lower drop in half-wave potential and surface area after 10000 cycles.

As SD-Pt is fabricated using a one-pot synthesis method in mild conditions and room temperature this method of liquid crystal templating of Pt with phytantriol may provide an attractive means of producing high performing catalyst material for fuel cell applications.

5.10. Future work

I believe there are a few directions in which this work could go. Firstly, more testing of SD-Pt for the ORR in alkali conditions should be performed, with testing in actual fuel cells. It would be great to benchmark the performance of the material in operating conditions. Research into depositing SD-Pt onto complex 3D electrodes should be undertaken which makes the integration of the material into functional fuel cells and other devices more tangible. The performance of SD-Pt could also be tested in acidic conditions, if the results are good, it would showcase the versatility of this method at fabricating high performance catalyst materials. Another direction this work could go in that I believe would be most beneficial is the fabrication of single diamond Pt-alloy structures using the phytantriol template. It has been widely reported in literature that Pt-alloys exhibit enhanced catalytic activity for the ORR and they also benefit from increased stability. Some alloys of interest for this work could be derivates of Pt with Cu, Au, Fe, Zn, Co, W and Ni as these have been seen to have great performance in the literature.[173–175]

The next chapter presents a study on the deposition of Pt using pulse electrodeposition within the double diamond phase of the phytantriol/Brij-56 system, assessed through detailed small-angle X-ray scattering investigations. The objective of this research was to evaluate the effectiveness of pulse electrodeposition compared to the conventional potential hold method.

6. Pulse electrodeposition of Pt through phytantriol/Brij-56

6.1. Introduction

As mentioned in the previous chapters Akbar *et al.*[20] utilised the addition of co-surfactant Brij-56 in the double diamond phase of phytantriol to produce a soft-template with size control. The lattice parameter of the liquid crystal template can be altered by controlling the amount of the Brij-56 added into the liquid crystal. However, it was reported that as the amount of Brij-56 in the template increased the resulting Pt nanostructure became less homogenous which was measured by broadening of the SAXS peaks. It was also reported that the relationship of the Pt lattice parameter being double that of the template's lattice parameter, $a(Pt) = 2 \times a(Q^{II}_{D})$, was not maintained when using the swollen template. The reason for this discrepancy is currently not known. One hypothesis is that the templates with larger amounts of Brij-56 are 'softer' and may shrink during the electrodeposition process. Another hypothesis is that there is localized heating during the electrodeposition process which causes a decrease in lattice parameter of phytantriol. A decrease in lattice parameter was reported when heating phytantriol in excess water by Barauskas *et al*.[8] This inhomogeneity of Pt produced via electrodeposition through phytantriol/Brij-56 was also reported by Samuel Richardson.[18] Richardson *et al.*[185] used out of plane SAXS to show that Pt deposited within the first few microns of the template are orientated with the (111) plane parallel to the substrate. This orientation occurs as the template, whilst being polydomain overall, is uniaxially aligned with the (111) plane parallel to the surface for the first few microns. Richardson reported that Pt electrodeposited through the phytantriol/Brij-56 templates exhibited this orientation in the (111) plane. However, this orientation was not seen when the weight % of Brij-56 in the template was above 15 % and the material was too disordered. This method could not confirm that the Pt formed the single diamond phase.[18] The increasing inhomogeneity of single diamond Pt with increasing Brij-56 in the template is an issue as inhomogeneity can create multiple problems. It can lead to performance variability in the materials physical and chemical properties making it challenging to achieve the desired characteristics consistently.

Structural integrity could also be an issue as stress concentrations and defects could lead to degradation. The aim in this work is to employ pulse electrodeposition in order to produce more uniform Pt structures from the phytantriol/Brij-56 templates.

There are various reports in the literature in which pulse electrodeposition has been advantageous over typical electrodeposition methods especially when dealing with templated deposition.[186–195] In hard templates such as porous aluminium oxide (PAO), varying parameters such as potential, current density, time between pulses and shape of the pulses can influence the structure, composition and crystallinity of the deposited material.[186,196–198] Azevedo *et al.*[197] used pulse electrodeposition to fabricate ultra-long Fe nanowires that fully fill alumina templates and reported that the rest time of the pulse was a significant parameter that affected the homogeneity of the nanowires. Dobrev *et al.*[199] used reversible pulse electrodeposition to grow copper single crystals in the pores of polymer ion-track membranes. The reversible pulse electrodeposition method consisted of applying a negative current density in order to deposit Cu then applying a positive current in order to oxidise (strip) Cu. They reported that this method led to more monocrystalline Cu as during the positive pulse some of the previously deposited material dissolved back into solution and this predominantly happens at defect sites, which then lead to a more monocrystalline material after subsequential deposition pules. Yang *et al.*[189,194] explored the effect of using pulse electrodeposition as opposed to typical electrodeposition of lithium and how this affected the materials cycling efficiencies for battery application. The lithium deposited using direct current resulted in needle-like structures which had larger surface areas, which lead to lower cycling efficiency, whereas lithium produced via a pulsed method lead to bigger particles and a higher cycling efficiency. Hessem *et al.*[195] explored direct electrodeposition compared to pulsed for SnO_2 thin films for application in Li-ion batteries. The result of the investigation is that SnO_2 fabricated by pulse deposition led to thin films which had higher porosity, finer morphology and smaller crystallite size which led to an enhanced performance for their use in Li-ion batteries when compared to SnO_2 produced from direct electrodeposition. It is clear that pulse electrodeposition can be a powerful tool for producing deposited material within templates.

6.2. SAXS of the phytantriol/Brij-56 system in HCPA

Lipid samples of phytantriol with increasing Brij-56 content of 7.5 and 20 wt% were prepared as thin films on a Au-DVD substrate, which was placed in an electrochemical cell filled with excess HCPA solution for SAXS analysis on the I22 beamline at the Diamond Light Source. The SAXS patterns, Figure 82, confirmed that all lipid mixtures formed the expected double diamond phase. The data extracted from the SAXS is reported in Table 16 and agrees with literature values previously reported by Akbar *et al*.[20] There is an increase in the lattice parameter with increasing Brij-56 content due to curvature modulation and the water channel width increased from 2.7 nm with no addition of Brij-56 to 7.2 nm when 20 % Brij-56 was present.

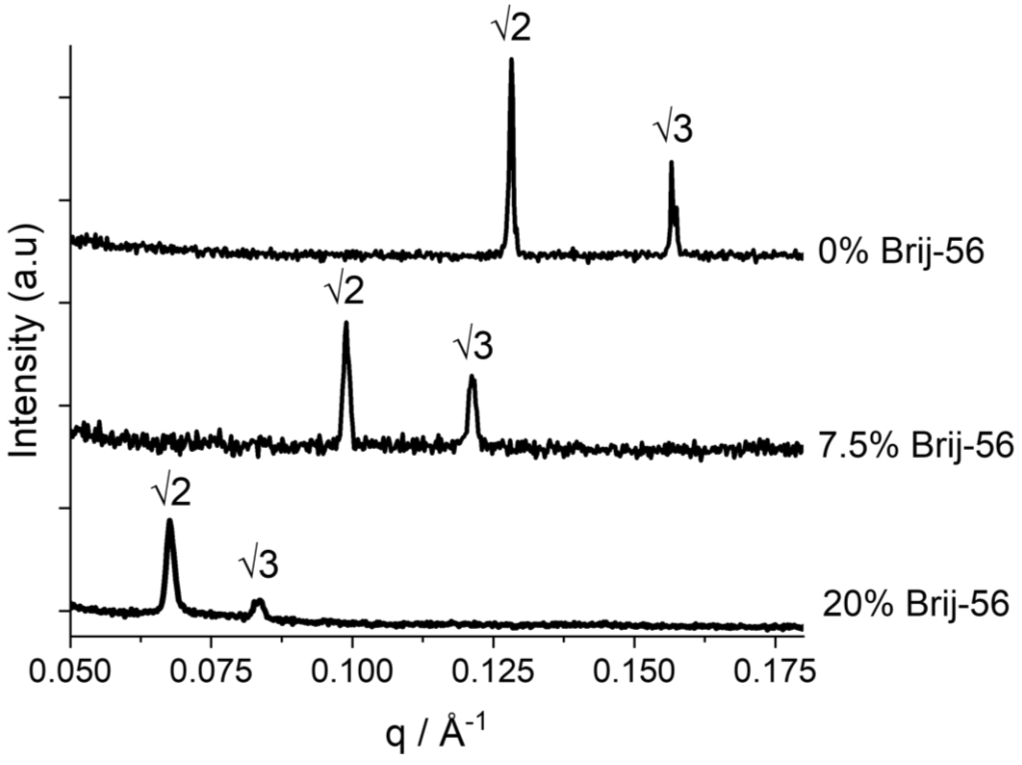

Figure 82 1D integrated SAXS patterns of phytantriol with differing amounts of Brij-56 additive in excess HCPA solution

Table 16 A table reporting the key results from SAXS of phytantriol and Brij-56 mixtures in excess HCPA conditions.

Template	phase	Lattice parameter ($Å^{-1}$)	Water channel width (nm)
Phytantriol/0% Brij-56	Double diamond	69.2 ± 0.2	2.7 ± 0.2
Phytantriol/7.5% Brij-56	Double diamond	91..6 ± 0.3	4.4 ± 0.3
Phytantriol/20%Brij-56	Double diamond	127.0 ± 0.3	7.2 ± 0.3

6.3. Potential hold deposition of Pt through phytantriol/Brij-56

Pt was electrodeposited through the templates onto a 2 mm Au-disc electrode by applying a potential of -0.245 V *vs* SCE until 22 mC of charge had passed. Figure 83 (a) Below shows the current time transients for the electrodepositions. For all templates the current density is significantly lower than the non-templated deposition. This is due to the template covering the electrode and limiting the diffusion of Pt ions to the electrode surface. The current density also increases with the amount of Brij-56. This is due to larger water channels within the template allowing for more diffusion of platinum ions to the electrode surface.

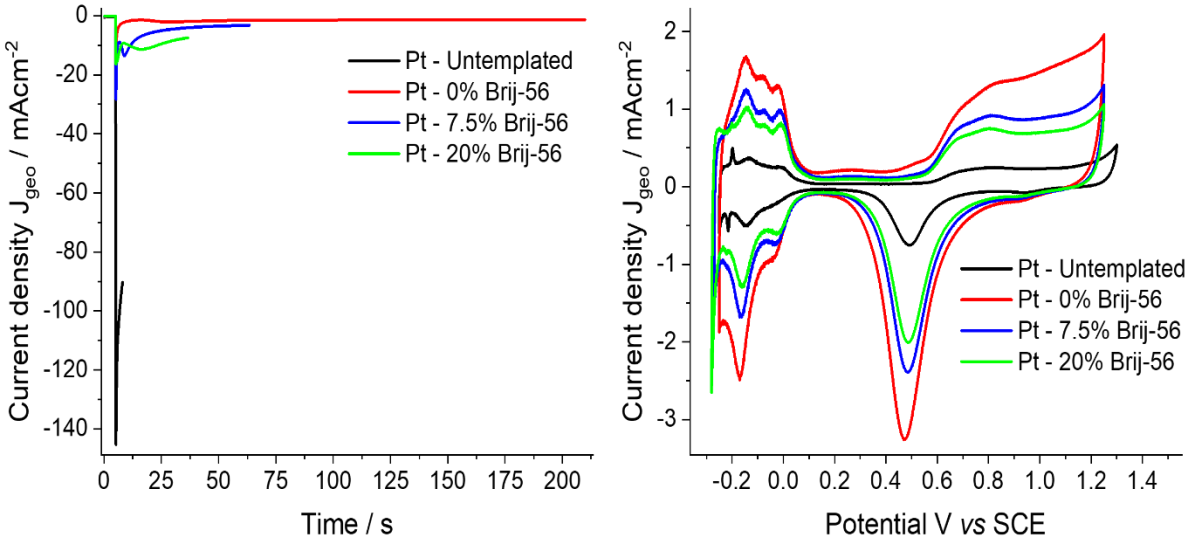

Figure 83 Current time transients of Pt electrodeposited through phytantriol/Brij-56 templates at a potential of -0.245 V vs SCE on a 2 mm Au electrode from a solution of 8 wt% hexachloroplatinic acid, with the depostion being halted once 22 mC of charge had passed. (a) Cyclic voltammograms of the Pt films in 0.5 M H_2SO_4 at a scan rate of 20 mV s^{-1}.

In order to determine the electrochemical active surface area of the deposited Pt, CVs were taken in 0.5 M H_2SO_4 which are shown in Figure 83 (b). It can be seen that in all cases of Pt produced by templating the current density of the hydrogen adsorption region is much larger than the Pt produced in the absence of a template. The results from the CVs are listed in Table 17 which show that the specific surface area, determined by hydrogen underpotential deposition, of Pt decreases with increasing Brij-56 content in the template. The surface areas appear to follow an inverse relationship with lattice parameter (reported in Table 18) following a typical area/volume scaling relationship. In the literature it was reported the surface area did not follow this simple scaling relationship with lattice parameter as the Pt occupies larger proportions of the unit cell with increasing Brij-56 content leading to a lower surface area than expected from the simple scaling relationship.[20]

Template	ECSA (cm^2)	RF	Specific surface area (m^2g^{-1})
No template	0.8 ± 0.2	11.2 ± 1.8	7.2 ± 1.2
Phytantriol/0% Brij-56	3.8 ± 0.5	53.3 ± 6.4	34.0 ± 4.1
Phytantriol/7.5% Brij-56	2.9 ± 0.3	41.1 ± 4.0	26.2 ± 2.5
Phytantriol/20%Brij-56	2.5 ± 0.2	34.9 ± 2.1	22.2 ± 1.3

Table 17 A table listing the surface area, specific surface area and roughness factor of electrodeposited Pt calculated from cyclic voltammetry studies.

6.4. SAXS of mesoporous Pt produced via potential hold

SAXS was performed on the resulting Pt films after template removal in ethanol in order to analyse their structure. The 1D integrated SAXS patterns are shown in Figure 84 with the results extracted from these reported in Table 18. As reported in the literature the peak position is shifted to lower *q* with increasing Brij-56 content, which corresponds to a larger lattice parameter. For Pt produced in the swollen templates no second peak is present, so it cannot be said definitively that the single diamond phase has been successfully made. However, a Bragg peak in the expected *q* position is a good indication that the material has formed the single diamond phase. As we increase the amount of Brij-56 in the template, the resulting Bragg peaks from the Pt become broader, which indicates there is more disorder on

the lattice parameter of the material. There is also a deviation from the expected lattice parameter of the Pt, as we expect the lattice parameter of the deposit to be double that of the lattice parameter of the template. With increasing Brij-56 content the deviation from this relationship increased. This was also reported by Akbar *et al*. [20]

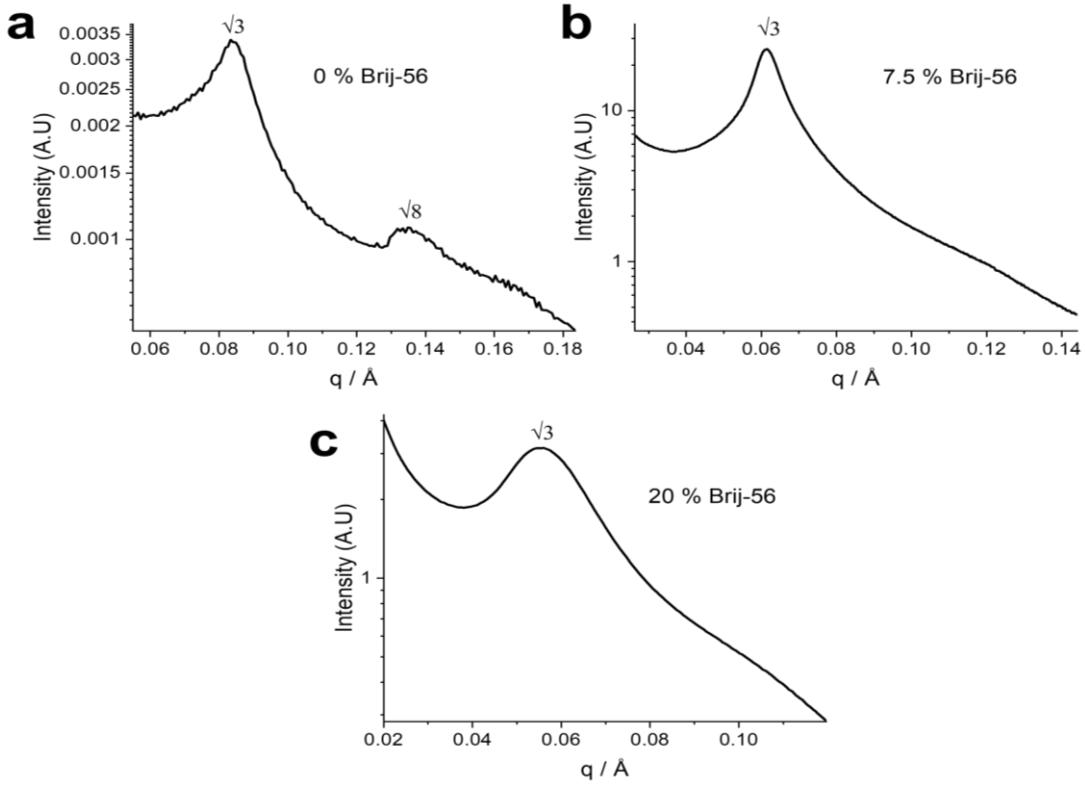

Figure 84 1D integrated SAXS patterns of Pt electrodeposited through phytantriol (a), phytantriol/Brij-56 (7.5%) (c) and phytantriol/Brij-56 (20%) (c) from a solution of 8 wt% hexachloroplatinic acid with a deposition potential of -0.245 V vs SCE.

Table 18 A table reporting the key results from the SAXS of Pt electrodeposited by applying a potential of -0.245 V vs SCE through phytantriol and Brij-56 mixtures.

Template	phase	Lattice parameter Pt ($Å^{-1}$)	Nanowire diameter (nm)	Pore width (nm)
Phytantriol/0% Brij-56	Single diamond	130.7 ± 1.9	2.4 ± 0.1	6.9 ± 0.1
Phytantriol/7.5% Brij-56	Single diamond	177.4 ± 1.9	4.2 ± 0.1	8.3 ± 0.1
Phytantriol/20%Brij-56	Single diamond	197.1 ± 2.8	5.0 ± 0.1	9.0 ± 0.1

6.5. Pulse electrodeposition of Pt through phytantriol/Brij-56

Pulse electrodeposition was performed by applying a potential in which no deposition occurs, named 'off pulse', followed by applying a potential in which the deposition of Pt occurs, named 'on pulse', for a chosen amount of time and repeating this for a pre-determined number of cycles. The chosen pulse profiles for the initial study were to apply an "on" pulse of -0.245 V *vs* SCE for 0.1 s and to vary the time of the "off" pulse from 0.2 to 0.3 s at 0.4 V *vs* SCE for 3000 cycles. Figure 85 shows the current-time profile for the first 3 cycles of Pt electrodeposition with an on time of 0.1 s and an off time of 0.3 s through the different phytantriol/Brij-56 templates. During the off pulse there is an anodic spike due to charging of the double layer, which then decays towards zero current density whereas after the on pulse there is a cathodic spike in current density which then decays to a current density that is attributed to the electrodeposition of Pt. As with the electrodeposition via potential hold the current density of the deposition increases with increasing Brij-56 content in the template due to the larger water channels.

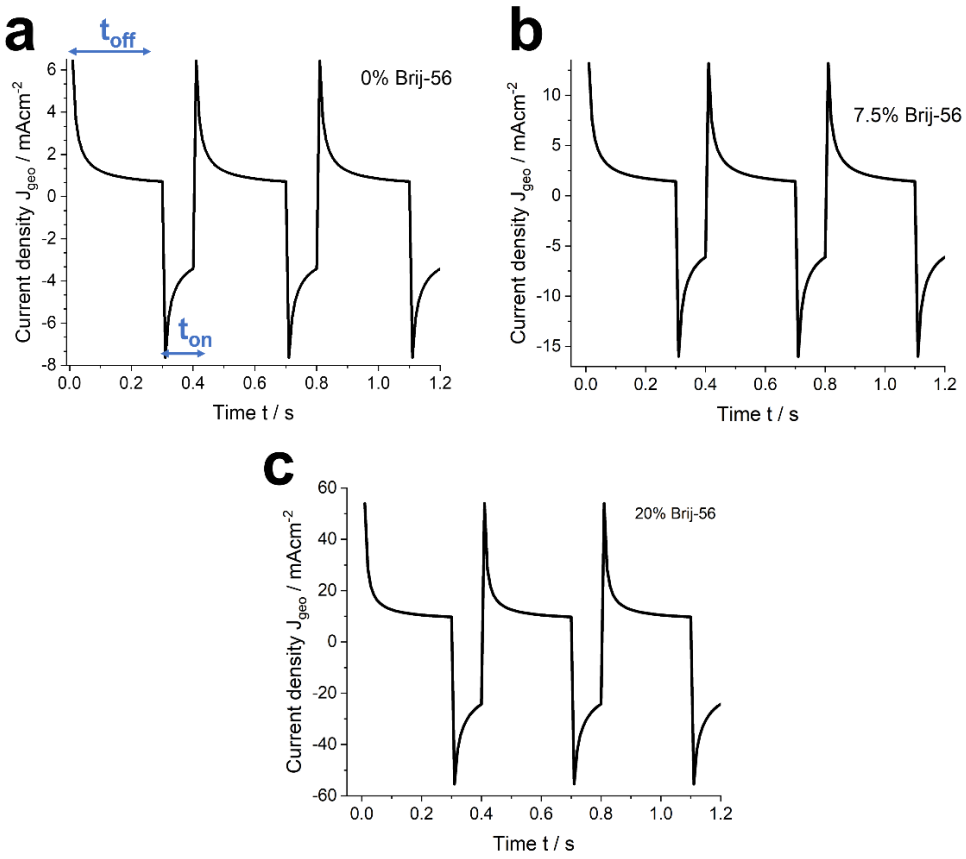

Figure 85 Current-time transient of the first 3 cycles of Pt electrodeposited onto a phytantriol modified Au-DVD electrode with a 0.1 s on pulse of -0.245 V vs SCE and an off pulse of 0.3 s at 0.4 V vs SCE from an 8 wt% HCPA solution.

6.6. SAXS of Pt produced via pulse electrodeposition

In order to determine how varying the off-pulse time would affect the resulting Pt deposited through the phytantriol/Brij-56 templates, a series of films were produced by varying the time for the off pulse from 0.2 and 0.3 seconds and analysed by SAXS, after template removal in ethanol. Figure 86(a) reveals that for Pt grown through phytantriol three Bragg peaks can be seen for all deposition methods however when the Pt was grown using pulse electrodeposition with 0.1 s on and 0.3 s off the third (311) peak is more resolved and has a smaller full width half maximum (FWHM) compared to the other (311) peaks. This tells us that the Pt grown with these conditions has a more ordered single diamond phase as we have better resolved Bragg peaks and the smaller FWHM shows that the lattice parameter is more homogenous in the sample. This is even more apparent when looking at the SAXS pattern for Pt electrodeposited through the swollen phytantriol/Brij-56(20 wt%) template in Figure 86 (b). The first Bragg peak for single diamond Pt is much sharper exhibiting a smaller FWHM for the pulse electrodeposited samples compared to the potential hold. For the Pt grown via

potential hold no second Bragg peak is observed which means that you cannot use SAXS alone to prove that the resulting structure is in fact single diamond phase. The Pt grown with pulse conditions 0.1 s on and 0.3 s off exhibits a sharper second Bragg peak and a third Bragg peak can be seen as a shoulder. It can also be noted that the peak positions for the pulsed Pt through phytantriol/Brij-56 (20 wt%) are at lower *q* than that from potential hold which means the material has a larger lattice parameter. Previously it had been reported that Pt grown via potential hold through the swollen template had a lattice parameter smaller than that expected not following the trend of a(Pt) = 2 x a(Q^{II}_{D}). Which means Pt grown using pulse had a closer lattice parameter to the expected value. This could mean that pulse electrodeposition removes the template shrinkage effect which had been previously reported. These results are a strong indication that pulse electrodeposition is advantageous over potential hold especially through the swollen template. As Pt produced from pulse deposition showed more than one Bragg peaks we can use SAXS to confirm the material has a single diamond phase as we cannot do this for Pt produced via potential hold.

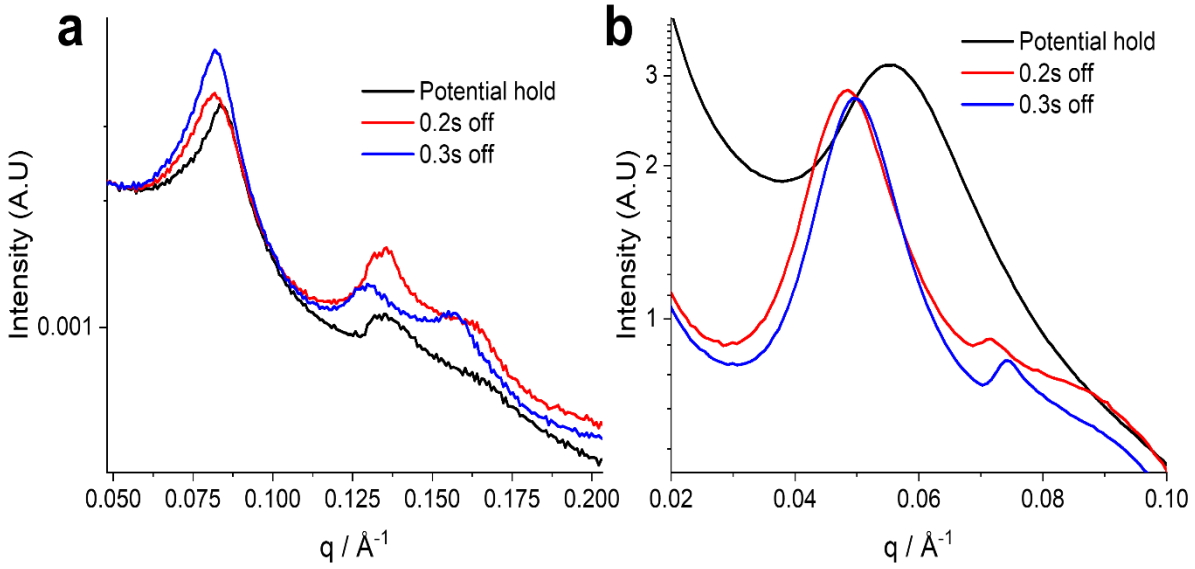

Figure 86 1D integrated SAXS patterns of Pt electrodeposited through phytantriol(a) and phytantriol/Brij-56 (20 wt%) (b) grown via potential hold and a series of pulsing conditions from a solution of 8 wt% hexachloroplatinic acid at room temperature. The on potential was -0.245 V vs SCE and the off potential was 0.4 V vs SCE.

6.7. In-situ SAXS of potential hold vs pulsed Pt

To get a better understanding of the difference between potential hold and pulse electrodeposition of Pt grown through the phytantriol/Brij-56 templates, in-situ SAXS measurements were used to monitor the Pt and the templates simultaneously during deposition. The in-situ measurements were carried out at the I22 beamline at Diamond Light Source using a custom-made 3D printed electrochemical cell which is discussed in greater detail in chapter 7. We have been able to measure the relationship more accurately between the template lattice parameter and resulting Pt lattice parameter as we are monitoring the same position on the electrode during deposition. Inhomogeneity between the amounts of Brij-56 locally within the template could lead to a varying lattice parameter in various locations of the template. As there has been a previous report of a deviation of the expected lattice parameter of Pt with increasing Brij-56 in the template it is important to measure these relationships accurately.

The first set of experiments was to grow platinum using the potential hold method. The results from these experiments are shown in Figure 87 where 1D integrated SAXS images are shown in time increments of Pt grown through phytantriol (a), phytantriol/Brij-56(7.5%) (b) and phytantriol/Brij-56(20%) (c). Due to the different symmetry of the platinum compared to the template distinguished Bragg peaks can be seen. The Bragg peak for the platinum deposited in the swollen template with 20 wt% Brij-56 becomes much broader with an increasing FWHM (in line with the ex-situ results). This means that the crystal is more disordered. It can also be noted that only one peak is seen for the Pt produced through this template so although this peak is in the expected position, we cannot say definitively that the Pt exhibits the desired single diamond phase. The data extracted from the SAXS is summarised in Table 19. It shows a direct comparison of the lattice parameter of the Pt and the template in the same position on the electrode. As before there is a deviation from the expected lattice parameter. This is unwanted as it gives us less control over the size of our produced single diamond material making it more difficult to fine tune the material's desired properties.

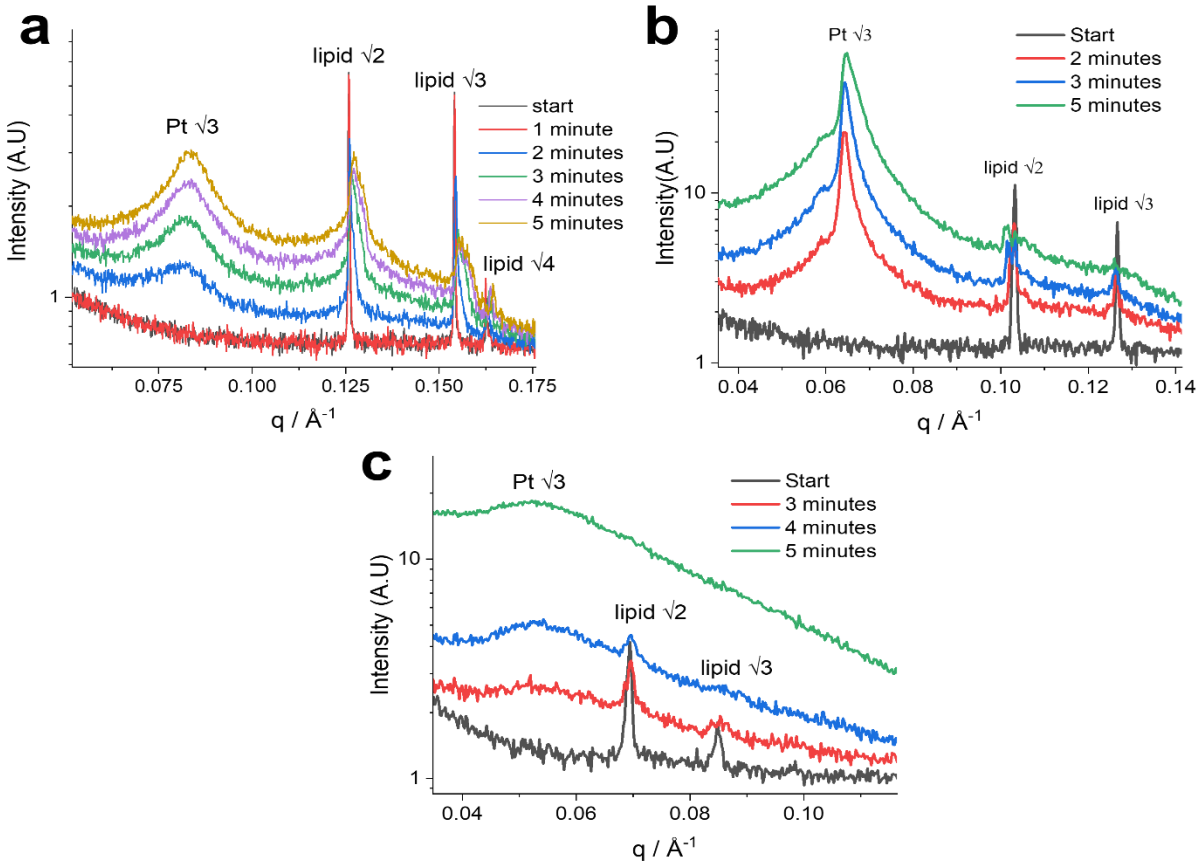

Figure 87 Stacked 1D integrated SAXS patterns taken at time intervals during the electrodeposition of platinum through phytantriol (a), phytantriol/Brij-56 (7.5%) (c) and phytantriol/Brij-56 (20%) (c) from a solution of 8 wt% hexachloroplatinic acid with a deposition potential of -0.245 V vs SCE.

Table 19 A table reporting the key results from in-situ SAXS of Pt electrodeposited by applying a potential of -0.245 V vs SCE through phytantriol and Brij-56 mixtures in excess HCPA conditions.

Template	Template Lattice parameter (Å)	Pt Lattice parameter (Å)
Phytantriol/0% Brij-56	70.6 ± 0.4	130.8 ± 2.9
Phytantriol/7.5% Brij-56	86.0 ± 0.6	137.7 ± 2.4
Phytantriol/20%Brij-56	128.1 ± 1.8	206.9 ± 6.4

For the in-situ experiments the conditions of the pulses applied to the working electrode for the on-pulse was -0.245 V *vs* SCE for 0.1 s and for the off pulse it was 0.4 V *vs* SCE for 0.3 s. The results from these experiments are shown in Figure 88 where single diamond platinum can be seen growing through phytantriol (a), phytantriol/Brij-56(7.5%) (b) and phytantriol/Brij-56(20%) (c). 1D SAXS images are shown at increments throughout the deposition. The data extracted from the SAXS is given in Table 20. The peak positions for the lipid templates and Pt are consistent with literature values and that of the potential hold experiments. As shown in (c) it is clear that the first Bragg peak from the Pt is much sharper and has a smaller FWHM when compared to the Pt produced via potential hold through phytantriol/Brij-56(20 wt%). This means that the Pt is more uniform in size. A major advantage of pulse electrodeposition is that the Pt exhibits two clear peaks relating to the (111) and (220) Bragg peaks so the single diamond phase can be confirmed whereas this could not have been said for Pt produced by potential hold. Another major advantage of pulse vs potential hold is that the Pt produced from the phytantriol/Brij-56(20 wt%) template had a lattice parameter much closer to the expected value of twice that of the templates lattice parameter. The Pt produced from pulse electrodeposition had a lattice parameter of 226.3 ± 3.8 Å (240.6 ± 2.8 Å expected) whereas from potential hold the lattice parameter was 206.9 ± 2.8 Å (256.2 ± 3.6 Å expected). This is extremely important as it allows us to more accurately predict and fine tune the resulting size of the produced single diamond Pt.

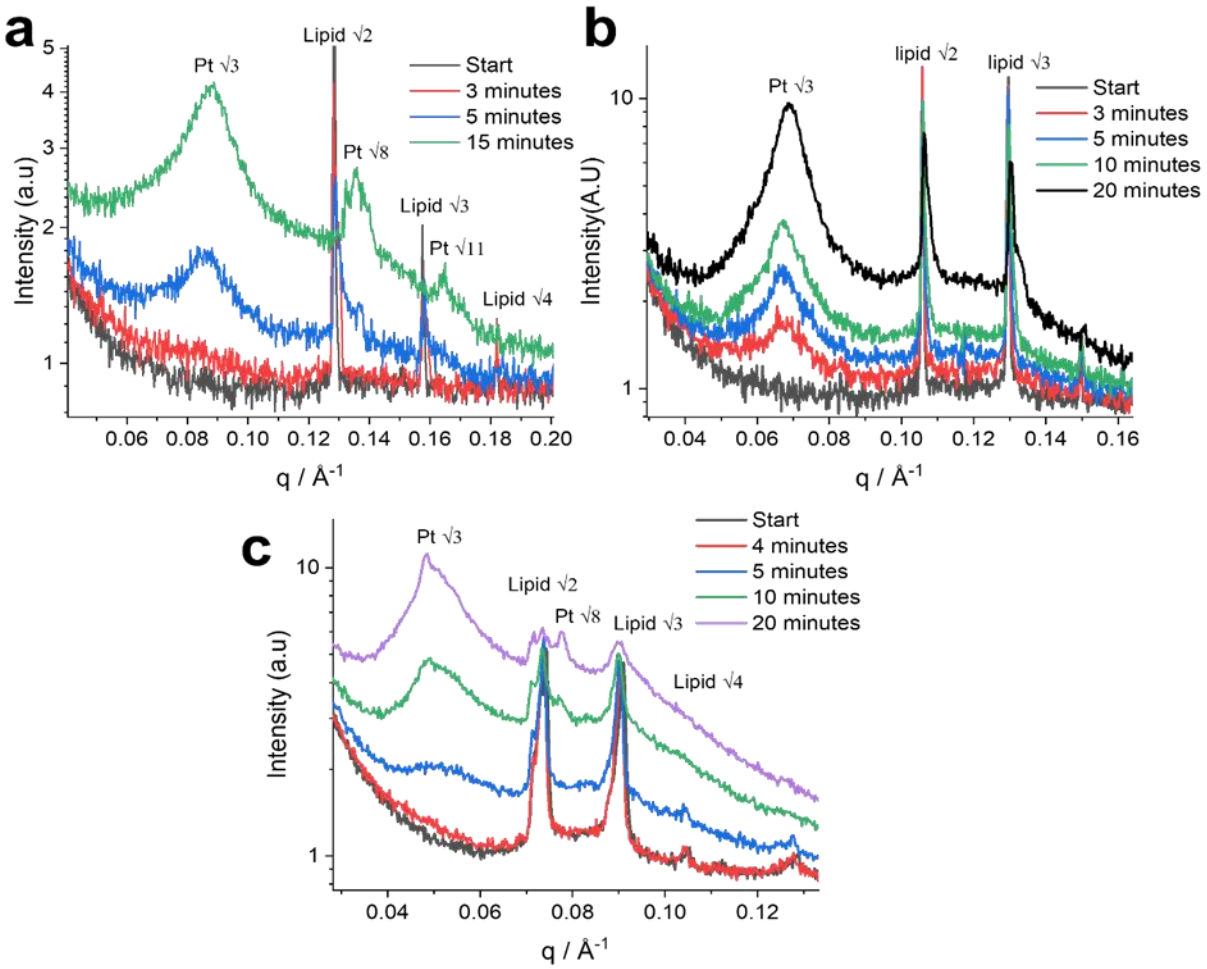

Figure 88 Stacked 1D integrated SAXS patterns taken at time intervals during the pulse electrodeposition of platinum through phytantriol (a), phytantriol/Brij-56 (7.5%) (c) and phytantriol/Brij-56 (20%) (c) from a solution of 8 wt% hexachloroplatinic acid with a deposition potential of -0.245 V vs SCE for 0.1 s and an off pulse at 0.4 V vs SCE for 0.3 s for a number of cycles.

Table 20 A table reporting the key results from in-situ SAXS of Pt electrodeposited by applying pulses of -0.245 V vs SCE for 0.1 s and 0.4 V vs SCE for 0.3 s through phytantriol and Brij-56 mixtures in excess HCPA conditions.

Template	**Template Lattice parameter ($Å^{-1}$)**	**Pt Lattice parameter ($Å^{-1}$)**
Phytantriol/0% Brij-56	69.1 ± 0.3	127.3 ± 5.3
Phytantriol/7.5% Brij-56	83.4 ± 0.4	131.1 ± 1.9
Phytantriol/20%Brij-56	120.3 ± 1.4	226.3 ± 3.8

From the SAXS data it appears that pulse electrodeposition did not have any major advantage compared to Pt grown in the pure phytantriol when compared to potential hold. The main advantage of the technique is when using the phytantriol/Brij-56 (20 wt%) template which previously exhibited a single broad peak. We believe that the improvement of the

electrodeposition via pulse comes from the “off” pulse as this allows the system time to rest between each “on” pulse so that Pt ions have time to diffuse through the water channels replacing those that have been depleted during the “on” pulse. This leads to a more controlled deposition with better filling yielding a more uniform single diamond phase Pt. This is important as we now present a method in which better size control of single diamond Pt is achieved via soft-templated electrodeposition.

6.8. Out of plane SAXS of single diamond Pt

As mentioned previously, Richardson used out of plane SAXS to confirm that the single diamond phase of Pt electrodeposited through phytantriol/Brij-56 exhibited orientation in the (111) plane parallel to the substrate up to 15 wt% Brij-56 in the template. At amounts larger than 15 wt% no orientation was seen and only a polydomain ring was present meaning this technique could not be used to provide extra evidence that the Pt did indeed form the single diamond phase. Figure 89 (a) shows a repeat of this experiment in which Pt grown via potential hold through phytantriol/Brij-56(20 wt%) on Au foil shows only a polydomain ring in out of plane SAXS and no orientation is seen. The Pt produced via pulse electrodeposition however, in Figure 89 (b), shows distinct spots around the ring which are typical for an orientated material.

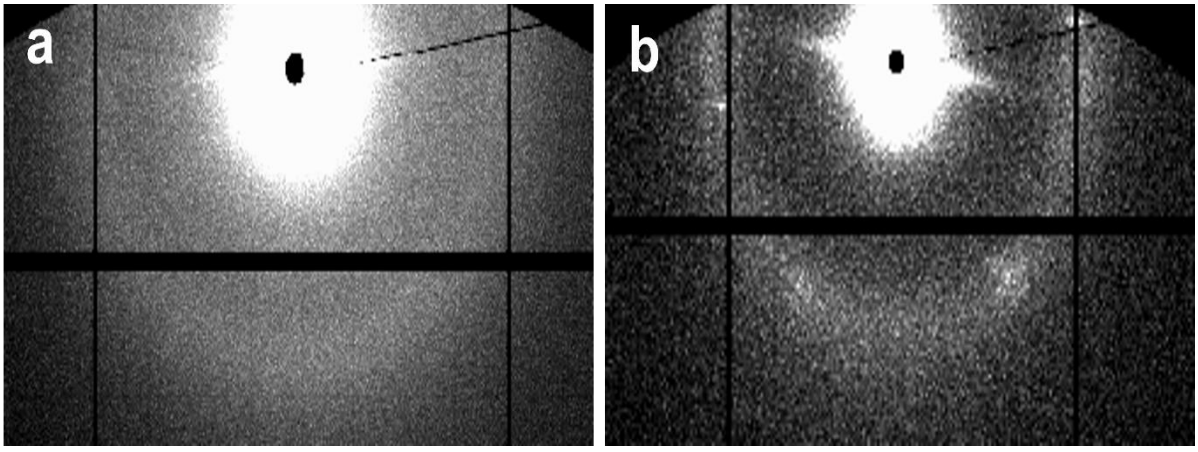

Figure 89 2D SAXS images taken in an out of plane orientation of Pt electrodeposited through phytantriol/Brij-56(20 wt%) on Au foil electrodes via potential hold (a) and pulse electrodeposition (b).

The predicted spot patterns for the single diamond phase orientated with the (111) plane parallel to the electrode surface is shown in Figure 90.[18] The spots are predicted to appear at angles of 0°, 70.5°, 109.5°, 180°, 250.5° and 289.5°.

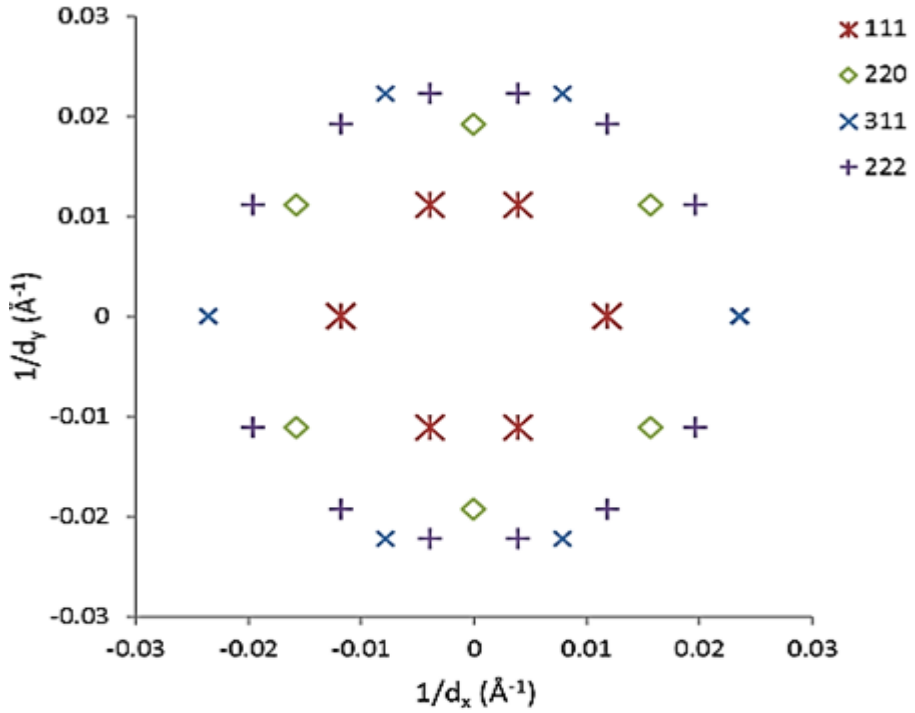

Figure 90 The predicted scattering pattern for a structure with single diamond (Fd3m) morphology orientated with the (111) plane parallel to the $1/d_y$ axis. Taken from.[18]

Taking the xy plane in the direction shown in Figure 91, we can see that the first two spots match the predicted patterns with angles of 0 ° and 70.5 ° however the other two spots are around 10° off the predicted angle. This means that we cannot use this data to confirm that the Pt is orientated with the (111) plane parallel to the electrode surface, however the presence of spots indicated that there is some degree of orientation which cannot be said for the Pt produced via potential hold.

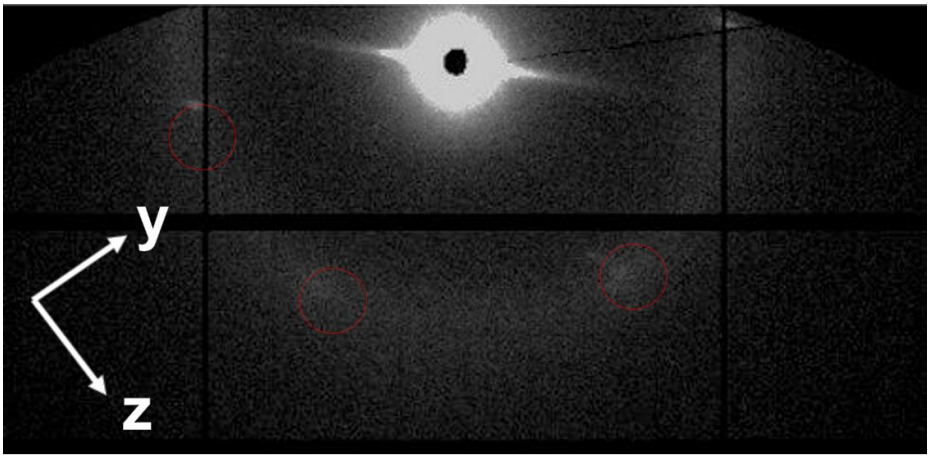

Figure 91 2D SAXS images taken in an out of plane orientation of Pt electrodeposited through phytantriol/Brij-56 (20 wt%) on Au foil via pulse electrodeposition, along with red circles which are an overlay of the predicted spot pattern locations for the single diamond phase orientated with the (111) plane parallel to the electrode surface.

This demonstrates that pulse electrodeposition is advantageous when compared to potential hold for deposition through the phytantriol/Brij-56 (20 wt%). Orientation is important as it can lead to improved properties of the material. It has been predicted that orientation should result in an enhancement in transport and mechanical properties.[200] Uniaxially aligned gold with gyroid morphology has been reported to have exotic optical properties that depend on nanostructure orientation. This shows that orientation can play an important role for a material's properties.[201,202]

6.9. TEM and SEM of single diamond phase Pt

TEM images of Pt produced via potential hold and pulse electrodeposition through the phytantriol/Brij-56 templates were collected to provide further evidence that the resulting material formed the desired single diamond phase. The images of the nanostructures could also be used to assess any differences between potential hold and pulse deposition on the resulting structure.

In Figure 92 we see that Pt produced by both electrodeposition methods through phytantriol, exhibit a mesoporous structure of interconnected nanowires. From the SAXS and TEM images we can confirm that the material has formed the desired single diamond phase. From the images it is difficult to make any comparisons between the resulting structures from the different deposition methods however, in Figure 92 (c) the Pt appears more homogenous into the bulk of the structure with long range ordering. Due to the destructive methods of prepping the TEM samples, this could potentially affect the quality of the structure and due to orientation of the samples the pores may be less visible.

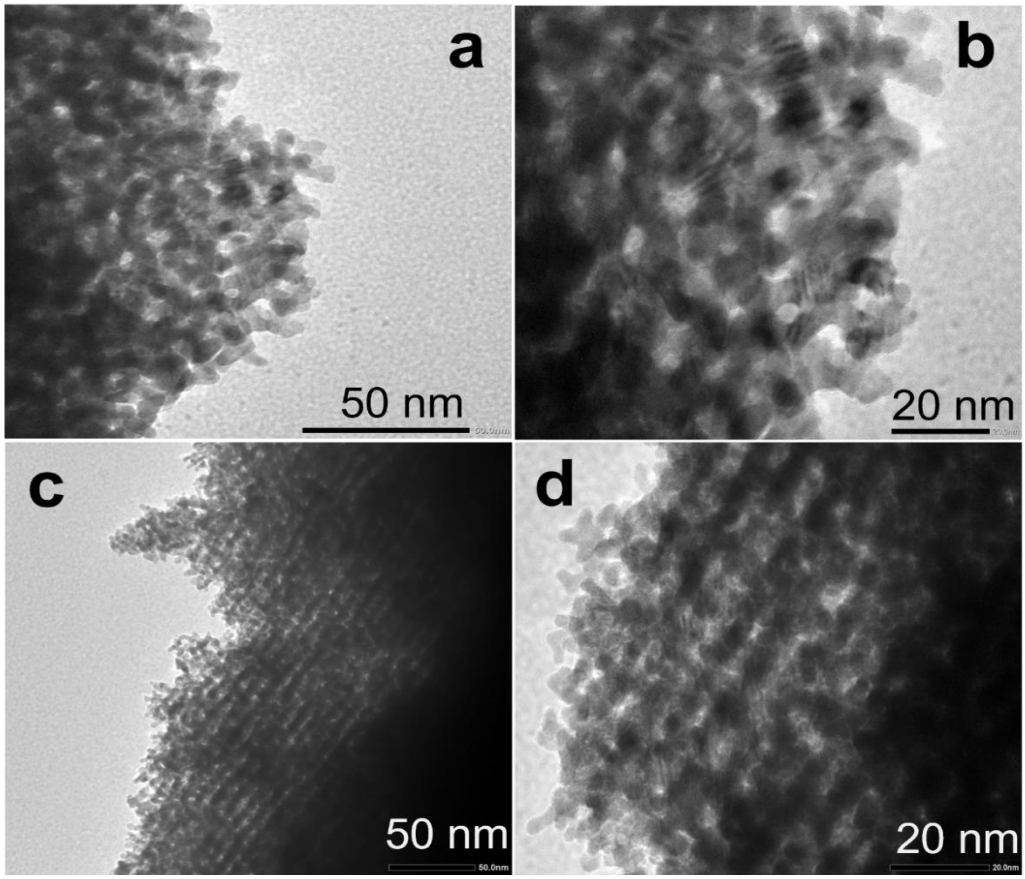

Figure 92 TEM images taken at different magnifications of Pt electrodeposited through phytantriol via potential hold (a&b) and pulse electrodeposition (c&d).

Figure 93 tells the same story in that Pt produced via both potential hold and pulse through phytantriol/Brij-56 (7.5 wt%) exhibits the desired single diamond phase. Again, the Pt produced via pulse (c & d) appears to be more uniform with the porous structure being more clearly visible into the bulk of the sample.

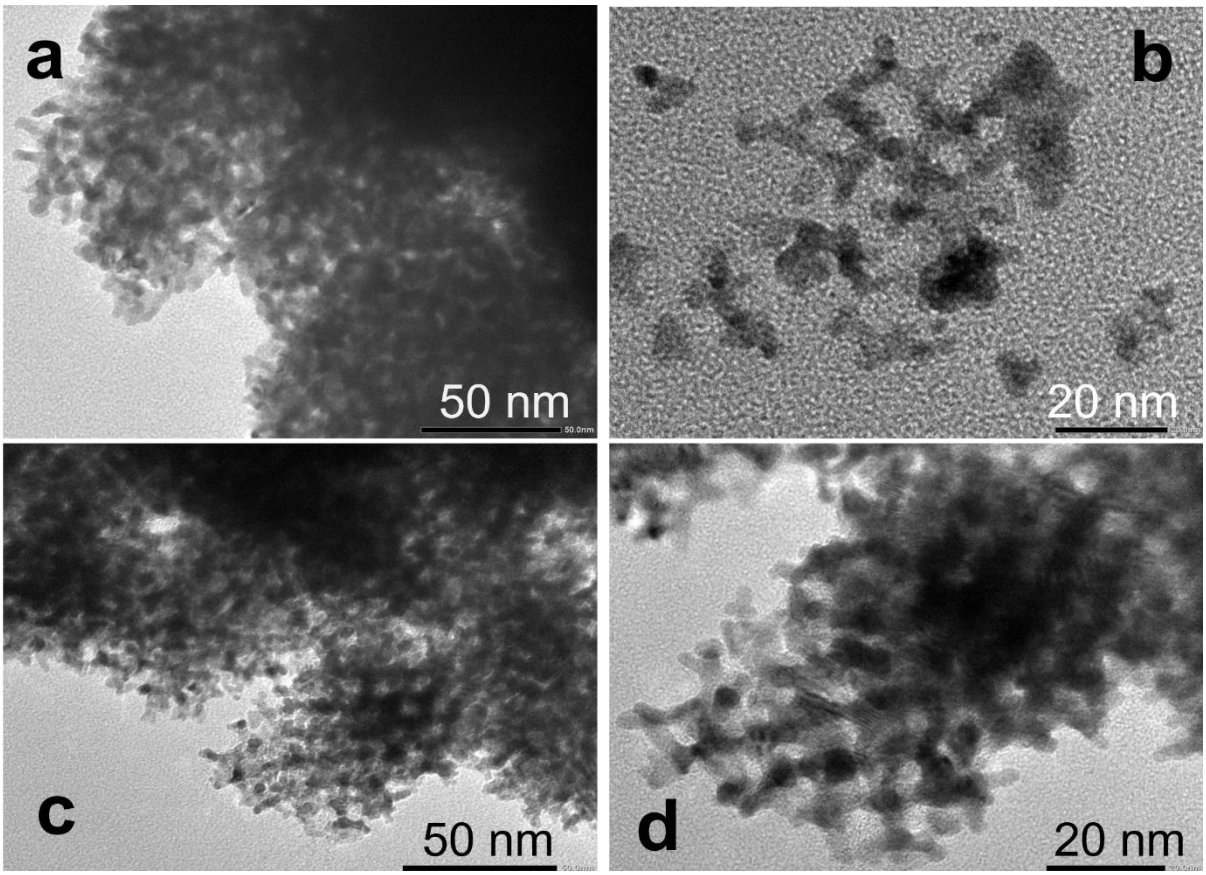

Figure 93 TEM images taken at different magnifications of Pt electrodeposited through phytantriol/Brij-56 (7.5 wt%) via potential hold (a&b) and pulse electrodeposition (c&d).

The biggest difference between Pt produced by potential hold compared to pulse electrodeposition comes from the images shown in Figure 94. The Pt deposited by potential hold (a & c) through phytantriol/Brij-56 (20 wt%) appears very disordered and it is hard to confirm the single diamond phase was achieved, although there are visible nanowires which form a porous structure. This disorder and inhomogeneity explains why the SAXS patterns seen in Figure 86 (b) and Figure 87 (c) produced by the material gives a broad peak. The Pt produced by pulse electrodeposition on the other hand, shown in Figure 94 (c & d), does exhibits the single diamond phase with clear nanowires visible forming a porous network. This

explains why we see SAXS patterns for Pt produced via pulse electrodeposition (Figure 86 (b) and Figure 88 (c)) with sharper Bragg peaks.

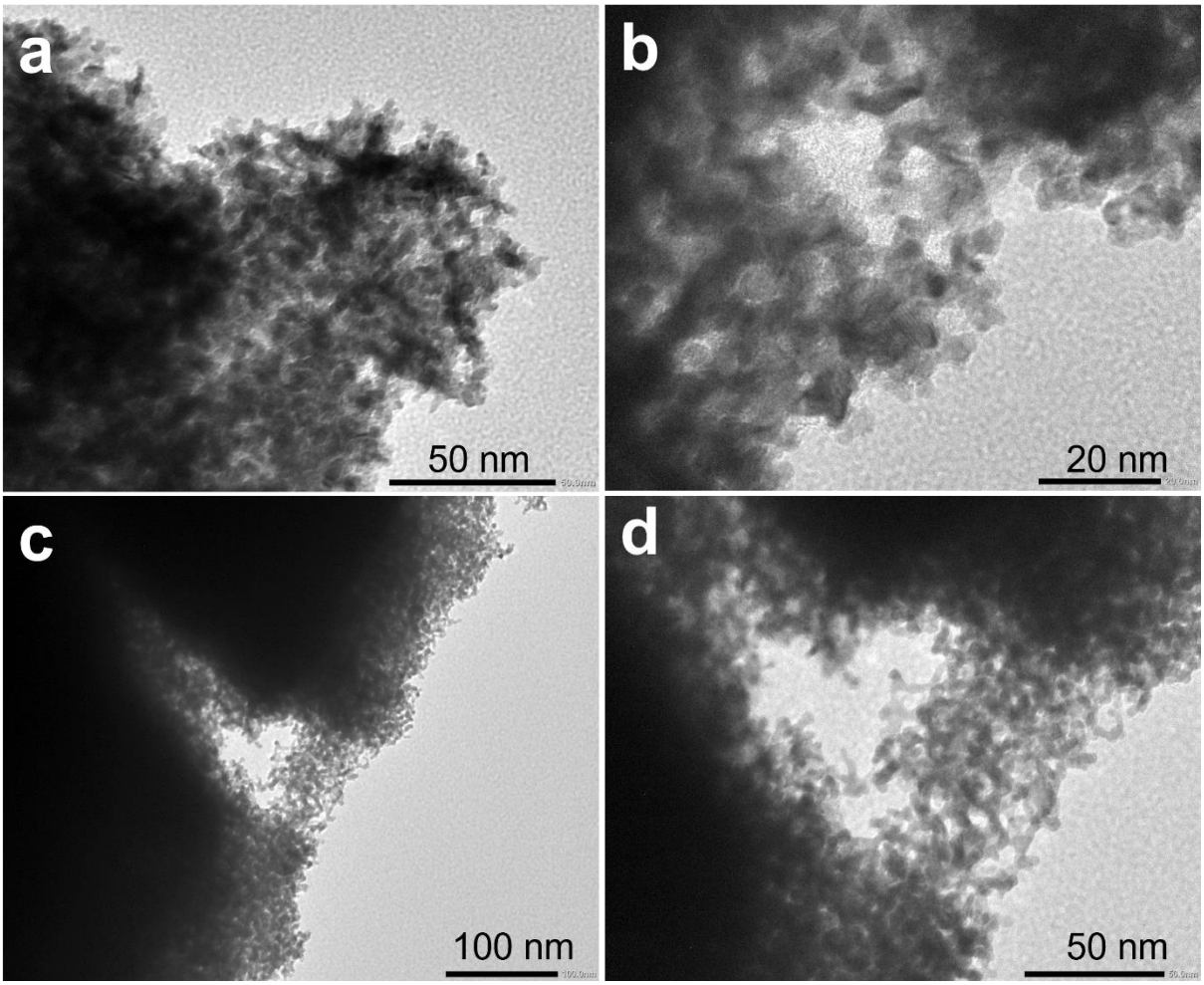

Figure 94 TEM images taken at different magnifications of Pt electrodeposited through phytantriol/Brij-56 (20 wt%) via potential hold (a&b) and pulse electrodeposition (c&d).

The TEM images have provided further evidence that pulse electrodeposition yields a more uniform single diamond phase material especially in the case when the swollen template with 20 wt% Brij-56 was used.

As the Pt produced using the swollen template phytantriol/Brij-56 (20 wt%) is larger it was possible to collect SEM images of the as deposited films without damaging the samples which was required in order to prepare them for TEM. Figure 95 shows that Pt electrodeposited via pulse electrodeposition forms an extremely uniform single diamond phase structure with visible pores and an interconnected 3D nanowire network. To the best of my knowledge this is the first time that the single diamond phase of Pt has been imaged using SEM, prior to these

images only TEM had been used to image the material. This gives us insight into how the Pt looks with high resolution as it is deposited as a thin film. We were unable to collect SEM images of value of Pt produced by potential hold deposition through this template. This itself may not indicate alone that Pt produced via pulse is more uniform as the orientation of the sample affects the ability to collect high resolution images of the structure as the pores may not be visible in the plane of the beam like they are in the images in Figure 95.

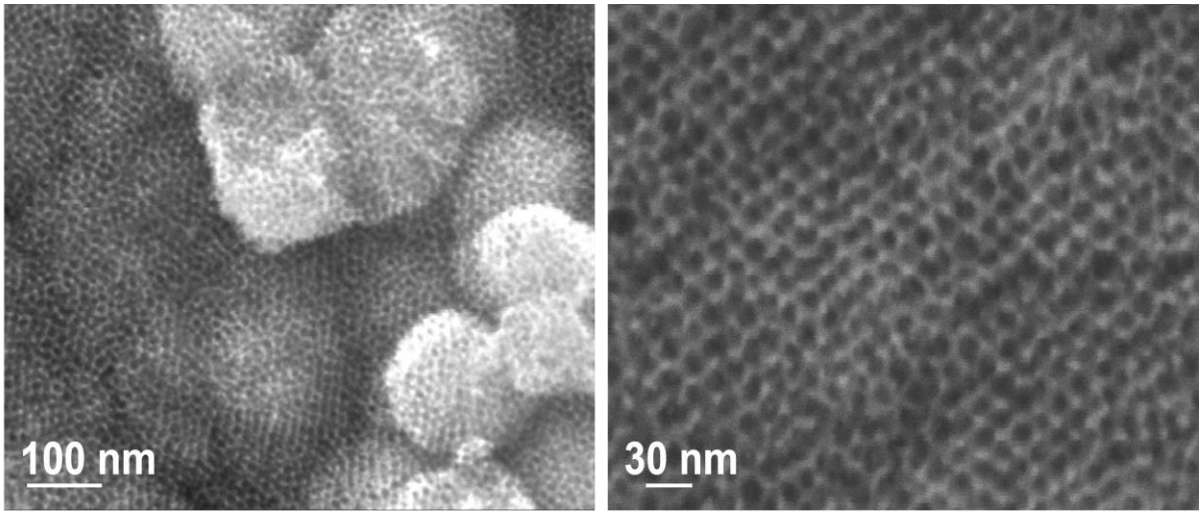

Figure 95 SEM images taken at different magnifications of Pt electrodeposited through phytantriol/Brij-56 (20 wt%) via pulse electrodeposition from a solution of 8 wt% hexachloroplatinic acid solution.

6.10. Conclusions

We have demonstrated by performing detailed SAXS investigations that pulse electrodeposition is beneficial over potential hold when depositing Pt through the swollen double diamond phase of phytantriol/Brij-56. This result was confirmed by SAXS in which the resulting patterns showed narrower Bragg peaks indicating a material with a more uniform lattice parameter and higher order Bragg peaks present, making it possible to confirm single diamond phase of the material when this was not possible for potential hold. TEM was also used to image the resulting Pt films and it was revealed that the Pt produced by electrodeposition was more uniform than that produced by potential hold. This indicates that pulse electrodeposition of Pt is advantageous over potential hold methods previously reported and may be able to be applied to other materials or liquid crystal templates.

6.11. Future work

For future work with this project, pulse electrodeposition can be applied to other materials through phytantriol and its derivates which could allow us to deposit materials that have previously failed to deposit inside the phytantriol water channels or have produced broad Bragg peaks in SAXS.

The next chapter delves into the innovative design and fabrication of a novel 3D printable electrochemical cell, which enables in-situ small angle scattering experiments. By leveraging the versatility of 3D printing, the electrochemical cell can be customed for a broad range of in-situ experiments.

7. 3D Printed custom in—situ SAS electrochemical cell

7.1. Introduction

Small angle X-ray scattering is a widely adopted technique for studying the nanoscale structure of materials such as nanoparticles,[203,204] inorganic materials,[205,206] polymers,[207,208] liquid crystals,[209,210] and biological macromolecules.[211,212] For electrochemical systems, in-situ characterisation of materials under controlled electrochemical conditions is important for understanding a material's behaviour and properties. Traditional electrochemical cells used in SAS experiments suffer from limitations in terms of design flexibility, cost and ease of use. 3D printing provides a technology which enables the fabrication of cells with complex and customisable geometries. 3D printing is also capable of rapid prototyping, which becomes advantageous when designing bespoke cells with specific experimental requirements. The flexibility of the technique also allows integration of various components such as working, reference and counter electrodes into a single cell. The cost-effectiveness of fabricating cells using 3D printing is also attractive as there is no need for expensive machining or specialised tooling and iterating designs quickly also reduces material waste, lowering overall costs. The cells fabricated for this work were printed in-house using stereolithography (SLA), in which a UV-laser is focused on a photosensitive liquid to induce polymerisation of the liquid into a solid which is built up layer by layer.[213] The increasing affordability and accessibility of 3D printers has facilitated their widespread utilisation in various research fields, contributing to innovation and experimentation. This technique was chosen as it allows the fabrication of complex geometries without the need for machining and the solid resin has good mechanical and chemical stability. The resin used in this work was Anycubic UV Resin.[214]

In-situ electrochemical-based SAXS experiments have been exploited to investigate fuel cells,[215,216] supercapacitors,[217] batteries[218,219] and electrodeposition.[10] There have been reports of cell designs for in-situ XRD studies highlighted by Brant,[220] however, there are significantly less reports of in-situ SAXS cells. Of the few reported,[216,221,222] the cells consist of multiple components or machined parts making them expensive and harder to use than the design described in this report. Asset *et al.* reported the design and use of a custom in-situ electrochemical cell in order to assess the ageing mechanism of PtNi/C nanoparticles during

operation as a fuel cell material.[215] The cell was machined from Kel-F (polychlorotrifluoroethylene) in multiple parts that needed to be screwed together. Efforts were made to keep the electrolyte thickness in the beam path short and the window material for the cell was Kapton®. Another example of as custom made in-situ cell is reported by Koczwara *et al.* in which they used an electrochemical cell out of PEEK (polyether ether ketone) to gather real time SAXS data of nano-porous carbon electrodes for applications in supercapacitors.[217] Work by Prehal *et al.* also used a similar cell to track structural arrangement of ions in carbon supercapacitors.[223] The cell consisted of a current collector, working electrode, separator, counter electrode and another current collector sandwiched together in PEEK housing using titanium endplates to maintain electrical contact. All of these examples use machined parts with multiple parts which become expensive when iterating through new designs and drives the cost of the cell up. Bogar *et al.*[216] reported the design and use of a 3D printed cell which was capable of performing in-situ grazing incidence SAXS (GISAXS) and wide angle X-ray scattering (WAXS) to study the catalyst degradation of fuel cell materials. The cell body was 3D printed and consisted of multiple parts that needed to be screwed together along with Kapton windows, the cell hosted a typical three electrode setup and allowed for the flow of electrolyte. Although the cell body here was 3d printed making it more accessible and cheaper, it being made of multiple parts makes it harder to use and requires more time when changing between samples on a beamline. Richardson *et al.*[10] reported details of the design of a cheap and simple 3D printed in-situ cell. The cell discussed in this report has multiple advantages over that previously described in terms of designated space for the different electrodes, leak proofing and smaller X-ray path length through the cell, all of which are discussed in more detail later.

The goals of the 3D printed cell was to provide a simple, easy to use and cheap cell which would enable in-situ SAXS experiments with a typical three electrode set-up. The cell's geometry needed to fit a working, reference and counter electrode whilst maintaining a short X-ray pathway through the electrolyte to minimise the amount of X-ray absorption, decreasing the signal-to-noise ratio of the SAXS data. Customisation was also kept in mind while designing the cell so it could be used as a template for tailored modifications to specific experimental conditions.

7.2. Cell design

When designing the in-situ cell there were a few main goals and challenges to keep in mind. The first was the choice of material for the windows. From the literature the consensus was that Kapton was an ideal window material as it was cheap, easy to cut to shape and is chemically resistant. In this work Kapton tape was cut to match the size of the cell window and then sealed around the edges using fast setting epoxy resin (Araldite), preventing any leakage of electrolytes. Another challenge to keep in mind was the window-to-window distance which would determine how much electrolyte the beam would have to pass through. A short beam path length through the cell is important in order to minimise the amount of scattering through the electrolyte, lowering the background noise. One of the main goals of this new cell design was to create adequate space for a typical three electrode set-up of a working electrode, reference electrode and counter electrode. The cell should be capable of repeating lab condition experiments.

The first iteration of the cell is shown in Figure 96. It consists of a hollowed-out cuboid which would hold the electrolyte solutions and 3 electrodes. The windows are 1 cm wide and 2 cm tall. The window-to-window length is 1 cm. The cell also had 4 legs with screw holes which would host M4 screws allowing the cell to be mounted and secured on generic sample stages. It became quickly apparent that loading up a 3-electrode setup into this cell would be difficult on a beamline with limited space. After printing the cell on an ELEGOO Mars 2 from UV resin we realised that the structural integrity of the cell was better than expected and thinner walls and a smaller window-to-window path length could be achieved.

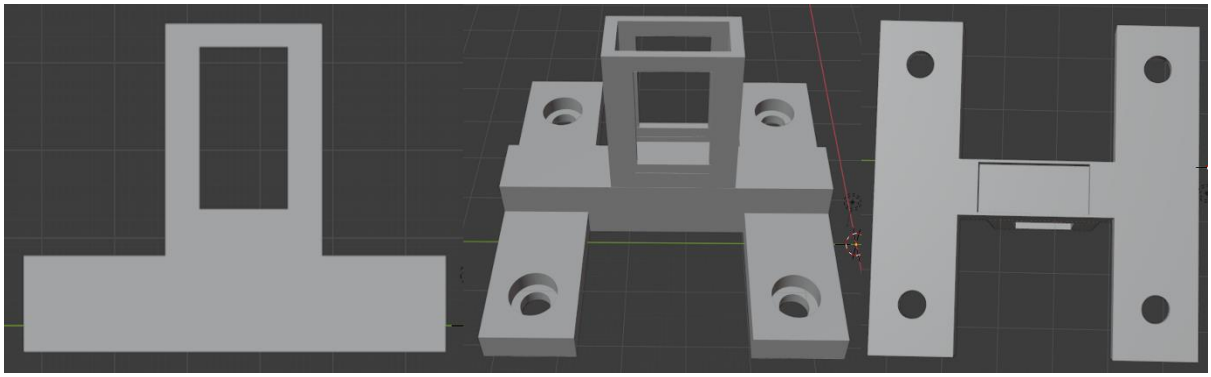

Figure 96 A schematic of the first iteration of in-situ SAS electrochemical cell designed in Blender 2.9.

The second iteration of the cell, shown in Figure 97, boasted multiple improvements over the first design. The cell has a backplate which enables a working electrode to be secured in place with a crocodile clip while also making an electrical connection, which creates stability for the working electrode. The geometry of the cell was also changed into this unique shape which allowed a small window-to-window path length of 5 mm which is half of that of the previous cell, while allowing extra space which is designated for the counter and reference electrode either side of the working electrode. This set-up allowed us to house the working, reference, and counter securely while mimicking lab conditions. The window size was reduced to 1 cm wide and 1.5 cm high which matched the working electrodes used in this work. 1.5 mL of electrolyte was enough to fill this cell whereas almost 10 mL was needed to fill the previous. This is beneficial when working with expensive electrolyte as using less is cost effective, but we found that 1.5 mL was enough to mimic lab conditions for the experiments presented in this thesis.

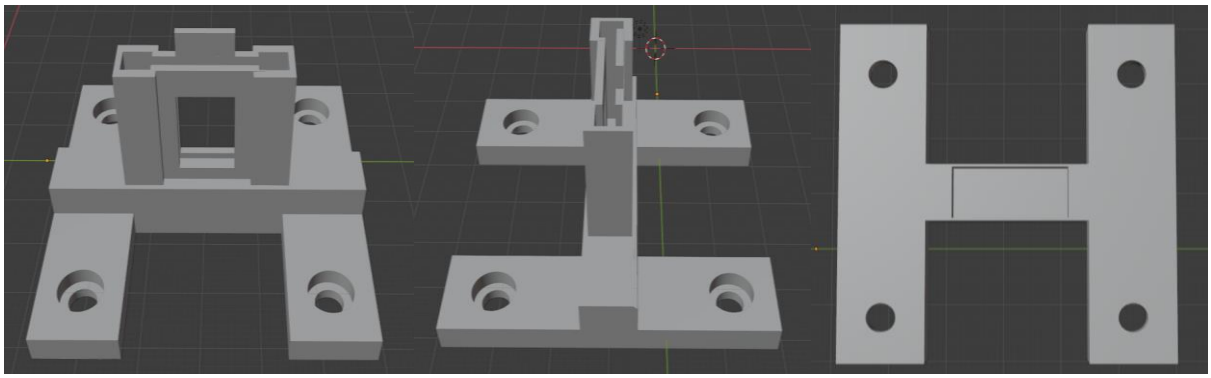

Figure 97 A schematic of the second iteration of in-situ SAS electrochemical cell designed in Blender 2.9.

Figure 98 shows the 3D printed version of the cell with Kapton windows and hosting a typical three-electrode setup that we use in the lab. While inserting the working electrodes, which were coated with a liquid crystal template layer, into the cell, occasional contact with the cell's edges and the Kapton window resulted in damage to the liquid crystal template and left residue on the window. This residue had the potential to impact subsequent SAS experiments. We recognised the need for further refinements before finalising the design.

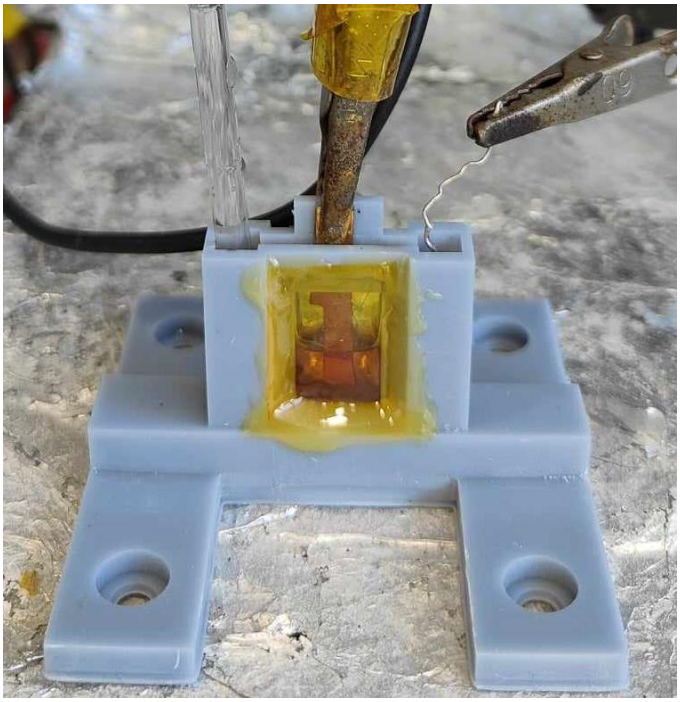

Figure 98 3D printed electrochemical cell of the second iteration of the design, along with a typical three-electrode setup.

Figure 99 highlights the final cell design alongside the 3D printed cell with a three-electrode setup mounted on the offline SAXS instrument Xeuss 3.0 at the Diamond Light Source. The best features of the previous cell were kept such as the narrow 5 mm window-to-window path length and window size of 1 cm wide by 1.5 cm tall. Again, the window material was kept as Kapton® and was sealed using epoxy resin (Araldite rapid adhesive ARA-400005). There were two main changes between the final design and the previous that were very advantageous. Firstly, the legs of the cell were removed and the screw holes were placed on the stand which still had space for M4 screws 5 cm apart, allowing the cell to be mounted securely to a sample stage. The major advantage this provided was that the radiation source could be brought closer to the cell to minimise the “in air” distance of the beam leading to less air scattering which acts to lower the background noise. The second improvement was the addition of rails on the inside of the cell. The addition of rails served to prevent the liquid crystal template from making direct contact with the windows of the cell during electrode insertion. This maintained the integrity of the liquid crystal template and minimised the risk of damage or contamination to the windows.

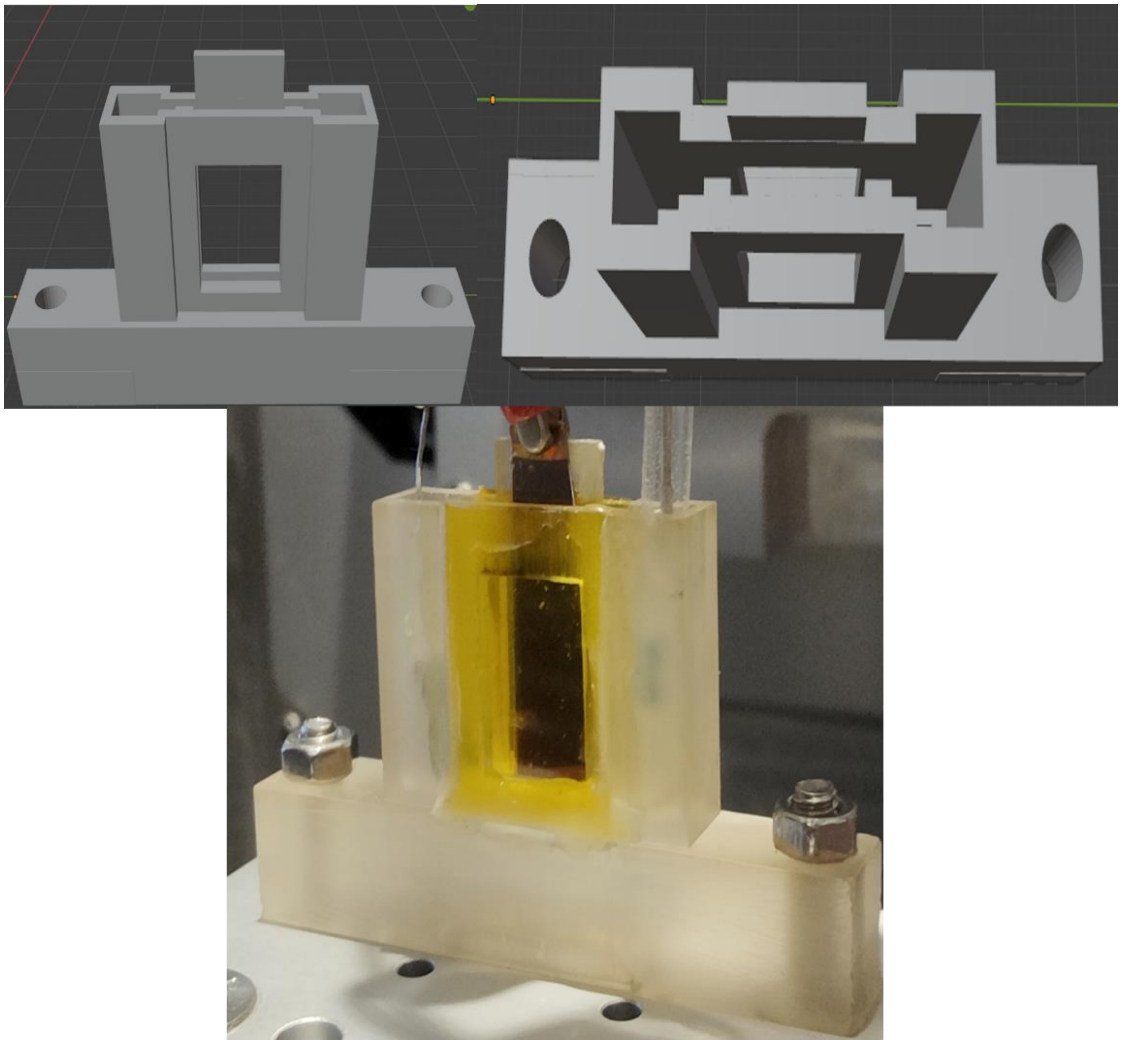

Figure 99 Model of the final in-situ electrochemical cell design made in Blender 2.9 along with the 3D printed version, hosting a typical three-electrode setup as used on the offline SAXS instrument Xeuss 3.0.

The cell has been designed in such a way that makes it very customisable to a range of experimental conditions. Window size, path length and many other attributes can all be altered in order to create a cell fit for purpose. The price to fabricate one cell as made in-house was £0.27, this can be made even cheaper by producing multiple cells simultaneously. The cost is also affected by the type of resin used. Due to the cheap cost of the cell many can be manufactured for to decrease the time between experiments when working on a beamline.

7.3. Example experiments

This cell was used for all the in-situ experiments on monitoring the growth of deposited material through phytantriol and phytantriol/Brij-56 liquid crystal templates in the previous chapters of this thesis. However, this cell was also used in collaborative work, successfully enabling multiple different in-situ electrochemical experiments to be performed.

In a collaboration with the University of Bath, I joined the experimental team at the Diamond Light source (experiment SM31449) on the offline SAXS instrument Xeuss 3.0. The experimental team consisted of me, Wanli Liu and Dr. Adam Squires in which we used the in-situ electrochemical cell to collect time resolved SAXS data on a liquid crystal phase during cyclic voltammetry experiments. The aims of the experiment were to study the amphiphilic ferrocenium molecule FC-12 which can be used as a redox probe to assist biosensing. It had been reported that when large contents of FC-12 are present in the liquid crystal phase the redox probes gradually lose activity, shown by a drop in current response during repetitive cycling. For this experiment lipid cubic phases of FC-12 (Dodecyl (ferrocenylmethyl) dimethylammonium bromide) and MO (monoolein) were prepared by melting monoolein in a water bath at 40 ^{o}C for 15 minutes then mixing it with FC-12 at a desired ratio, then vortexing the mixture followed by ultrasonication at 40 ^{o}C for 10 mins for dissolution. This mixture of FC-12/MO was then mixed with a phosphate buffer in a 60/40 lipid/buffer ratio in order to create a lipid paste. This lipid paste was then applied to a Au-DVD working electrode from Delkin Devices and placed into the electrochemical cell filled with buffer electrolyte. The potential was then cycled between 0.2 and 1.2 V *vs* Ag/AgCl and SAXS patterns were collected in transmission mode at different time intervals during the cycling. The results from this experiment are shown in Figure 100. From this data we can see that upon cycling the potential the magnitude of current drops with each cycle. The SAXS patterns of the lipid show that the paste was indeed a gyroid liquid crystal phase however over time during the cycling the peaks remained unchanged as expressed by Figure 100 (c) which shows that the first peak position remained unchanged. This means that there was no swelling or shrinking of the liquid crystal and there was no phase change either. This was a surprising result as these changes to the liquid crystal were expected to cause the drop in current. It can also be noted that after

cycling, a red solid formed on the electrode surface which was later confirmed to be Au-Br complexes.

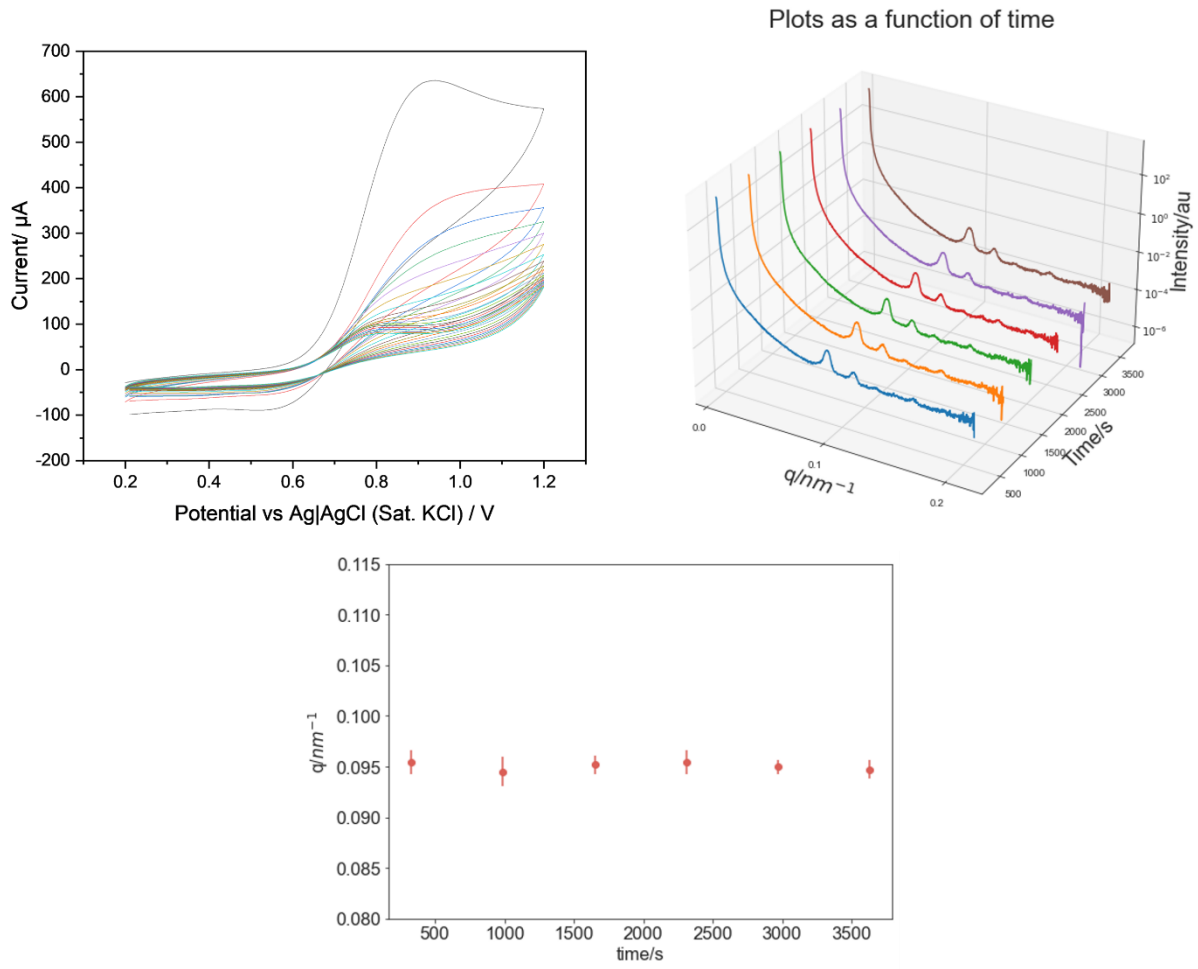

Figure 100 Cyclic voltammogram on a 1 cm² Au/DVD electrode covered with FC-12/MO in a phosphate buffer solution. 1D integrated SAXS patterns taken during the cyclic voltammetry at different time intervals and the associated q position of the first Bragg peak over time.

The conclusions gained from this work was that a different ion other than bromine was needed in order to test the system, FC-12 did not leach out into the bulk solution and no phase changes occurred during potential cycling. This experiment demonstrated that the cell designed for this work can have a wide array of application in the in-situ SAS area for different electrochemical experiments.

I also designed a customised version of this cell to be used on I22 at the Diamond Light source (experiment SM31380), in collaboration with Dr. Courtney Patterson and Professor Dave Adams from the University of Glasgow. The aim of this experiment was to monitor the electro-

polymerisation and growth of a polymer which formed a gel when a potential is applied to an electrode. For this experiment a customised version of the cell was designed shown in Figure 101, which shows the cell along with it set up in the I22 beamline.[224]

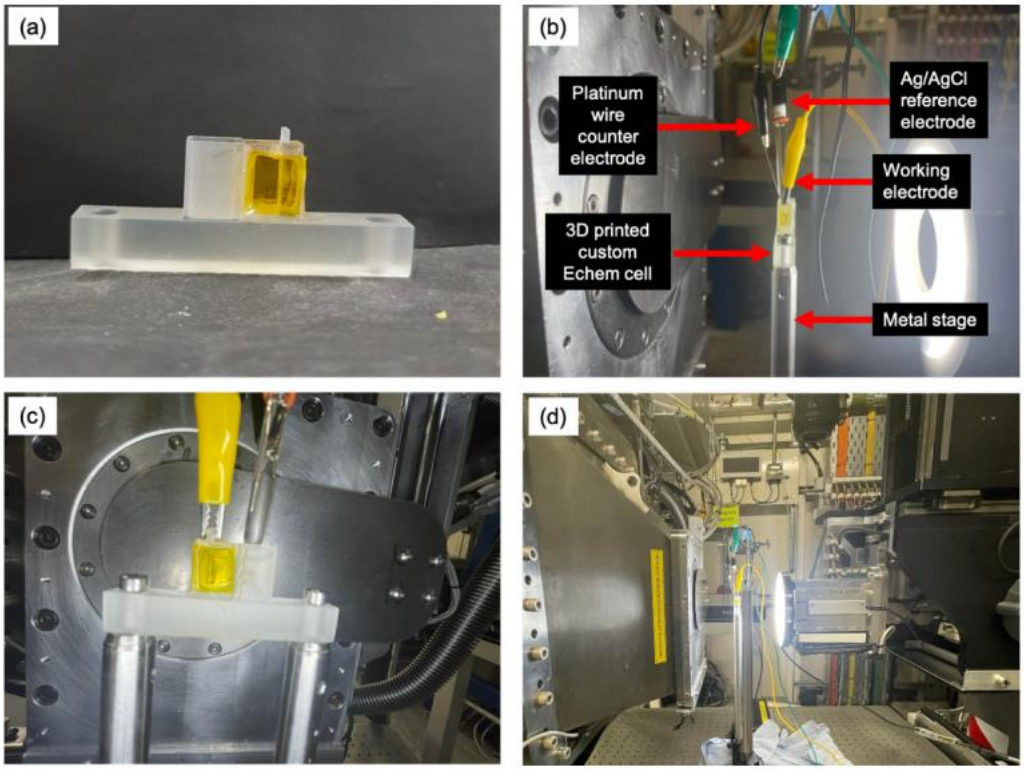

Figure 101 Images of a custom-made 3D printed electrochemical cell and it's setup on the I22 beamline for the collaborative work with the university of Glasgow. Taken from.[224]

The cell allowed for the placement of an FTO (fluorine doped tin oxide) electrode to orientated so that it was parallel to the X-ray beam. There was then space made to host a counter and reference electrode in the cell which was made mountable to the sample stage.

A summary of the results from this "first-of-its-kind" experiment are shown in Figure 102, in which a series of overlaying SAXS patterns are plotted at 6 different positions moving away from the electrode surface during the electro-polymerisation of Carb-Ala gel.[224] These plots were used to track the growth of the gel and a heat-map, Figure 103, was created using the intensity of the patterns at a q value of 0.01 nm^{-1}. From this data we see that for positions 0 to 4, the scattering intensity increases with each scan as the gel grows.

The 3D printed electrochemical cell enabled the time resolved monitoring of the gel growth at different positions away from the electrode surface while collecting structural information

on the gel. This demonstrates the versality of how 3D printed cells can be used to perform bespoke in-situ SAXS experiments.

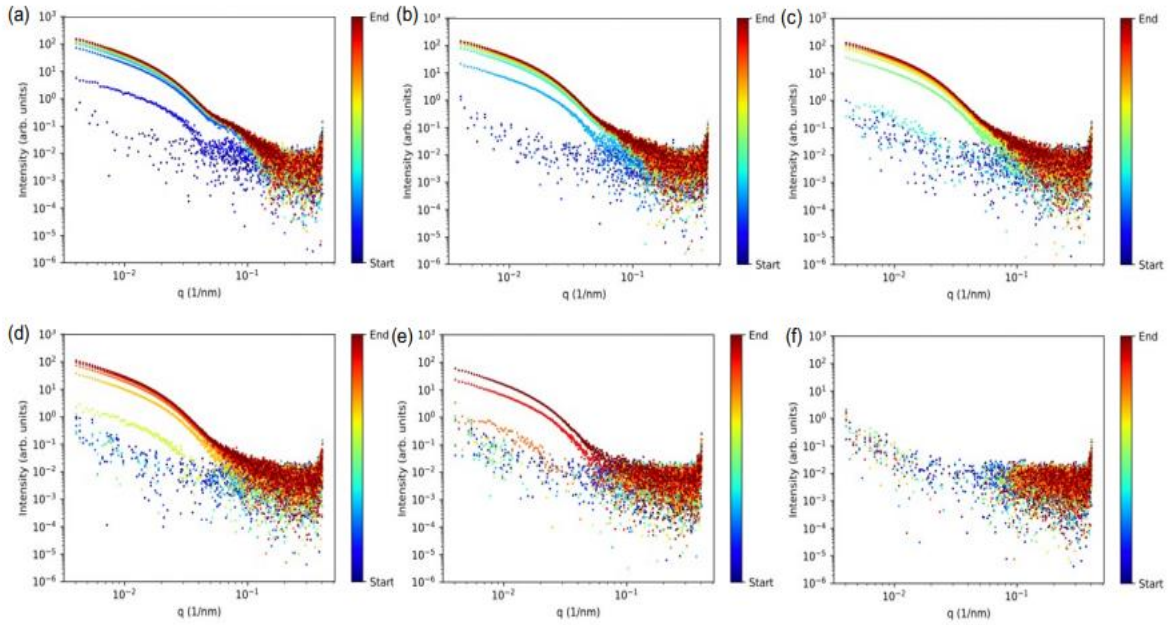

Figure 102 A series of 1D integrated SAXS plots for each position of the Carb-ALA hydrogel from the electrode surface with time. Position 0 being closest to the electrode and position 5 the furthest. (a) position 0 (b) position 1 (c) position 2 (d) position 3 (e) position 4 (f) position 5. Each position was separated by a distance of 2 mm. Gel growth can be seen using the colour spectrum with blue being the start of the experiment and red the end. Images taken from.[224]

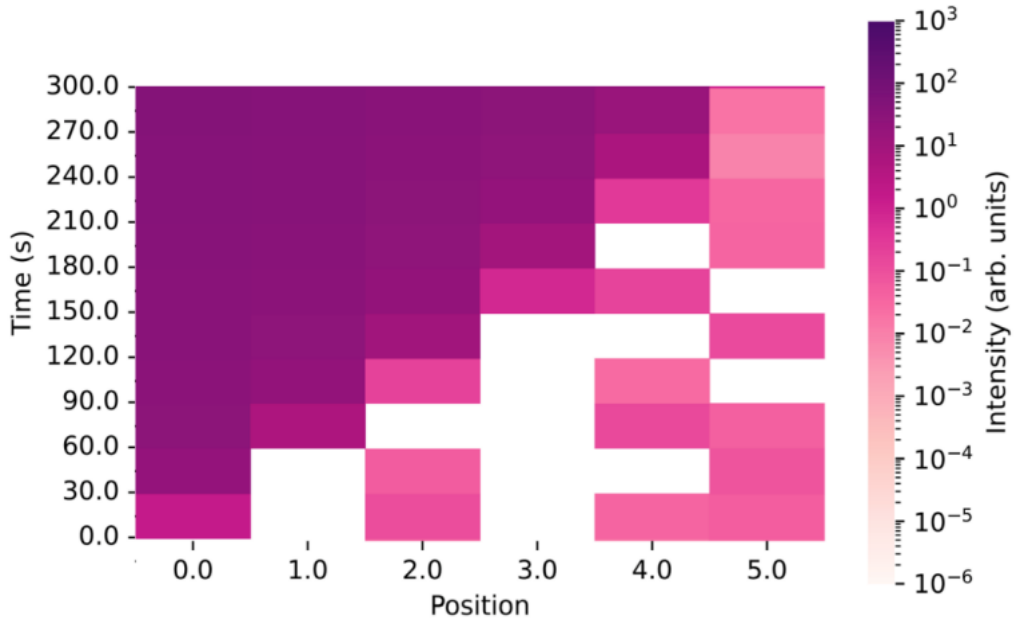

Figure 103 A heatmap generated from the SAXS plots of Carb-ALA hydrogel at the relative positions from the electrode showing the growth of the material over time. This image was taken from.[224]

7.4. Small angle neutron scattering experiments.

Small angle neutron scattering (SANS) was used to probe the deposited material and the phytantriol template. The goal was to use contrast matching techniques in order to gather more information on the deposit and template system. To achieve this goal, a version of the in-situ cell was designed and employed which allowed us to use SANS to analyse thin film electrodes modified with phytantriol in different solutions. The cell that was used is shown in Figure 104, the basic design of the cell is the same as the previous version used for in-situ SAXS experiments however, we have used thinner walls and a shorter window to window path length of 3 mm in order to minimise the path length of the neutrons through the electrolyte. This was an extremmely important feature of the cell as we would be using water for some of the experiments and hydrogen atoms lead to high backgrounds stemming from incoherent scattering. The cell would also enable us to perform in-situ expertiments.

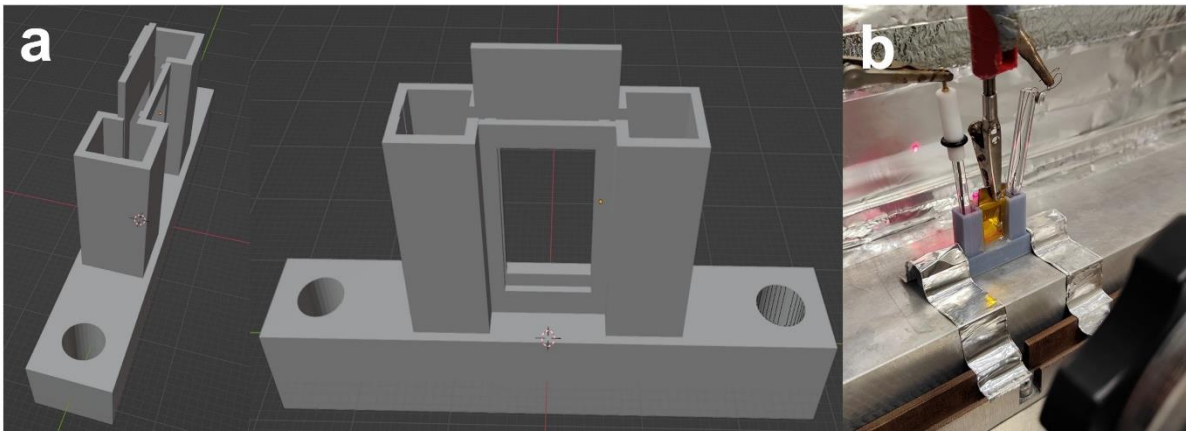

Figure 104 The design of the small angle neutron electrochemical cell (a) along with how it was setup on ZOOM at ISIS Neutron and Muon source in a typical three electrode configuration.

One of the major advatanges of SANS is that we can use contrast matching in theory to analyse separate parts of the system such as viewing only the deposited material, or only the template by varying the D_2O/H_2O ratio of the solution or by using different ratios of phytantriol and deuterated phytantriol (D-phytantriol) as the template. This technique can be beneficial when compared to SAXS as we cannot use this contrast matching effect and we only collect scattering patetterns for the entire system at once. When Bragg peaks overlap or some parts of the system scatter more than others we may be losing valueable information about the system.

The first goal was to use SANS to confirm that phytantriol and D-phytantriol formed a stable double diamond phase in different D_2O/H_2O ratios. Figure 105 (a) revelaed that phytantriol does form a stable double diamond phase in D_2O and that it took approxiamtely 35 minutes for the phytantriol to self-assemple into the liquid crystal phase. It was also revelaed that D-phytantriol also formed the double diamond phase in excess D_2O/H_2O in a ratio of (35 % D_2O and 65 % H_2O). The only noticable difference between phytantriol and D-phyantriol is that D-phytantriol took an hour until it it formed the stable double diamond phase, shown in Figure 105 (b). This allowed us to adjust our depostion procedure and allow the D-phytantriol a minimum of one hour to hydrate before performing electrodeposition through the template. The scattering pattern in Figure 105 (b) is much noisier with a higher background compared to Figure 105 (a) due to the presence of H in the solvent which has a large contribution to incoherent scattering of the neutron beam. The lattice paramter of phytantriol was 64.7 ± 0.6 Å and for D-phytantriol it was 66.0 ± 1.3 Å which is consistent with literature values and shows that D-phytantriol behaves the same as phytantriol as expected.

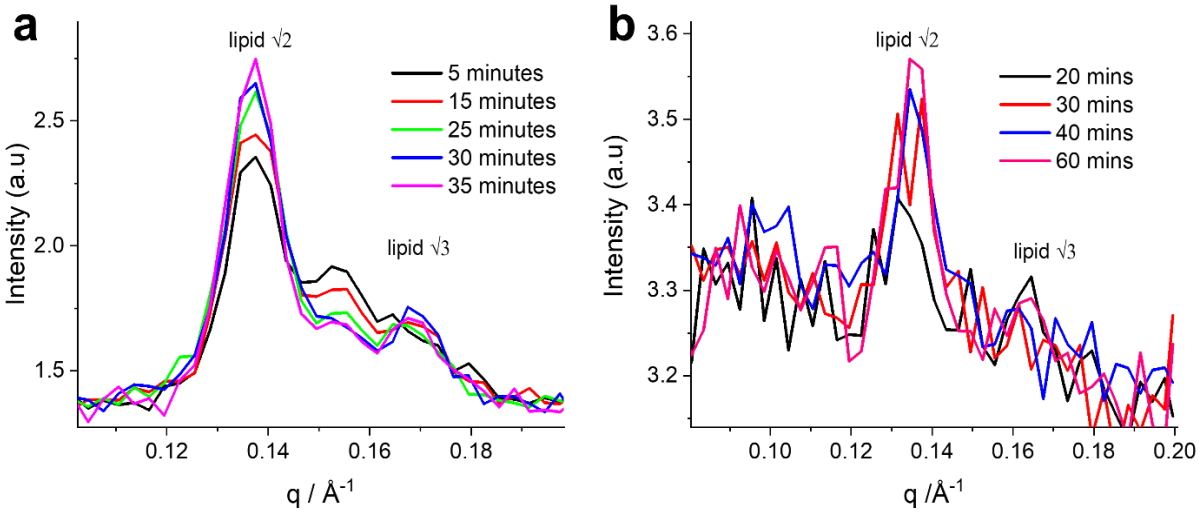

Figure 105 Stacked 1D integrated SANS patterns taken at different time intervals of phytantriol on a Au/Si electrode in excess D_2O (a) and deuterated phytantriol on a Au/Si electrode in 35% D_2O and 65% H_2O.

As previously mentioned, we can use different ratios of H_2O and D_2O in the solvent/electrolyte in order to contrast match. The ratios needed are determined by using Equation 49 where *SLD* is scattering length density of species and *a* and *b* respectively and *x* is the ratio to be determined.

Equation 49 $$SLD = xSLD(a) + (1 - x)SLD(b)$$

D-phytantriol has a very similar *SLD* to D_2O (6.8×10^{-6} Å^{-2} and 6.5×10^{-6} Å^{-2} respectively) so in pure D_2O solution we should not be able to see peaks from the double diamond phase as there is little contrast between the solution and the liquid crystal template. Phytantriol on the other hand has an *SLD* of -1.1×10^{-7} Å^{-2} so using Equation 49 it was calculated that a D_2O/H_2O solution containing 6.4 % D_2O would contrast match phytantriol. Figure 106 shows SANS patterns of phytantriol and D-phytantriol in different ratio D_2O/H_2O solutions. For phytantriol it can be seen that as the ratio of D_2O decreases from 100 % to 6.4 % the Bragg peaks diminish in intensity relative to the background. At 6.4 % we can no longer see scattering from the phytantriol as it is successfully contrast matched with the solution, matching the ratio determined by Equation 49. For D-phytantriol in H_2O we can clearly see the peaks from the double diamond phase, these peaks diminish in intensity relative to the background with increasing D_2O content until we can no longer see any scattering in the SANS from D-phytantriol. These experiments prove that we can manipulate the solutions in order to selectivity contrast match with both phytantriol and D-phytantriol.

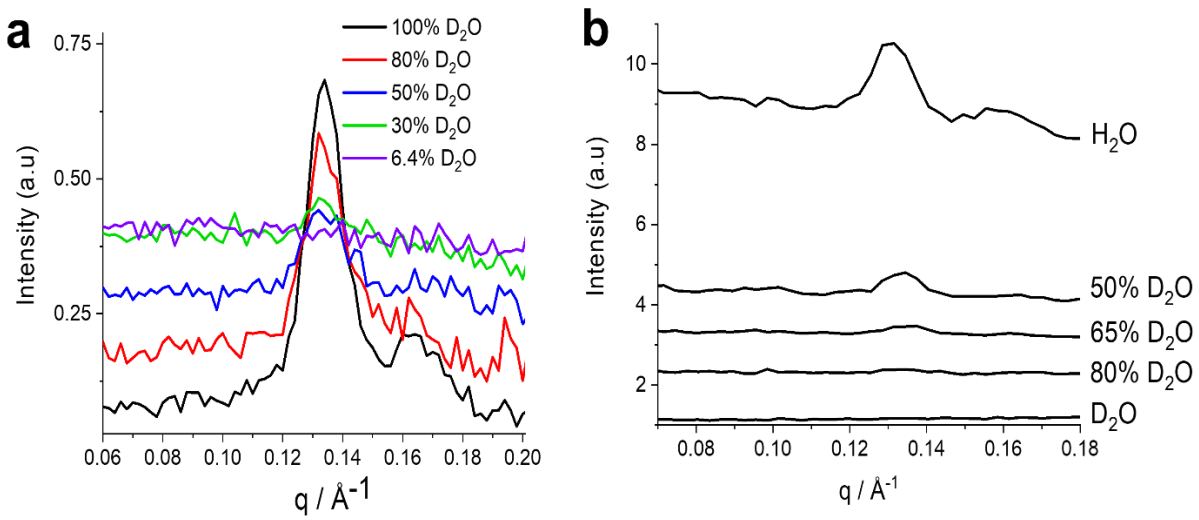

Figure 106 1D integrated SANS patterns taken in different H_2O/D_2O ratio solutions of phytantriol (a) and deuterated phytantriol (b) thin films on a Au/Si electrode.

Taking this a step further we can also create a mixture of phytantriol/D-phytantriol enabling us to manipulate the *SLD* of the template itself. This can be an incredibly useful method, enabling us to as contrast match the template to the solution or material being deposited within the template. This would allow us to selectively collect SANS patterns of individual parts of the system such as the solution, deposited material, and the template.

Phytantriol and D-phytantriol were mixed in a ratio of 76 % phytantriol and 24 % D-phytantriol which gives a scattering length density equal to that of a mixture of 30 % D_2O in H_2O. Figure 107 revealed that a mixture of phytantriol and D-phytantriol successfully forms a stable double diamond phase in different D_2O/H_2O mixtures. The lattice parameter of the template was 61.9 ± 0.8 Å and the Bragg peaks from the template are seen diminishing as the D_2O content is decreased in the solution until no scattering from the phytantriol/D-phytantriol mixture is seen with 30 % D_2O, showing a successful contrast match. This shows that we are able to successfully manipulate the scattering length density of the template and the solution. This method allows the tailoring of experiments to collect SANS of selective parts of the system.

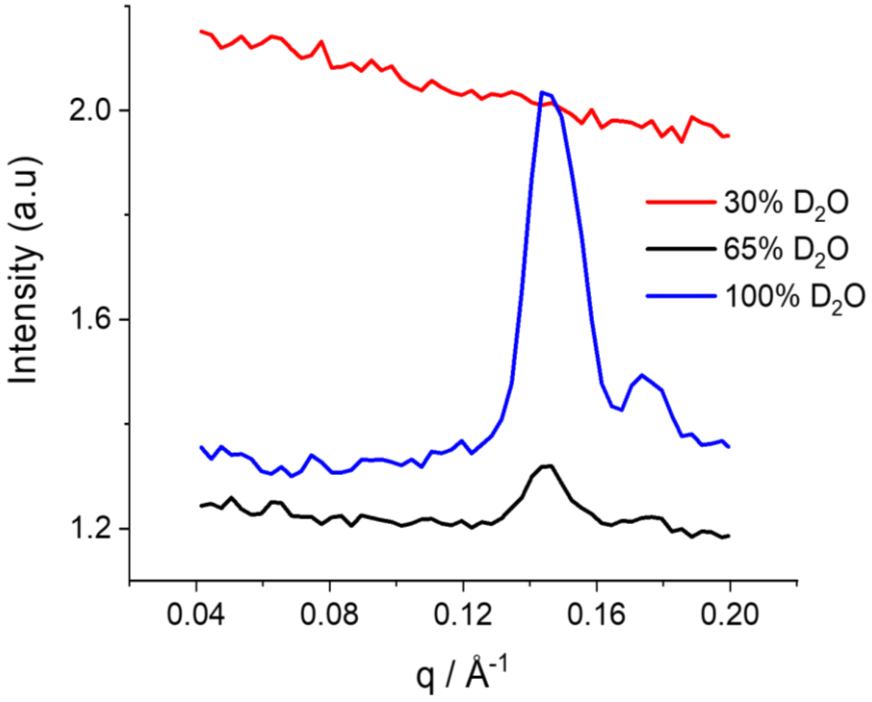

Figure 107 1D integrated SANS patterns of a 24 % D-phytantriol / 76 % phytantriol mixture thin film on a Au/Si electrode in different D_2O/H_2O ratio solutions.

As Pt, D_2O and D-phytantriol all have a very similar scattering length density we decided to electrodeposit Pt through D-Phytantriol and collect SANS of the Pt still in the template in different D_2O/H_2O ratios. The aim of this experiment was to probe the water channel in the phytantriol template that does not take part in the electrodeposition. The current understanding of why deposition only occurs in one of the double diamond's channels is that one is capped to the electrode surface and the electrolyte. This would mean that when we

change the D_2O/H_2O ratios of the solution, the electrolyte from the electrodeposition should remain in the capped channel, producing contrast to the Pt and the template.

Pt was electrodeposited on D-phytantriol modified Au/Si electrode from a solution of aqueous 8 wt% HCPA acid and the current time transient is shown in Figure 108 (a). The current time transient is typical of a successful templated electrodeposition with a steady current seen. Immediately after the deposition process the electrode was removed from the HCPA solution and instantly placed in H_2O/D_2O mixtures for SANS analysis.

The resulting SANS patterns in the solutions show that the template remained in the double diamond phase after deposition of Pt as two Bragg peaks in the ratios of $\sqrt{2}$ and $\sqrt{3}$ can be seen from the patterns in pure H_2O and 50 % D_2O in H_2O. This gives us some information about the system as it tells us that after deposition both water channels inside the double diamond phase can interact with the external solution, as if HCPA was still inside the channels after deposition, we would see peaks in the SANS in D_2O as HCPA will not contrast match with D-phytantriol, Pt or D_2O. This is an interesting result as the current understanding of the electrodeposition process within phytantriol is that the deposition occurs asymmetrically within one of the channels as the other remains blocked off to the external solution and the electrode surface.

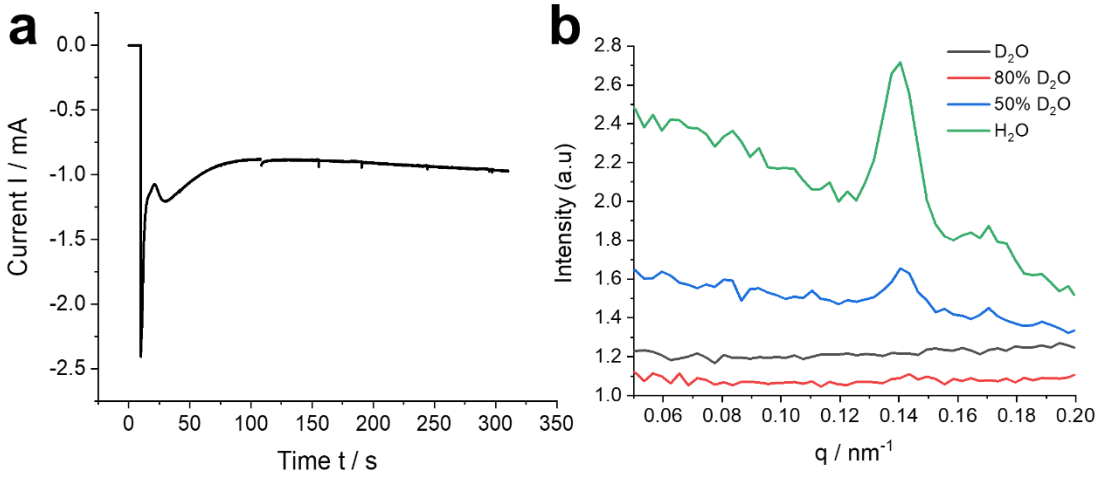

Figure 108 Time-current transient of Pt electrodeposited at a potential of -0.245 V vs SCE from a solution of 8 wt% hexachloroplatinic acid on a deuterated phytantriol modified Au/Si electrode. (a) 1D integrated SANS patterns of Pt deposited in deuterated phytantriol on a Au/Si electrode in various D_2O/H_2O ratio solutions.

These results suggest that even after deposition both channels remain open and interact with the external solution. If this closed water channel was filled with HCPA we would expect to see a Bragg peak from the single diamond phase of the individual channel. This result may challenge our understanding of why deposition only occurs within one of the water channels and a different mechanism may be responsible for this. Larsson who reported that the capping of one of the water channels in the double diamond phase, studied the system in an aqueous dispersion rather than the material being a thin film on an electrode so it may behave differently.[225]

A reason why the electrodeposition occurs asymmetrically may be due to only one channel having contact with the electrode surface. It has been shown in the literature that the double diamond phase of phytantriol is orientated with the (111) plane parallel to the electrode surface up to 2.8 ± 0.3 µm from the surface. [185] Figure 109 shows the (111) plane of the double diamond phase with the light and dark regions representing the two water channel networks running through the structure.[15] If the material was orientated, only one water channel would have access to the electrode surface. This means that the electrodeposition could only occur in one of the channels resulting in the asymmetric deposition.

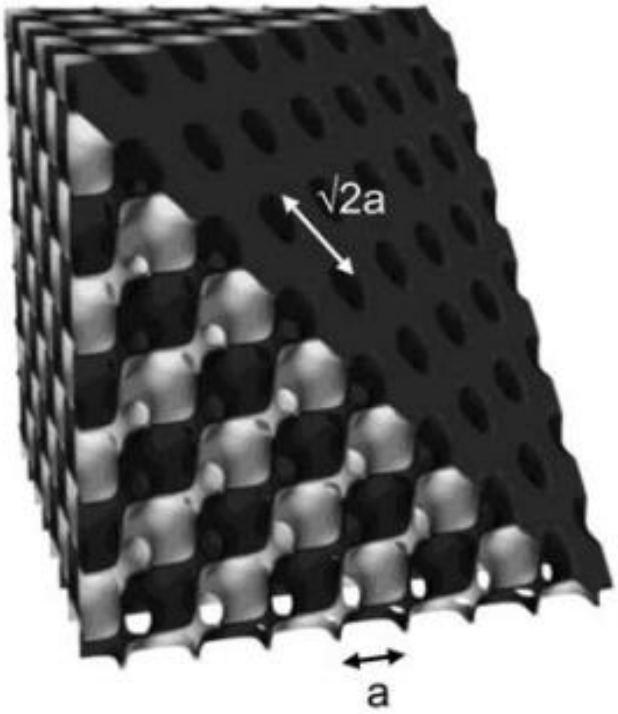

Figure 109 The (111) plane through the double diamond phase with the light and dark surfaces representing the two water channel networks. The white channel is capped at the surface. Taken from.[15]

We can also rule out that the electrodeposition of the Pt within one channel has not altered the template giving the second empty channel access to the external solution, as the SANS patterns in Figure 106 give us the same information in that when the phytantriol thin films are placed into different solutions, the new solution interacts with both water channels, otherwise we would expect to see Bragg peaks from solution remaining in one of the water channels. It can be noted that this result may be arising from the transfer of the phytantriol film from one solution to the other, however this is done as fast as possible, and the films remained wetted with the previous solution during the transfer.

It can also be noted that we do not see any Bragg peaks from the single diamond phase Pt from the SANS in H_2O which we expected to see. This could mean that the electrodeposition of Pt in the single diamond phase was not successful or that the amount of Pt present is minor compared to the amount of D-phytantriol and is under the detection limit for neutrons. To validate which reason was responsible for us not seeing single diamond Pt, the D-phytantriol was removed by soaking in ethanol and the resulting Pt film was then placed back in the neutron beam in air. The resulting SANS pattern, Figure 110 (a), shows that we do not see any peaks from Pt in the single diamond phase meaning that the deposition failed or we are unable to see scattering from the Pt. SAXS of the Pt film, Figure 110 (b), revealed that we did see Bragg peaks at the expected *q* positions for single diamond Pt and that the deposition of through D-phytantriol was in fact successful, confirming we were unable to see SANS of the Pt film. This was a disappointing result as it meant that we could not use SANS to collect information on the Pt deposited through D-phytantriol.

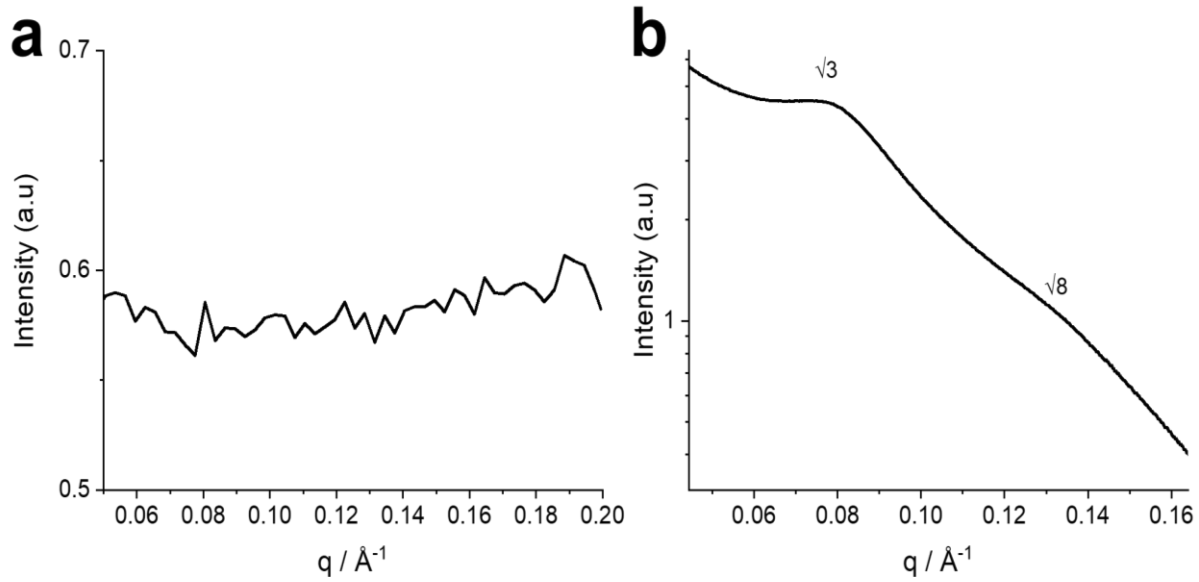

Figure 110 (a) 1D intergrated SANS pattern of Pt electrodeposited through D-phytantriol at a potential of -0.245 V vs SCE from a solution of 8 wt% hexachloroplatinic acid on a Au/Si electrode after template removal in air. (b) 1D integrated SAXS pattern of the same sample.

Overall, we successfully demonstrated that by mixing deuterated and un-deuterated phytantriol we can selectively tune the scattering length density of the material to match that of the desired solution or deposited material. Using this method, it is possible to single out the SANS of different parts of the system where SAXS cannot do this. These experiments where made possible by using a custom designed 3D printed cell in which thin film electrodes can be placed in the neutron beam in different solutions. We gathered new information about the phytantriol system with evidence suggesting that both water channels interact with external solution whereas before the assumption was this one water channel was capped.

7.5. Conclusions

Electrochemical cells which were well suited for a range of in-situ electrochemical small angle scattering experiments were successfully developed and 3D printed. The main advantages of the cells were that they could be 3D printed in one solid piece removing the need for machining multiple parts which increases cost of production and complexity. The cells were cheap and easy to use and it was possible to print a batch of multiple cells which made rapid screening of multiple samples during beamtimes at synchrotron sources quick and very efficient. The ability to customise the design of these cells in order to tailor their functionalities to suit the experimental requirements is extremely advantageous.

The cell performed well over different in-situ experiments from electrodeposition, gel formation and lipid phase monitoring on both lab-based and synchrotron radiation sources. This cell enabled us to perform complex in-situ experiments which gave us a great understanding over the studied systems.

We have demonstrated that 3D printing is an extremely powerful technique, which allows for the rapid fabrication of bespoke electrochemical cells that enable us to perform complex and dynamic in-situ experiments.

8. Conclusion

In this thesis, we have systematically explored the electrodeposition of 3D mesoporous nanomaterials through the double diamond phase of liquid crystal templates, particularly focusing on the materials CdTe, Pd and Pt. The research demonstrates the tuneability and versatility of liquid crystal templating.

Initially, there were challenges reproducing single diamond phase CdTe using the established phytantriol template method previously reported for Pt and other materials. By introducing a cosurfactant, Brij-56, the deposition process was improved, resulting in a stoichiometric thin film of CdTe with a 3D nanowire network. The material exhibited promising properties including a band gap suitable for solar photovoltaic applications.

We also demonstrated the successful electrodeposition of single diamond Pd with control over the materials lattice parameter, nanowire diameters and pore widths by adjusting the amount of Brij-56 in the template. This method produced Pd with high electroactive surfaces and tuneable catalytic activity for the formic acid oxidation reaction. This work demonstrated the ability to fine tune the properties of single diamond Pd through curvature modulation of the liquid crystal template.

The fabrication of single diamond Pt revealed its potential as an efficient catalyst for the oxygen reduction reaction in alkaline conditions. The single diamond Pt exhibited superior performance and durability compared to a commercial Pt/C catalyst, indicating its suitability for fuel cell applications. This provided a pathway in which mesoporous Pt can be produced via a one-pot synthesis method. We also explored the effect of pulse electrodeposition of Pt

through the phytantriol/Brij-56 templates and found that pulse electrodeposition enhances the uniformity of the deposited Pt measured by SAXS.

To support our experimental investigations, a novel 3D printable electrochemical cell was designed and fabricated which was tailored for in-situ small angle scattering experiments. These cells enabled rapid, cost effective and customisable setups for a wide range of in-situ electrochemical experiments, enhancing our ability to gain deeper insights into the electrodeposition process.

Overall, this thesis demonstrated the potential of soft templated electrodeposition and 3D printing technology to advance the fabrication and characterisation of nanomaterials. The findings from this work provide valuable contributions to the fields of material science and electrochemistry, demonstrating methods of producing high performance materials for catalytic applications.

References

1 I. Nandhakumar, J. M. Elliott and G. S. Attard, *Chemistry of Materials*, 2001, **13**, 3840–3842.

2 P. N. Bartlett, *Electrochemical Society Interface*, 2004, **13**, 28–33.

3 G. S. Attard, S. A. A. Leclerc, S. Maniguet, A. E. Russell, I. Nandhakumar and P. N. Bartlett, *Chemistry of Materials*, 2001, **13**, 1444–1446.

4 M. R. Burton, C. Lei, P. A. Staniec, N. J. Terrill, A. M. Squires, N. M. White and I. S. Nandhakumar, *Sci Rep*, 2017, **7**, 5–10.

5 H. M. Al-Bishri, I. S. El-Hallag and E. S. H. El-Mossalamy, *Bull Korean Chem Soc*, 2010, **31**, 3730–3734.

6 T. Gabriel, I. S. Nandhakumar and G. S. Attard, *Electrochem commun*, 2002, **4**, 610–612.

7 G. S. Attard, P. N. Bartlett, N. R. B. Coleman, J. M. Elliott, J. R. Owen and J. H. Wang, *Science (1979)*, 1997, **278**, 838–840.

8 J. Barauskas and T. Landh, *Langmuir*, 2003, **19**, 9562–9565.

9 S. Akbar, J. M. Elliott, M. Rittman and A. M. Squires, *Advanced Materials*, 2013, **25**, 1160–1164.

10 S. J. Richardson, M. R. Burton, X. Luo, P. A. Staniec, I. S. Nandhakumar, N. J. Terrill, J. M. Elliott and A. M. Squires, *Nanoscale*, 2017, **9**, 10227–10232.

11 Matthew Burton, PhD thesis, University of Southampton, 2017.

12 M. Burton, A. Selvam, J. Lawrie-Ashton, A. Squires, N. Terrill and I. Nandhakumar, *ACS Appl Mater Interfaces*, 2018, **10**, 37087–37094.

13 M. Burton, A. Selvam, J. Lawrie-Ashton, A. Squires, N. Terrill and I. Nandhakumar, *ACS Appl Mater Interfaces*, 2018, **10**, 37087–37094.

14 K. Larsson, *Curr Opin Colloid Interface Sci*, 2000, **5**, 64–69.

15 M. Rittman, M. Frischherz, F. Burgmann, P. G. Hartley and A. Squires, *Soft Matter*, 2010, **6**, 4058–4061.

16 M. R. Burton, S. J. Richardson, P. A. Staniec, N. J. Terrill, J. M. Elliott, A. M. Squires, N. M. White and I. S. Nandhakumar, *Electrochem commun*, 2017, **76**, 71–74.

17 S. Akbar, J. M. Elliott, A. M. Squires and A. Anwar, *Journal of Nanoparticle Research*, 2020, **22**, 1-9.

18 S. J. Richardson, Phd thesis, University of Reading, 2016.

19 S. J. Richardson, M. R. Burton, X. Luo, P. A. Staniec, I. S. Nandhakumar, N. J. Terrill, J. M. Elliott and A. M. Squires, *Nanoscale*, 2017, **9**, 10227–10232.

20 S. Akbar, J. Boswell, S. Waters, S. Williams, J. M. Elliott and A. M. Squires, *ACS Appl Nano Mater*, 2021, **4**, 5717–5725.

21 A. Lončar, P. Jovanovič, N. Hodnik and M. Gaberšček, *J Electrochem Soc*, 2023, **170**, 044504.

22 R. Henderson, *Q Rev Biophys*, 1995, **28**, 171–193.

23 F. Reading, *Microscopy*, 1992, 114–124.

24 A. Yoshida, Y. Kaburagi and Y. Hishiyama, *Scanning Electron Microscopy*, Tsinghua University Press Limited, 2016.

25 A. I. I. Tyler, H. M. G. Barriga, E. S. Parsons, N. L. C. McCarthy, O. Ces, R. V. Law, J. M. Seddon and N. J. Brooks, *Soft Matter*, 2015, **11**, 3279–3286.

26 T. G. Meikle, S. Yao, A. Zabara, C. E. Conn, C. J. Drummond and F. Separovic, *Nanoscale*, 2017, **9**, 2471–2478.

27 G. J. Long, *Comprehensive Coordination Chemistry II*, 2004, **2**, 83–90.

28 Scattering Length Density Calculator, https://www.ncnr.nist.gov/resources/sldcalc.html, (accessed 4 January 2024).

29 N. R. Zaccai, C. W. Sandlin, J. T. Hoopes, J. E. Curtis, P. J. Fleming, K. G. Fleming and S. Krueger, *Methods Enzymol*, 2016, **566**, 159–210.

30 T. Zdanowicz, T. Rodziewicz and M. Zabkowska-Waclawek, *Solar Energy Materials and Solar Cells*, 2005, **87**, 757–769.

31 Photovoltaics Solar Cells, https://g2voptics.com/photovoltaics-solar-cells/, (accessed 17 June 2021).

32 P. R. Pudasaini, S. K. Srivastava, Y. Zhan, F. Ruiz-Zepeda and B. Pandit, *International Journal of Photoenergy*, 2017, **2017**, 2–4.

33 E. Garnett and P. Yang, *Nano Lett*, 2010, **10**, 1082–1087.

34 A. P. Amalathas and M. M. Alkaisi, *Micromachines (Basel)*, 2019, **10**, 1–18.

35 K. Taretto and U. Rau, *Progress in Photovoltaics: Research and Applications*, 2004, **12**, 573–591.

36 E. C. Garnett and P. Yang, *J Am Chem Soc*, 2008, **130**, 9224–9225.

37 M. Marsili, S. Botti, M. Palummo, E. Degoli, O. Pulci, H. C. Weissker, M. A. L. Marques, S. Ossicini and R. Del Sole, *Journal of Physical Chemistry C*, 2013, **117**, 14229–14234.

38 J. Li, J. Gayles, N. Kioussis, Z. Zhang, C. Grein and F. Aqariden, *J Electron Mater*, 2012, **41**, 2745–2753.

39 J. Singh, PhD thesis, Sheffield Hallam Univeristy, 2011.

40 J. Britt and C. Ferekides, *Appl Phys Lett*, 1993, **62**, 2851–2852.

41 X. Wu, R. G. Dhere, D. S. Albin, T. A. Gessert, C. Dehart, J. C. Keane, A. Duda, T. J. Coutts, S. Asher, D. H. Levi, H. R. Moutinho, Y. Yan, T. Moriarty, S. Johnston, K. Emery and P. Sheldon, *17th European PVSEC*, 2001, 995–1000.

42 E. Wesoff, First Solar on the Future of Photovoltaics: Part 2, https://www.greentechmedia.com/articles/print/First-Solar-on-the-Future-of-Photovoltaics-Part-2, (accessed 15 May 2021).

43 First Solar Sets New World Record for CdTe Solar Cell Efficiency, https://investor.firstsolar.com/news/press-release-details/2013/First-Solar-Sets-New-World-Record-for-CdTe-Solar-Cell-Efficiency/default.aspx, (accessed 15 May 2021).

44 A. Rix, J. Steyl, M. J. Rudman, U. Terblanche and J. van Niekerk, *First Solar's CdTe module technology – performance, life cycle, health and safety impact assessment Centre for Renewable and Sustainable Energy Studies*, 2015.

45 G. She, T. Cai, T. Cai, L. Mu, W. Shi and W. Shi, *CrystEngComm*, 2020, **22**, 4301–4305.

46 M. L. Markham, J. J. Baumberg, D. C. Smith, X. Li, T. Gabriel, G. S. Attard and I. Nandhakumar, *Appl Phys Lett*, 2005, **86**, 1–3.

47 X. Li, I. S. Nandhakumar, T. Gabriel, G. S. Attard, M. L. Markham, D. C. Smith, J. J. Baumberg, K. Govender, P. O'Brien and D. Smyth-Boyle, *J Mater Chem*, 2006, **16**, 3207–3214.

48 I. Nandhakumar, T. Gabriel, X. Li, G. Attard, M. Markham, D. Smith and J. Baumberg, *Chemical Communications*, 2004, **4**, 1374–1375.

49 I. M. Dharmadasa, A. E. Alam, A. A. Ojo and O. K. Echendu, *Journal of Materials Science: Materials in Electronics*, 2019, **30**, 20330–20344.

50 S. S. Oluyamo, A. A. Faremi, O. I. O. Olusola and Y. A. Odusote, *Mater Today Proc*, 2019, **38**, 558–563.

51 M. Sima, I. Enculescu, C. Trautmann and R. Neumann, *Journal of Optoelectronics and Advanced Materials*, 2004, **6**, 121–125.

52 X. Li, I. S. Nandhakumar, T. Gabriel, G. S. Attard, M. L. Markham, D. C. Smith, J. J. Baumberg, K. Govender, P. O'Brien and D. Smyth-Boyle, *J Mater Chem*, 2006, **16**, 3207–3214.

53 S. Kapoor, H. Ahmad, C. M. Julien and S. S. Islam, *J Alloys Compd*, 2019, **809**, 151765.

54 X. Wang, G. Li, H. Zhu, J. C. Yu, X. Xiao and Q. Li, *Appl Catal B*, 2013, **147**, 17–21.

55 T. Ohgai, L. Gravier, X. Hoffer and J. P. Ansermet, *J Appl Electrochem*, 2005, **35**, 479–485.

56 A. W. Zhao, G. W. Meng, L. D. Zhang, T. Gao, S. H. Sun and Y. T. Pang, *Appl Phys A Mater Sci Process*, 2003, **76**, 537–539.

57 A. Smith, S. Alcock, L. Davidson, J. Emmins, J. Hiller Bardsley, P. Holloway, M. Malfois, A. Marshall, C. Pizzey, S. Rogers, O. Shebanova, T. Snow, J. Sutter, E. Williams and N. Terrill, *J Synchrotron Radiat*, 2021, **28**, 939–947.

58 R. D. Engelken and T. P. Van Doren, *J Electrochem Soc*, 1985, **132**, 2910–2919.

59 V. Dzimbeg-Malcic and Z. Barbaric-Mikocevic, Appl. Phys. Lett, 1993, **62**, 2851-2852.

60 C. D. M. Donegá and R. Koole, *Journal of Physical Chemistry C*, 2009, **113**, 6511–6520.

61 V. P. Singh, R. S. Singh and K. E. Sampson, *Nanostructured Materials for Solar Energy Conversion*, 2006, **6**, 167-190.

62 M. Singh, M. Goyal and K. Devlal, *Journal of Taibah University for Science*, 2018, **12**, 470–475.

63 Y. Mastai and G. Hodes, *J. Phys. Chem. B*, 1997, **101**, 2685-2690.

64 J. Ding, Z. Liu, X. Liu, B. Liu, J. Liu, Y. Deng, X. Han, W. Hu and C. Zhong, *Angewandte Chemie*, 2020, **132**, 5130–5139.

65 U. N and C. YX, *Chem Sci J*, 2017, **8**, 2150-3494.

66 Y. Zhu, S. Y. Ha and R. I. Masel, *J Power Sources*, 2004, **130**, 8–14.

67 S. Uhm, H. J. Lee and J. Lee, *Physical Chemistry Chemical Physics*, 2009, **11**, 9326–9336.

68 A. K. Singh, S. Singh and A. Kumar, *Catal Sci Technol*, 2016, 6, 12–40.

69 S. Manna and A. P. Antonchick, *ChemSusChem*, 2019, **12**, 3094–3098.

70 X. Chen, Y. Liu and J. Wu, *Molecular Catalysis*, 2020, **483**, 110716.

71 S. C. Perry, P. ki Leung, L. Wang and C. Ponce de León, *Curr Opin Electrochem*, 2020, 20, 88–98.

72 S. C. Perry, *Electrochemical Carbon Dioxide Reduction*, De Gruyter, 2021.

73 L. Schlapbach and A. Züttel, 2001, **414**, 353–358.

74 M. Grasemann and G. Laurenczy, *Energy Environ Sci*, 2012, **5**, 8171–8181.

75 M. Shao, J. Odell, M. Humbert, T. Yu and Y. Xia, *Journal of Physical Chemistry C*, 2013, **117**, 4172–4180.

76 X. H. Xia and T. Iwasita, *J. Electrochem. Soc*, **140**, 2559-2564 .

77 K. Jiang and W. Bin Cai, *Appl Catal B*, 2014, **147**, 185–192.

78 W. Yuan, Y. Cheng, P. K. Shen, C. M. Li and S. P. Jiang, *J Mater Chem A Mater*, 2015, **3**, 1961–1971.

79 V. Mazumder, Y. Lee and S. Sun, *Adv Funct Mater*, 2010, 20, 1224–1231.

80 T. Shen, J. Zhang, K. Chen, S. Deng and D. Wang, *Energy and Fuels*, 2020, **34**, 9137–9153.

81 L. Juárez-Marmolejo, B. Maldonado-Teodocio, M. G. M. de Oca-Yemha, M. Romero-Romo, E. M. Arce-Estrada, A. Ezeta-Mejía, M. T. Ramírez-Silva, J. Mostany and M. Palomar-Pardavé, *Catal Today*, 2022, **394–396**, 190–197.

82 Q. Wang, Y. Liao, H. Zhang, J. Li, W. Zhao and S. Chen, *J Power Sources*, 2015, **292**, 72–77.

83 G. Samjeské and M. Osawa, *Angewandte Chemie - International Edition*, 2005, **44**, 5694–5698.

84 H. Okamoto, W. Kon and Y. Mukouyama, *Journal of Physical Chemistry B*, 2005, **109**, 15659–15666.

85 J. Kim, C. Jung, C. K. Rhee and T. H. Lim, *Langmuir*, 2007, **23**, 10831–10836.

86 C. Xu, Q. Hao and H. Duan, *J Mater Chem A Mater*, 2014, **2**, 8875–8880.

87 D. Xu, S. Bliznakov, Z. Liu, J. Fang and N. Dimitrov, *Angewandte Chemie - International Edition*, 2010, **49**, 1282–1285.

88 Y. She, Z. Lu, W. Fan, S. Jewell and M. K. H. Leung, *J Mater Chem A Mater*, 2014, **2**, 3894–3898.

89 W. Zhang, H. Huang, F. Li, K. Deng and X. Wang, *J Mater Chem A Mater*, 2014, **2**, 19084–19094.

90 S. Yang, C. Shen, Y. Tian, X. Zhang and H. J. Gao, *Nanoscale*, 2014, **6**, 13154–13162.

91 M. Navlani-García, D. Salinas-Torres, F. D. Vázquez-Álvarez and D. Cazorla-Amorós, *Catal Today*, 2022, **397–399**, 428–435.

92 B. T. Sneed, A. P. Young, D. Jalalpoor, M. C. Golden, S. Mao, Y. Jiang, Y. Wang and C. K. Tsung, *ACS Nano*, 2014, **8**, 7239–7250.

93 B. S. Choi, J. Song, M. Song, B. S. Goo, Y. W. Lee, Y. Kim, H. Yang and S. W. Han, *ACS Catal*, 2019, **9**, 819–826.

94 F. Lan, D. Wang, S. Lu, J. Zhang, D. Liang, S. Peng, Y. Liu and Y. Xiang, *J Mater Chem A Mater*, 2013, **1**, 1548–1552.

95 B. Zhang, H. Peng, L. Yang, H. Li, H. Nan, Z. Liang, H. Song, H. Su, C. Li and S. Liao, *J Mater Chem A Mater*, 2015, **3**, 973–977.

96 Y. Tang, R. E. Edelmann and S. Zou, *Nanoscale*, 2014, **6**, 5630–5633.

97 Y. Suo and I.-M. Hsing, *Electrochim Acta*, 2009, **55**, 210–217.

98 W. Ju, R. Valiollahi, R. Ojani, O. Schneider and U. Stimming, *Electrocatalysis*, 2015, **7**, 149–158.

99 W. P. Zhou, A. Lewera, R. Larsen, R. I. Masel, P. S. Bagus and A. Wieckowski, *Journal of Physical Chemistry B*, 2006, **110**, 13393–13398.

100 P. N. Bartlett, B. Gollas, S. Guerin and J. Marwan, *Physical Chemistry Chemical Physics*, 2002, **4**, 3835–3842.

101 S. Guerin and G. S. Attard, *Electrochemistry Communications*, 2001, **3**, 544-548 .

102 D. A. J. Rand and R. Woods, *J Electroanal Chem Interfacial Electrochem*, 1971, **31**, 29–38.

103 M. A. Ehsan, M. Sohail, R. Jamil and A. S. Hakeem, *Electrocatalysis*, 2019, **10**, 214–221.

104 L. Xu, X. C. Wu and J. J. Zhu, *Nanotechnology*, 2008, **19,** 305601.

105 D. Sun, L. Si, G. Fu, C. Liu, D. Sun, Y. Chen, Y. Tang and T. Lu, *J Power Sources*, 2015, **280**, 141–146.

106 X. Qiu, H. Zhang, P. Wu, F. Zhang, S. Wei, D. Sun, L. Xu and Y. Tang, *Adv Funct Mater*, 2017, **27**, 1603852.

107 J. Jia, M. Shao, G. Wang, W. Deng and Z. Wen, *Electrochem commun*, 2016, **71**, 61–64.

108 N. Yang, Z. Zhang, B. Chen, Y. Huang, J. Chen, Z. Lai, Y. Chen, M. Sindoro, A. L. Wang, H. Cheng, Z. Fan, X. Liu, B. Li, Y. Zong, L. Gu and H. Zhang, *Advanced Materials*, 2017, **29**, 1700769.

109 L. Zhang, S. Il Choi, J. Tao, H. C. Peng, S. Xie, Y. Zhu, Z. Xie and Y. Xia, *Adv Funct Mater*, 2014, **24**, 7520–7529.

110 H. Xu, B. Yan, K. Zhang, J. Wang, S. Li, C. Wang, Y. Du, P. Yang, S. Jiang and S. Song, *Appl Surf Sci*, 2017, **416**, 191–199.

111 J. Ding, Z. Liu, X. Liu, B. Liu, J. Liu, Y. Deng, X. Han, W. Hu and C. Zhong, *Angewandte Chemie*, 2020, **132**, 5130–5139.

112 Y. Wang, B. Wu, Y. Gao, Y. Tang, T. Lu, W. Xing and C. Liu, *J Power Sources*, 2009, **192**, 372–375.

113 Y. Wang, X. Wu, B. Wu and Y. Gao, *J Power Sources*, 2009, **189**, 1020–1022.

114 S. Themsirimongkon, P. Waenkaew, K. Ounnunkad, J. Jakmunee, L. Fang and S. Saipanya, *Fullerenes Nanotubes and Carbon Nanostructures*, 2019, **27**, 830–845.

115 F. Li, B. Liu, Y. Shen, J. Liu, C. Zhong and W. Hu, *Catalysts*, 2011, **11**, DOI:10.3390/catal11040522.

116 L. Y. Zhang, X. Meng, W. Zhang, T. Zeng, W. Yuan and Z. Zhao, *ACS Appl Energy Mater*, 2021, **4**, 12336–12344.

117 F. K. Yang, Y. Fang, F. F. Li, W. L. Qu and C. Deng, *Dalton Transactions*, 2023, **52**, 14428–14434.

118 C. Hu and L. Dai, *Angewandte Chemie*, 2016, **128**, 11910–11933.

119 L. Yang, J. Shui, L. Du, Y. Shao, J. Liu, L. Dai and Z. Hu, *Advanced Materials*, 2019, **31**, 1804799

120 J. M. Andújar and F. Segura, *Renewable and Sustainable Energy Reviews*, 2009, **13**, 2309–2322.

121 S. Sultana, R. Hossain, K. Ahmed, P. K. Jiwanti and B. Y. Wardhana, *J Electrochem Soc*, 2023, **170**, 100509.

122 Z. Yang, H. Nie, X. Chen, X. Chen and S. Huang, *J Power Sources*, 2013, **236**, 238–249.

123 M. Liu, X. Xiao, Q. Li, L. Luo, M. Ding, B. Zhang, Y. Li, J. Zou and B. Jiang, *J Colloid Interface Sci*, 2022, **607**, 791–815.

124 Y. Wang, Y. Pang, H. Xu, A. Martinez and K. S. Chen, *Energy Environ Sci*, 2022, **15**, 2288–2328.

125 W. R. W. Daud, R. E. Rosli, E. H. Majlan, S. A. A. Hamid, R. Mohamed and T. Husaini, *Renew Energy*, 2017, **113**, 620–638.

126 F. Van Der Linden, E. Pahon, S. Morando and D. Bouquain, *J Power Sources*, 2023, **575**, 233168.

127 F. Bacon, T. Fry, *Proc. R. Soc. Lond*, 1973, **334**, 427-452.

128 B. Ruiz-Camacho, A. Medina-Ramírez, R. Fuentes-Ramírez, R. Navarro, C. Martínez Goméz and A. Pérez-Larios, *Int J Hydrogen Energy*, 2022, **47**, 30147–30159.

129 A. T. Hamada, M. F. Orhan and A. M. Kannan, *Energy Reports*, 2023, **9**, 6396–6418.

130 S. Zarabi Golkhatmi, M. I. Asghar and P. D. Lund, *Renewable and Sustainable Energy Reviews*, 2022, **161**, 112339.

131 Q. Xu, Z. Guo, L. Xia, Q. He, Z. Li, I. Temitope Bello, K. Zheng and M. Ni, *Energy Convers Manag*, 2022, **253**, 115175.

132 S. Hussain and L. Yangping, *Energy Transitions*, 2020, **4**, 113–126.

133 E. Berretti, L. Osmieri, V. Baglio, H. A. Miller, J. Filippi, F. Vizza, M. Santamaria, S. Specchia, C. Santoro and A. Lavacchi, *Electrochemical Energy Reviews*, 2023, **6**, 33.

134 L. Yaqoob, T. Noor and N. Iqbal, *RSC Adv*, 2021, **11**, 16768–16804.

135 R. N. Singh, Madhu and R. Awasthi, in *New and Future Developments in Catalysis: Batteries, Hydrogen Storage and Fuel Cells*, Elsevier B.V., 2013, 453–478.

136 S. K. Safdar Hossain, J. Saleem, M. Mudassir Ahmad Alwi, F. A. Al-Odail and M. Mozahar Hossain, *Chemical Record*, 2022, **22**, 202200045.

137 N. M. Aslam, M. S. Masdar, S. K. Kamarudin and W. R. W. Daud, *APCBEE Procedia*, 2012, **3**, 33–39.

138 N. V. Rees and R. G. Compton, *Journal of Solid State Electrochemistry*, 2011, **15**, 2095–2100.

139 A. Dessalle, J. Quílez-Bermejo, V. Fierro, F. Xu and A. Celzard, *Carbon N Y*, 2023, **203**, 237–260.

140 F. Cheng and J. Chen, *Chem Soc Rev*, 2012, **41**, 2172–2192.

141 K. A. Stoerzinger, M. Risch, B. Han and Y. Shao-Horn, *ACS Catal*, 2015, **5**, 6021–6031.

142 A. A. Gewirth and M. S. Thorum, *Inorg Chem*, 2010, **49**, 3557–3566.

143 E. Marra, H. Grimler, G. Montserrat-Sisó, R. Wreland Lindström, B. Wickman, G. Lindbergh and C. Lagergren, *Electrochim Acta*, **435**, 2022, 141376.

144 Z. Zhao, C. Chen, Z. Liu, J. Huang, M. Wu, H. Liu, Y. Li and Y. Huang, *Advanced Materials*, 2019, **31**, DOI:10.1002/adma.201808115.

145 E. Marra, H. Grimler, G. Montserrat-Sisó, R. Wreland Lindström, B. Wickman, G. Lindbergh and C. Lagergren, *Electrochim Acta*, 2022, **435**, 141376.

146 C. Sealy, *Materials Today*, 2008, **11**, 65–68.

147 N. Tachibana, Y. Yukawa, K. Morikawa, M. Kawaguchi and K. Shimanoe, *SN Appl Sci*, 2021, **3** 338.

148 K. Miyatake and Y. Shimizu, *ACS Omega*, 2017, **2**, 2085–2089.

149 Y. Shao-Horn, W. C. Sheng, S. Chen, P. J. Ferreira, E. F. Holby and D. Morgan, *Top Catal*, 2007, **46**, 285–305.

150 M. Nesselberger, S. Ashton, J. C. Meier, I. Katsounaros, K. J. J. Mayrhofer and M. Arenz, *J Am Chem Soc*, 2011, **133**, 17428–17433.

151 K. J. J. Mayrhofer, K. Hartl, V. Juhart and M. Arenz, *J Am Chem Soc*, 2009, **131**, 16348–16349.

152 A. Velázquez-Palenzuela, F. Masini, A. F. Pedersen, M. Escudero-Escribano, D. Deiana, P. Malacrida, T. W. Hansen, D. Friebel, A. Nilsson, I. E. L. Stephens and I. Chorkendorff, *J Catal*, 2015, **328**, 297–307.

153 A. S. Petersen, K. D. Jensen, H. Wan, A. Bagger, I. Chorkendorff, I. E. L. Stephens, J. Rossmeisl and M. Escudero-Escribano, *ACS Catal*, 2023, **13**, 2735–2743.

154 J. Kim, Y. Lee and S. Sun, *J Am Chem Soc*, 2010, **132**, 4996–4997.

155 C. Zhang, B. Ma, Y. Zhou and C. Wang, *Journal of Electroanalytical Chemistry*, 2020, **865**, 114142.

156 J. Kim, H. E. Kim and H. Lee, *ChemSusChem*, 2018, **11**, 104–113.

157 M. Zhu, M. T. Nguyen, W. J. Sim and T. Yonezawa, *Mater Adv*, 2022, **3**, 8967–8976.

158 Q. Sun, X. H. Li, K. X. Wang, T. N. Ye and J. S. Chen, *Energy Environ Sci*, 2023, **16**, 1838-1869.

159 B. Narayanamoorthy, B. V. V. S. P. Kumar, M. Eswaramoorthy and S. Balaji, *Mater Res Bull*, 2014, **55**, 137–145.

160 S. Sun, G. Zhang, D. Geng, Y. Chen, R. Li, M. Cai and X. Sun, *Angewandte Chemie - International Edition*, 2011, **50**, 422–426.

161 Z. Chen, M. Waje, W. Li, M. Sun and Y. Yan, in *2007 AIChE Annual Meeting*, 2007.

162 B. Roul, D. B. Gorle, G. Raj, K. Kumar, M. Kumari, K. K. Nanda and S. B. Krupanidhi, *J Mater Chem C Mater*, 2023, **11**, 11072–11081.

163 R. Sharma, Y. Wang, F. Li, J. Chamier and S. M. Andersen, *ACS Appl Energy Mater*, 2019, **2**, 6875–6882.

164 O. Diaz-Morales, T. J. P. Hersbach, C. Badan, A. C. Garcia and M. T. M. Koper, *Faraday Discuss*, 2018, **210**, 301–315.

165 R. Rizo, E. Herrero, V. Climent and J. M. Feliu, *Curr Opin Electrochem*, 2023, **38**, 101240.

166 Z. Dongping, J. Velmurugan and M. V. Mirkin, *J Am Chem Soc*, 2009, **131**, 14756–14760.

167 S. Trasatti and O. A. Petrii, *Pure & Appl. Chem*, 1991, **63**, 711–734.

168 M. Rahman, K. Inaba, G. Batnyagt, M. Saikawa, Y. Kato, R. Awata, B. Delgertsetsega, Y. Kaneta, K. Higashi, T. Uruga, Y. Iwasawa, K. Ui and T. Takeguchi, *RSC Adv*, 2021, **11**, 20601–20611.

169 Y. Hu, J. Jensen, P. Bretzler, L. Cleemann, J. Yu and Q. Li, *Electrochim Acta*, 2021, **391**, 138963.

170 Y. Zhu, J. Peng, X. Zhu, L. Bu, Q. Shao, C. W. Pao, Z. Hu, Y. Li, J. Wu and X. Huang, *Nano Lett*, 2021, **21**, 6625–6632.

171 J. Kibsgaard, Y. Gorlin, Z. Chen and T. F. Jaramillo, *J Am Chem Soc*, 2012, **134**, 7758–7765.

172 X. Lyu, W. N. Zhang, G. Li, B. W. Shi, Y. N. Zhang, H. Chen, S. C. Li and X. Wang, *ACS Appl Nano Mater*, 2020, **3**, 8586–8591.

173 D. Chen, Z. Li, Y. Zhou, X. Ma, H. Lin, W. Ying and X. Peng, *Chemical Communications*, 2020, **56**, 4898–4901.

174 Y. Xie, Y. Yang, D. A. Muller, H. D. Abrunã, N. Dimitrov and J. Fang, *ACS Catal*, 2020, **10**, 9967–9976.

175 W. Jiao, C. Chen, W. You, G. Chen, S. Xue, J. Zhang, J. Liu, Y. Feng, P. Wang, Y. Wang, H. Wen and R. Che, *Appl Catal B*, 2020, **262**, 118298.

176 Z. Li, W. Niu, Z. Yang, N. Zaman, W. Samarakoon, M. Wang, A. Kara, M. Lucero, M. V. Vyas, H. Cao, H. Zhou, G. E. Sterbinsky, Z. Feng, Y. Du and Y. Yang, *Energy Environ Sci*, 2020, **13**, 884–895.

177 Z. Cui, Y. Li, G. Fu, X. Li and J. B. Goodenough, *Advanced Materials*, 2017, 29, 1702385.

178 Z. Dong, M. Li, W. Zhang, Y. Liu, Y. Wang, C. Qin, L. Yu, J. Yang, X. Zhang and X. Dai, *ChemCatChem*, 2019, **11**, 6039–6050.

179 C. Han, Q. Li, D. Wang, Q. Lu, Z. Xing and X. Yang, *Small*, 2018, **14**, 1703642.

180 Y. Yuan, J. Wang, S. Adimi, H. Shen, T. Thomas, R. Ma, J. P. Attfield and M. Yang, *Nat Mater*, 2020, **19**, 282–286.

181 Q. Lai, J. Zheng, Z. Tang, D. Bi, J. Zhao and Y. Liang, *Angewandte Chemie - International Edition*, 2020, **59**, 11999–12006.

182 W. Zang, A. Sumboja, Y. Ma, H. Zhang, Y. Wu, S. Wu, H. Wu, Z. Liu, C. Guan, J. Wang and S. J. Pennycook, *ACS Catal*, 2018, **8**, 8961–8969.

183 Z. Jin, H. Nie, Z. Yang, J. Zhang, Z. Liu, X. Xu and S. Huang, *Nanoscale*, 2012, **4**, 6455–6460.

184 M. Yang, H. Chen, D. Yang, Y. Gao and H. Li, *RSC Adv*, 2016, **6**, 97259–97265.

185 S. J. Richardson, M. R. Burton, P. A. Staniec, I. S. Nandhakumar, N. J. Terrill, J. M. Elliott and A. M. Squires, *Nanoscale*, 2016, **8**, 2850–2856.

186 A. Esmaeili, M. Almasi Kashi, A. Ramazani and A. H. Montazer, *J Magn Magn Mater*, 2016, **397**, 64–72.

187 K.-R. Yeo, J. Eo, M. J. Kim and S.-K. Kim, *J Electrochem Soc*, 2022, **169**, 112502.

188 E. V. A. Premalal, R. M. G. Rajapakse and A. Konno, *Electrochim Acta*, 2011, **56**, 9180–9185.

189 F. Ye, L. Chen, J. Li, J. Li and X. Wang, *Electrochem commun*, 2008, **10**, 476–479.

190 A. Sharma, S. Bhattacharya, S. Das and K. Das, *Surface Engineering*, 2016, **32**, 378–384.

191 F. Ye, J. Li, T. Wang, Y. Liu, H. Wei, J. Li and X. Wang, *Journal of Physical Chemistry C*, 2008, **112**, 12894–12898.

192 F. Cheng, H. Wang, Z. Sun, M. Ning, Z. Cai and M. Zhang, *Electrochem commun*, 2008, **10**, 798–801.

193 A. N. Belov, S. A. Gavrilov, V. I. Shevyakov and E. N. Redichev, *Appl Phys A Mater Sci Process*, 2011, **102**, 219–223.

194 H. Yang, E. O. Fey, B. D. Trimm, N. Dimitrov and M. S. Whittingham, *J Power Sources*, 2014, **272**, 900–908.

195 R. Hessam, P. Najafisayar and S. S. Rasouli, *Mater Renew Sustain Energy*, 2022, **11**, 259–266.

196 M. Almasi Kashi, A. Ramazani, F. Najafabadi and Z. Heydari, *Appl Surf Sci*, 2011, **257**, 9347–9350.

197 J. Azevedo, C. Sousa, J. Ventura, A. Apolinario, A. Mendes and J. Araujo, *Mater Res Express*, 2014, **1**, 015028.

198 G. Sauer, G. Brehm, S. Schneider, K. Nielsch, R. B. Wehrspohn, J. Choi, H. Hofmeister and U. Gösele, *J Appl Phys*, 2002, **91**, 3243–3247.

199 D. Dobrev, J. Vetter, N. Angert and R. Neumann, *Appl. Phys. A*, 1999, **69**, 233–237.

200 J. Biggins, M. Warner and K. Bhattacharya, *Phys Rev Lett*, 2009, **103**, 037802.

201 S. Vignolini, N. Yufa, P. Cunha, S. Guldin, I. Rushkin, M. Stefik, K. Hur, U. Wiesner, J. Baumberg and U. Steiner, *Advanced Materials*, 2012, **24**, 23-27.

202 J. Dolan, B. Wilts, S. Vignolini, J. Baumberg, U. Steiner and T. Wilkinson, *Adv Opt Mater*, 2015, **3**, 12–32.

203 P. Prins, J. van der Bok, T. van Swieten, S. M. Hinterding, A. Smith, A. Petukhov, A. Meijerink and F. Rabouw, *Angewandte Chemie - International Edition*, 2023, **62**, 1–8.

204 H. Barriga, I. Pence, M. Holme, J. Doutch, J. Penders, V. Nele, M. Thomas, M. Carroni and M. Stevens, *Advanced Materials*, 2022, **34**, 2200839.

205 T. Stawski, R. Besselink, K. Chatzipanagis, J. Hövelmann, L. Benning and A. Van Driessche, *Journal of Physical Chemistry C*, 2020, **124**, 8411–8422.

206 D. Genova, R. Brooker, H. Mader, J. Drewitt, A. Longo, J. Deubener, D. Neuville, S. Fanara, O. Shebanova, S. Anzellini, F. Arzilli, E. Bamber, L. Hennet, G. La Spina and N. Miyajima, *Sci Adv*, 2020, **6**, eabb0413.

207 J. Guild, S. Knox, S. Burholt, E. Hilton, N. Terrill, S. Schroeder and N. Warren, *Macromolecules*, **56**, 2023, 6426-6435.

208 M. Povey, R. Ettelaie, K. Lewtas, A. Price, X. Lai and F. Sheng, *Journal of Chemical Physics*, 2023, **158**, 174501.

209 X. Zeng, B. Glettner, U. Baumeister, B. Chen, G. Ungar, F. Liu and C. Tschierske, *Nat Chem*, 2023, **15**, 625–632.

210 A. Yaghmur, B. V. Tran and S. M. Moghimi, *Molecules*, 2020, **25**, 1–14.

211 K. Le Vay, B. Carter, D. Watkins, T. Dora Tang, V. Ting, H. Cölfen, R. Rambo, A. Jmith, J. Ross Anderson and A. Perriman, *J Am Chem Soc*, 2020, **142**, 20640–20650.

212 G. Day, W. Zhang, B. Carter, W. Xiao, M. Sambrook and A. Perriman, *ACS Appl Mater Interfaces*, 2021, **13**, 60433–60445.

213 Guide to Stereolithography (SLA) 3D Printing, https://formlabs.com/uk/blog/ultimate-guide-to-stereolithography-sla-3d-printing/, (accessed 18 June 2023).

214 Anycubic UV Resin for 3D printing, https://uk.anycubic.com/collections/materials/products/colored-uv-resin-0-5kg?variant=44184023302429, (accessed 18 June 2023).

215 T. Asset, C. Gommes, J. Drnec, P. Bordet, R. Chattot, I. Martens, J. Nelayah, N. Job, F. Maillard and L. Dubau, *ACS Catal*, 2019, **9**, 160–167.

216 M. Bogar, I. Khalakhan, A. Gambitta, Y. Yakovlev and H. Amenitsch, *J Power Sources*, 2020, **477**, 229030.

217 C. Koczwara, C. Prehal, S. Haas, P. Boesecke, N. Huesing and O. Paris, *ACS Appl Mater Interfaces*, 2019, **11**, 42214-42220.

218 G. O. Park, J. Yoon, E. Park, S. Bin Park, H. Kiim, K. H. Kim, X. Jin, T. J. Shin, H. Kim, W. S. Yoon and J. M. Kim, *ACS Nano*, 2015, **9**, 5470–5477.

219 G. Möhl, E. Metwalli and P. Müller-Buschbaum, *ACS Energy Lett*, 2018, **3**, 1525–1530.

220 W. Brant, S. Schmid, G. Du, Q. Gu and N. Sharma, *J Power Sources*, 2013, **244**, 109–114.

221 X. Wang, H. Jungbluth, G. Goerigk and W. Schilling, *J Mol Struct*, 1996, **383**, 283–289.

222 A. Braun, S. Shrout, A. Fowlks, B. Osaisai, S. Seifert, E. Granlund and E. Cairns, *J Synchrotron Radiat*, 2003, **10**, 320–325.

223 C. Prehal, D. Weingarth, E. Perre, R. Lechner, H. Amenitsch, O. Paris and V. Presser, *Energy Environ Sci*, 2015, **8**, 1725–1735.

224 Courtenay Patterson, *PhD thesis, University of Glasgow, 2023.*

225 S. Richardson, P. Staniec, G. Newby, N. Terrill, J. Elliott, A. Squires and W. Góźdź, *Langmuir*, 2014, **30**, 13510–13515.